MICRORING RESONATOR BASED PHOTONIC DEVICES USING HIGH-CONTRAST WAVEGUIDES

STEVANUS DARMAWAN

Supervised by
A/P Chin Mee Koy

School of Electrical & Electronic Engineering

A thesis submitted to the Nanyang Technological University
in fulfillment of the requirements for the degree of
Doctor of Philosophy

2009

Untuk Papi & Mami

ACKNOWLEDGMENT

First of all, I would like to thank NTU for providing me an opportunity to study and conduct my research successfully. I wish to express my heartfelt gratitude to my supervisor, Prof. Chin Mee Koy, for his kind encouragement, invaluable guidance, and precious time with me that have resulted in outstanding progress of the whole work. My gratitude also goes to the *Singapore Millennium Foundation* for their generous financial support given through a scholarship.

Great thanks to my colleagues: Mr. Landobasa Yosef Mario, Ms. Lee Shuh Ying, Dr. Lee Chee Wei, and Mr. Ang Yong Long, for our wonderful fellowship in research. I would like to thank Dr. Pieter Dumon and Prof. Roel Baets for the fruitful collaboration we had with Ghent University and IMEC in Belgium. Thanks for Dr. Jean-Marc Fedeli for his assistance in fabricating some of our devices in CEA LETI, France. I would also like to thank the lab technicians, Yvonne and Kat for their assistance in dealing with administration related works. My gratefulness also extended to all the students and staffs in Photonics Research Centre (PhRC) and Microfabrication Facilities (MFF) for making our working environment a pleasant one.

Last but not least, I would like to thank my beloved family, father, mother, brothers and my fiancée, for their unfailing love and prayers during my study in NTU, Singapore. Eventually, I would like to thank the Lord for all the blessings He has given to me. Soli Deo Gloria.

ABSTRACT

Photonics as a field began in the 1960s with the invention of laser. The inventions of semiconductor laser diode in the 1970s and Erbium-doped fiber amplifier (EDFA) in the late 1980s have revolutionized the telecommunication of the late 20th century and provided the infrastructure for the internet worldwide. The evolution of photonics follows the path of electronics, which is towards device miniaturization and integrated circuits (IC). However, Photonic Integrated Circuits (PIC) has developed much more slowly than the Electronic Integrated Circuit (EIC), since PIC involves many more diverse devices each with different and often contrasting requirements. The various devices form important building blocks used to realize even more complex circuits which may perform wider range of functionalities on optical signals used in various applications, such as optical communication, instrumentation, sensing, and signal processing. Some of these circuits, mainly based on passive devices, are the subject of this thesis, although some theoretical works on their active applications are also included.

In this thesis, we introduce and develop many devices concepts derived from basic building blocks such as directional couplers (DC), multi-mode interferometers (MMI), Mach-Zehnder interferometers (MZI) and microring resonators (μRR). These devices are used in a wide range of applications from switches to sensors. The thrust of the research is to combine these building blocks in novel ways that tap their synergistic interactions to achieve innovative circuit configurations with improved performance and functionality.

The thesis is focused, in particular, on the combination of microring resonators and Mach-Zehnder interferometers. Microring resonators are tiny ring-shaped waveguides that has the function of a simple optical wavelength filter. I began my research by investigating the concept of *critical coupling* and *oscillation* condition in coupled resonators. Critical coupling refers to the critical value of the coupling coefficient in a lossy ring at which complete destructive interference takes place precisely around resonance, producing effectively zero transmission output. Physically, it corresponds to the situation in which the light fully resonates and vanishes inside the cavity due to loss. The oscillation refers to the condition in which the transmission is theoretically infinite (i.e., the inverse of critical coupling) in the presence of optical gain. The concept of critical coupling and oscillation was first borrowed from microwave field and applied to one-ring-one-bus (1R1B) system by Yariv [1, 2]. Thus, it is of logical consequence to extend the study to higher-order ring-resonator systems consisting of multiple coupled rings. In tandem, the pole-zero approach is used as a convenient tool to complement the study, as the zeros (poles) are directly associated with the critical coupling (oscillation) condition.

Filter design based on coupled resonators has always been an important field in research driven by the need to meet stringent requirements of optical communication systems. An ideal optical filter must have a square and flat-top transmission band, and sharp roll-off and sidelobe-free stopbands. Most of the filters found in the literature are based linear coupled resonators, which can be arranged in mutually coupled (Type I) or periodically coupled (Type II) fashion. “Box-like” response can be engineered by tailoring the individual coupling coefficients precisely according to fixed formulas, a process known as apodization. These periodic arrays of resonators, like other more conventional periodic dielectric structures, also behave like a photonic crystal and exhibit photonic bandgap properties. Our innovation is to combine the Type I and the Type II arrays and devise a hybrid 2D-RR array which is theoretically shown to be capable of realizing an ideal bandpass filter profile. Such ideal response is made possible due to complementary and non-overlapping photonic bandgaps of both Type I and Type II filters. In the perspective of the pole-zero approach, it can also be seen that although apodization is not directly applied, the 2D-RR array exhibits similar effect of apodization to the ones in conventional apodized filters. We also combine the 2D-RR arrays with the MZI and study the nonlinear phase enhancement which translates into the amplitude variation in the MZI output. The proposed structure can be regarded as a generalized form of ring-coupled MZI.

The most important work in my thesis is the conceptualization of two novel ring-based MZI devices: (1) Nested-ring Mach-Zehnder interferometer (NRMZI) and (2) Two-ring Mach-Zehnder interferometer (2RMZI). These two devices combine the novel phase response of the coupled resonators with the simplicity and flexibility of MZI to give unique transmission properties not achievable by the individual components. The nested ring, for instance, is expected to exhibit a periodic phase response with sharp nonlinear phase changes. This phase response can be translated to a power spectrum with flat-top filter-like response when the nested ring is coupled to one arm of a MZI. The flat-top response is shaped by the double-Fano resonances, created by interference among the different optical pathways available in the nested-ring (i.e., the inner-loop and the outer-loop resonances) and in the MZI. In this work, we show that the NRMZI is capable of producing such a box-like transmission spectrum with sharp transition edges, which is highly desirable as a “digital” sensor or switch as well as a filter. On the other hand, the 2RMZI is composed of a two-ring structure which is coupled with the MZI. The two-ring configuration alone is designed to highly localize the light in the outer-ring (i.e., anti-resonance in the inner-ring), resulting in a significant resonance narrowing. By combining the two-ring configuration with the MZI, it is possible achieve a more complete destructive interference off the narrow resonance due to the additional interference contributed by the optical pathway in the MZI, thereby giving improved resonance characteristic in terms of finesse, contrast ratio (CR), and modulation depth (MD). The CR (MD) is defined as the ratio (difference) between the maximum and minimum transmissions. In collaboration with Dr. Pieter Dumon and Prof. Roel Baets from University of Ghent, IMEC of Belgium, and with assistance from Dr. Jean-Marc Fedeli of CEA LETI (France), the NRMZI and the 2RMZI devices were fabricated and

demonstrated on silicon-on-insulator (SOI) material using complementary metal–oxide–semiconductor (CMOS) based deep UV lithography. By taking account of the intrinsic phase imbalance between the MZI arms, good agreement is obtained between theory and experiment verifying the analysis and the assumptions used.

Lastly, we propose a theoretical scheme for bistability engineering in ring-coupled MZI devices, namely one-ring MZI (1RMZI) and 2RMZI devices. The aim is to achieve bistability switching with much lower switching threshold and reasonably high extinction ratio (ER) and modulation depth (MD). Their performance in terms of ER, MD, optical bandwidth and switching threshold are presented in a best case scenario.

In summary, in my research I have conceptualized and designed several innovative optical integrated circuits based on a combination of ring resonators, and of ring resonators and Mach-Zehnder interferometer, that exhibit better performance and functionality beyond what the individual components are capable of. Some of these circuits have been fabricated and tested in the laboratory to be in good agreement with the theory. The research has resulted in 13 journal and 7 conference publications.

TABLE OF CONTENTS

LIST OF FIGURES AND TABLES

Figures:

Tables:

Chapter 1

Overview, objectives, and significant contributions

1.1. Motivation

Photonics as a field began in 1960 with the invention of laser. Optical communication took off with the invention of semiconductor laser diodes in the 1970s and the development of optical fibers as a medium for transmitting information using light beams, and culminated with the invention of Erbium-doped fiber amplifier (EDFA) in the late 1980s. These inventions formed an important basis for the telecommunication revolution of the late 20th century, and provided the infrastructure for the internet worldwide.

The evolution of photonics follows the path of electronics, which has developed much earlier. The trend in electronics towards device miniaturization and integrated circuits (IC) applies to photonic devices as well, because of the common benefits that derive from miniaturization and integration. Like electronic IC, photonic integration reduces cost and improves reliability and footprint by using batch fabrication of many more smaller devices on the same chip, drastically cutting back the cost of packaging and interconnection of otherwise discrete devices. However, Photonic Integrated Circuits (PIC) has developed more slowly as it is much more challenging, involving the integration of many more diverse devices each with different and often contrasting requirements. These devices include active and passive components which range from light sources, detectors, and amplifiers, to beam

splitters, gratings, couplers, polarizers and interferometers. The various devices are the fundamental building blocks used to realize more complex circuits which perform a wide range of functionalities on optical signals used in various applications, such as optical communication, instrumentation, sensing, and signal processing. In particular, the integration of both active and passive devices may require different material properties that complicate monolithic integration. Hence, PIC has developed largely in small incremental steps, and finds niche applications in specialized circuits involving a relatively small number of similar devices. Some of these circuits will be discussed below, where they form the backbone of this thesis. As the range of possible devices and circuits are vast, we will focus mostly on passive devices, although some active devices will also be discussed.

1.2. Waveguide materials and high-contrast waveguides

The types of devices and their applications are largely determined by the material. Some materials like III-V compound semiconductors are optimum for active (e.g. light-emitting) devices, while others, e.g., polymers, glass and silicon, have more limited applications. Some polymers have high nonlinear optical properties and are ideal for all-optical switches [17]. Glass has very low loss and is ideal for long passive waveguides (e.g. optical delay lines). Silicon is the most common semiconductor with the most matured industrial process technology ever developed. The choice of materials is wide-ranging and is largely driven by application and fabrication considerations.

In this thesis, we introduce and develop many device concepts that are applicable to various material systems – they are material-agnostic. Some of the devices discussed in this thesis, however, are realized in SOI waveguides because of the availability of industrial CMOS foundry process. They were fabricated through a collaboration with University of Ghent and IMEC of Belgium, and CEA LETI of France, as part of the European e-Pixnet research platform [16].

In optical circuits, light is guided in optical waveguides fabricated in the same material as the devices (which are often waveguides themselves). The strength of guiding depends on the refractive index difference between the waveguide core and the surrounding (cladding). Waveguides with high index difference (say, more than 2:1) are referred to as high index contrast waveguides. Only high contrast waveguides are capable of bending light around sharp corners with minimal radiation loss, and hence they are essential components for making very compact devices and circuits involving many curves and bends, and necessary ingredients for device miniaturization. Some examples are S-curves used in making Y branches (splitters) and ring waveguides used to make ring resonators (RR) or lasers, which will be discussed in the next section.

1.2.1. SOI waveguides

Silicon-on-insulator (SOI) is a high contrast waveguide based on silicon. It is formed by growing a thick buffer (>1μm) layer of silicon oxide (SiO_2) on the silicon substrate, followed by a relatively thin

core layer of silicon (Si). The waveguide is then formed by lithographic patterning and dry etching. After etching, the waveguide may be covered with another layer of SiO_2 for passivation. Such embedded waveguide is sometimes known as a "photonic wire". The index contrast is that between Si (n~3.5) and SiO_2 (n~1.45), hence has a value greater than 2. If the etched waveguide sidewall is exposed to air, then the index contrast in the lateral direction is even greater. The sidewall may be etched all the way through the core layer, in which case the waveguide is called a *ridge* waveguide, otherwise it is called a *rib* waveguide [Fig.1.1].

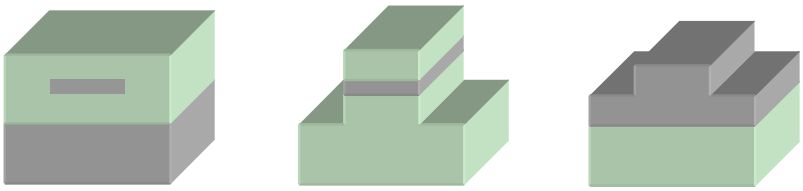

(a) (c)

Fig. 1.1(a) 'Photonic wire' waveguide, (b) ridge waveguide, (c) rib waveguide.

In actual devices, waveguide made of high index materials tends to have higher loss, especially when the sidewall is directly exposed to air. The loss is mainly due to scattering from surface roughness. The effect of roughness is reduced if the sidewall is covered with SiO_2, since the index difference is then smaller. The loss is even greater when the waveguide cross section dimension is small, such as is required of a *single-mode* waveguide. The typical dimension of a single-mode waveguide is 0.4 μm squared. Such a small waveguide is less confining hence the field amplitude at the sidewall is greater. A smooth sidewall is thus essential to minimizing the waveguide loss. Using state-of-the-art CMOS process with deep-UV lithography, a loss less than 1 dB/cm can be achieved routinely, with thinner SOI waveguides (~200nm thick Si photonic wire) [18].

Silicon is not just a passive waveguide material. Although it has an indirect bandgap, it is a good absorber. Its bandgap is 1.12eV (λ~1.1μm), hence is transparent at the telecom wavelength of 1.5 μm. However, 1.5μm is more than half-bandgap hence two photon absorption (TPA) can occur under strong laser excitation. This TPA is generally described by the expression [19, 20]

$$\partial I / \partial z = -(\alpha + \alpha_f) I - \beta I^2 \tag{1.1}$$

where I is the intensity of the light, α and α_f are the linear propagation loss and free-carrier absorption loss respectively, and β is the TPA coefficient in silicon.

The TPA is associated with an index change or refractive effect which can be useful for optical switching or modulation. Such index change can also be achieved by injecting electrical carriers (electrons or holes) into the silicon. The plasma effect causes an index change proportional to the carrier concentrations [5, 21]

$$\Delta n = \Delta n_e + \Delta n_h = -[8.8\times10^{-22}\Delta N + 8.5\times10^{-18}\Delta P^{0.8}] \quad (1.2)$$

where Δn_e is the refractive-index change due to electron concentration change, Δn_h is the refractive-index change due to hole concentration change, ΔN (cm^{-3}) is the electron concentration change, and ΔP (cm^{-3}) is the hole-concentration change.

1.3. Fundamental devices

The high contrast waveguides are the backbone for many compact fundamental devices that are, in turn, the fundamental building blocks for several important PIC. Three examples are discussed in this section.

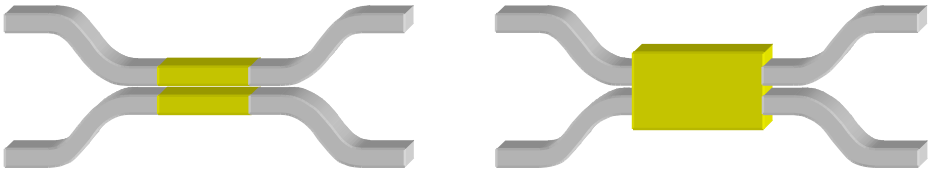

Fig. 1.2. The schematic of conventional directional coupler (left) and multi-mode interferometer (right).

Fig. 1.2 shows a directional coupler (DC) [22] and a multi-mode interference (MMI) coupler, which are two of the most basic devices for optical signal routing and processing. In particular, since its introduction in 1995 by Soldano and Penning [23], MMI has been widely used in power coupling, splitting, switching and coarse wavelength-division multiplexing, due to its compactness, polarization insensitivity and higher fabrication tolerance relative to DCs. Traditionally, these devices have been made in rib or buried waveguides which are weakly guiding. Hence, the resulting devices tend to be large, especially where waveguide bends are involved. In recent years, with increasing focus on photonic integration, strongly guiding high contrast waveguides are increasingly being used as building blocks for optical devices. For examples, using single-mode high-contrast waveguides, MMI and DCs with coupling lengths as small as 20μm [24, 25] and bends with radii of a few microns have been demonstrated [26].

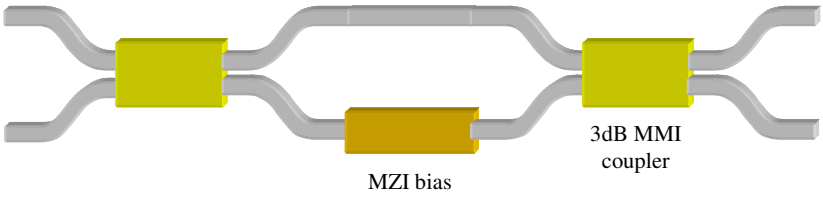

Fig. 1.3. Mach-Zehnder interferometer based on 3dB MMI coupler.

Fig. 1.3 shows a Mach-Zehnder interferometer (MZI), which is a common device that can be used as an optical modulator, switch, or sensor, and can be simply constructed, from two MMI and several S-bends and straight guides. The overall length of an MZI can be just a few hundred microns using high contrast waveguides, hence making a cascaded MZI structure in a small footprint feasible. Such a cascaded MZI device can be used as a wavelength filter with customized spectral output profile [27, 28].

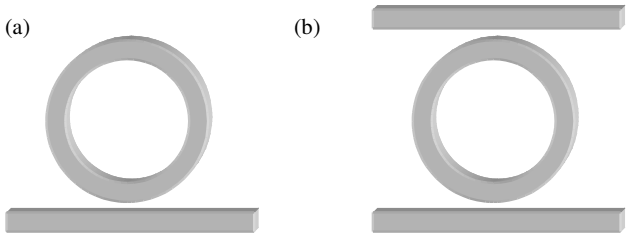

Fig. 1.4. A single ring-resonator configuration forming as: (a) one-ring-one-bus (1R1B) and (b) one-ring-two-bus (1R2B). The 1R2B configuration is the integrated analog of Fabry-Perot etalon.

An optical filter is an important basic device for wavelength division multiplexing (WDM) optical communication systems. A basic configuration of such a filter is the Fabry-Perot (FP) etalon which consists simply of two parallel mirrors separated by a small gap. The mirrors form a cavity in which photons can resonate giving full transmission when the constructive interference condition is met, hence acting as a wavelength-selective filter with periodic passbands. If the gap size is tunable then so is the filter. In integrated optics, an FP etalon can be realized using a ring cavity coupled with two bus waveguides (we refer to this as 1R2B), as shown in Fig 1.4(b). The evanescent coupling between the bus and the ring is equivalent to the transmittivity of the mirror. Since the evanescent coupling is very sensitive to the gap size, it may be easier to use the MMI as the coupler [29-31]. The circumference of the ring is the cavity length which determines the resonance wavelengths and the free spectral range (FSR) of the filter. With SOI high contrast waveguides, the MMI can be ultra-compact and the ring can have a radius as small as 1.5 μm [32], hence capable of giving a very large FSR that encompasses the full C+L band in WDM systems. The small size of the ring cavities also means that a large array of them still has a small footprint, hence it is advantageous to design complex arrayed structures to achieve desired properties such as a “box-like” spectral profile which is superior to the simple Lorentzian profile of a single-ring filter. The purposeful design of coupled structures making use of interaction between the coupled rings is also a possible source of new phenomena and functionalities, some of which will be discussed in later chapters of this thesis. A particular example is a simple two-ring structure that can give rise to resonance enhancement, which is discussed in Chapter 6.

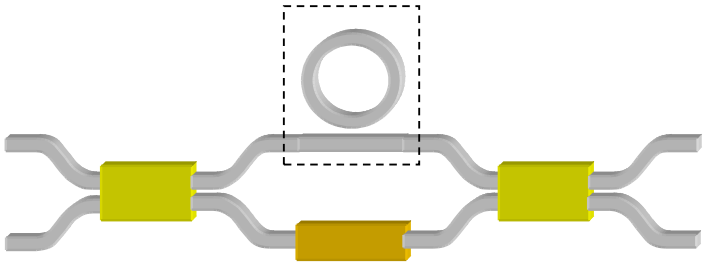

Fig. 1.5. Ring enhanced Mach-Zehnder interferometer (REMZI).

Novel applications often emerge by combining different devices together. An example is the combination of MZI and ring resonator (RR), the simplest configuration of which is shown in Fig. 1.5, known as the ring-enhanced MZI (REMZI) [33], or the one-ring MZI (1RMZI). Ideally, the RR should have no loss, and being coupled only to one bus waveguide, it acts as an all-pass filter with a phase-only response on resonance. REMZI was first proposed to enhance the sensitivity of MZI as an optical sensor, making use of the resonant phase response of the RR. The MZI itself gives two complementary outputs and provides the flexibility where a phase bias can be introduced in the other arm to generate asymmetric resonances known as *Fano* resonances [34-36]. Such devices have been experimentally realized in the AlGaAs platform [6, 7]. Variations of this basic structure, including the use of more than one ring and different ring configurations, are shown to lead to novel filter profile and even the possibility of very efficient bistability switching. In the thesis, we have demonstrated similar ring-based MZI devices in SOI material. These will be discussed in Chapters 5 and 6.

In summary, the focus of this thesis is the study of a combination of these basic devices: (i) MMI, (ii) MZI, and (iii) coupled-resonators, with the objective of bringing out the synergies of integration to achieve greater functionality and novel applications.

1.4. Literature review

As MZI and MMI are conventional devices with a long history and for which the principles are well established, the literature review will focus on developments of the ring resonators which are relatively recent. Advances in this area have been made possible by nanofabrication technology which is essential for realizing the sub-micron high-contrast waveguide devices.

Earlier work on coupled microring resonators was carried out by many researchers such as: B. E. Little [3, 37-39], J. E. Heebner [40, 41], J. Poon [42-45], Y. Chen [14, 46], F. Xia [4, 47], Grover [48], C. K. Madsen [27], S. Orta [49], A. Melloni [50, 51], M. Lipson [52], and J. Scheuer [53], and so on, with the focus largely on filters and their designs. In general, two common arrays of identical resonators have been used to realize high-order filters with sharp out-of-band rejection: (1) Where the each rings are mutually coupled and light propagates from ring to ring when they are resonant [3, 42, 49, 54, 55]. We refer to this as Type I. In the literature it is also sometimes called coupled-resonator optical waveguide (CROW). (2) Where the rings are periodically coupled to one or two bus

waveguides with periodic spacing [37, 40, 41, 50, 56, 57], a configuration which allows the microrings to be indirectly coupled via the bus waveguide. We refer to this as Type II. For a finite array, good sideband suppression can be achieved only if the coupling coefficients are varied from ring to ring in a definite pattern, a process known as *apodization* [27, 49].

Much effort is needed to minimize the waveguide loss which is detrimental to large arrays. A technique has been to use special polymer-based material known as Hydex to achieve very good control and low loss in generating up to 11 coupled rings [3]. These filters exhibit low loss, flat tops and out-of-band rejection ratios that can exceed 80dB which is very suitable for commercial applications, as shown in Fig. 1.6.

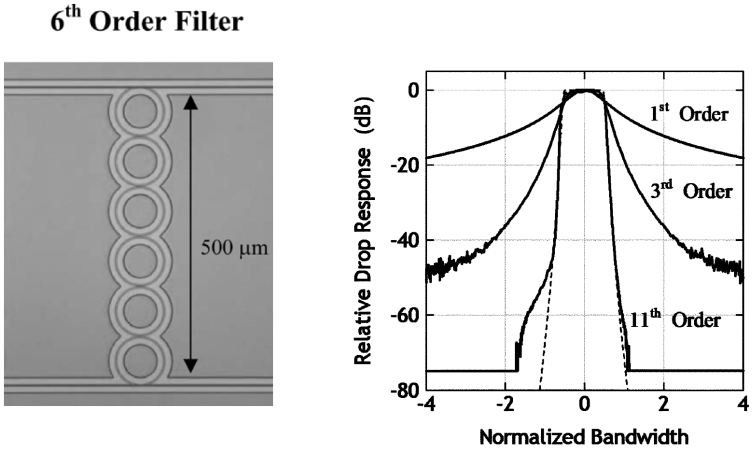

Fig. 1.6. A very high-order microring resonator having form 1 to 11 coupled cavities are demonstrated using high-index Hydex material, reported by B. E. Little et al [3].

Another way is to apply oxidation to smoothen the waveguide sidewall. For instance, a 0.8dB/cm transmission loss for a single-mode strip Si/SiO_2 waveguide with submicron cross-sectional dimensions has been realized, using combination of oxidation smoothing and anisotropic etching [18]. This, by far is the lowest reported loss for a high-index difference system such as a Si/SiO_2 strip waveguide. Another important milestone is the realization of ultrahigh-quality-factor (Q) SOI microring resonator based on silicon photonic wire which has propagation loss as low as 1.9±0.1dB/cm in a curved waveguide with a bending radius of 20μm and a Q-factor as high as 139,000±6000 [58]. These are the highest values reported for a curved SOI waveguide device and for any directly structured semiconductor microring fabricated without additional melting-induced surface smoothing. In December 2006, IBM demonstrated on-chip optical delay lines based on SOI waveguides that consist of up to 100 microring resonators cascaded in either coupled-resonator or all-pass filter (APF) configuration [4]. The propagation loss is measured to be as small as 1.7±0.1dB/cm, which compares favorably with the best results published to date [16, 26, 59-61].

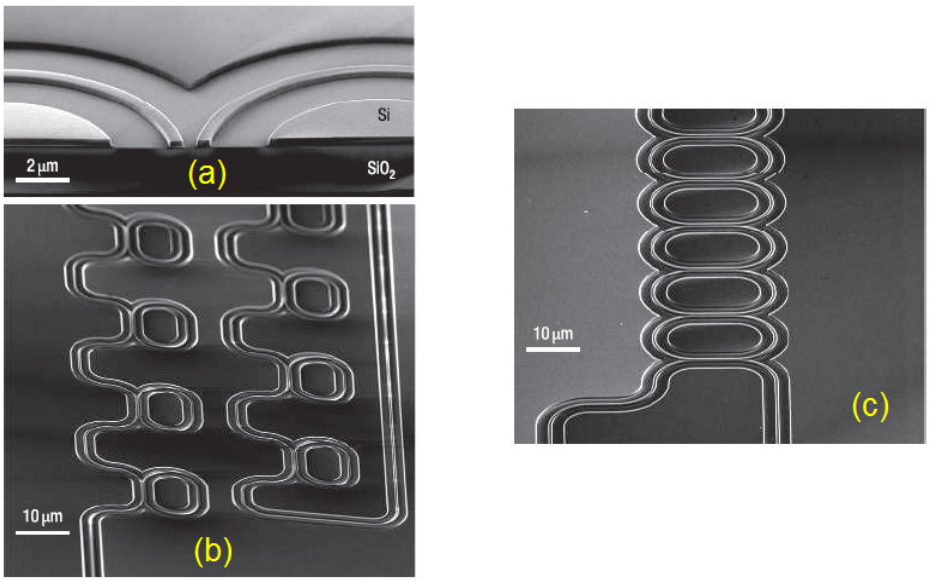

Fig. 1.7. The scanning electron micrographs (SEM) of resonantly enhanced optical delay lines based on photonic-wire waveguides, reported by Fengnian Xia et al [4].

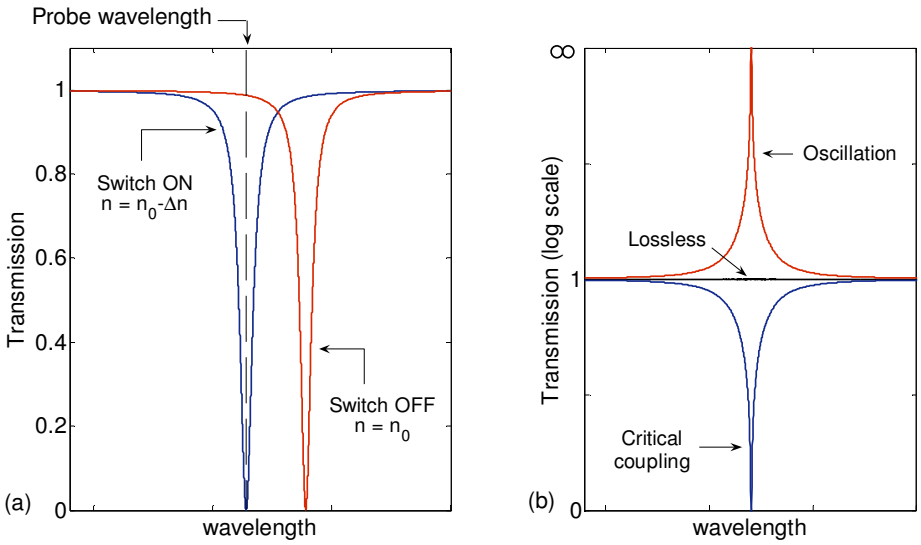

Fig. 1.8. The normalized transmission of one-ring-one-bus (1R1B) configuration: (a) All-optical switching by altering the index of refraction which shifts the resonance wavelength [5]. (b) The critical coupling, lossless, and oscillation conditions, achieved by varying the internal loss of the resonator [1, 2]. The y-axis is in logarithmic scale from [0 to ∞].

Fig. 1.8 illustrates an example of using the critical coupling and the oscillation for all-optical switching or modulation in a conventional one-ring-one-bus (1R1B) structure. Fig. 1.8(a) shows how optical switching is performed by slightly modifying the index of refraction of the guiding material. Due to their strong-light-confinement nature, a small index-of-refraction change induces a strong

tuning of the resonances (i.e., resonance shift). If the probe wavelength is tuned around the resonance wavelength (dashed line), one can observe that the transmission changes significantly, resulting in a strong intensity modulation of the transmitted signal. The modulation depth (MD), which is normally defined as the difference between the logic "1" and "0" transmission, is the highest if the *critical coupling* condition is satisfied. The critical coupling refers to the critical value of the coupling coefficient in a lossy ring at which complete destructive interference takes place precisely around resonance, producing effectively zero transmission output. Physically, it corresponds to the situation in which the light fully resonates and vanishes inside the cavity due to loss. The strong modulation (high MD) of the probe intensity occurs as a result of the spectral tuning (from 0 to ~0.99 when the modulator is switched from the OFF to the ON state). We also show Fig. 1.8(b) which illustrates the 1R1B transmission under critical coupling, lossless, and *oscillation* conditions. The oscillation refers to the condition in which the transmission is theoretically infinite (i.e., the inverse of critical coupling) in the presence of optical gain.

The critical coupling, oscillation and its control scheme in 1R1B was originally proposed by Yariv [1, 2] and experimentally been demonstrated in fiber using Erbium doped fiber amplifier (EDFA) by Choi [62]. V. M. Menon demonstrated the integration of ring resonators with SOA using a vertically stacked asymmetric twin waveguide structure on compressively strained InGaAsP multiple quantum well structures. A modulation contrast of ~10dB with quality factor of 22,000 is demonstrated by altering the internal loss in the ring by means of an integrated SOA [63]. Similarly, Rabus Dominik demonstrated a monolithic single-mode InGaAsP-InP double microring resonator coupled laser [64]. The laser comprises two passive ring resonators, semiconductor optical amplifiers (SOA) in the bus waveguides, and 3-dB codirectional couplers. Similar tunability is also demonstrated using integrated platinum resistors on top of the waveguides in the rings. Such accumulative works in the literature strongly indicate the importance of critical coupling and oscillation for all-optical switching and modulation in coupled resonator systems.

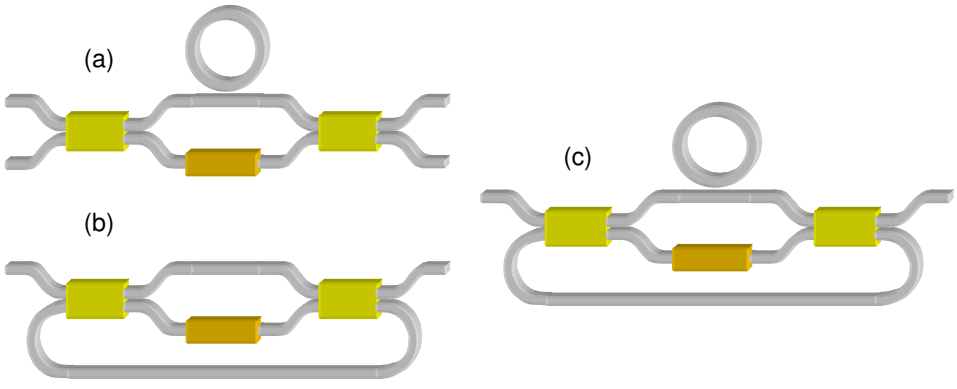

Fig. 1.9. The schematic of various ring-coupled MZI configurations such as: (a) REMZI [6, 7], (b) RFMZI [8], (c) The combination between (a) and (b) [9]. The MZI section is based on the 3dB MMI couplers. Active tuning is typically adopted in the MZI section.

Next, we shall discuss various types of ring-based MZI devices found in the literature. REMZI, as the name implies, is designed to enhance nonlinear phase shift in one arm of the MZI arm, which can be used to further enhance the nonlinear switching performance of the MZI. Such enhancement also leads to important consequences for micro-photonic switching and for the construction of an all-optical switching device with a greatly reduced threshold power or size. It is also interesting to find that the same REMZI device can be engineered to realize a flat-top filter with relatively high rejection band [65, 66] or a linearized modulator [67-69]. The trick is done by engineering the phase imbalance between MZI arms with proper lower MZI bias and coupling coefficient values between the microring and the bus waveguide (please refer to Appendix B for more details on linearity in REMZI). In 2003, a ring-feedback Mach-Zehnder interferometer (RFMZI) was proposed by Chung-Yen Chao and L. Jay Guo [8] which is basically a modified conventional Mach-Zehnder interferometer (MZI) with a provision of a feedback path between one of the MZI outputs and the input [Fig. 1.9(b)]. Due to the feedback mechanism, the device possesses large transmission intensity change with a small phase imbalance between the two arms of the MZI. This property can greatly enhance the sensitivity by one to two orders of magnitude compared with traditional MZI-based sensors. The same configuration can be further enhanced in slope and detection range with introduction of small gain into the feedback path. In 2005, similar device which is a thermooptically tunable InGaAsP-InP MZI is used to electrically control the coupling coefficient to an integrated racetrack resonator [9]. The proposed configuration corresponds to the one illustrated in Fig. 1.9(c), which is a hybrid of REMZI [Fig. 1.9(a)] and RFMZI [Fig. 1.9(b)]. A minimum switching power of 26mW is measured for the hybrid device, while a conventional MZI fabricated for comparison is measured to require 40 mW for complete switching. These results demonstrate the reduction in switching power theoretically predicted for the hybrid MZI/resonator geometry.

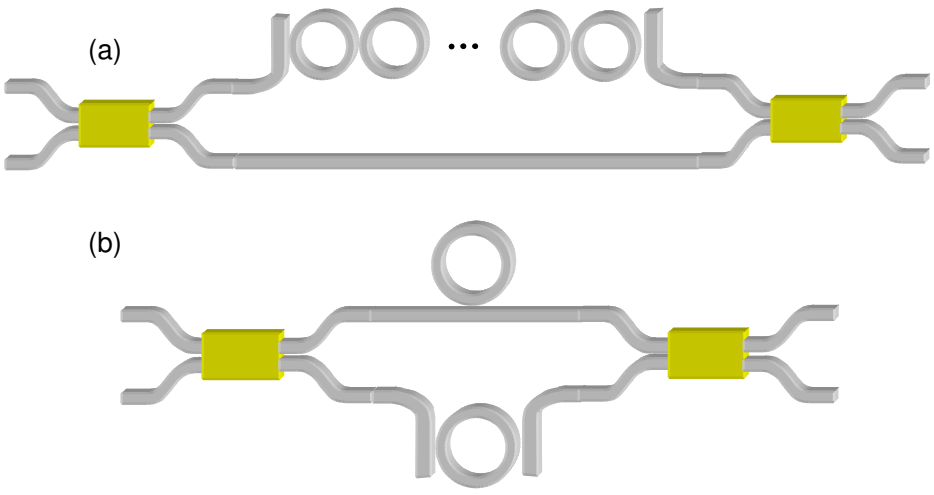

Fig. 1.10. A novel geometry of ring-coupled Mach-Zehnder interferometer: (a) A CROW coupled MZI [10], (b) 1R1B (1R2B) coupled to the upper (lower) MZI arm [11].

In another twist, a novel geometry of a Mach-Zehnder interferometer in which one arm of the interferometer consists of serially coupled microresonators (CROW) is demonstrated [10]. The structure was fabricated in an optical polymer and its spectral characteristics were measured at telecommunications wavelengths. The serially coupled rings are modeled using a simple transfer matrix approach. Good agreement is found between the measurement and the theory. Another interesting ring-based MZI geometry is a 1R1B (and 1R2B) coupled into the upper (and lower) MZI arm, to produce coupled resonator-induced transparency (CRIT) and absorption (CRIA) effects [11]. The CRIT and CRIA are analogous to the electromagnetically induced transparency (EIT) and absorption (EIA) in atomic system respectively [70-74]. The EIT can be defined as a coherent optical nonlinearity which renders a medium (or system) transparent over a narrow spectral range within an absorption line. Extreme dispersion usually follows within this transparency "window" which leads to "slow light". In [11], CRIT and CRIA effects occurs over a frequency range when the two microresonator are identical and Fano-resonances manifest when the sizes of two microresonators are unequal. The optical bistability characteristic based on CRIT for this device has also been theoretically investigated [11]. In Chapter 6, we propose the use of two-ring MZI (2RMZI), which will outperform the ring-based MZI device reported in [11]. The optical bistability switching related to the proposed device is optimized for best case performance.

1.5. Objectives

Based on the exhaustive literature works highlighted earlier, there is no doubt that photonics is a broad area which involves many building blocks, architectures and material platforms, both active and passive. In this thesis, we shall focus on several basic devices namely, multimode interferometers, Mach-Zehnder interferometers, coupled resonators, and the possible combinations derived from the above mentioned devices. The key objectives driving my research are summarized in the following manner:

(1) First is to study the basic passive devices such as DC and MMI based on high-contrast waveguides. This forms an important basic step in designing more complex devices including the MZI. The first two chapters focused on a study of bus-coupled resonator systems (Chapter 2), especially higher-order multi-ring system (Chapter 3). I started by investigating the concept of critical coupling and oscillation condition, which was borrowed from microwave field and applied to 1R1B system by Yariv (in the context of optics) [1, 2]. Thus, it is of logical consequence to extend the study and explore the critical coupling and oscillation to higher-order ring-resonator system. In parallel, the pole-zero approach is used as a convenient tool to complement the study, as the zeros (poles) are directly associated with the critical coupling (oscillation) condition.

(2) Filter design based on coupled resonators has been a key trend in research. As discussed in the last section, there are two main configurations of coupled resonators optical lattice filters: Type I and Type II. In both configurations, the bandpass response is much better compared to a single ring-resonator which has a Lorentzian response, but there are other deficiencies such as ripples in the passband for the mutually coupled array (Type I) and sidelobes in the stopband for periodically coupled array (Type II). An ideal bandpass filter should have a square and flat-top transmission with sharp roll-off and sidelobe-free stopbands, as well as a linear phase response with zero dispersion over larger range of bandwidth. Normally, apodization has been proposed and may be used to suppress the sidelobes in the periodically coupled array, but it also reduces the sharpness at the transition edges [57]. Filter shaping can be achieved by applying digital filter design theory to synthesize any specified Nth-order filter transfer function, which requires the N resonators to have N (or N+1) specific values of coupling coefficients [27]. Depending on fabrication capability, such level of control over the coupling coefficients is not always practical, especially when E-beam lithography is not used. To overcome such problems, we propose an alternative approach using a third configuration that is a geometric hybrid of both Type I and Type II configurations (dual-bus configuration). This new configuration is a 2D-RR array that can be constructed as a periodically coupled array with each "tooth" consisting of a higher-order coupled ring filter. The expectation here is that by combining the complementary features of the two, this configuration will give improved performance. Periodic structures of coupled resonators have been analyzed by the matrix method [40, 42, 49] as well as in the time domain [56] and analytically [50]. For our case, the transfer matrix method is adopted as it is most suitable for analyzing any periodic structures. In terms of pole-zero approach, it can also be seen that although apodization is not directly applied, however, the 2D-RR array exhibits similar effect of apodization to the ones in conventional apodized filters. To the best of our knowledge, the idea of using 2D-RR array configuration to realize a "perfect filter" is novel and as it has never been shown in the literature before.

(3) The combination of RR and MZI has many potential applications in optical switching, modulation, filtering and sensing. The main objective is to study and explore various types of ring coupled MZI structures, starting first with the 2D-RR arrays coupled with MZI which gradually progresses into the design and fabrication of nested-ring MZI (NRMZI). The nested ring by itself is expected to exhibit a periodic phase response with sharp nonlinear phase changes. This phase response can be translated to a power spectrum with flat-top filter-like response when the nested ring is coupled to one arm of a MZI. Physically, the flat-top response is shaped by the double-Fano resonances, created by interference among the different optical pathways available in the nested-ring (i.e., the inner-loop and the outer-loop resonances) and the MZI. The main idea is to show that the NRMZI is capable of producing

such a box-like transmission spectrum with sharp transition edges, which is highly desirable as a "digital" sensor or switch as well as a filter. The experimental part of this project is a collaboration work with P. Dumon and R. Baets from Ghent University using the fabrication facility in IMEC (Belgium).

(4) Recently, the two-ring configuration was proposed by Landobasa in single-bus (2R1B) [15] and double-bus (2R2B) excitation [75, 76]. These structures consist of two mutually coupled rings of possibly different sizes, where only one ring, referred to as the inner ring, is coupled to the waveguide bus(es). A significant resonance narrowing is predicted and observed [75] when the size of the outer ring (ring 2) is twice that of the inner ring (ring 1), which implies that the outer-ring resonance coincides with the inner-ring anti-resonance. In that case, the two-ring system can effectively localize the light strongly inside the outer ring, giving rise to a sharp resonance with finesse limited only by the intrinsic and coupling losses. In the 2R2B case, the finesse is expected to be lower because of double the coupling loss, but it has the advantage of having two complementary outputs – Through (T) and Drop (D), which is useful as an add-drop filter. The narrow resonance is associated with the ~2π resonant phase response from the outer ring which leads to rapid successive destructive and constructive interference. However, the destructive interference in the 2R2B case is incomplete resulting in an off-resonant dip that never goes to zero (i.e., poor realization of logic "0"). Amplitude wise, such unwanted effect is manifested as a background envelope which limits the application of such narrow resonances, e.g., for switching, modulation, or sensing. To alleviate this problem, we propose to excite the 2R1B with a MZI (2RMZI). By doing so, we obtain three benefits: (1) The double-bus excitation is converted into single-bus excitation, giving improved light localization inside the two-ring system. (2) The output is similar to 2R2B as the MZI has both complementary cross and bar outputs. In a balanced MZI, the bar (cross) port is similar to the Drop (add) port of the 2R2B. (3) The additional optical pathway through the MZI, together will the optical pathways in the 2R1B structure, allows complete destructive interference off the anti-resonance of ring 1 thereby giving improved resonance contrast ratio (CR) (i.e., the ratio between logic "1" to "0"), modulation depth and finesse for the narrow resonance. The fabrication of the 2RMZI is based on a complementary metal–oxide–semiconductor (CMOS) based deep-ultraviolet (DUV) process. This part of the project is also a collaboration work with P. Dumon and R. Baets from Ghent University using the fabrication facility in CEA LETI (France).

(5) Lastly, it is desirable to combine the resonances created by the 1R1B or 2R1B with the flexibility of MZI in tuning the asymmetricity of Fano resonances [34-36] to achieve bistability switching with much lower switching threshold and reasonably high extinction ratio (ER) and modulation depth (MD) [Note: The ER is the same with CR]. Since the switching threshold is determined only by the finesse of the resonance it is not affected by

the phase bias on the other arm of the MZI. Such delinking simplifies the concurrent optimization of switching threshold, ER and MD, making it possible to develop a complete optimization scheme for both 1RMZI and 2RMZI and compare their performances based on ER, MD, optical bandwidth and switching threshold. The bistability switching is simulated using the parametric formulation based on *Kerr* effect, similar to the one adopted by Sanchez [77]. The focus of the work is on the optimization scheme (bistability engineering). For simplicity, we neglect other nonlinear effects such as the two-photon absorption (TPA), free carrier absorption (FCA), and free carrier dispersion (FCD), in the theoretical modeling.

1.6. Significant contributions

In tandem with the driving objectives discussed in the last section, the original research contributions of this thesis may be summarized as follows:

(1) A detailed look at the structural similarity between DC and MMI revealed a deeper and continuous transformational relationship between their modal properties when the basic coupled waveguide structure is modified from that of DC (with a air gap in between) to that of MMI (where the gap is removed) [78, 79]. This work, however, is peripheral to the theme of this thesis and hence is omitted from the thesis.

(2) As discussed in the literature, the critical coupling and the oscillatory conditions formed two important aspects that determine the overall performance of optical switching and modulation performance in any coupled resonator devices. Such findings encourage us to carry out a theoretical study to generalize the concept and conditions of critical coupling and oscillation for arrayed structures involving Type I and Type II. The fundamental analytical relationships among coupling coefficient, internal loss, and oscillation frequency for critical coupling and oscillation conditions are derived for two and three rings coupled to single- and double-bus waveguides using the transfer-matrix method and Sylvester's theorem [80].

(3) Filter designs using various techniques have been a key thrust in ring resonator research and application. As we highlighted earlier in the literature review, using filter synthesis, the Type I and Type II structures can be apodized in order to realize a flat-top filter with high rejection band [3, 27, 48-51, 57]. Novel methods of applying pole-zero diagrams to photonic filter design in a way similar to digital filter theory [27], aimed at tailoring the spectral characteristics, have been demonstrated by Kaalund [81] in designing ring resonator-based filters for optical wavelength interleavers and deinterleavers. Such work motivates us to study the pole-zero dynamics of high-order ring-resonator filters in which, we may deduce the critical coupling and oscillation in the perspective of the pole-zero diagram. We further show that the pole-zero dynamics for the two types of array filter are complementary to each other, and that the pole-zero plots are closely related to the conditions of critical coupling and

oscillation. Moreover, we show a pole-zero analysis for the apodization of these filters based on an actively tunable Mach-Zehnder (or MMI) type coupler, where it is shown that apodization corresponds to designing pole-zero pairs with wide separations, while the specific values of the coupling coefficient are determined by the required bandwidth. The proposed structure may be useful for active-apodization which may lead to further design flexibility for various applications in the future.

(4) We have shown, as part of this thesis work, that periodic arrays of identical rings with identical coupling behave as a photonic bandgap (PBG) structure with photonic bands in which light is reflected. Such a band is called a photonic bandgap, analogous to the electronic bandgap in solid state electronics. The PBG properties of the two types of arrays, Type I and Type II, are complementary and non-overlapping. Hence, in a 2D-RR array formed by a hybrid combination of the two arrays, the non-overlapping photonic bandgaps can hybridize to give a 2D bandgap that has similar effect of apodization, and is capable of generating a box-like transmission. This work was mainly carried out by my colleague Mr. Landobasa, and I was involved in a secondary role. We further combine the 2D-RR arrays with the MZI and study the nonlinear phase enhancement which translates into the amplitude variation in the MZI output. The proposed structure can be regarded as a generalized form of ring-coupled MZI [10], which has never been shown by anyone in the literature.

(5) The most significant contributions in this thesis are the conceptualization and demonstration of two novel devices based on SOI material platform: (1) Nested-ring Mach-Zehnder interferometer (NRMZI) and (2) Two-ring Mach-Zehnder interferometer (2RMZI). The NRMZI design, in particular, is novel as it has never been reported in the literature. To the best of our knowledge, we are the first to highlight the idea of using double-Fano resonances in realizing a flat-top filter. The 2RMZI design, in particular, is derived from the two-ring configuration, which was originally proposed by my colleague, Landobasa [15, 75, 76]. As previously discussed in the objectives, the combination of the 2R1B and MZI produces a more complete destructive interference among the optical pathways in the 2R1B and the optical pathway in the MZI, which effectively suppresses unwanted background envelope found in the 2R2B system [75]. As a result, the contrast ratio, modulation depth and finesse associated to the narrow resonance are improved. Such enhancement is highly desired for switching, modulation, or sensing applications. It is interesting to note that similar manifestation of background envelope is also found in other ring-based MZI [11] due to incomplete destructive interference [refer to Fig. 1.10(b)]. This highlight the advantage of 2RMZI over other ring-based MZI devices reported in the literature. In this work, a projected finesse enhancement of ~355 with modulation depth of ~0.19 is shown to be a realistic performance that can be achieved by the fabricated 2RMZI only if the fabrication-induced imbalanced in the MZI can be canceled out by some tuning mechanism (e.g., thermal tuning).

(6) Lastly, we develop a scheme for bistability engineering by altering the Fano lineshape by means of using proper initial detuning (operating wavelength) and the MZI biases. In this work, we theoretically demonstrate a switching threshold reduction by two orders of magnitude, verifying the signature of resonance enhancement associated with the 2RMZI device as compared to the conventional 1RMZI counterpart. A comprehensive comparison between the two devices is presented in terms of extinction ratio, modulation depth, optical bandwidth, and switching threshold.

1.7. Report organization

Chapter 2 presents the basic theory of single-bus RR (1R1B) and dual-bus RR (1R2B) and some experimental results of basic waveguide structures. Chapter 3 presents the analysis of the 2D-RR array and its pole-zero approach in the context of critical coupling and oscillatory conditions. A brief discussion on photonic bandgap is presented. Chapter 4 presents the design of 2D-RR arrays coupled to MZI and a phase engineering study of this ring-based MZI. The study focuses on the nonlinear phase enhancement and how it is translated into the amplitude variation in the MZI output. The formulation and experimental verification of NRMZI is presented in Chapter 5. Chapter 6 discusses formulation and experimental verification of 2RMZI. Chapter 7 presents the bistability engineering for ring-coupled MZI. Finally, the author's publications, appendices and references are presented.

Chapter 2

Basics of ring resonators

2.1. Introduction

The idea of using waveguide ring resonator (RR) as a bandpass filter has been proposed in 1969 by E. A. Marcatili [82]. The single-ring structure is an integrated circuit analogue of the Fabry-Pérot (FP) etalons [83] and the Gires-Tornois (GT) etalons [84]. The principle of FP was invented in 1898 by the French physicists Charles Fabry and Alfred Pérot whereas the principle of GT was invented in by F. Gires, and P. Tournois in 1964. The FP/GT interferometer is modeled using two flat mirrors which are perfectly aligned to be parallel with a free space in between them. The light reflections between the two mirrors lead to constructive and destructive interference of these waves within the cavity. This results in a series of allowed stationary or standing electromagnetic (EM) waves inside the cavity. Figure 2.1 illustrates the analogy between the etalons and the single-RR configuration.

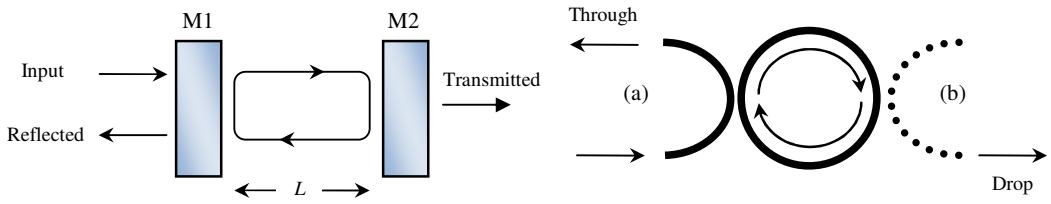

Fig. 2.1. The analogy between FP interferometer with (a) GT interferometer with the single-bus ring resonator (1R1B) and (b) with the double-bus ring resonator (1R2B).

Based on the Fig. 2.1, we note that when mirror 2 (M2) is fully reflective; the setup is effectively a single-bus ring resonator analogous to the GT interferometer. On the other hand, when M2 is partially reflective, a fraction of the light will pass through (reflected) the same bus and the rest is transmitted to the other output port denoted as "Drop" in Fig. 2.1(b) via the ring cavity. The ring cavity can only support modes (standing wave) as long as the resonance condition is fulfilled, i.e., $m(\lambda/2) = nL$ where λ is the wavelength, n is the effective index of the guided mode inside the cavity and L is the FP cavity length which is equivalent to half of the ring circumference. The FP optical cavities are commonly used in lasers, interference filters and many other spectroscopic applications. For example, by tuning the cavity length L, one may control the allowed wavelength oscillation inside the cavity.

Based on the literature, RR has previously been implemented in fibers [33, 62, 85-98] and in various material systems such as AlGaAs/GaAs [6, 48, 99-103], InGaAsP/InP [9, 48, 104-110], Silicon-on-insulator [16, 31, 52, 111-123], polymers [3, 10, 43-45, 124-133] and Si_3N_4/SiO_2 [134-139] and glasses [38, 39, 140-143]. RR has a vast range of applications as it can be utilized as (1) optical switches [9, 33, 62, 99, 103, 144, 145], (2) modulators [52, 68, 118, 119, 130, 146, 147], (3) add/drop filters [3, 37, 39, 48-51, 56, 57, 100, 136, 141, 143, 148], (4) dispersion compensators [94, 145, 149-152], (5) delay lines [45, 53, 117, 152], (6) sensors/biosensors [123, 140, 153, 154], and (7) lasers [107, 110, 145, 146, 155-165]. Multiple ring arrays have also been demonstrated in many different unique configurations [3, 10, 37, 38, 40, 42, 48-50, 56, 57, 166, 167] which may find special applications, especially in relation to the photonic bandgap (PBG) devices. RR can also be easily integrated with many other devices such as Mach-Zehnder interferometer to serve various purposes [9, 10, 34, 57, 68, 147, 168, 169]. Active semiconductor ring lasers have also received much attention [110, 146, 156, 157, 159, 162-165], simply because they are an attractive light source candidate in optics and photonics. Another significant milestone is the integration of semiconductor optical amplifiers (SOA) with RR in an integrated optic circuit [106]. Such integration is an important advance from the earlier fiber-optic version of SOA+RR [62, 145, 155, 158, 160, 161, 170]. In this chapter, we shall present the basic theory of RR and introduce important figures of merit (FOM) relevant to the device. We then present the experimental measurements for some basic device structures and compare the results with theory.

2.2. Basic theory of single-bus RR

Ring resonators (RR) are of considerable interest because of their potential as building blocks for chip-scale photonic integrated circuits. The basic device building block is a ring coupled to a bus waveguide, denoted 1R1B for short, as shown in Fig. 2.1.

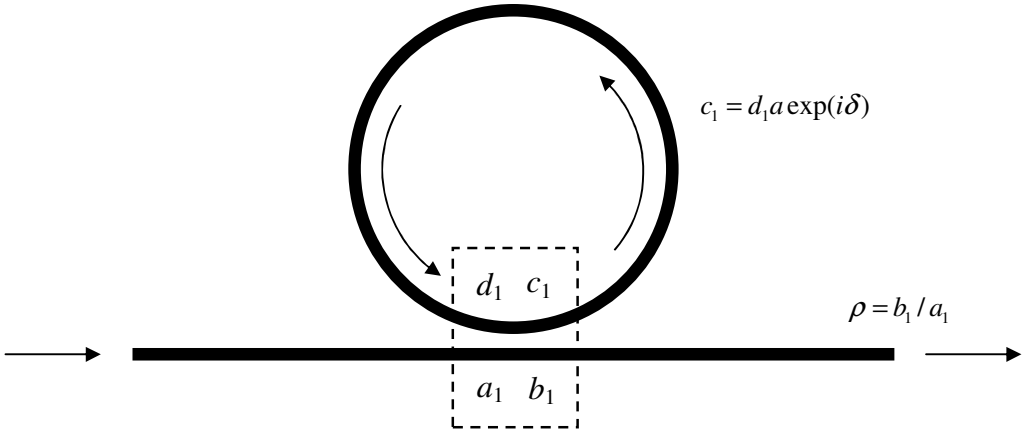

Fig. 2.2. All-pass filter with a single-bus RR (1R1B).

The electromagnetic field amplitudes inside the ring and in the bus, as denoted in Fig. 2.2, are related by the simple transfer matrix relation,

$$\begin{pmatrix} b_1 \\ c_1 \end{pmatrix} = \begin{pmatrix} r & i\kappa \\ i\kappa & r \end{pmatrix} \begin{pmatrix} a_1 \\ d_1 \end{pmatrix} \tag{2.1}$$

where r is the reflectivity of the coupler which is related to the coupling coefficient κ, by $\kappa = (1-r^2)^{1/2}$; $a \equiv \exp(-\alpha L_c / 2)$ is the round-trip amplitude transmission factor (a = 1 for lossless case), α is the power loss coefficient, and L_C is the roundtrip length. After simple algebraic manipulation, we can express the steady-state output as,

$$R = |\rho|^2 = \left|\frac{b_1}{a_1}\right|^2 = \left|\frac{r - a\exp(i\delta)}{1 - ra\exp(i\delta)}\right|^2 = \frac{r^2 + a^2 - 2ra\cos\delta}{1 + r^2a^2 - 2ra\cos\delta} \tag{2.2}$$

where δ = $\omega n L_c$ is the round-trip phase. Typically, the n value is approximated by a group index n_g of $n - \lambda \partial n / \partial \lambda$, which is commonly used for highly dispersive system such as microring resonators. Optical materials display normal dispersion throughout their transparent regions, so the envelope (the pulse or the energy) travels slower than the phase [27]. For normal dispersion, $\partial n / \partial \lambda$ is negative and the group velocity (v_g) is smaller than the phase velocity (v_p). As a consequence, the group index can be much larger than the effective index for highly dispersive systems. For example, the effective index in typical photonic wire in SOI is ~2.5 where as the group index can be as large as ~4.6 [16].

As a filter, the δ contains the frequency dependence, and can be written in the form $\delta = 2\pi f / FSR = 2\pi(m + \Delta f / FSR)$, where $\Delta f \equiv f - f_0$ is the frequency detuning, f_0 is the resonance frequency, and $FSR = c/(nL_c) = 1/T_R$ is the free spectral range where T_R is the roundtrip time and c is the speed of light (~ 3×10^8 m/s). Hence the frequency dependence is periodic. Most of the interesting features of this resonator occur near resonance where δ = 2πm. As a convention, we shall name the output of the Through port as 'reflection' and the output at the Drop port as

'transmission', in analogy to the Fabry-Pérot resonator. Note that on resonance, when $\delta = 2\pi m$, the reflection is zero when $r \sim a$, corresponding to a coupling condition known as *critical coupling* [1]. In the next subsection we will first introduce some figures of merit (FOM) commonly used to characterize the performance of RR devices.

2.2.1. The build-up factor and finesse

The light build-up factor is the ratio between the intensity inside the ring and that at the input waveguide. It is a measure of the resonance of light in the cavity, a property that determines the sensitivity of the device as a filter or a switch. In a nonlinear optical device, the higher the build-up factor B, the lower will the required input power needed to induce nonlinear effects. The build-up factor B is given by,

$$B = \left|\frac{c_1}{a_1}\right|^2 = \left|\frac{i\kappa}{1 - ar\exp(i\delta)}\right|^2 = \frac{1-r^2}{1-2ar\cos\delta + a^2r^2} \tag{2.3}$$

Fig. 2.3 shows the build-up factor B as a function of the roundtrip phase (δ).

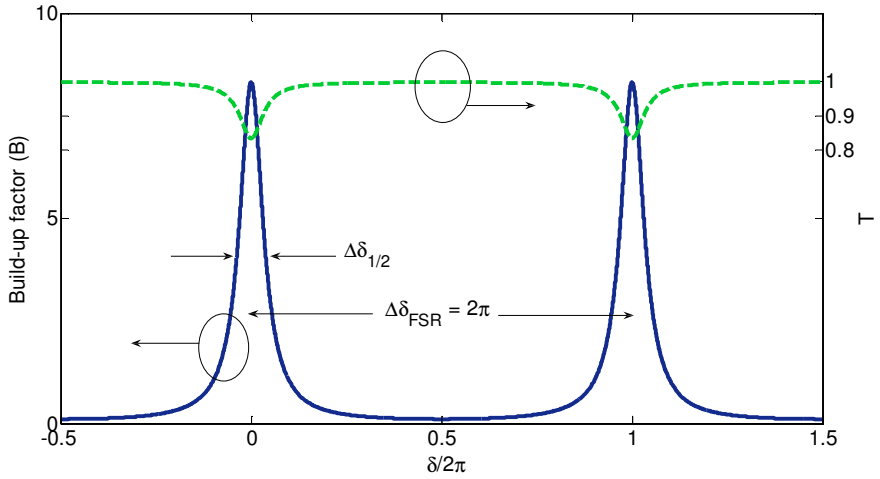

Fig. 2.3. The build up factor B vs. the normalized detuning δ for a single-bus RR device (simulated parameters: $r = 0.8$, $a = 0.99$).

In the lossless limit where $a \approx 1$, the maximum value of Eq. (2.3), when $\delta = 2\pi m$ (m an integer), is given by

$$B_1\big|_{a\approx 1} = \left(\frac{1+r}{1-r}\right) \tag{2.4}$$

Hence, the larger the r value (or the smaller the coupling coefficient, κ), the higher the maximum build-up factor. More commonly, a resonance is characterized by the *finesse* which is defined as the ratio between the free-spectral range and the full-width half maximum (FWHM) linewidth:

$$F = \frac{\Delta\delta_{FSR}}{\Delta\delta_{1/2}} = \frac{2\pi}{\Delta\delta_{1/2}} \tag{2.5}$$

The Lorentzian transmission profile of the 1R1B follows the shape of the build-up factor, hence the FWHM linewidth can be found by taking the points where the build-up factor is ½ of the maximum value (refer to Fig. 2.3). After some algebraic manipulations, we obtain the expression,

$$\Delta\delta_{1/2} = 2\cos^{-1}\left(\frac{(1-ar)^2}{2ar}\right) \tag{2.6}$$

Using Taylor's expansion in high finesse approximation ($\cos\delta \approx 1-\delta^2/2$), one can simplify the expression of FWHM into $\Delta\delta_{1/2} \approx 2(1-ar)/\sqrt{ar}$. Substituting this value back into Eq. (2.5), the finesse can be determined as,

$$F_1 = \frac{\pi\sqrt{ar}}{1-ar} \xrightarrow{a\approx 1} = \frac{\pi\sqrt{r}}{(1+r)}\left(\frac{1+r}{1-r}\right) = \frac{\pi B_1\sqrt{r}}{1+r} \xrightarrow{r\approx 1} = \frac{\pi B_1}{2} \tag{2.7}$$

The subscripts in B_1 and F_1 refer to the case of 1R1B (later on we shall use B_2 and F_2 for the case of 1R2B). Eq. (2.7) simply tells us that the finesse is directly proportional to the build-up factor inside the ring.

2.2.2. The cavity Q-factor

It is very common to characterize the resonance in terms of the quality factor Q which is defined as the resonant frequency divided by the bandwidth. In analogy with electrical circuits, the quality factor of an optical cavity due to its internal losses and external coupling loss can be defined as,

$$\frac{1}{Q} \equiv \frac{\text{energy dissipated}}{\omega \times \text{energy stored}} \tag{2.8}$$

where ω is the frequency of the lightwave coupled into the cavity. In other words, the quality factor is simply related to the finesse multiplied by the number of optical wavelengths per ring circumference:

$$Q \equiv \frac{\lambda_0}{\Delta\lambda_{1/2}} = \frac{\delta_0}{\Delta\delta_{1/2}} = \frac{2\pi nL/\lambda}{2(1-ar)/\sqrt{ar}} = (nL/\lambda)F_1 = mF_1 \tag{2.9}$$

where $m \equiv \delta/2\pi$ can be regarded as the resonant orders. Here, the Q-factor of the resonator is a function of the ring dimensions, mode effective index, and the operating wavelength λ, as well as the finesse which depends on (r, a). Large optical mode volume, smaller operating wavelength coupled with high finesse is the fundamental recipe for high Q factor devices.

2.2.3. The effective phase shift

Based on the transfer output characteristic derived in Eq. (2.2), we can further derive the phase response of the single-bus RR where $\rho = |\rho| \angle \varphi$. The corresponding phase term φ can be deduced as,

$$\varphi = -\tan^{-1}\left(\frac{a\sin\delta}{r - a\cos\delta}\right) + \tan^{-1}\left(\frac{ra\sin\delta}{1 - ra\cos\delta}\right) + 2\pi m \tag{2.10}$$

Eq. (2.2) can also be rewritten in the form of $\rho = e^{i(\pi+\delta)}(a - re^{-i\delta})/(1 - rae^{i\delta})$ and thus the phase term can be deduced as,

$$\varphi = \pi + \delta + \tan^{-1}\left(\frac{r\sin\delta}{a - r\cos\delta}\right) + \tan^{-1}\left(\frac{ra\sin\delta}{1 - ra\cos\delta}\right) \tag{2.11}$$

When the 1R1B is lossless, the device behaves as an all-phase filter with unity transmission. In the high finesse regime, the phase jump occurs each time the resonant condition is fulfilled and the slope of the phase response gets steeper as the finesse is higher. More details are given in the next subsection.

2.2.4. The critical coupling

Fig. 2.4 shows the plot of the phase response (φ) of a 1R1B under 3 different coupling conditions, namely: (1) under-coupled ($r > a$), (2) critically coupled ($r = a$) and (3) over-coupled ($r < a$). The term 'under-coupled' implies that the amount of light coupled into the cavity is insufficient to overcome the cavity loss. Thus there is no optical phase build up when the light is on resonance. The term 'critically coupled' implies that the amount of light coupled into the ring is equal to the amount of light lost inside the cavity. Thus 100% of the light vanishes inside the cavity when it is on resonance, giving rise to zero transmission (or reflection R) and zero net phase buildup. (3) The term 'over-coupled' implies that the amount of light coupled into is more than that lost inside the ring. This means that the amount of light coupled into the cavity overcomes the loss and there will be a net optical phase build-up when the light is on resonance. This optical phase build-up is represented by a phase jump of ~2π across the resonance. It is also interesting to study the under-, critical-, and over-coupling conditions in terms of the linear time domain response. Please refer to Appendix B for more details on such study.

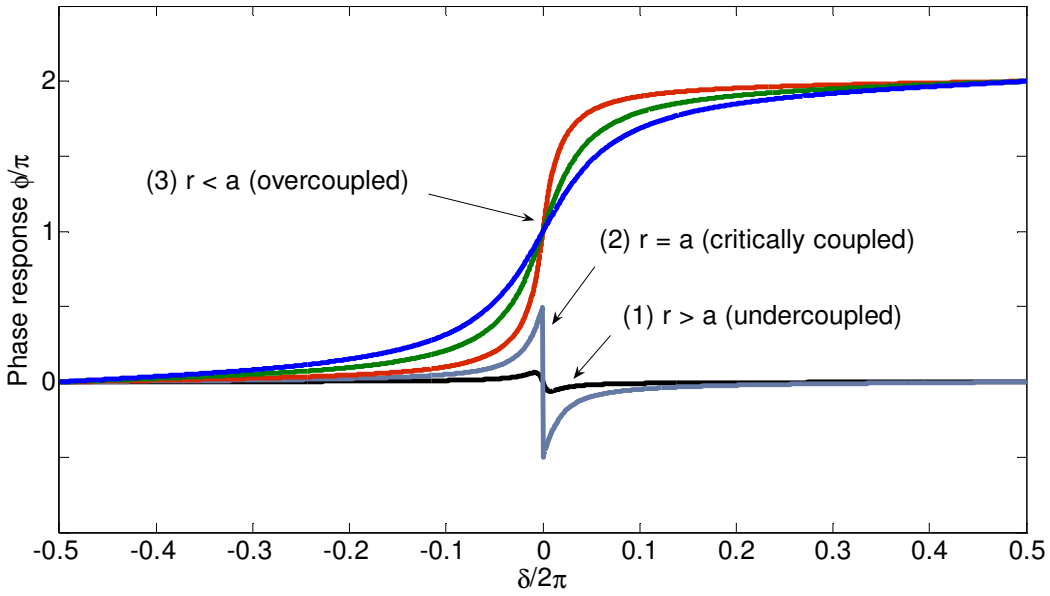

Fig. 2.4. The phase response (φ) of a 1R1B showing three different coupling conditions.

We can also investigate the relation between critical-coupling and build-up factor *B* for a 1R1B. Fig. 2.5 illustrates how the build-up factor B changes with *r* when the light is on-resonance ($\delta = 2\pi m$). As expected, the build-up is the highest when the critical coupling condition is fulfilled ($r = a$), and is given by

$$B = \frac{1}{1-r^2} \tag{2.12}$$

This is because critical coupling is a critical point of operation where 100% of the light is resonated inside the ring and none leaks into the bus waveguide. Although in practice it is impossible to have a 'perfect' critical coupling, in practice it is sufficient to operate just close the critical coupling to achieve less than -15dB transmission. There are some applications where critical coupling condition is desirable because the change in output is most sensitive to the shift in resonance under this condition [1, 2, 5, 62]. However, there are also applications which utilize the phase response but require a large output at the same time, in which case critical coupling should be avoided. For example, when a 1R1B is coupled to one arm of a Mach-Zehnder interferometer (MZI), one has to operate further away from the critical coupling. This is because all of the light will vanish in RR and there will be no meaningful output produced in the MZI output due to incomplete interference. We shall see this more later on as we go further into the ring-based devices in the subsequent chapters.

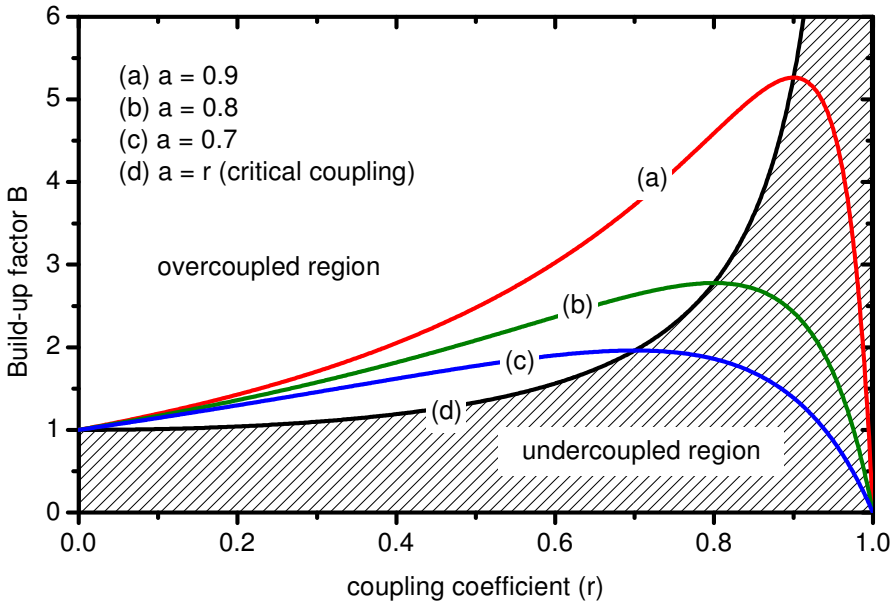

Fig. 2.5. The build-up factor B vs. coupling coefficient (r) for various loss values when the light is on-resonance ($\delta = 2\pi m$). The shaded region refers to the undercoupled regime where as the white region refers to the overcoupled regime. The critical coupling condition is fulfilled in between these two regions as highlighted by the solid line (d).

2.2.5. The group delay (GD) and group delay dispersion (GDD)

The group delay is directly related to the phase sensitivity. The phase sensitivity is interpreted as the effective number of roundtrips light traverses in the cavity. Also, since the group delay is frequency dependent, it is inherently dispersive. Mathematically, GD and GDD can be expressed by taking the first and second derivatives of the phase response with respect to the normalized frequency (δ),

$$GD = \frac{\partial \varphi}{\partial \delta}, \qquad GDD = \frac{\partial^2 \varphi}{\partial \delta^2} \tag{2.13}$$

The phase response of 1R1B is a ratio of two polynomials. The GD and GDD are related to the poles and zeros of the polynomials, hence the derivatives can be found in the z domain by using the Z-transform technique commonly used in digital filter theory. In this technique, the transfer function $H(z)$, is generally expressed as a ratio of two polynomials in z, where $z^{-1} = \exp(i\delta)$.

$$H(z) = \frac{\sum_{m=0}^{M} b_m z^{-m}}{1 + \sum_{n=1}^{N} a_n z^{-n}} = \frac{\Gamma z^{N-M} \prod_{m=1}^{M} (z - z_m)}{\prod_{n=1}^{N} (z - p_n)} \tag{2.14}$$

Digital filters are classified by the polynomials defined. Normally, a moving average (MA) filters has only zeros whereas an autoregressive (AR) filter has only poles. Filters with both poles and zeros are referred to as autoregressive moving average (ARMA) filters. Thus the single-bus RR can be considered as an ARMA filter since it has one pole and one zero, as can be seen from Eq. (2.2) which may be written as $\rho(z^{-1}) = (r - az^{-1})/(1 - raz^{-1})$. The group delay for the single pole case can be found from the result for a single zero. Its transfer function is expressed as $H_{1p}(\delta) = \Gamma e^{-i\varphi_{1z}(\delta)} / \left|H_{1z}(\delta)\right|$. Therefore, $\varphi_{1p}(\delta) = -\varphi_{1z}(\delta)$ and $\tau_{1p}(\delta) = -\tau_{1z}(\delta)$. More generally, for multiple-zeros and multiple poles case (as when multiple rings are coupled), the group delay for a single zero can easily be extended to multiple zeros. The phase of the overall transfer function is the sum of the phases for each root, i.e., $H(\delta) = \left|H_{1z}(\delta)\right| ... \left|H_{Mz}(\delta)\right| e^{i[\varphi_{1z}(\delta) + ... + \varphi_{Mz}(\delta)]}$. Note that the group delay is proportional to the derivative of the phase, thus they are additive in nature. The group delay for N poles and M zeros can be expressed as [27],

$$\tau(\delta) = \underbrace{\sum_{i=1}^{M} \frac{r_{zi}[r_{zi} - \cos(\varphi_{zi} + \delta)]}{1 - 2r_{zi}\cos(\varphi_{zi} + \delta) + r_{zi}^2}}_{\text{contribution from zeros}} - \underbrace{\sum_{i=1}^{N} \frac{r_{pi}[r_{pi} - \cos(\varphi_{pi} + \delta)]}{1 - 2r_{pi}\cos(\varphi_{pi} + \delta) + r_{pi}^2}}_{\text{contribution from poles}} \tag{2.15}$$

The notion $r_{pi}\angle\varphi_{pi}$ and $r_{zi}\angle\varphi_{zi}$ corresponds to the location of the poles and zeros in the pole-zero diagram respectively. Fig. 2.6 shows the transmission, phase, GD and GDD for the case of a lossless 1R1B along with the pole-zero diagram when *r* = 0.8 (over-coupled case). The output is that of an all-pass filter giving full transmission with a phase-only response. Note that the group delay is the highest when the light is precisely on resonance while the dispersion is highest at slightly off-resonance. The location of poles and zeros are governed by $p = ra\angle 2\pi$ and $z = (a/r)\angle 2\pi$, as a result, it can be seen that as *r* increases to unity, the poles and zeros will move and converge to the location $a\angle 2\pi$. In the lossless case, the pole and zero will meet at z = 1. In filter terminology, a filter with transfer function $H(z) = B(z)/A(z)$ is said to be stable if all its poles are inside the unit circle. On top of that, the filter is said to be maximum (minimum) if all of the zeros are outside (inside) the unit circle. So depending on the value of *r* and *a*, the 1R1B can be either minimum or maximum-phase filter, as the zero could easily fall inside or outside the unity circle. For example, in a low loss microring ($a \approx 1$), *r* is usually less than *a*. Thus, the 1R1B can be categorized as maximum-phase filters. Lastly, if no gain is introduced, the poles are always inside the unity circle which implies that the filter is stable.

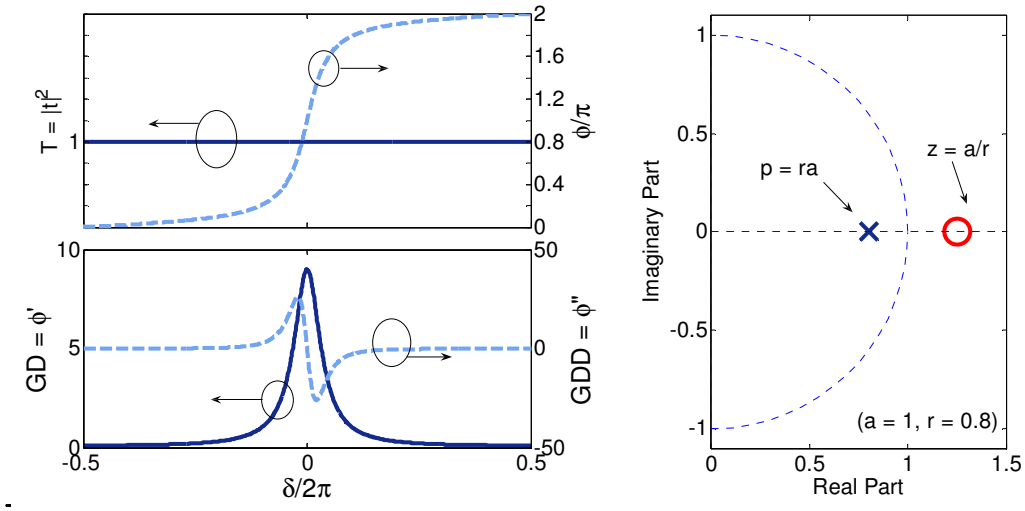

Fig. 2.6. Left: The transmission, group delay (GD) and group delay dispersion (GDD). Right: The pole-zero diagram representing lossless 1R1B as maximum-phase filters (all-pass filter). A single ring has one pole and one zero.

2.3. Double-bus ring resonator

In this section we shall briefly discusses the double-bus ring resonator (1R2B) configuration, as shown in Fig. 2.7. This configuration is the analogue of the FP interferometer, with the two couplers acting as the mirrors. As in a FP resonator, complete destructive interference occurs only if the two reflected field amplitudes are equal, which in the presence of cavity loss implies $r_1 = ar_2$, where r_1 and r_2 are the reflectivities of the two mirrors. For simplicity, we assume the configuration to be symmetric, i.e., the coupling coefficient is the same at both the bus-ring couplers ($r_1 = r_2 = r$).

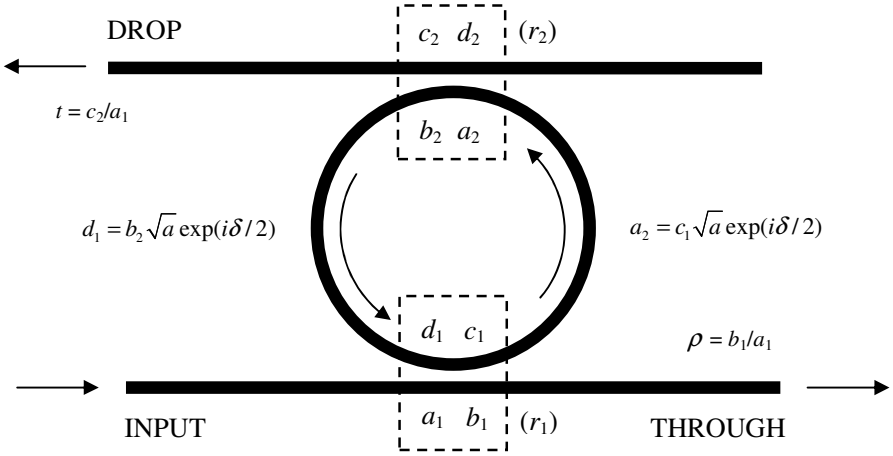

Fig. 2.7. A double-bus RR as an add-drop filter.

The Drop and Through outputs are given by,

$$R = |\rho|^2 = \left|\frac{b_1}{a_1}\right|^2 = \left|\frac{r(1-a\exp(i\delta))}{1-r^2 a\exp(i\delta)}\right|^2 = \frac{r^2 + r^2a^2 - 2r^2a\cos\delta}{1+r^4a^2-2r^2a\cos\delta} \tag{2.16}$$

$$T = |t|^2 = \left|\frac{c_2}{a_1}\right|^2 = \left|\frac{-\kappa^2\sqrt{a}\exp(i\delta/2)}{1-r^2a\exp(i\delta)}\right|^2 = \frac{(1-r^2)^2 a}{1+r^4a^2-2r^2a\cos\delta} \tag{2.17}$$

The Drop port is denoted as *T* since it corresponds to *transmission* of the FP interferometer whereas the Through port is denoted as *R* corresponding to *reflection* in the FP interferometer.

2.3.1. The build-up factor, finesse and Q factor

In this section, we shall briefly introduce the build-up factor, finesse and Q factor of 1R2B. First, the light build-up inside the 1R2B can be expressed as,

$$B = \left|\frac{c_1}{a_1}\right|^2 = \left|\frac{i\kappa}{1-ar^2\exp(i\delta)}\right|^2 \xrightarrow{\delta=2\pi m} = \frac{\kappa^2}{1-2ar^2\cos\delta+a^2r^4} \tag{2.18}$$

Similar to build-up factor of the 1R1B case, the build-up factor of the 1R2B is also linearly proportional to (κ^2). The only difference lies in the additional bus which is reflected in the additional factor (r) in the denominator of Eq. (2.18). In the lossless case around resonance, Eq. (2.18) can be simplified to,

$$B_2\big|_{a\approx1,\delta\approx0} = \frac{1}{1-r^2} \tag{2.19}$$

Using the same finesse definition defined in Eq. (2.5) and applying similar Taylor's expansion in the high finesse approximation, we can express the FWHM as $\Delta\delta_{1/2} \approx 2(1-ar^2)/r\sqrt{a}$. Substituting this value back into Eq. (2.5), the finesse of 1R2B can be calculated as,

$$F_2 = \frac{\pi r\sqrt{a}}{1-ar^2} \xrightarrow{a\approx1} = \frac{\pi r}{(1-r^2)} \xrightarrow{r\approx1} = \pi B_2 \tag{2.20}$$

Comparing the build-up factor B_1 of 1R1B and B_2 of 1R2B, we calculate the ratio between the two build-up factors,

$$\frac{B_1}{B_2}\bigg|_{a\approx1,\delta\approx0} = \left(\frac{1+r}{1-r}\right)\Big/\left(\frac{1}{1-r^2}\right) = (1+r)^2 \xrightarrow{r\approx1} 4 \tag{2.21}$$

In the high finesse and lossless limit, Eq. (2.20) simply tells us that the finesse of 1R2B (F_2) is ½ of the finesse of 1R1B (F_1). Similarly, Eq. (2.21) shows that the build-up factor B_2 of 1R2B is ¼ of the build-up factor B_1 of 1R1B. This is not surprising as the additional bus waveguide in the 1R2B (i.e.,

the Drop port) doubles the cavity leakage loss hence halving the finesse of the overall device and reducing the build-up by a factor of ~ $(1+r)^2$. Lastly, the quality factor of 1R2B can be written as,

$$Q \equiv \frac{\lambda_0}{\Delta\lambda_{1/2}} = \frac{\delta_0}{\Delta\delta_{1/2}} = \frac{2\pi nL/\lambda}{2(1-ar^2)/r\sqrt{a}} = (nL/\lambda)F_2 = mF_2 \tag{2.22}$$

The Q-factor is no different than Eq. (2.9), only the finesse is now based on the 1R2B (F_2).

2.3.2. The effective phase shift

Based on the transfer output characteristics given by Eqs. (2.16) and (2.17), we can further derive the phase response of the 1R2B where $\rho = |\rho| \angle\varphi_R$ and $t = |t| \angle\varphi_T$. The corresponding phase term φ_R can be deduced as,

$$\varphi_R = -\tan^{-1}\left(\frac{a\sin\delta}{1-a\cos\delta}\right) + \tan^{-1}\left(\frac{r^2 a\sin\delta}{1-r^2 a\cos\delta}\right) + 2\pi m \tag{2.23}$$

Eq. (2.16) can also be rewritten in the form of $\rho = r\,\mathrm{e}^{i(\pi+\delta)}(a-\mathrm{e}^{-i\delta})/(1-r^2 a\,\mathrm{e}^{i\delta})$ and thus the phase term can also be expressed in the alternative form,

$$\varphi_R = \pi + \delta + \tan^{-1}\left(\frac{\sin\delta}{a-\cos\delta}\right) + \tan^{-1}\left(\frac{r^2 a\sin\delta}{1-r^2 a\cos\delta}\right) \tag{2.24}$$

On the other hand, the phase term φ_T is given by,

$$\varphi_T = \pi + \frac{\delta}{2} + \tan^{-1}\left(\frac{r^2 a\sin\delta}{1-r^2 a\cos\delta}\right) \tag{2.25}$$

Fig. 2.8 shows the transmission and the phase response of the 1R2B (Through and Drop port) under the (1) lossy ($a < 1$), (2) lossless ($a = 1$) and (3) gain ($a > 1$) conditions.

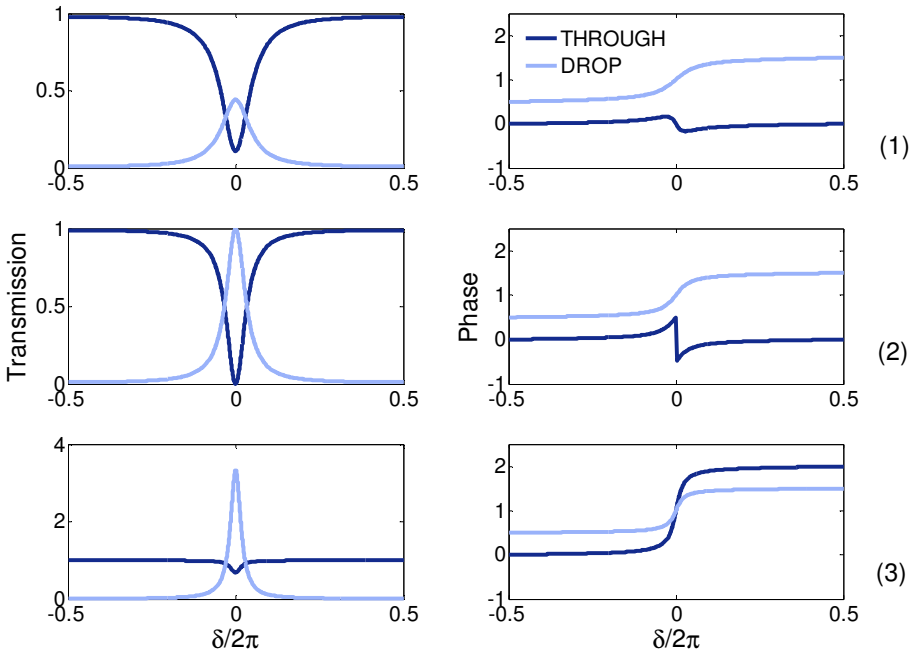

Fig. 2.8. Transmission (left) and phase response (right) of 1R2B when (1) $a = 0.9$, (2) $a = 1$, (3) $a = 1.1$ ($r = 0.9$).

By comparing with Fig. 2.4 for the 1R1B case, we note that the Drop output phase is always similar to the overcoupled case whereas the Through output phase can look similar to the under-, critically- and over-coupled case depending on the a value. When $a = r$ (case 1) the Through port is undercoupled, in contrast with the 1R1B case where critical coupling would occur, because of the additional coupling loss to the Drop bus. If the 1R2B is lossless (case 2), then the power coupled into the resonator is equal to the power lost in the Drop-port, and thus the output is zero in the Through-port, corresponding to complete destructive interference. This is similar to critical coupling in the 1R1B case, where all the power is consumed by propagation loss inside the resonator instead of coupling loss at the Drop port. Lastly, when gain is incorporated into 1R2B, the Through port can be over-coupled when light coupled into the resonator exceeds the loss at the Drop bus. More generally, for arbitary value of a, as stated earlier, zero reflection can always be obtained by using asymmetric mirrors, such that $r_1 = ar_2$. In 1R1B, this condition reduces to the critical coupling condition $r = a$.

2.3.3. The group delay (GD) and group delay dispersion (GDD)

In this section we shall briefly discuss the GD and GDD for the 1R2B configuration. In line with the results presented earlier in Fig. 2.8, Fig. 2.9 presents the corresponding GD and GDD of both Through and Drop output under-, critically, and over-coupled for the Through output. Since only the Through has both a single pole and zero (the Drop has the same pole), thus it is sufficient to show only the

pole-zero diagram for the Through port. The zero is located as $z = a\angle 2\pi$ and the pole is located as $p = r^2 a\angle 2\pi$. Three cases are highlighted: (a) When the Through output is undercoupled, the zero is located within the unity circle (minimum phase zero) which produces negative group delay for the Through port. (b) When the Through output is critically coupled under the lossless situation, there is virtually no difference between the Drop and the Through output since the system is lossless and independent of any given port excitations. This is also verified by the fact that the system is only dependent on the same pole, which is shared by both Drop and Through output. (c) When gain is applied and the Through port is overcoupled, the zero is located outside the unity circle (maximum phase zero) which produces positive group delay for the Through port. As a result, the overall GD and GDD are larger for the case of Through port as compared to the Drop port.

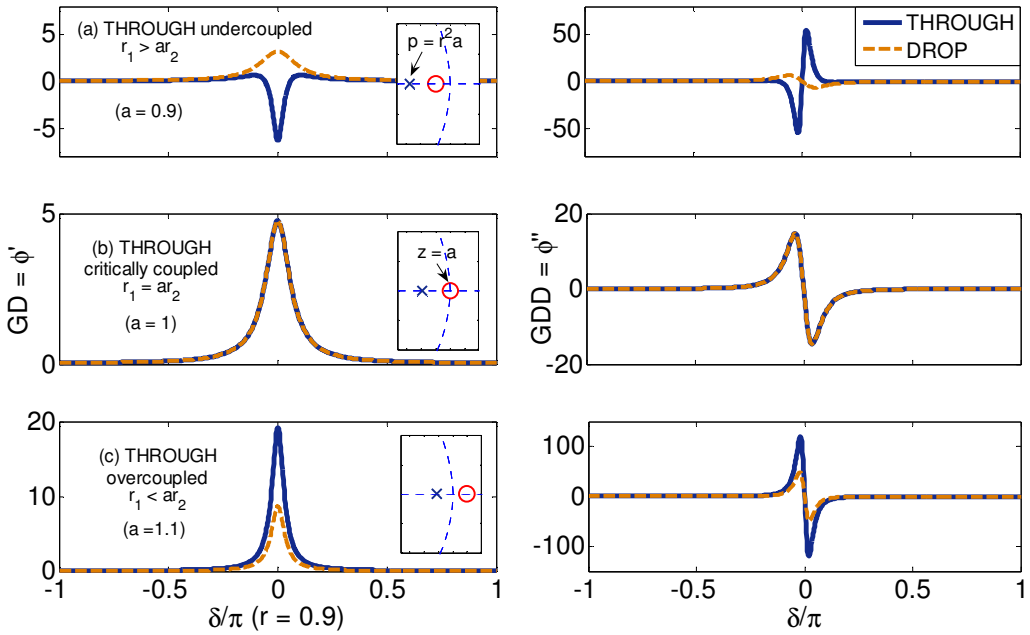

Fig. 2.9. The GD (left) and GDD (right) of the 1R2B for Through and Drop output.

In summary, the important figure-of-merits (FOMs) for both the 1R1B and the 1R2B are summarized in Table. 2.1. In general the 1R2B has additional factor *r* due to the additional Drop-bus waveguide.

FOM	1R1B	1R2B
R,T	$R=\left\|\frac{r-a\exp(i\delta)}{1-ra\exp(i\delta)}\right\|^2$	$R=\left\|\frac{r(1-a\exp(i\delta))}{1-r^2a\exp(i\delta)}\right\|^2 \quad T=\left\|\frac{-\kappa^2\sqrt{a}\exp(i\delta/2)}{1-r^2a\exp(i\delta)}\right\|^2$
B	$B=\left\|\frac{i\kappa}{1-ar\exp(i\delta)}\right\|^2$	$B=\left\|\frac{i\kappa}{1-ar^2\exp(i\delta)}\right\|^2$
F	$F=\frac{\Delta\delta_{FSR}}{\Delta\delta_{1/2}}=\frac{2\pi}{\Delta\delta_{1/2}}=\frac{\pi\sqrt{ar}}{1-ar}$ $\Delta\delta_{1/2}\simeq 2(1-ar)/\sqrt{ar}$	$F=\frac{\Delta\delta_{FSR}}{\Delta\delta_{1/2}}=\frac{2\pi}{\Delta\delta_{1/2}}=\frac{\pi r\sqrt{a}}{1-r^2a}$ $\Delta\delta_{1/2}\simeq 2(1-ar^2)/r\sqrt{a}$
φ	$\varphi=\pi+\delta+\tan^{-1}\left(\frac{r\sin\delta}{a-r\cos\delta}\right)+\tan^{-1}\left(\frac{ra\sin\delta}{1-ra\cos\delta}\right)$	$\varphi_R=\pi+\delta+\tan^{-1}\left(\frac{\sin\delta}{a-\cos\delta}\right)+\tan^{-1}\left(\frac{r^2a\sin\delta}{1-r^2a\cos\delta}\right)$ $\varphi_T=\pi+\frac{\delta}{2}+\tan^{-1}\left(\frac{r^2a\sin\delta}{1-r^2a\cos\delta}\right)$

Table. 2.1. The important FOMs for both 1R1B and 1R2B: The transmission output (*R*,*T*), the build-up factor (*B*), the finesse (*F*), and the phase response (φ).The GD and GDD is not shown here due to very complicated mathematical representations. The quality factor Q is simply calculated as $Q=mF$ where *m* is the resonant order. The cavity lifetime is calculated as $\tau_{CAV}=FT_R$ where T_R is roundtrip time (*nL*/c).

2.4. Experimental measurements of basic device parameters

In this section we shall cover the experimental aspect pertaining to the basic structures, such as the straight waveguides, serpentines, and the 1R2B structures. All of the devices presented in this chapter were fabricated in LETI (France) using a CMOS based deep-UV process [16]. The SOI consists of ~196nm thick Silicon on a 2μm oxide buffer layer. In the DUV lithography process, the exposure dose is incrementally stepped up from the left to the right of the 8" wafer such that the gap width (waveguide width) increases (decreases) from left to right of the wafer. These variations imply that different devices on the wafer will have different coupling coefficients, and hence one can study the behavior of the directional coupler (DC) with various κ values of interest. The UV resist is then used as the etch mask for an ICP etch through the Si layer to form the photonic wire waveguides. To facilitate fiber coupling, a second-order grating is integrated with the device [12]. The fiber is butt-coupled to the grating 10° off the vertical axis. The coupling efficiency has a Gaussian spectral profile with a bandwidth of about 30 nm. The device is excited with a broadband source with wavelength ranging from 1.42 μm to 1.61 μm. The output power is then passed through a 90:10 splitter, where

10% power goes to a fiber power meter for alignment purpose, whereas the rest goes to an optical spectrum analyzer for normalization with the input spectrum. Fig. 2.10(a) illustrates the fiber-to-grating mechanism (left) and the actual fabricated grating (right). The grating is fabricated at the two ends of the 10μm-wide input/output port waveguides and then is adiabatically tapered to the single-mode photonic wire (~0.45 μm wide) which later goes into our respective devices under test (DUT).

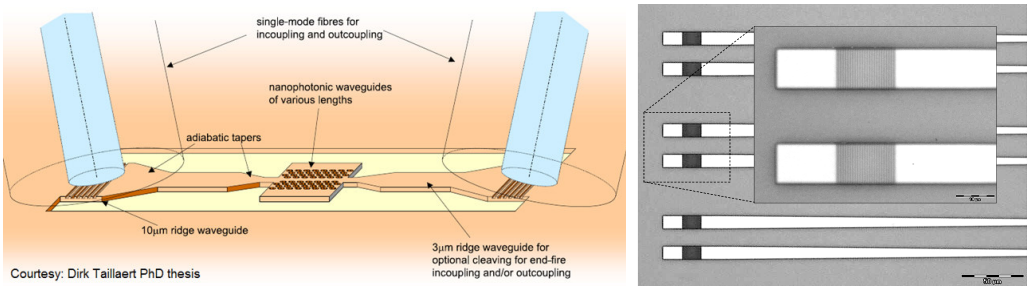

(a)

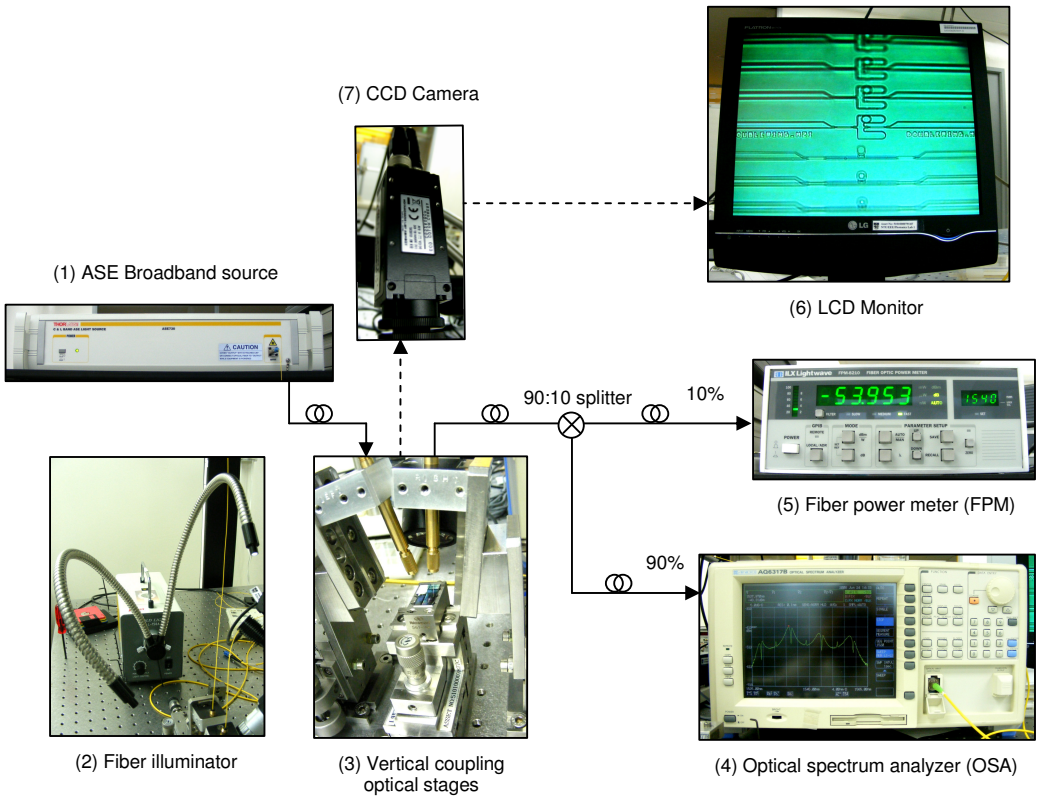

(b)

Fig. 2.10(a) Left: The illustration of near vertical coupling [12], Right: The fabricated grating. (b) The measurement setup showing: (1) the ASE broadband source, (2) the fiber illuminator, (3) the optical stages with 10° off-vertical fiber-to-grating coupling mechanism, (4) the optical spectrum analyzer (OSA), (5) the fiber-pigtailed power meter (FPM), (6) the LCD monitoring screen, (7) the CCD camera.

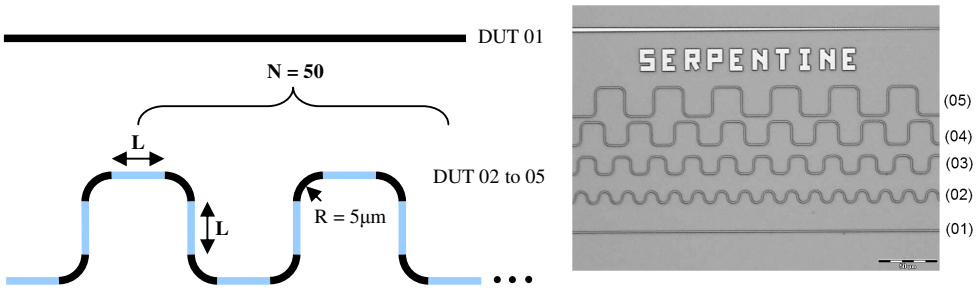

Fig. 2.11. Straight waveguide (DUT 01) and serpentine structures (DUT 02 to 05). Note that the serpentine bending radius is 5µm and its unit cell is repeated over 50 times (N). The straight section in the serpentine structure (L) is varied from 0, 5, 10 and 15µm for DUT 02, 03, 04 and 05 respectively.

2.4.1. Straight and serpentine waveguide structures

The fabricated SOI photonic wire has a thickness of 196nm and width of 450nm. To estimate the intrinsic waveguide losses and the bending losses, we have the straight waveguide and serpentine structures fabricated. The unit cell which is composed of 4 sections of straight waveguides and 4 sections of 90° bends, is repeated 50 times. This is to average out the overall loss so that the bending loss can be estimated more accurately. Fig. 2.12 shows the measurement results for these 5 types of devices, namely DUT 01 to 05. The DUT 01 represents the output of the straight WG whereas the DUT 02 to 05 represents the output of the serpentine structures.

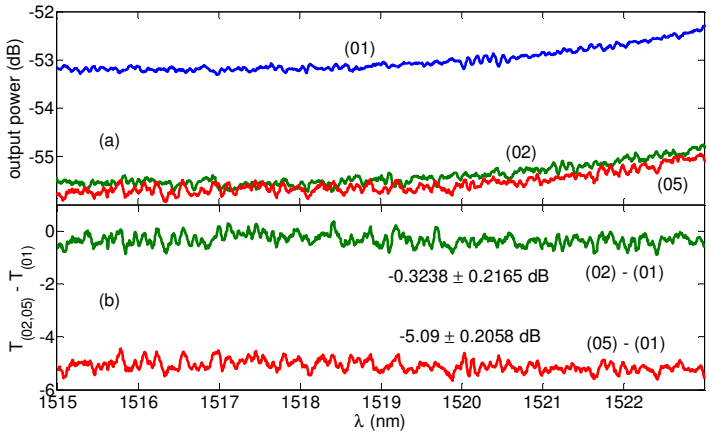

Fig. 2.12(a) The measured output power of DUT 01 to 05 (not yet normalized), (b) The normalized measured output power for DUT (02) and (05) along with the calculated mean and standard deviation.

The measured power of the serpentines structures (DUT 02 to 05) fluctuates within the range of -0.3238±0.2165dB. This implies that such additional loss is contributed by the additional length of $50\times 2L$ = 0.15cm. Based on this remark, the intrinsic waveguide loss is roughly estimated to be ~

2.1587±1.4433 dB/cm, which is comparable to the loss reported in [16]. The bending loss is estimated based on the -5.09±0.2058dB offset which is contributed by the 200 sets of 90° bends. Thus, the bending loss is estimated at ~0.0255±0.001dB per 90° bend. Typically, the waveguide loss is deduced using Fabry-Perot (FP) method by estimating the fringes contrast of the interference pattern in the transmission spectra. However, such interference pattern is not applicable here as fiber-grating is used for coupling mechanism. Therefore, we estimate the waveguide loss directly from the power reading at the measured output, using serpentine waveguide structures. Of course, the calculation here is based on the assumption that the grating is uniform throughout the sample and the fiber-to-grating coupling is done consistently for each measurement taken.

2.4.2. One-ring-two-bus (1R2B) structure

Next, we move on into the characterization of 1R2B structures equivalent to the 1R2B. Fig. 2.13 shows the fabricated 1R2B using the "racetrack" couplers which are miniature directional couplers (DC). Below is the list of parameter variations associated with the devices. For each set of ring radius, the coupler length (L_C) is varied by 2μm increment in length. This way, we could estimate the coupling coefficient of the DC and plot the *r* value as a function of the DC length.

DUT #	R	L_C #0	L_C #1	L_C #2	L_C #3	L_C #4
6 to 10	5	0	2	4	6	8
11 to 14	10	-	10	12	14	16
15 to 18	15	-	18	20	22	24

Table. 2.2. The 1R2B-DUTs with variations in the coupler length and ring radius. All length units are indicated in μm.

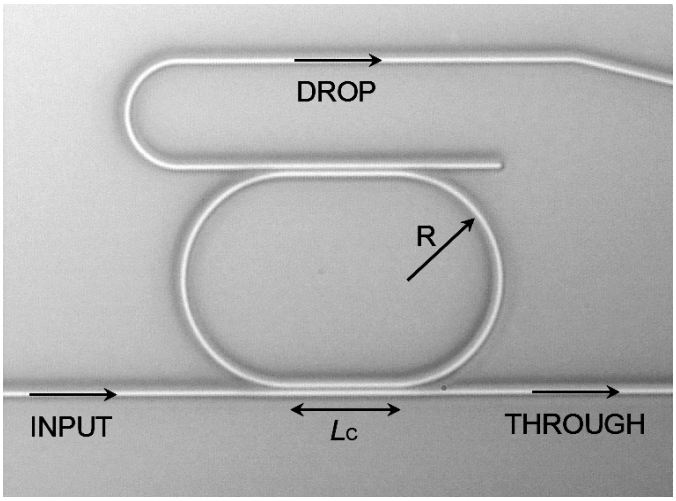

Fig. 2.13. The 100× microscope view of the fabricated 1R2B device.

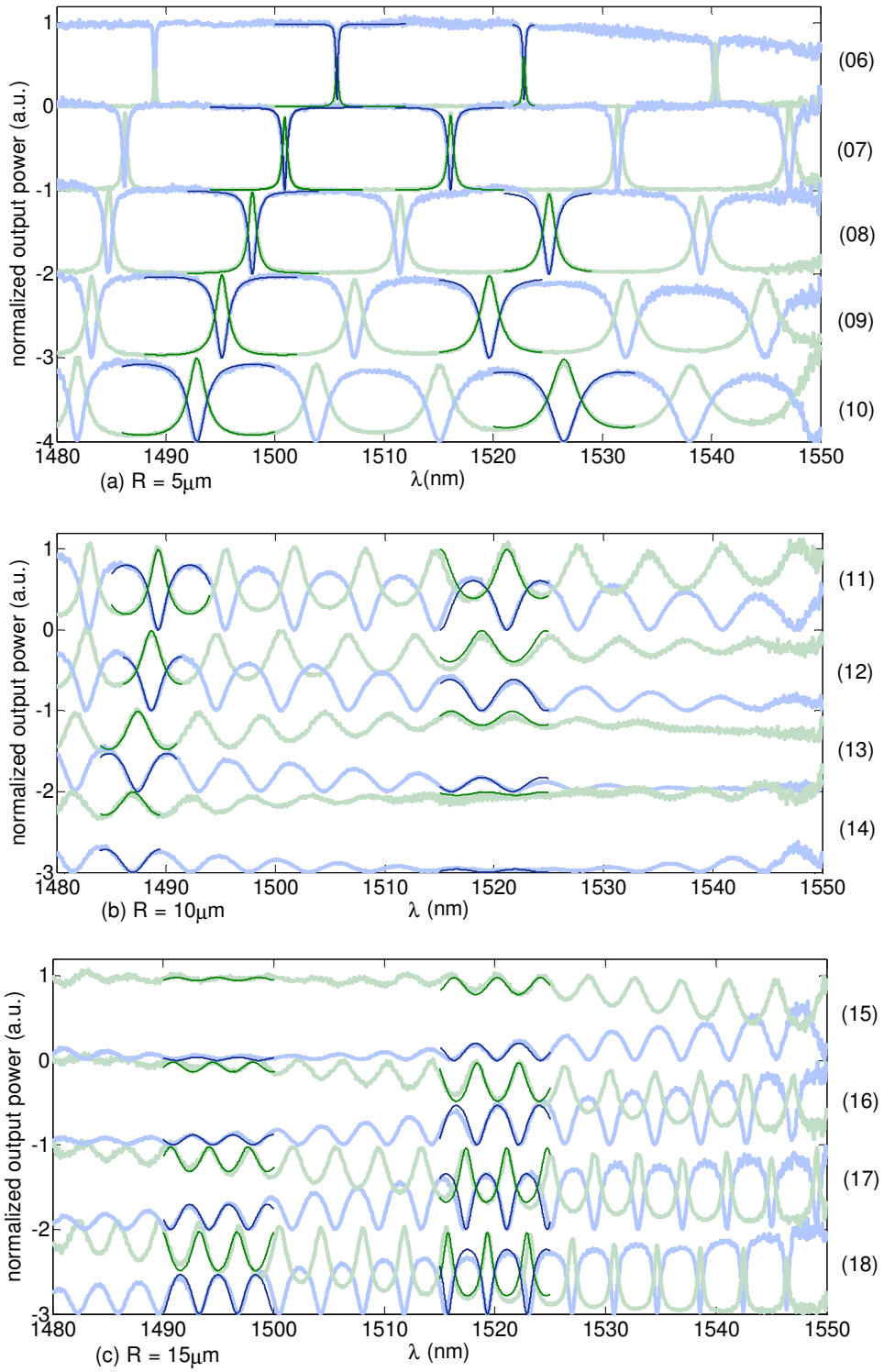

Fig. 2.14. The 1R2B measured spectra with the theoretical fit imposed to obtain the (r) values. The Drop (Through) port is indicated by the green (blue) spectra. The numbers on the right column indicate the devices under test. The estimated group index n_g is ~4.3 for 450nm width SOI photonic wire (wire thickness of ~196nm).

By fitting the theoretical model to the measured data we extracted the group index (n_g) in the ring, the coupling factor (r) and the propagation loss (a) in the cavity waveguide. The group index is obtained by matching the round trip phase shift δ to be the nearest multiple integer of 2π. Fig. 2.15 shows the plotted finesse (left axis), maximum Drop D_{MAX} (right axis) and group index (inset), as a function of coupling length (DUT 06 to 10). We obtain an average group index value of ~4.3 which is smaller than the one reported in [16] (~220nm) because the fabricated waveguide is 24nm thinner (~196nm). The group index gradually decreases as the coupler length increases. This is because shorter coupler length causes light to stay longer inside the resonator (higher finesse), thereby increasing its dispersive properties and consequently causes higher group index. We further obtain a finesse value of ~60 with quality factor of ~5,400 for DUT 06, which is based on a point-coupler, comparable to the 1R2B reported in [16]. Also, when the finesse is higher; the light build-up is higher and causing more effective losses inside the ring. This is shown by the overall trend in Fig. 2.15 where the D_{MAX} gradually decreases as the finesse increases.

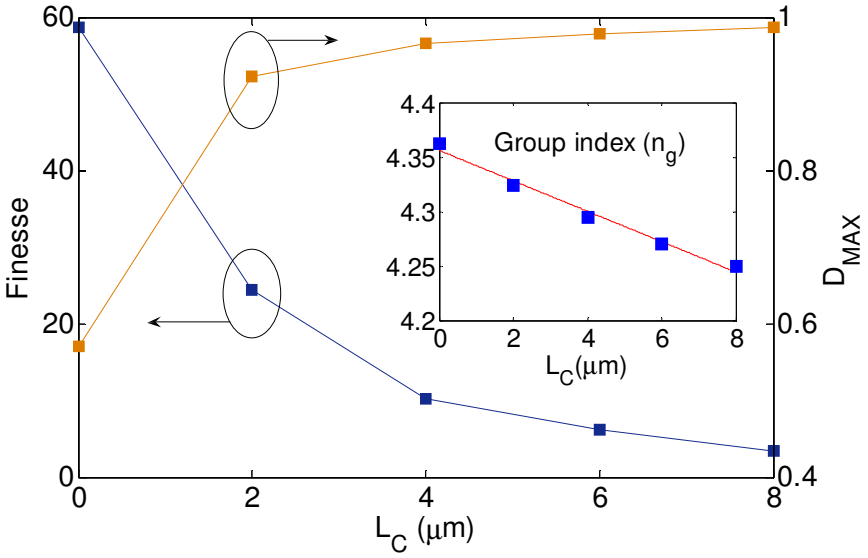

Fig. 2.15. The finesse (left axis) and the D_{MAX} (right axis) versus coupling length L_C for DUT 06 to 10. The inset shows the estimated group index. The results are based on the fitting around ~1520nm (refer to Table 2.3).

DUT	r	a	n_g	Finesse	D_{MAX}
6	0.98	0.987	4.3626	58.7176	0.5705
7	0.94	0.995	4.3236	24.3645	0.9236
8	0.86	0.995	4.295	10.164	0.9673
9	0.78	0.995	4.2703	6.1261	0.9797
10	0.65	0.995	4.2495	3.3899	0.9878

Table. 2.3. The fit parameters for DUT 06 to 10 for r, a, n_g and the corresponding finesse and D_{MAX}.

The (r) values can be easily obtained by matching resonance linewidth (i.e, the Lorentzian envelope) between the experiment and the theory for both Through and Drop transmissions, simultaneously. However, fitting (a) is a bit more tricky, due to its dependency on other effects which alter the normalization factor (i.e., the grating envelope effect, insertion loss, etc). Fortunately, such dependency can be regarded as negligible for higher-finesse rings as the loss is dominated by the cavity loss instead of the other losses, making the estimation of (a) to be more accurate. Thus, the (a) value is approximated only for DUT 6 to 10 ($r > 0.65$). Furthermore, the Drop output is preferred for fitting due to higher sensitivity of D_{MAX} to (a) when the light is on-resonance.

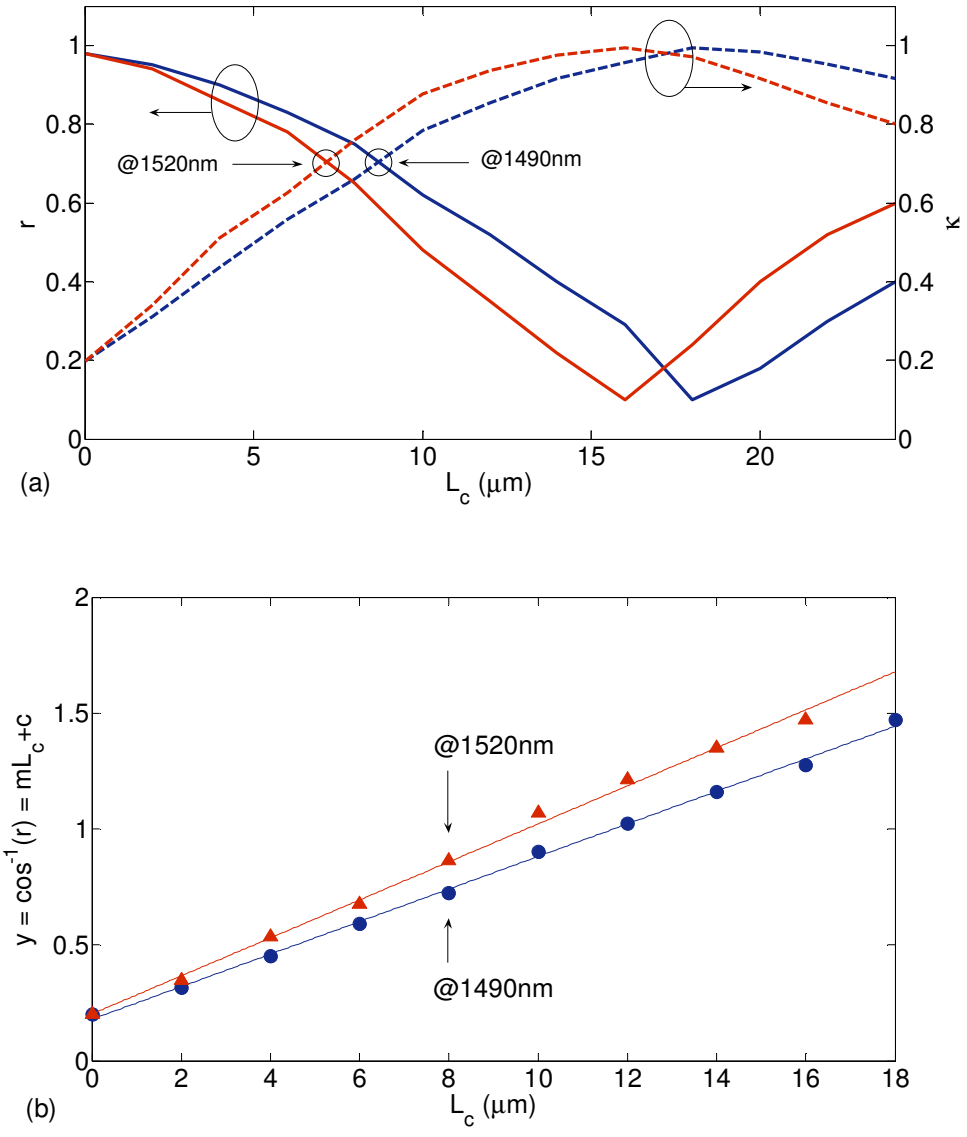

Fig. 2.16(a) The (r) values as a function of DC length (L_C) measured around 1490nm and 1520nm; (b) The linear regression applied in order to approximate the coupling length ($L_\pi = \pi L_0 / 2c$) by taking account of the offset ($L_0 = c/m$) which is regarded as the effective length of a point coupler.

Fig. 2.16 shows the estimated *r* values as a function of the DC length L_C for DUT 06 to 18. In general, the *r* value gradually follows a cosine relationship in which it decreases to ~0.1 at L_C ~ 19μm and increases back when *L* is slightly greater than L_π. The *r* value also becomes more sensitive to λ as L_C increases due to lower finesse. In order to obtain a consistent result, the value of (*r*) is interpolated around the same λ for the case of lower ring finesse. This is partly the reason why we apply the theoretical fit around 1490nm and 1520nm for Fig. 2.14. In the longer wavelength regime, the DC length relative to λ is smaller. Thus, the coupling length (L_π) should also be shorter. For example, we can rougly estimate that the coupling length at λ ~ 1490nm is around 19μm whereas the coupling length at 1520nm is around 16 μm. This implies ~1μm L_π difference over ~10nm wavelength variation.

To estimate a more precise value of the coupling length L_π, we apply a linear regression in Fig. 2.16(b) by making use the relation $y = \cos^{-1}(r) = \pi(L_C + L_0)/(2L_\pi) = mL_C + c$, where the parameter $L_0 = c/m$ may be regarded as the *effective length* of the zero point coupler. The linear fit is obtained based on the coupling coefficients extracted from Fig. 2.16(a) for two different wavelengths (1490 and 1520nm). The $[L_0, L_\pi]$ values of [22.38μm, 2.56μm] around 1490nm and $[L_0, L_\pi]$ values of [19.17μm, 2.4767μm] around 1520nm are obtained respectively. The measurement of (*r*) here will be useful as we study the 2RMZI devices in Chapter 6. This is because the 2RMZI is based on the two-ring-one-bus (2R1B) with racetrack couplers. Thus, it is important to obtain independent theoretical fitting of (*r*) based on standalone 1R2B devices. This way, the theoretical fitting is done consistently throughout the thesis.

2.5. Conclusion

To sum up, we have introduced basic ring-resonator structures such as the 1R1B and 1R2B devices. Their basic properties such as its transfer function, phase response, build-up factor, finesse, Q-factor, cavity lifetime, group delay and dispersion are introduced. The basic serpentine waveguides and 1R2B devices are fabricated by CEA LETI (France) using CMOS-based deep-UV lithography. Good agreement is obtained between the theory and the experimental work, verifying the analysis and assumptions being used. The 1R2B fabricated parameters such as group indexes, coupling coefficients and cavity losses are deduced accordingly. The fitting parameters obtained will serve as independent fitting in estimating the fabricated parameters of the 2R1B structures in Chapter 6.

Chapter 3

Ring resonator arrays

3.1. Introduction

Ring Resonator (RR) arrays is an exciting research area due to its immense potential in diverse applications as direct consequences of having many different possible array configurations. For instance, the linear and nonlinear optical properties of mutually coupled arrays (Type I) and periodically coupled arrays (Type II) were studied in [37, 38, 40, 42, 45, 53]. Synthesis of optical filters making use of RR arrays were developed in [37, 49, 50, 56, 57] and fabricated in many different material platforms. In this Chapter, we propose a novel type of filter making use of the photonic bandgap properties of Type I and Type II arrays which leads to the design of a 'perfect' filter based on the 2D-RR array configuration. The pole-zero approach [81] is applied to understand better the mechanism of the 2D-RR array in the context of apodization. This way, we can better understand the device based on two complementary perspectives.

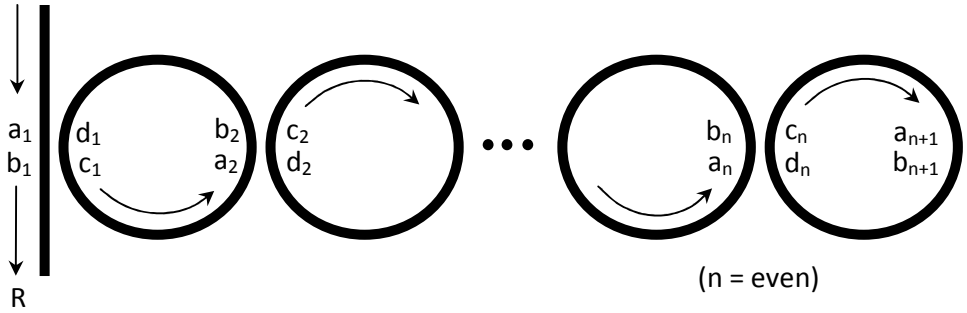

Fig. 3.1. Coupled ring resonators with one bus waveguide (single-bus Type I). Note that *n* is the number of ring resonators, as well as the number of couplers.

3.2. Single-bus Type I

Fig. 3.1 depicts the structure of the coupled ring resonator with one bus waveguide. For simplicity, the coupling between the ring resonators and that between the ring and the waveguide are all assumed identical and lossless, as described by the matrix relation [167, 171],

$$\begin{bmatrix} b_n \\ c_n \end{bmatrix} = \begin{bmatrix} r & i\kappa \\ i\kappa & r \end{bmatrix} \begin{bmatrix} a_n \\ d_n \end{bmatrix} \tag{3.1}$$

where r is the reflectivity as defined before, and $r^2 + \kappa^2 = 1$. It is convenient to derive the output field in a periodic structure such as this by using the transfer matrix formulation. Noting that $a_{n+1} = c_n \exp(i\delta/2)$, $d_n = b_{n+1}\exp(i\delta/2)$, we obtain the following recursive transfer matrix relation:

$$\begin{bmatrix} a_{n+1} \\ b_{n+1} \end{bmatrix} = \begin{bmatrix} A & B \\ C & D \end{bmatrix} \begin{bmatrix} a_n \\ b_n \end{bmatrix} = \begin{bmatrix} A & B \\ C & D \end{bmatrix}^N \begin{bmatrix} a_1 \\ b_1 \end{bmatrix} \equiv M \begin{bmatrix} a_1 \\ b_1 \end{bmatrix} \tag{3.2}$$

$$A = -\frac{\sqrt{a}}{i\kappa}\exp(i\delta/2) \qquad B = \frac{r\sqrt{a}}{i\kappa}\exp(i\delta/2)$$

$$C = -\frac{r}{i\kappa\sqrt{a}}\exp(-i\delta/2) \qquad D = \frac{1}{i\kappa\sqrt{a}}\exp(-i\delta/2)$$

Note that the *ABCD* matrix is *unimodular* (even in the presence of loss), i.e., *AD-BC* = 1, hence the matrix *M* is also unimodular. This is because the ring resonators are assumed to be symmetric and identical, and hence *reciprocal*. Using the Sylvester's theorem [80], we may express the matrix coefficient m_{11}, m_{12}, m_{21}, m_{22} in terms of the Chebysev polynomials of the second kind:

$$M = \begin{bmatrix} m_{11} & m_{12} \\ m_{21} & m_{22} \end{bmatrix} = \begin{bmatrix} AU_{N-1}(x) - U_{N-2}(x) & BU_{N-1}(x) \\ CU_{N-1}(x) & DU_{N-1}(x) - U_{N-2}(x) \end{bmatrix} \tag{3.3}$$

$$U_0(x) = 1,\ U_1(x) = 2x,\ U_2(x) = 4x^2 - 1,\ U_3(x) = 8x^3 - 4x, \text{ etc}$$

where $x = (A+D)/2$. Additional polynomials can readily be obtained from the recursion relation $U_{N+1} - 2xU_N + U_{N-1} = 0$ (Note: $U_i = 0$ when $i < 0$). Applying the continuity condition $a_{n+1} = b_{n+1}$ to Eq. (3.2) leads to the equation for the reflection coefficient:

$$\rho = \frac{b_1}{a_1} = \frac{m_{11} - m_{21}}{m_{22} - m_{12}} = \frac{AU_{N-1}(x) - U_{N-2}(x) - CU_{N-1}(x)}{DU_{N-1}(x) - U_{N-2}(x) - BU_{N-1}(x)} \tag{3.4}$$

In this equation, the zeros and poles correspond respectively, to the critical coupling and the oscillation conditions. Thus, the general critical coupling condition for the case of *n* rings can be expressed as:

$$A - C = U_{N-2}(x)/U_{N-1}(x) \tag{3.5}$$

while the oscillation condition is given by

$$D - B = U_{N-2}(x)/U_{N-1}(x) \tag{3.6}$$

Here we consider the cases of 1, 2, and 3 rings. For N = 1, Eq. (3.5) reduces to $A - C = 0$, which has the solution $\delta = 2\pi m$, where m is an integer, and $r = a$. Likewise, the oscillation condition is given by $D = B$, which implies $\delta = 2\pi m$, and $r = 1/a$. For N = 2, the critical coupling condition can be expressed by $A - C = 1/(A+D)$ or $(a^2 + r)\cos\delta + i(a^2 - r)\sin\delta = ar(1+r)$. Hence critical coupling requires $r = a^2$ and occurs at the values of δ given by $\cos\delta = a(1+a^2)/2$. Likewise, the oscillation condition is given by $D - B = 1/(A+D)$, which leads to $(ra^2 + 1)\cos\delta + i(ra^2 - 1)\sin\delta = ar(1+r)$. Hence, oscillation requires $r = a^{-2}$ and occurs at frequencies given by $\cos\delta = (1 + 1/a^2)/(2a)$. For N = 3, the critical coupling condition is given by $A - C = 1/\left[A + D - 1/(A+D)\right]$, which reduces to two sets of equations:

(i) $\delta = 2\pi m$, and $ar^3 + (-2a^2 + a)r^2 + (-a^2 + a - 1)r + a^3 = 0$ (3.7a)

(ii) $$\sin^2(\delta/2) = \frac{-ar^3 - (2a^2 + a)r^2 - (a^2 + a - 3)r + 3a^3}{4(r + a^3)} \tag{3.7b}$$

and $(a^4 - 2a^2)r^3 + (a^4 - a^2 + 1)r^2 + a^4 r - a^6 = 0$

These can be solved numerically to give the combinations (*a, r*, δ). Similarly, the oscillation condition is given by $D - B = 1/\left[A + D - 1/(A+D)\right]$, which has two sets of solutions:

(iii) $\delta = 2\pi m$, and $-a^2 r^3 + (-a^2 + 2a)r^2 + (a^3 - a^2 + a)r - 1 = 0$ (3.8a)

(iv) $$\sin^2(\delta/2) = \frac{-a^2 r^3 - (a+2)ar^2 + (3a^2 - a - 1)ar + 3}{4(ra^3 + 1)} \tag{3.8b}$$

and $(-2a^4 + a^2)r^3 + (a^6 - a^4 + a^2)r^2 + a^2 r - 1 = 0$

As the number of rings increases, the equations become mathematically more complex to express analytically. However, it is apparent that the critical coupling condition has the general form of a continued fraction:

$$A - C = \frac{1}{A + D - \dfrac{1}{A + D - \dfrac{1}{A + D - \ldots}}} \tag{3.9}$$

and similarly for the oscillation condition. For N rings, there will be n critical coupling points for $a < 1$, and N oscillation points for $a > 1$. This is due to the splitting of the original resonance as a result of mutual coupling between the N rings. In Fig. 3.2 we plot the relationships between a and r under the critical coupling and oscillation conditions for n = 1, 2, 3. Note that these relationships assume that a and r are independent variables, which is a good approximation. We can see that the linear relation $r = a$ only applies for the case n = 1. As the number of rings increases, the relationships become nonlinear, and the required r values become smaller. This is because the critical coupling coefficient $\kappa = (1 - r^2)^{1/2}$ has to increase in order to compensate for the increased total internal loss. Note that, for N = 3, there are two critical values of r for each value of a, given by Eqs. 3.7(a) and (b) respectively.

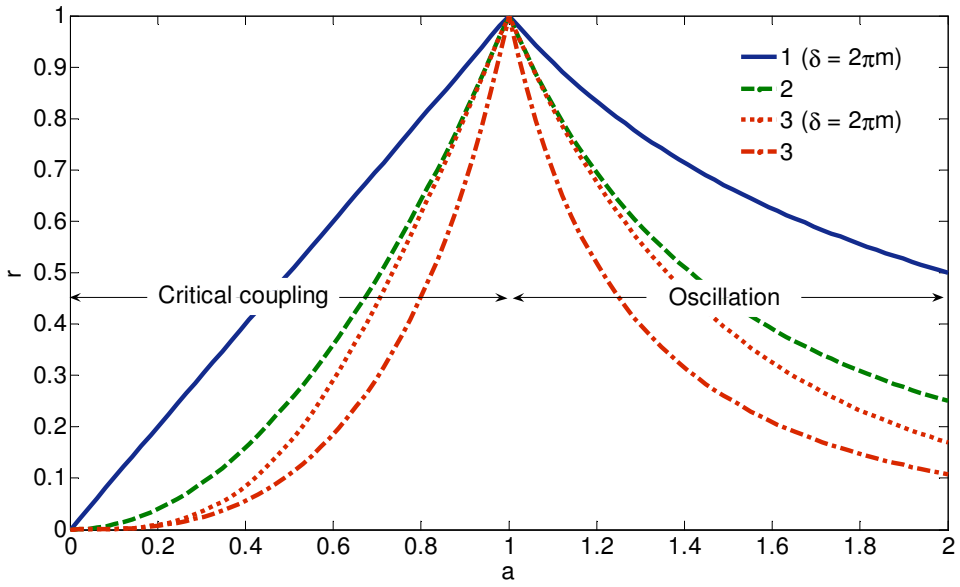

Fig. 3.2. The relationships between a and r for critical coupling and oscillation conditions for a single-bus Type I configuration with 1, 2, and 3 rings.

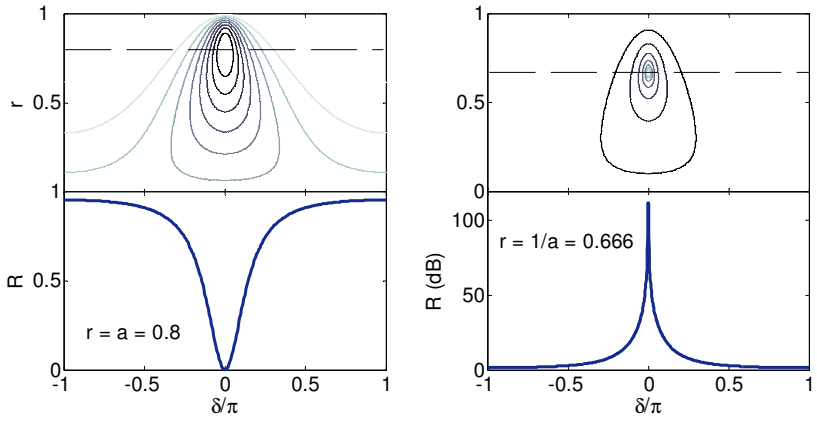

(a) $N = 1$

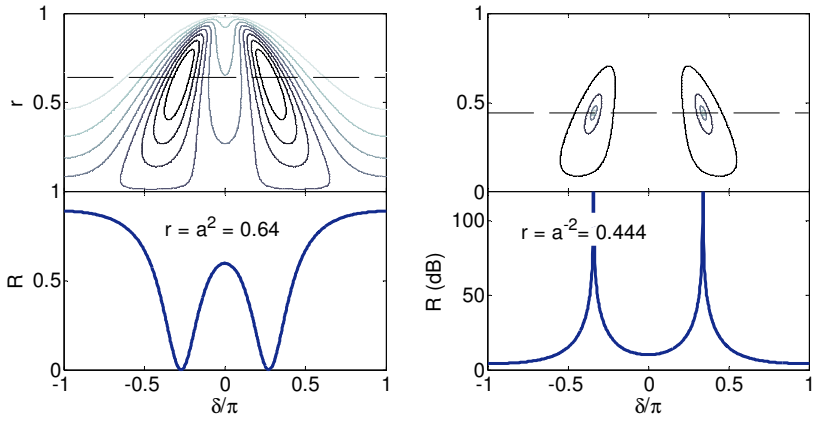

(b) $N = 2$

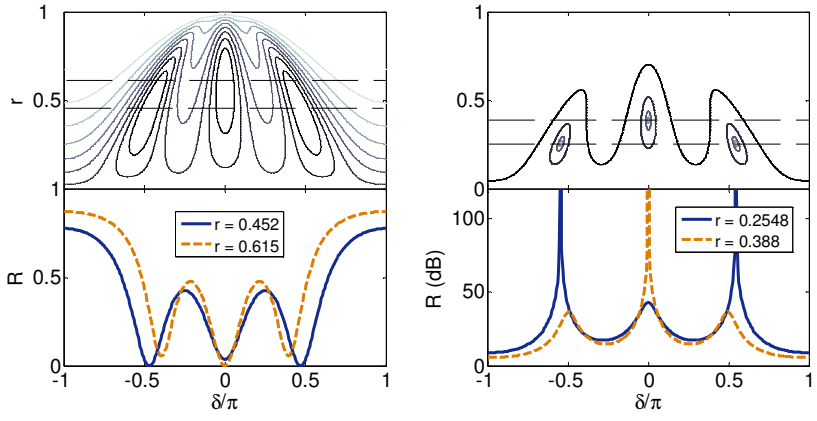

(c) $N = 3$

Fig. 3.3. Upper: Simulated output R in contour plot for N rings single-bus Type I, as a function of ring reflectivity r and round-trip phase δ for a given a. Lower: The spectra around the critical coupling (left, $a = 0.8$) and oscillation (right, $a = 1.5$) conditions. The curves are symmetrical about $\delta = 0$.

Using the required combinations of a and r, the frequencies δ which critical coupling or oscillation occurs can be calculated. In general, the zero frequencies are symmetrically located about the resonance frequencies $\delta = 2\pi m$. These are shown by some numerical simulations in Fig. 3.3, for $N = 1$ to 3. The contour plots show R as a function of r and δ, for a fixed value of a. The crosses are the critical points where the reflection is either zero (for $a < 1$) or infinity (for $a > 1$). The curves below the contour plots are the reflection spectra when the conditions for either critical coupling or oscillation are satisfied.

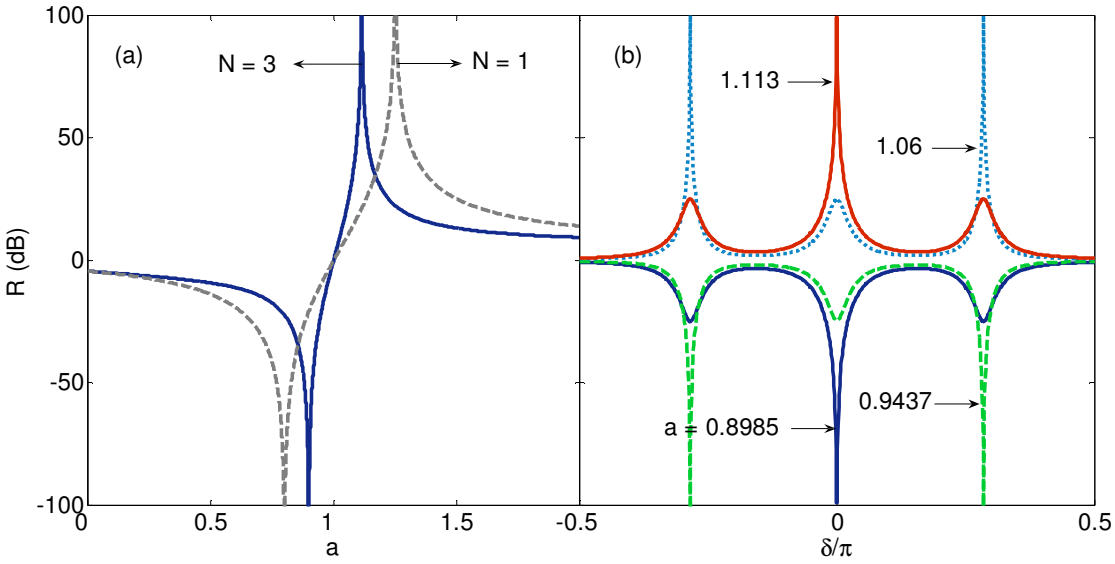

Fig. 3.4 (a) Reflection at the resonance frequency ($\delta = 2\pi m$) as a function of a, for 1- and 3-ring single-bus Type I, showing the turning points at critical coupling and at oscillation condition. (b) Reflection spectra for the 3-ring Type I, for various values of a ($r = 0.8$).

When the reflection at resonance frequency is plotted as a function of a (for a fixed r), as shown in Fig. 3.4(a) for $N = 1$ and 3, it shows the two signature turning points at both the critical coupling and the oscillation conditions. Note that the two turning points are closer for the case of 3 rings and further apart for 1 ring. This implies that the three-ring structure is more sensitive to a variation in a about the critical coupling point. Furthermore, the three-ring structure has three resonance frequencies, and the output at each of these frequencies can be modulated by varying a. This is shown in Fig. 3.4(b) where a is varied from the critical coupling values (different for different frequencies) to the oscillation values. The spacing between the resonance frequencies is determined by r: the smaller r is, the stronger the interaction between rings, and hence the larger the splitting of the ring resonance. Note that in the model so far δ is assumed to be independent of a. In reality, any change in absorption or gain is always accompanied by a perturbation in the refractive index, which will then cause a shift in δ. In principle, this effect can be included to obtain more accurate results, but the qualitative outcome will not change.

3.3. Double-bus Type I

Fig. 3.5 depicts the structure of the coupled ring resonator with a double bus waveguides. Because of the second bus waveguide, the input light may now be reflected or transmitted depending on the optical frequency. When the resonators are on resonance, the Type I filter is maximally transmissive.

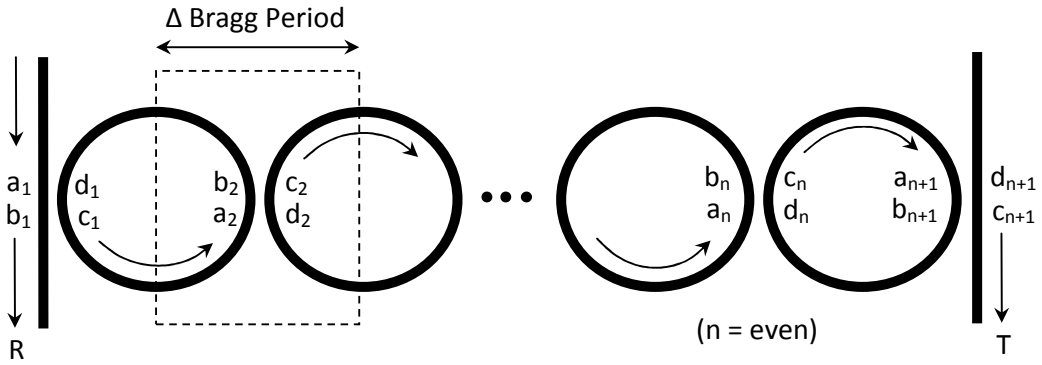

Fig. 3.5. Coupled ring resonators with two bus waveguide; *n* is the number of ring resonators, and Δ is the spatial period.

When the rings are off resonance, the light is reflected. Hence, there are non-overlapping reflection and transmission bands which make the Type I a very good high-order wavelength-dropping filter [167] (In filter terminology, the reflection band corresponds to the "Through" channel, and the transmission band corresponds to the "Drop" channel). However, because of inter-resonator coupling, there are ripples (sidelobes) in the transmission (reflection) band. The conditions for the reflection minima (or transmission maxima) can be found analytically, similar to that in the single-bus case. With reference to Fig. 3.5 and using Eqs. (3.1) and (3.2), it can be shown that,

$$\begin{bmatrix} c_{n+1} \\ d_{n+1} \end{bmatrix} = \frac{1}{i\kappa}\begin{bmatrix} -1 & r \\ -r & 1 \end{bmatrix}\begin{bmatrix} a_{n+1} \\ b_{n+1} \end{bmatrix} = \frac{1}{i\kappa}\begin{bmatrix} -1 & r \\ -r & 1 \end{bmatrix}\begin{bmatrix} m_{11} & m_{12} \\ m_{21} & m_{22} \end{bmatrix}\begin{bmatrix} a_1 \\ b_1 \end{bmatrix} \tag{3.10}$$

Applying the boundary condition $d_{n+1} = 0$ (i.e., there is no input on the right bus waveguide) gives the reflection and transmission coefficients as follows:

$$\rho = \frac{b_1}{a_1} = \frac{rm_{11} - m_{21}}{m_{22} - rm_{12}} = \frac{r\left[AU_{N-1}(x) - U_{N-2}(x)\right] - CU_{N-1}(x)}{DU_{N-1}(x) - U_{N-2}(x) - rBU_{N-1}(x)} \tag{3.11}$$

$$t = \frac{c_{n+1}}{a_1} = \frac{i\kappa}{m_{22} - rm_{12}} = \frac{i\kappa}{DU_{N-1}(x) - U_{N-2}(x) - rBU_{N-1}(x)} \tag{3.12}$$

where m_{11}, m_{12}, m_{21}, m_{22} are the same Chebysev polynomials used in Eq. (3.3). The zeros in Eq. (3.11) give the conditions for *reflection minima* analogous to the critical coupling condition for the single-bus case:

$$rA - C = U_{N-2}(x)/U_{N-1}(x) \tag{3.13}$$

The poles, which are identical for both reflection and transmission, give the oscillation conditions:

$$D - rB = U_{N-2}(x)/U_{N-1}(x) \tag{3.14}$$

Eq. (3.12) also suggests that t cannot be zero, although it can be very small as we will show in later section. Again, we consider the cases of N = 1, 2, 3. For n = 1, Eq. (3.13) reduces to $rA - C = 0$, which has the solutions $\delta = 2\pi m$, where m is an integer, and $a = 1$, regardless of the value of r. The oscillation condition is given by $D = rB$, which implies $\delta = 2\pi m$, and $r = a^{-1/2}$. For N = 2, the critical coupling condition can be expressed as $rA - C = 1/(A + D)$ or $(a^2 + 1)\cos\delta + i(a^2 - 1)\sin\delta = a(1 + r^2)$, which admits only the solution a = 1, regardless of the value of r. The corresponding two values of δ are given by $\cos\delta = (1 + r^2)/2$. Likewise, the oscillation condition are given by $D - rB = 1/(A + D)$, or $(r^2a^2 + 1)\cos\delta + i(r^2a^2 - 1)\sin\delta = 2r^2a$. Hence, oscillation requires $r = a^{-1}$ and occurs at two values of δ given by $\delta = \pm\cos^{-1}(r)$. For N = 3, the critical coupling condition is given by $rA - C = 1/\left[A + D - 1/(A + D)\right]$, which reduces to two sets of equations:

$$\text{(i)} \qquad \delta = 2\pi m, \text{ and } (a-1)(a^2 - 2ar^2 + 1) = 0 \tag{3.15a}$$

$$\text{(ii)} \qquad \sin^2(\delta/2) = \frac{(-2a^2 - 2a)r^3 + (3a^3 - a^2 - a + 3)r}{4r(a^3 + 1)} \tag{3.15b}$$

$$\text{and } (-2a^4 + 2a^2)r^2 + a^6 - a^4 + a^2 - 1 = 0$$

Again the only solution is a = 1, regardless of the value of r ($0 \le r \le 1$), and there are three reflection zeros, one at resonance $\delta = 2\pi m$ and two at $\delta\big|_{a=1} = \pm 2\sin^{-1}\left[(1 - r^2)/2\right]^{1/2}$, which depend only on r. Likewise, the oscillation condition is given by $D - rB = 1/\left[A + D - 1/(A + D)\right]$, which reduces to two sets of equations:

$$\text{(iii)} \qquad \delta = 2\pi m, \text{ and } -a^2r^4 + (a^3 - 2a^2 + 3a)r^2 - 1 = 0 \tag{3.16a}$$

$$\text{(iv)} \qquad \sin^2(\delta/2) = \frac{-a^2r^4 + (3a^3 - 2a^2 - 3a)r^2 + 3}{4(r^2a^3 + 1)} \tag{3.16b}$$

$$\text{and } (a^6 - 3a^4 + a^2)r^4 + 2a^2r^2 - 1 = 0$$

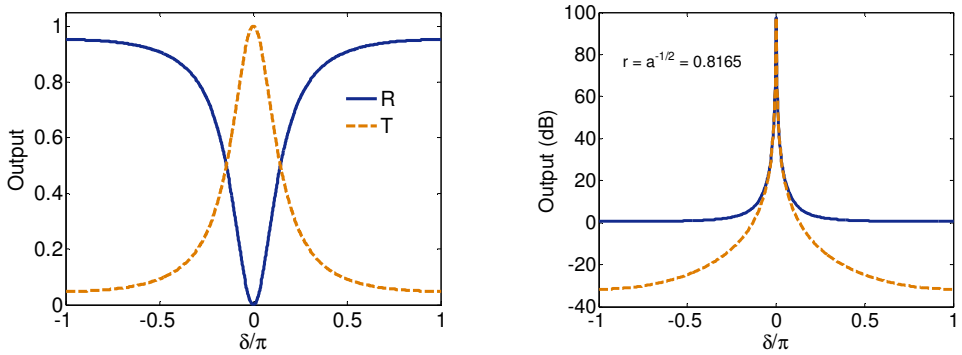

(a) $N = 1$

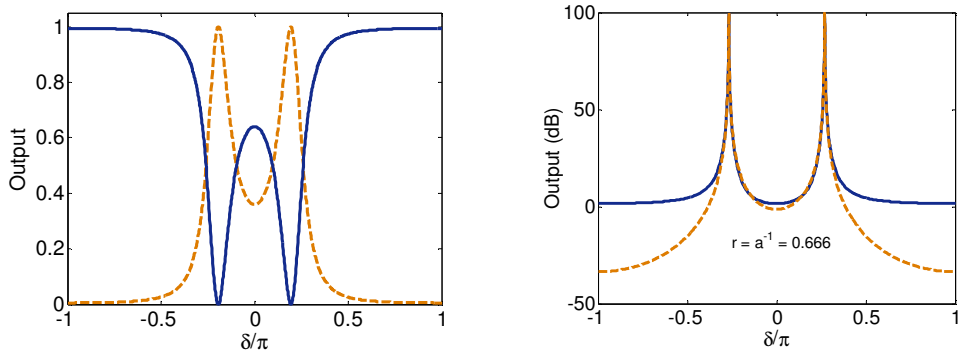

(b) $N = 2$

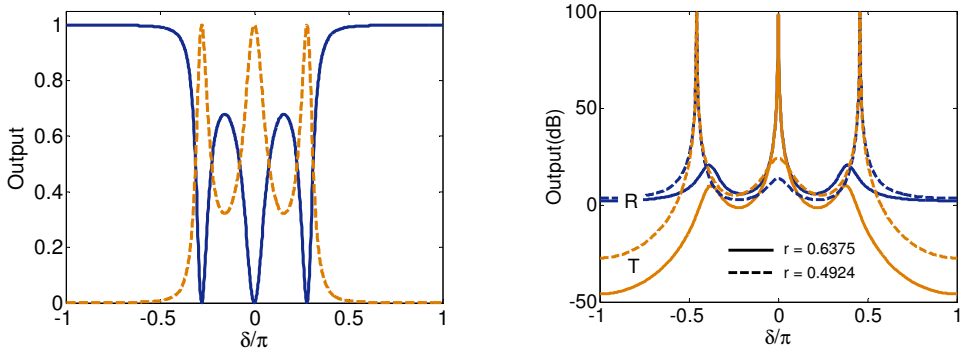

(c) $N = 3$

Fig. 3.6. Transmission and reflection spectra of a double-bus Type I configuration with various number of rings (N = 1, 2, 3). Left: a = 1 (lossless case) and r = 0.8, showing the critical coupling in the reflection port. Right: The R and T spectra for $a = 1.5$, showing the oscillation frequencies and their corresponding coupling conditions (a, r).

The allowed solutions for (a, r), where $a \geq 1$, are similar to that shown in Fig. 3.2. Oscillation can occur at resonance, $\delta = 2\pi m$ and at two other frequencies that depend on both the a and r values.

For illustration we show the reflection $(R = |\rho|^2)$ and transmission $(T = |t|^2)$ spectra for $N = 1, 2, 3$ rings in Fig. 3.6. On the right is the oscillation case, where $a > 1$ implies that the ring structure has a uniform gain. When a is sufficiently large, both R and T may be greater than 1 near the resonance frequency. Far from resonance R approaches 1 and T tends to 0. On the left is shown the lossless case where $a = 1$, which implies that $R + T = 1$. Note that there are n reflection zeros for N rings, and again far from resonance R approaches 1 and T approaches 0. For the more general case where $a < 1$, the spectra are similar except that the minimum R is non-zero and the maximum is less than 1.

Fig. 3.7 shows the transfer functions R and T at the ring resonance frequency ($\delta = 2\pi m$) as a function of a for the 1-ring and 3-ring Type I configuration. As in the single-bus case, R behaves similarly except that one of the turning points ($R = 0$) is always fixed at $a = 1$, irrespective of the coupling coefficient. It can be seen that both curves are simply shifted to the right compared with the single-bus case. The two turning points are closer for the case of 3 rings and further apart for 1 ring. This implies that the three-ring structure is more sensitive to a variation in a about the critical coupling point. T, on the other hand, has only one turning point, and is a slowly varying function of a except near oscillation.

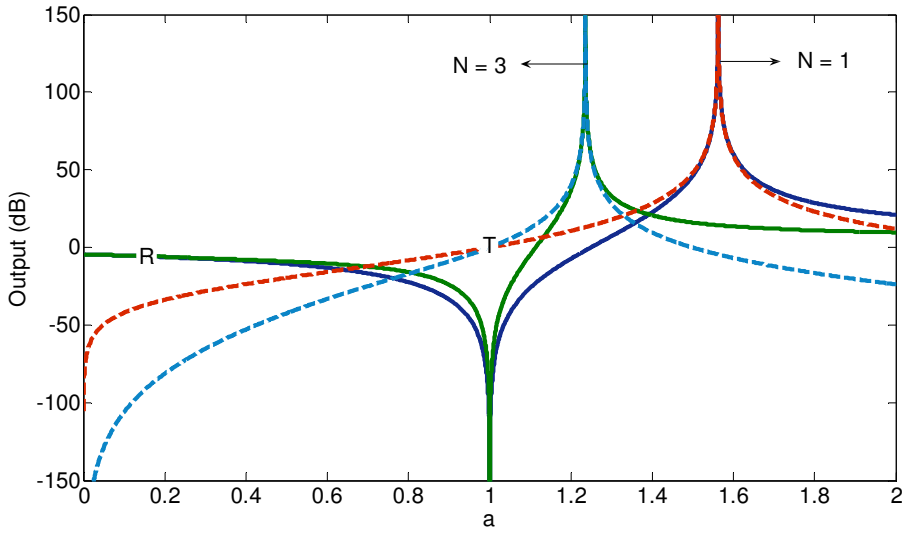

Fig. 3.7. Double-bus Type I configuration: Reflection and transmission at the resonance frequency as a function of a, for $N = 1$ and 3. The point where $R = 0$ always occurs at $a = 1$ regardless of the value of r.

Furthermore, the three-ring structure has three resonance frequencies at each of which the outputs can be modulated by varying a. This is shown in Fig. 3.8 which gives the modulations in R and T spectra in response to loss or gain modulation around the critical point $a = 1$. The spacing between the resonance frequencies is again determined by r. The value $a = 1.2354$ corresponds to $r = 0.8$ required

for oscillation at the resonance frequency ($\delta = 2\pi m$), while $a = 1.1246$ corresponds to the oscillation at the other two frequencies.

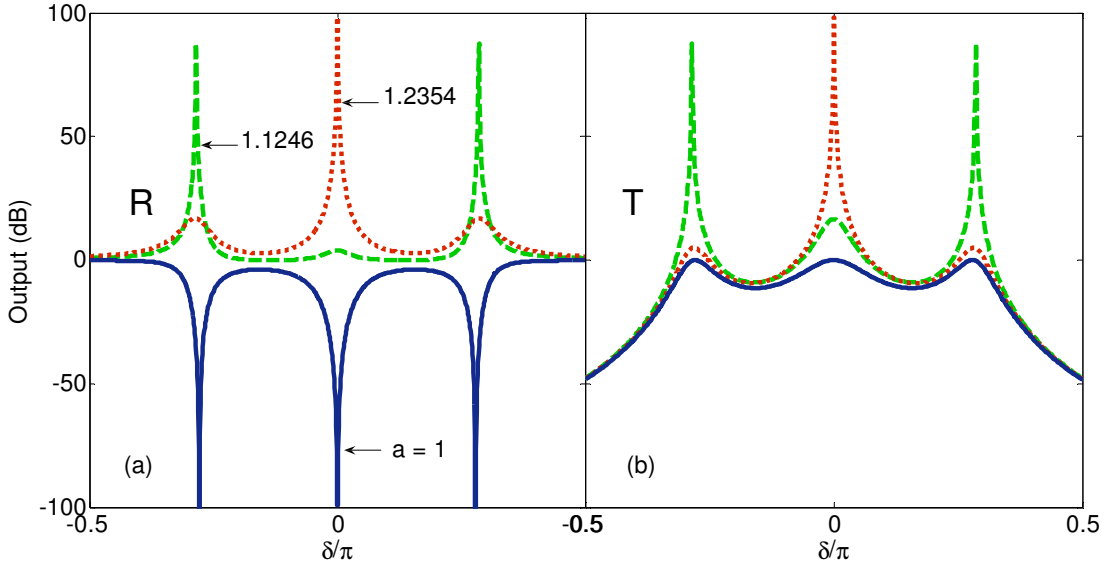

Fig. 3.8(a) Reflection and (b) transmission spectra for a 3-ring double-bus CROW with $r = 0.8$.

3.3.1. Photonic bandgap structure of infinite rings for double-bus Type I

We note that in Fig. 3.6 the oscillations (or ripples) in R and T are confined within a frequency band centered at the ring resonance frequency ($\delta = 2\pi m$) with the band width determined by the coupling coefficient. As the number of rings increases, the transitions at the band edges become steeper, and R and T approach more closely to 1 and 0 respectively. Indeed, as shown below, the reflection bands approach closely the photonic bandgaps of an infinite periodic structure.

Photonic bandgaps are frequency bands in which no light is transmitted [167]. The photonic band structure can be derived by applying the Bloch theorem to the transfer matrix and assuming lossless situation [172]:

$$\begin{bmatrix} a_{n+1} \\ b_{n+1} \end{bmatrix} = \exp(i\beta\Delta) \begin{bmatrix} a_n \\ b_n \end{bmatrix} \tag{3.17}$$

where β is the Bloch wavevector, and $\Delta = L_b$ is the Bragg period as shown in Fig. 3.5. Combining this with Eq. (3.2) gives the characteristic relation,

$$\cos(\beta\Delta) = (A + D)/2 = -\sin(\delta/2)/\kappa \tag{3.18}$$

which is plotted in the left half of Fig. 10. The photonic bandgap is the region where β is pure imaginary. Compared with the calculated transmission spectra for $n = 1$, 3 and 5 rings, as shown on

the right, we can see that with just 5 rings (in the lossless case), the transmission spectrum already exhibits a band with near-zero amplitude similar to a photonic bandgap. Propagation through the coupled resonators is allowed only when the resonators are on resonance. When the resonators are off resonance, the wave is reflected by the Type I device. Hence, the transmission properties of the coupled resonator array are similar to a multi-layer stack, with narrow transmission bands and wide forbidden (reflection) regions. This feature is the reverse of the previous uncoupled case, which exhibits narrow reflection resonances (bandgaps) and broad transmissions bands.

Many interesting properties can be derived from the dispersion relation (3.18). For example, the group velocity, v_g, which is proportional to the slope of the dispersion curve, is given by:

$$v_g = \frac{d\omega}{d\beta} = \frac{2\kappa \cdot FSR \cdot \Delta \sin(\beta\Delta)}{\cos(\delta/2)} \tag{3.19}$$

where *FSR* is the free spectral range. From this and Fig. 3.9, it can be seen that the group velocity is maximum at the centre of the passband where $\sin(\beta\Delta) = 1$, and zero at the band edges where $\sin(\beta\Delta) = 0$. This is approximately true also for finite structures. The slowing of the wave at the band edge is in contrast to the case of a single resonator where the group delay is maximum at resonance. Thus, for higher-order filters having large number of coupled resonators, the group delay and the dispersion are shifted to and greatly enhanced at the band edges [40]. Although this will restrict the usable bandwidth of the filter, it is still preferable to the single-ring case.

The group velocity is insensitive to geometry as the product $FSR \cdot \Delta$ is approximately constant, but it can be increased or reduced by varying κ. Changing κ will also affect the transmission bandwidth, which can be found from the condition $\sin(\delta/2)/\kappa = 1$ to be:

$$B = \frac{2}{\pi} FSR \cdot \sin^{-1}(\kappa) \tag{3.20}$$

The larger the κ, the greater the interaction between the rings, and hence the broader the bandwidth. Within the transmission band, the dispersion curve is quite linear. This implies that the Type I structure behaves as a uniform slab waveguide forming a Fabry Perot cavity, hence the ripples in the transmission spectra can be interpreted as due to the Fabry-Perot interference effect, whereby the number of maxima is equal to the number of rings. Outside the band, at each zero crossing of the sidelobes there is a π-phase discontinuity which has no physical relevance, since the delay is undefined when the reflectance is zero.

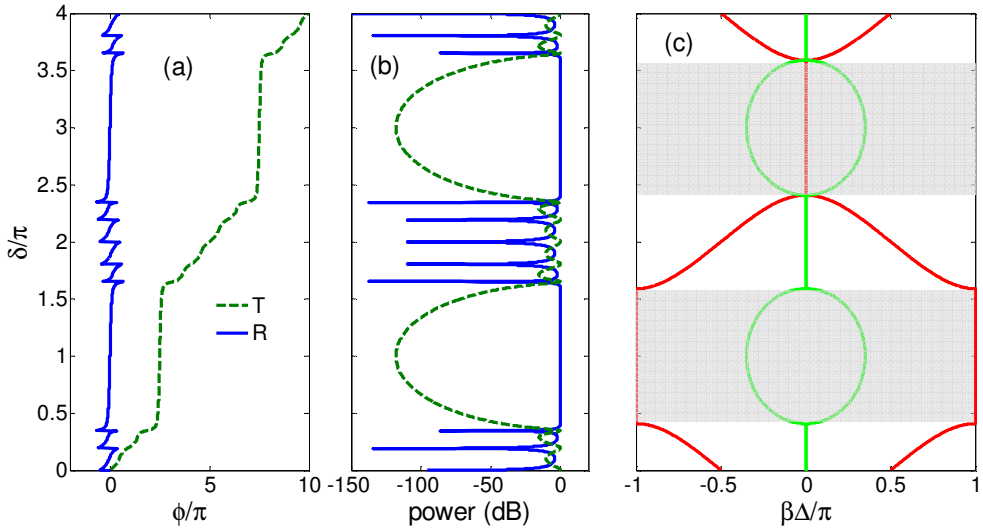

Fig. 3.9(a) The phase response, (b) the output power, (c) the dispersion diagram showing the real (in red) and imaginary (in green) parts of the Bloch wave propagation constant β as a function of normalized frequency δ. The result is based on a double-bus 5 rings Type I configuration (r = 0.8). Ripples from the reflection spectra occur in the transmission bands.

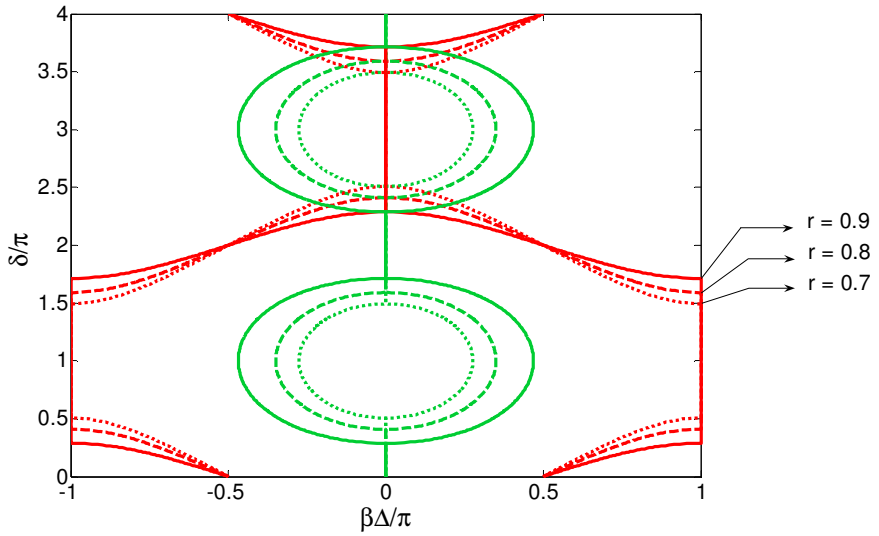

Fig. 3.10 The dispersion diagram for various coupling coefficients (r) in the lossless double-bus Type I configuration.

3.4. Double-bus Type II

In the case of Type II configuration, as shown in Fig. 3.11, the light is input as a_0 and is either "transmitted as b_{N-1} or "reflected" as c_0. Separated by the period L_b, the fields in adjacent rings are related by $d_{N-1} = c_N \exp(i\gamma L_b)$ and $a_N = b_{N-1} \exp(i\gamma L_b)$. The array is similar to a distributed feedback grating, giving rise to Bragg resonances in addition to the ring resonances.

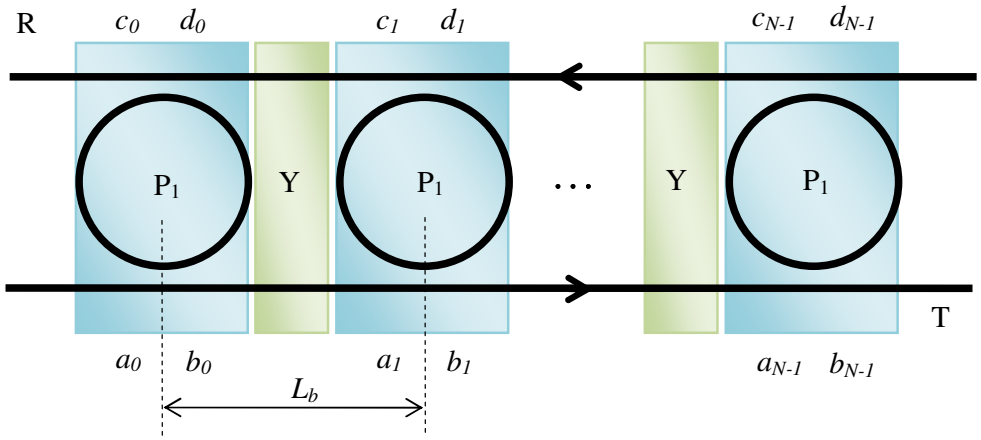

Fig. 3.11. The double-bus Type II configuration.

The Bragg resonances arise when the Bragg condition, $\lambda_j = 2n_{eff} L_b / j$ (j = 1, 2, 3…), is satisfied. These resonances will overlap with the ring resonances if we set $L_b = L_c/2$. This is the most useful case, for which the transfer matrix relation is

$$\begin{bmatrix} b_{N-1} \\ d_{N-1} \end{bmatrix} = (P_1 Y)^{N-1} P_1 \begin{bmatrix} a_0 \\ c_0 \end{bmatrix} \equiv \begin{bmatrix} E & F \\ G & H \end{bmatrix} \begin{bmatrix} a_0 \\ c_0 \end{bmatrix} \tag{3.21}$$

P and Y are unimodular matrices representing the two-bus single-ring resonator and the inter-resonator bus waveguide respectively, and are given by

$$\begin{aligned} P &= \frac{1}{r(\exp(-i\delta) - a)} \begin{bmatrix} r^2 \exp(-i\delta) - a & -\kappa^2 \sqrt{a} \exp(-i\delta/2) \\ \kappa^2 \sqrt{a} \exp(-i\delta/2) & \exp(-i\delta) - r^2 a \end{bmatrix} \\ Y &= \begin{bmatrix} a^{1/2} \exp(i\delta/2) & 0 \\ 0 & a^{-1/2} \exp(-i\delta/2) \end{bmatrix} \end{aligned} \tag{3.22}$$

Note that for simplicity, we have assumed uniform loss throughout the waveguides. Similar to the previous case, the matrix $(PY)^{N-1}$ can be also expressed using the Sylvester theorem, and the final output are $t = b_N / a_0 = (EH - GF)/H = 1/H$ and $\rho = c_0 / a_0 = -G/H$.

Similar to the Type I case, this structure is also periodic in series. Hence, it must exhibit a photonics bandgap for the transmitted waves. The band structure is derived by implementing the

Bloch theorem on the matrix that is periodic in nature with determinant of 1 (reciprocity must be satisfied). Since the matrix already (*PY*) fulfills the reciprocity condition, thus we can express the bandgap matrix as:

$$\begin{bmatrix} a_{N+1} \\ c_{N+1} \end{bmatrix} = PY \begin{bmatrix} a_N \\ c_N \end{bmatrix} = \begin{bmatrix} m_{11} & m_{12} \\ m_{21} & m_{22} \end{bmatrix} \begin{bmatrix} a_N \\ c_N \end{bmatrix} = \exp(i\beta\Delta) \begin{bmatrix} a_N \\ c_N \end{bmatrix} \tag{3.23}$$

Based on this equation, we may solve for the eigenvalues with the characteristic equation as follow:

$$\cos(i\beta\Delta) = \frac{m_{11} + m_{22}}{2} \tag{3.24}$$

Fig. 3.12 shows the output and the phase response for both the transmission (T) and the reflection (R) ports. Since the Type II is a periodic structure, thus it also exhibits a photonic bandgap property in the periodic direction. The forbidden bandgap will inhibit light passing through the transmission (T) port since such port goes through the periodicity of the rings. Also, since the transmission and reflection are complementary to each other, any light forbidden in (T) will be redirected to the (R) port. Such relationship is clearly illustrated by Fig. 3.12(a) and (b).

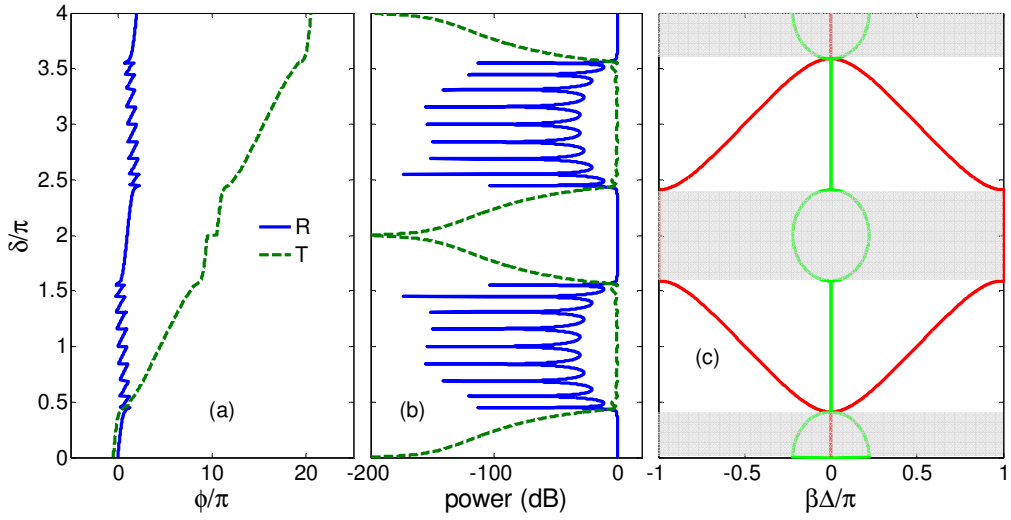

Fig. 3.12(a) The phase response, (b) the output power, (c) the dispersion diagram showing the real (in red) and imaginary (in green) parts of the Bloch wave propagation constant β as a function of normalized frequency δ. The result is based on 10 rings Type II configuration (r = 0.8). Ripples from the reflection port occur in the transmission bands.

Outside the reflection bands are a number of *sidelobes* proportional to *N* (in the transmission spectrum these sidelobes become *ripples*). Here, it can be seen that the slope of the dispersion curve is quite constant, so the ring structure behaves as a uniform slab with a constant group refractive index and a thickness proportional to *N*. Therefore, the ripples in the passband of (T) may be interpreted as the Fabry-Perot interference within the slab; the thicker the slab, the greater the number of ripples.

Moreover, the wider the bandgap, the higher will be the group index (i.e., the smaller the slope of the dispersion curve), and hence the larger the ripple amplitude. The width of the bandgap is dependent on the coupling between the waveguide and the resonator. The stronger the coupling (i.e., the smaller the r^2), the stronger will be the feedback between the resonators, and hence the wider the bandgap.

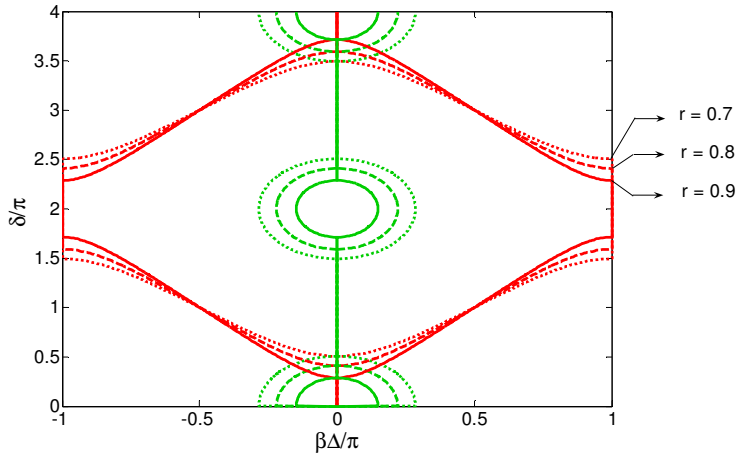

Fig. 3.13. The dispersion diagram for various (r) in lossless double-bus Type II.

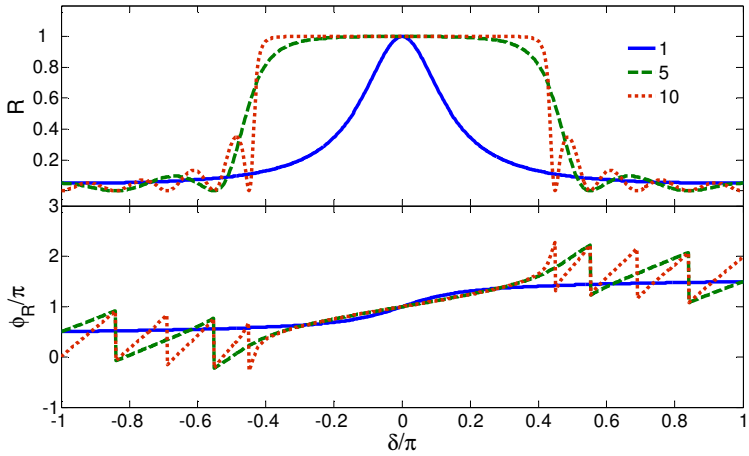

Fig. 3.14. The reflection amplitude and phase responses for the double-bus Type II (N = 1, 5, and 10).

The *reflection* amplitude and phase responses for various values of N are also shown in Fig. 3.14. The reflection (R) changes from Lorentzian for a single ring to a broad square shape with only a relatively small number of resonators. This is because each element in the array is a high-Q symmetric resonator with unity transmission at resonance and therefore has a significant contribution to the overall response [50]. Similarly, the phase response φ_R changes from a highly nonlinear shape for the single-ring case to become more linear with increasing N, but the effective phase shift across the reflection band remains roughly π just as for a single ring. Near the band edges, however, the phase becomes steeper and more nonlinear with increasing N, giving rise to higher group delay and more dispersion.

Outside the band, at each zero crossing of the sidelobes, there is a π-phase discontinuity which has no physical relevance, since the delay is undefined when the reflectance is zero. This phase ripple does not exist for a single ring and thus, like the reflection sidelobes, can be attributed to interference in the multi-ring structure. This behavior is similar to the FBG filter, and is related to the nature of a type of filter called *minimum phase* filter [27], which is important later on in understanding the behavior of the 2D-RR arrays.

3.5. 2D-RR array

By comparing the Type I and Type II dispersion diagram carefully, it can be seen that the two types of array have non-overlapping complementary photonic bandgaps. For example, in Type I the bandgap falls around $\delta = (2m+1)\pi$ whereas in Type II, the bandgap falls when $\delta = 2\pi m$. In this bandgap region, the transmission (T), which propagates along the periodicity of the structure, is inhibited whereas the ripple from the reflection (R) is suppressed. This finding motivates us to devise a double-bus 2D-RR array configuration which is a hybrid of both Type I and Type II arrays.

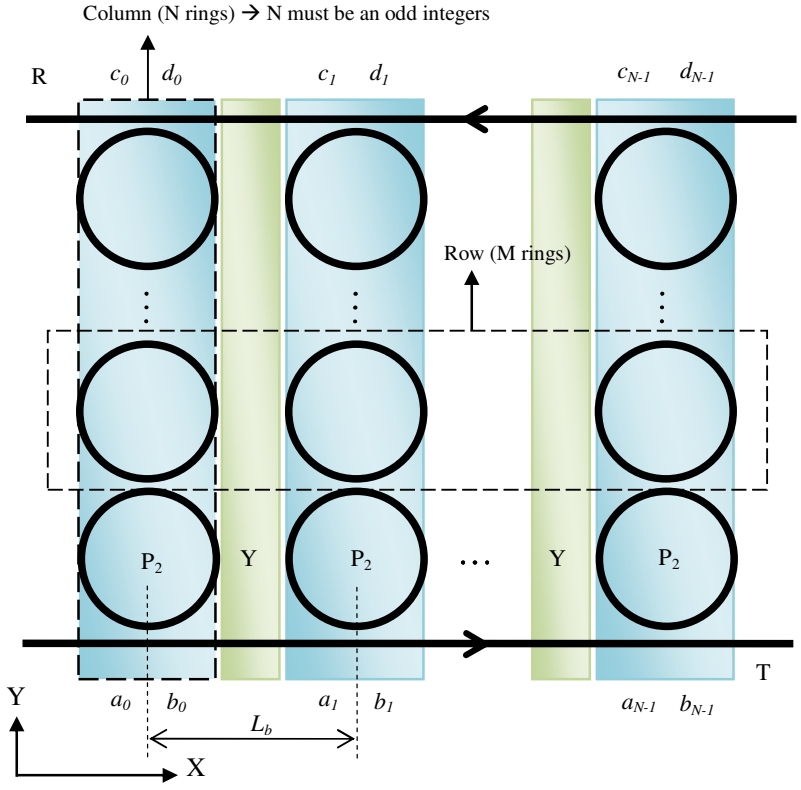

Fig. 3.15. Double-bus 2D-RR array configuration. Note that M (N) is the number or rings inside one row (column). In other words, M (N) is the number of columns (rows).

Fig. 3.15 shows the schematic of the 2D-RR array configuration. The device is composed of a series of Type I structures arranged periodically in a sequential manner similar to that in the Type II. For the Type I building block, we can reuse Eq. (3.10),

$$\begin{bmatrix} c_0 \\ d_0 \end{bmatrix} = \frac{1}{i\kappa}\begin{bmatrix} -1 & r \\ -r & 1 \end{bmatrix}\underbrace{\begin{bmatrix} m_{11} & m_{12} \\ m_{21} & m_{22} \end{bmatrix}}_{\text{Sylvester's Theorem}}\begin{bmatrix} a_0 \\ b_0 \end{bmatrix} = \begin{bmatrix} p_{11} & p_{12} \\ p_{21} & p_{22} \end{bmatrix}\begin{bmatrix} a_0 \\ b_0 \end{bmatrix} \tag{3.25}$$

and expressing in a similar way to the matrix block P_1 used in the Type II case,

$$\begin{bmatrix} b_0 \\ d_0 \end{bmatrix} = \frac{1}{p_{12}}\begin{bmatrix} -p_{11} & 1 \\ p_{12}p_{21} - p_{11}p_{22} & p_{22} \end{bmatrix}\begin{bmatrix} a_0 \\ c_0 \end{bmatrix} = P_2\begin{bmatrix} a_0 \\ c_0 \end{bmatrix} \tag{3.26}$$

Again, the Bragg resonances arise when the Bragg condition, $\lambda_j = 2n_{eff}L_b / j$ (j = 1,2,3…), is satisfied. These resonances will overlap with the ring resonances if we set $L_b = L_c/2$. This is the most useful case, for which the transfer matrix relation can finally be expressed as:

$$\begin{bmatrix} b_{N-1} \\ d_{N-1} \end{bmatrix} = (P_2Y)^{M-1}P_2\begin{bmatrix} a_0 \\ c_0 \end{bmatrix} \equiv \begin{bmatrix} I & J \\ K & L \end{bmatrix}\begin{bmatrix} a_0 \\ c_0 \end{bmatrix} \tag{3.27}$$

Similar to the previous case, the matrix $(P_2Y)^{M-1}$ can be expressed using the Sylvester theorem, and the output is expressed as $t = b_N / a_0 = (IL - KJ)/L = 1/L$ (Drop port) and the reflection as $\rho = c_0 / a_0 = -K/L$ (Through port) respectively. Note that the 1D-filter always have ripples and sidelobes associated in the passband. Here, we show that the 2D-RR array is capable of realizing an ideal filter profile with flat-top, ripple-free and a sharp bandedge response. The overall bandwidth is determined by the coupling coefficient. The flat-top response is due to the bandgap of side coupled resonator array in the X-direction (the Type II effect), whereas the sidelobe suppression due to the bandgap of the coupled resonators in the Y-direction (the Type I effect).

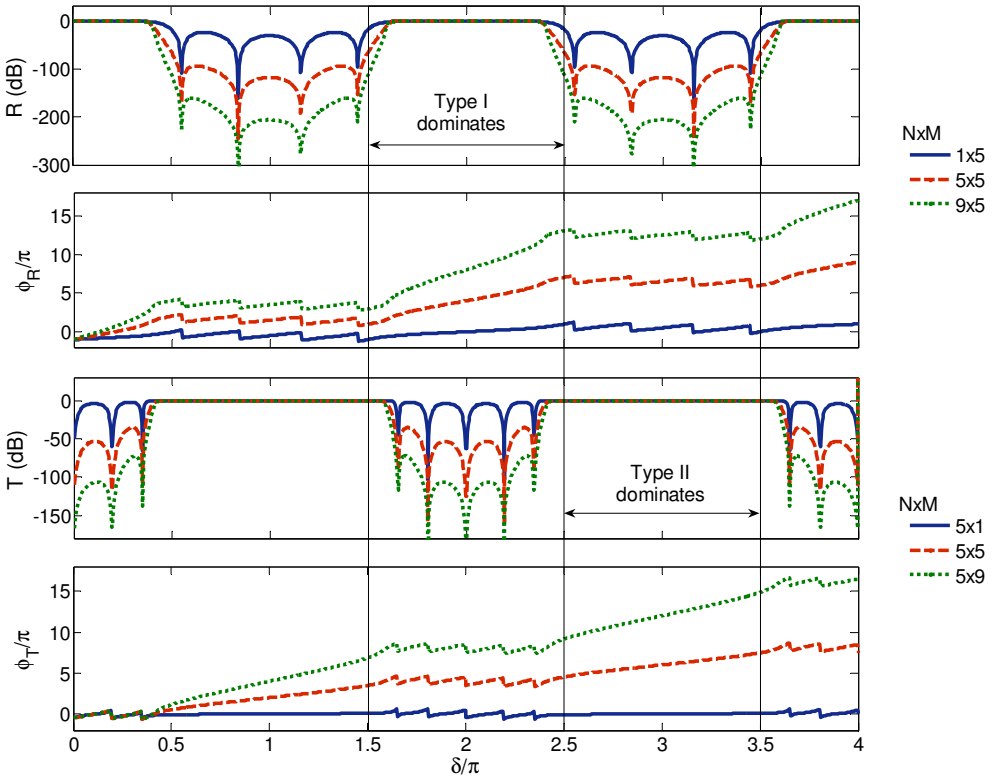

Fig. 3.16. The reflection (R) and transmission (T) of the 2D-RR array along with the corresponding phase response in the lossless case ($r = 0.8$).

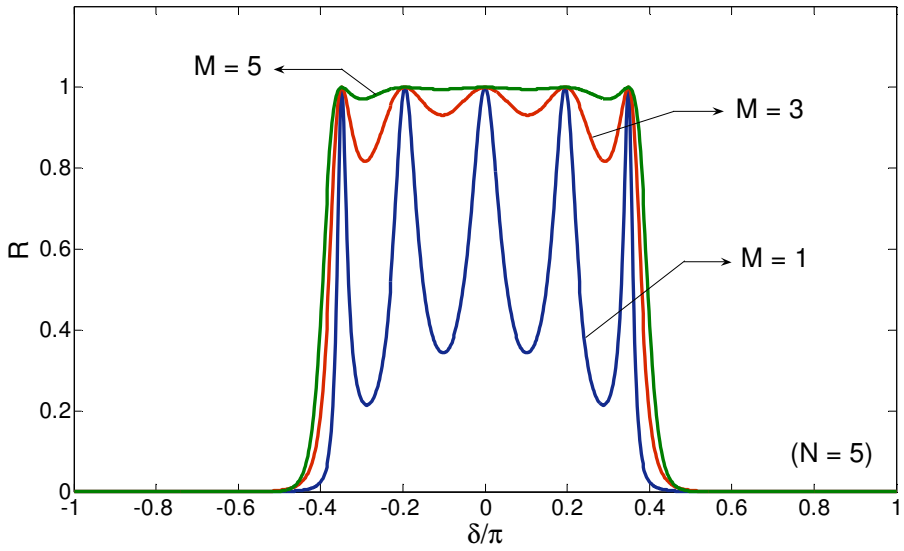

Fig. 3.17. The reflection (R) spectra of the lossless 2R-RR array as the number of column (M) increases ($r = 0.8$).

Based on Fig. 3.16, we can see that when the ring is on-resonance at $\delta = 2\pi m$, the light will enter the rings and propagate along the Y-direction and will consequently be dropped to the port (R). When the ring is off-resonance at $\delta = (2m+1)\pi$, the light is forbidden to enter the rings. Instead, it will propagate along the X-direction and consequently be transmitted to the port (T). Concurrently, we study the effect of adding the number of rows and columns respectively. For instance, adding more rows (columns) will suppress the sidelobes of the reflection (transmission) spectra. The sidelobes suppression is due to the photonic bandgap which has a stronger effect as the periodicity of the rings increases. Fig. 3.17 shows how the ripple of the reflection (Drop) spectra is gradually being flattened as the number of columns (M) increases. The additional columns provide the means for the light to be reflected back in to the (R) port and the ripples to vanish eventually.

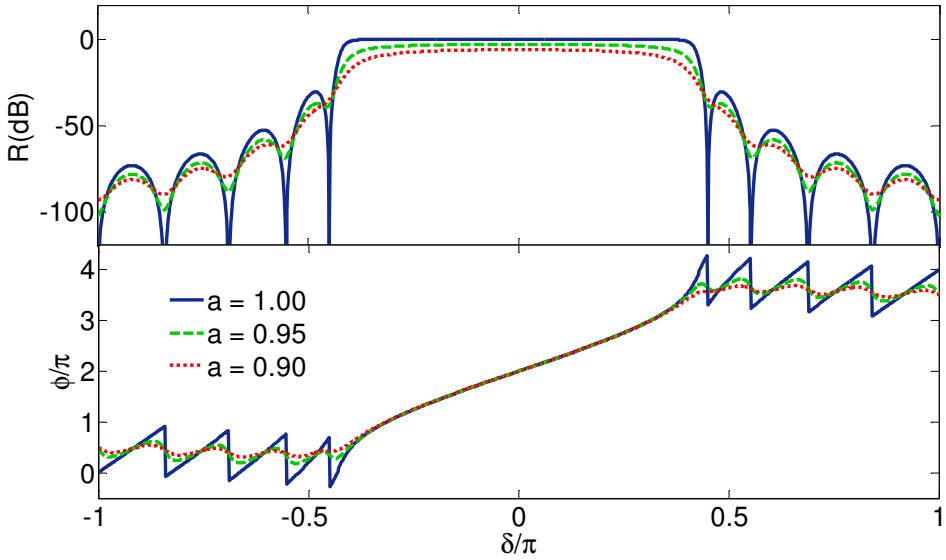

Fig. 3.18. The effect of resonator loss on the transmission spectra, for a 3×10 array. The round-trip loss is given by (1-*a*).

So far we have assumed the resonators to be lossless. Unfortunately any loss could be detrimental. Fig. 3.18 shows the effect of propagation loss on a 3×10 array. Here, the transmission spectra are shown for various round-trip losses (1-*a*). It can be seen that even 5% round-trip loss significantly reduces the passband magnitude and degrades the transition edge. The rounding off at the shoulder is due to the larger increase in the imaginary part of β in the bandedge noted above. Low loss is particularly important for the coupled rings in the column, since the signal in the passband must pass through all of them. On the other hand, the number of rings in the row direction is larger, even though not all the light passes through all of them. Hence, these filter designs are suitable only if all the rings have very low loss. This requirement will severely restrict the implementation of these filters. Recently, very high order multi-ring filters with very high Q resonators have been realized using low-loss Hydex material [3], showing the technological possibility of realizing large and uniform resonator arrays.

3.6. Pole-Zero dynamics of double-bus high-order RR filters

The transfer functions for ρ and t, in general, have poles and zeros and hence can be expressed in the following equivalent polynomial form in Eq. (2.15) where the substitution $z^{-1} = \exp(i\delta)$ has been done. The reflection and transmission of double-bus Type I filter may be expressed in the form

$$\rho(z) = \frac{r_0 \prod_{n=1}^{N}(z - z_n)}{\prod_{n=1}^{N}(z - p_n)} \qquad t(z) = \frac{(i)^{N+1}(az)^{\frac{N}{2}} \prod_{n=0}^{N} \kappa_n}{\prod_{n=1}^{N}(z - p_n)} \tag{3.28}$$

where N is the polynomial order of the double-bus Type I filter with N rings. Similarly, the reflection and the transmission of double-bus Type II filter in general can be expressed in the form

$$\rho(z) = \frac{-\kappa_{N-1}^2 \sqrt{a} \prod_{n=0}^{N-1}(z - z_n)}{\sqrt{z} \prod_{n=0}^{N-1}(z - p_n)} \quad t(z) = \frac{a^{\frac{N-1}{2}} z^{\frac{N-3}{2}} (z - a) \prod_{n=0}^{N-1} r_n}{\prod_{n=0}^{N-1}(z - p_n)} \tag{3.29}$$

where N-1 is the polynomial order (number of intra-ring cavities) of the double-bus Type II filter with N rings. The poles (p_n) and zeros (z_n) are calculated by solving the roots of the polynomials in the denominators and numerators of the transfer functions using MATLAB. A pole-zero diagram is a graph representing the poles and zeros of the transfer functions on the complex z-plane. In this diagram, the normalized frequency δ of the periodic spectrum is mapped to the angle in the complex plane. The zero angle corresponds to the ring resonance δ = 0. A complete circuit of the unit circle corresponds to the free spectral range (FSR) of the filter.

Eq. (3.28) show that for Type I, both the reflection and transmission functions have poles but only the reflection functions have complex zeros. In the parlance of filter theory [27], the reflection of Type I filter is an auto-regressive moving average (ARMA) filter, whereas the transmission of Type I filter is an auto-regressive (AR) filter. Similarly, the reflection of Type II filter is an ARMA filter, whereas the transmission of Type II filter resembles an AR filter (if one were to exclude the zero at z = a). The (reflection) amplitude coefficient Γ of the ARMA filter is the reflectivity value of the first coupler r_0 for Type I and the last coupler $-\kappa_{N-1}^2\sqrt{a}$ for Type II. Likewise, the (transmission) amplitude of the AR filter is given as $\sqrt{a^N}\prod_{n=0}^{N}\kappa_n$ for Type I and $\sqrt{a^{N-1}}\prod_{n=0}^{N-1} r_n$ for Type II.

In order to show both poles and zeros of the ARMA filter, we plot in Fig. 3.19 the reflection spectra $R = |\rho|^2$ and their corresponding pole-zero plots, for Type I and Type II, assuming no loss (a = 1), for two different values of r. In the lossless case, the reflection and transmission spectra are complementary, i.e., $R+T=1$, where $T=|t|^2$. Note that the two types of arrays have many complementary features: (i) when Type I has high reflection then Type II has low reflection, and vice versa; (ii) the reflection band of Type I is centered at $\delta = (2m+1)\pi$, while that of Type II is centered at

$\delta = 2\pi m$; and (iii) the reflection bandwidth of Type I increases with increasing reflectivity r while that of Type II decreases. Finally, we note that (i) the reflection bands are free of ripples; ripples occur only in the transmission bands due to interference between waves from different rings as light propagates through the array; (ii) the maximum R is always less than 1, which is consistent with the fact that transmission has no zeros, unless the coupling coefficient is zero (refer to Eq. 3.12).

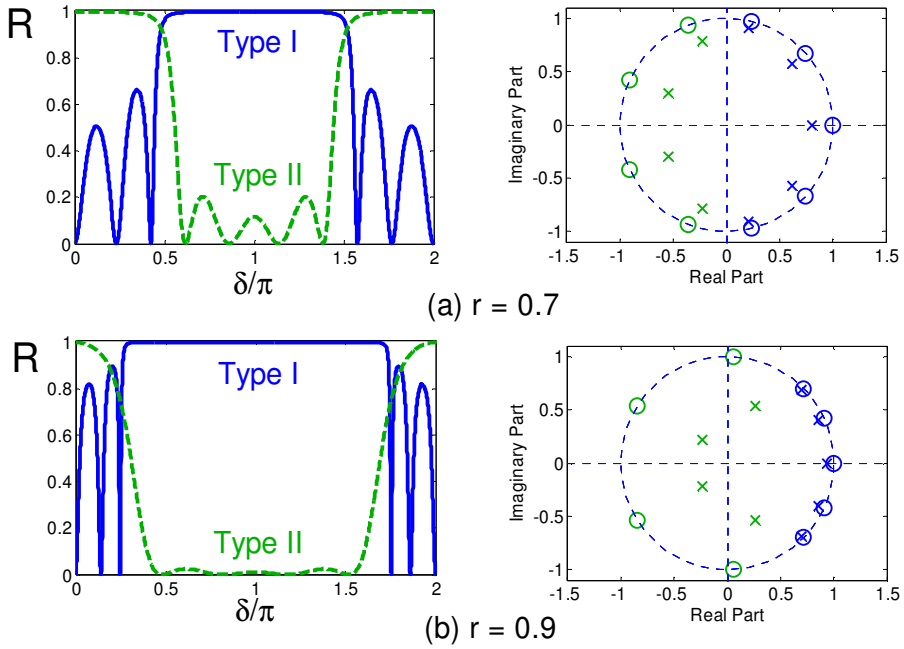

Fig. 3.19. Pole-zero diagrams with their corresponding reflection spectra for double-bus Type I array – blue (N = 5), and for Type II – green (N = 5). The pole-zero pairs in darker blue (lighter green) are calculated based on the reflection port of Type I (Type II). The transmission is complementary to the reflection spectra for the lossless case.

In the corresponding pole-zero diagrams, all the zeros lie on the unit circle because we have assumed the rings to be lossless (a = 1). The number of pole-zero pairs is equal to N (the number of rings) for Type I, and N-1 for Type II. Hence, in order to have equal number of poles, Type II must have one more ring than Type I (this is analogous to the case of a diffraction grating). Note that the symmetry of the reflection spectra is reflected in the symmetry of the poles and zeros about the horizontal axis of the z-plane, and the complementary nature of the Type I and Type II spectra is reflected in the fact that the poles and zeros for Type I and Type II are found on opposite half-planes. The poles and zeros are found only in the transmission bands where they give rise to the ripples, with each zero corresponding to a reflection zero (or transmission maximum). For Type I, the poles and zeros are located on the right-half plane, meaning that the *reflection* bands are centered at $\delta = (2m+1)\pi$. For Type II, the poles and zeros are located mostly in the left-half plane, meaning that the reflection bands are centered at $\delta = 2\pi m$. Note that the angular range in which the poles and zeros are distributed corresponds to the bandwidth of the transmission band (there are no poles and zeros inside

the reflection bands), and the separation in each pole-zero pair determines the sharpness of the ripple in the transmission band; the smaller the separation, the sharper are the peaks. When the coupling is reduced [i.e., as when r increases from 0.7 in Fig. 3.19(a) to 0.9 in Fig. 3.19(b)], the poles and zeros approach each other for Type I, and recede from each other for Type II. This opposite dependence on r reflects the difference in the effect of coupling on Type I and Type II, which underlies the complementary nature of their spectra. Similarly, for a 2D-RR array filter that combines both Type I and Type II [167], the pole-zero behavior will share the features of both filters but in limiting cases will approach one or the other. When r is sufficiently high, the array behaves like a Type I filter, and when r is sufficiently small, it behaves like a Type II filter.

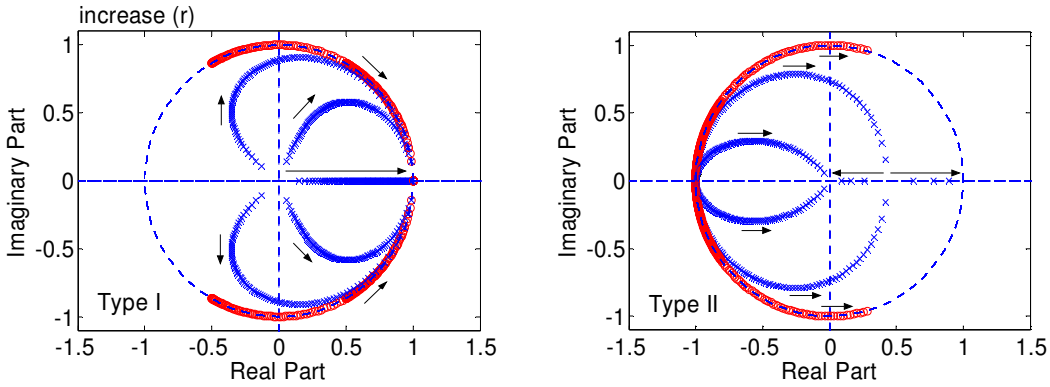

Fig. 3.20. Pole-zero diagram illustrating the universal dynamics of the poles and zeros movement in the reflection output of the double-bus Type I and Type II structures as r is varied between near zero to near unity (lossless case). Note that the number of pole-zero pair is N-1 for Type II. The zero (pole) is indicated in red (blue) respectively. Note that the zeros have fixed magnitude of $|z_n| = a$ for a double-bus Type I and Type II filter.

Since the coupling coefficient is the primary parameter that determines the pole-zero plot and hence the filter characteristics, it is useful to study how the poles and zeros move in the z-plane as we vary the value of r. This is shown in Fig. 3.20 for various cases of N, again assuming $a = 1$. As we increase r from 0 to 1, we note that, for Type I, all poles and zeros move from left to right towards the point $z = 1$ (i.e., $\delta = 0$). The zeros move along a circle while the poles trace out various trajectories that are symmetric about the real axis. Furthermore, as they move, the pole-zero separation also decreases. This means that as r increases, the bandwidth of the reflection spectrum increases and the N resonances outside the reflection band become stronger and sharper. For Type II, the dynamics is opposite. As r is increased from 0 to 1, the poles and zeros move from left to right, starting in the left half-plane, thus the zeros and poles are more and more spread out and separated from each other. This implies that as r increases, the bandwidth of the reflection spectrum decreases and the (N-1) resonances outside the reflection band become weaker and broader, in complete complementary to the behavior of Type I.

3.6.1. Pole-zero dynamics for critical coupling and oscillation in Type I

In this section we investigate the critical coupling and oscillation conditions for several ring configurations in the context of pole-zero dynamics. This extends our previous work presented in [172], where it was shown analytically, for $N = 1$ and 2, that the critical coupling conditions are given by $r = a$ and $r = a^2$, and the oscillations conditions are given by $r = 1/a$ and $r = 1/a^2$ respectively. For more than two rings, the equations become too complex to express analytically, and the actual r values must be solved numerically. Fig. 3.21 shows the pole-zero dynamics for the single-bus Type I configuration with 5 rings. Note that for N rings, there are N reflection dips when $a < 1$ and N reflection resonances when $a > 1$, at frequencies corresponding to the zero and pole angles respectively. For the filter to be stable, all the poles must lie within the unit circle [27]. Note that for small enough r, all the poles can lie within the circle even for $a > 1$. However, as r increases, more and more poles move outside the unit circle and the filter becomes unstable. The pole-zero plots show that critical coupling occurs when the zeros cross the unit circle, and oscillation occurs when the poles cross the unit circle. One general feature of pole-zero plots is that, when there is overall loss in the system, all of the poles will be inside the circle and thus there can be no oscillation, and when there is gain, all of the zeros will be outside the circle and thus there will be no critical coupling.

For the case of double-bus Type I configuration, analytical solution of Eq. (3.11) shows that critical coupling only occurs when $a = 1$ (i.e., in the lossless limit), regardless of the values of r [172]. It is easier to see this through the pole-zero diagrams in Fig. 3.22, which show that, unlike the case of the single-bus Type I, the zeros for the double-bus Type I move in circles with constant radii fixed by the transmission factor (a). Due to this reason, the zeros never cross the unit circle of the complex plane unless $a = 1$. On the other hand, the oscillation condition is similar to the case of single-bus Type I. The main difference here is that the oscillation occurs for both transmission and reflection. When a is sufficiently large, both R and T may be greater than 1 near the oscillation frequency. Far from resonance R approaches 1 and T tends to 0. Again, the oscillation happens when the poles cross the unit circle.

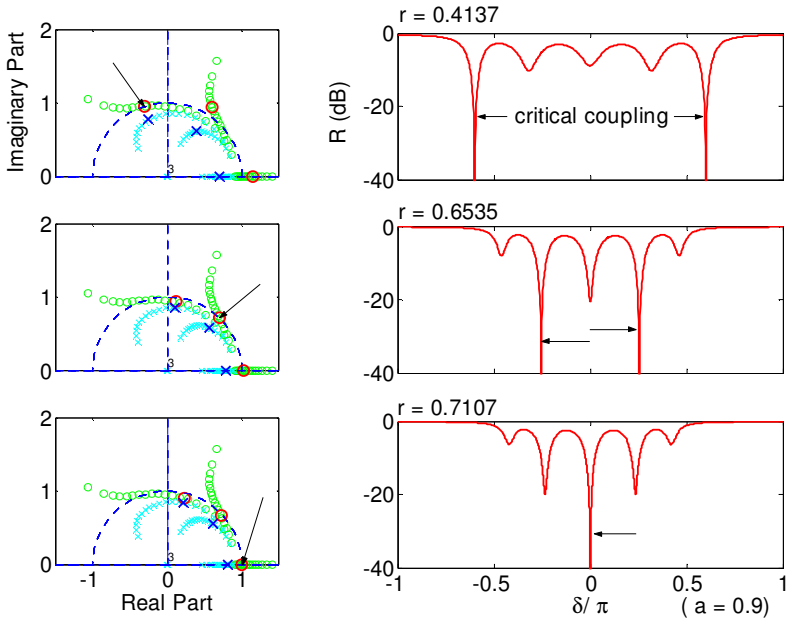

(a) Critical coupling (a = 0.9)

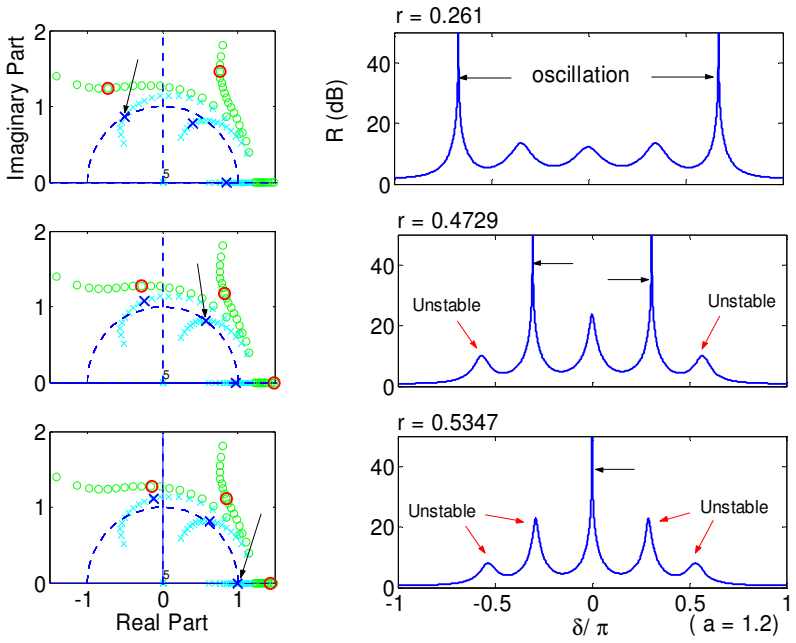

(b) Oscillation (a = 1.2)

Fig. 3.21. Single-bus Type I array with 5 rings: Pole-zero dynamics and the reflection transfer functions showing (a) the critical coupling and (b) the oscillation conditions. Left: The pole (zero) trajectory is indicated in cyan (green) color as the reflectivity r value is increased from zero to unity. The zeros (poles) corresponding to critical coupling (oscillation) are indicated by the black arrows. The unstable gain peaks indicated by the red arrows correspond to the poles outside the unit circle $|p_n| > 1$.

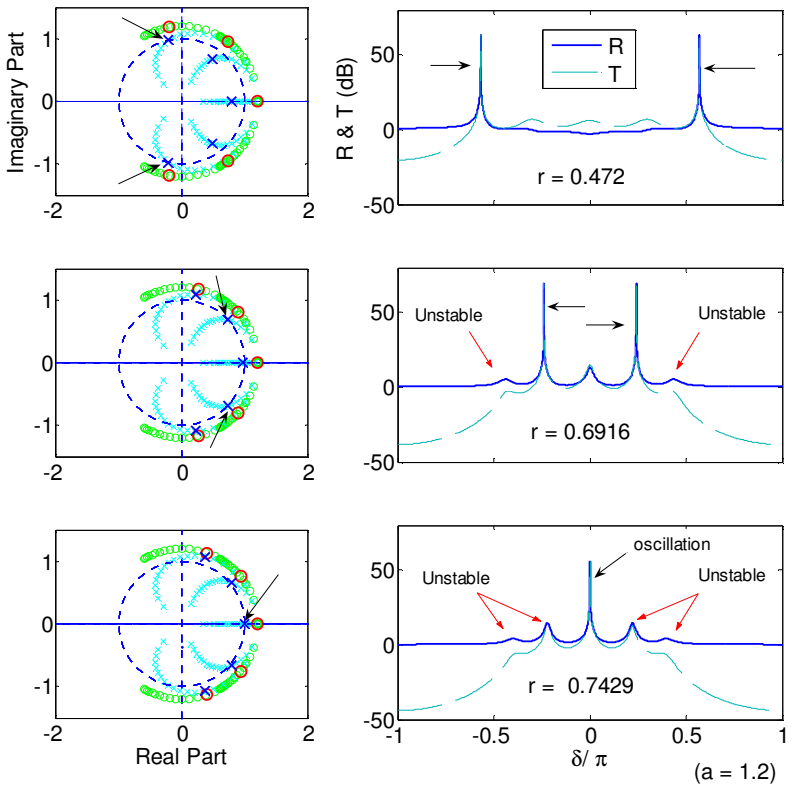

Fig. 3.22. Double-bus Type I arrays with 5 rings. Left: The pole-zero diagrams extracted from the reflection (R) functions Right: The R and T spectra when a = 1.2, showing the oscillation frequencies and their corresponding coupling conditions. Note that $|z_n| = a$ for symmetric double-bus Type I and Type II filters. The pole (zero) trajectory in the left is indicated in cyan (green) color as the reflectivity r value is increased from zero to unity. The poles corresponding to oscillation are indicated by the black arrows. The unstable gain peaks indicated by the red arrows correspond to the one with poles outside the unit circle $|p_n| > 1$.

For the purpose of simple illustration we have discussed oscillation assuming a fixed value of a = 1.2 and ignoring details such as the associated index change Δn and the shift in resonance frequency. Here, we briefly discuss the practical means for realizing $a > 1$ [106, 173]. There are two ways of incorporating gain within the ring resonator: (i) The implementation of semiconductor optical amplifier (SOA) sections, either by selective area epitaxial regrowth or quantum well intermixing. A fairly compact SOA have been realized with optical gain of 20 dB or more [174-176]; (ii) The fabrication of the devices using all-active waveguide, including Erbium doped fibers, for example, a = 1.43 has been experimentally demonstrated by Yariv's group [62]. Such work could potentially be extended to implement Type I and Type II filter configurations.

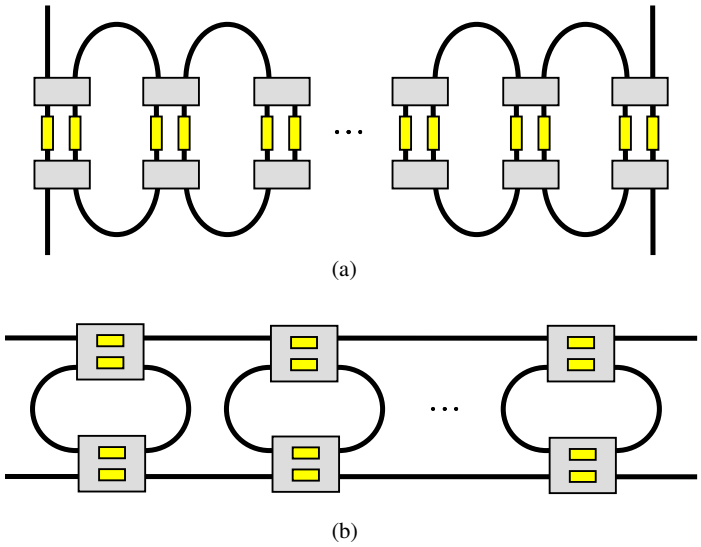

Fig. 3.23. Proposed filters with active coupling mechanisms: (a) MZI-based couplers used in Type I filter, and (b) Alternative MMI-based couplers used in Type II filters [13]. Yellow pads signify the active tuning.

3.6.2. Active Apodization

The ripples (or sidelobes) present in the spectra of both Type I and Type II filters limit their crosstalk performance. Apodization is a well known technique to suppress these sidelobes in order to have a more box-like filter response. Apodization involves tuning the inter-ring coupling coefficients from one end of the array to the other, in order to minimize reflections from the terminations that cause the interference ripples. For the Type II structures, apodization has been demonstrated by using a tapered separation between the bus waveguides and the rings [56]. Such tapering is more difficult to apply to Type I structures. The common drawback is that it is difficult to control the coupling coefficients through fabrication, and the coupling coefficients are fixed once the structure is fabricated. To alleviate this problem, one may adopt an active coupling device between the waveguides that will make it easier to achieve any arbitrary apodization function. The only drawback of this approach is that the free spectral range (FSR) of the filter will be reduced because of the increased cavity length. Such an active coupling device may consist of a very compact Mach-Zehnder interferometer (MZI) [9] as shown in Fig. 3.23(a), or an active multi-mode interferometer (MMI) [13] as shown in Fig. 3.23(b). The MZI can be implemented using MMI as the 3-dB couplers. The power split at the two outputs gives the coupling coefficient and the reflectivity as $\kappa = \cos(\Delta\varphi/2)$ and $r = \sin(\Delta\varphi/2)$ respectively, where $\Delta\varphi$ is the differential phase shift applied between the two arms of the coupler using electro-optic or other means. In the case of active MMI, an electric bias is applied at the middle of the MMI switch where the two 3dB self-images are formed, to create an index modulation that can change the output split ratio.

3.6.3. Pole-zero analysis of apodization

In apodization, the *r* value is varied from the edge to the center in a symmetric way. For Type I, the *r* value is smaller at the edge and larger at the center, while for Type II the reverse is true. The objective is to suppress the ripples in the transmission band while retaining the sharp bandedges. In the pole-zero analysis, therefore, apodization is achieved by designing the pole locations to be further from the unit circle, with the distance decreasing from the center to the edges of the passband, as clearly illustrated in Fig. 3.23. For the reflection spectra the zeros all fall on the unit circle in the lossless case, hence the distance corresponds to the pole-zero separation discussed earlier in Section 3.6. These pole locations correspond to a specific combination of *r* values.

The specific values of the coupling coefficient are determined by the required bandwidth. In the following, we show the distributions of *r* values for transmission spectra with various bandwidths. The transmission spectra correspond to the AR filter responses for both Type I and Type II. We focus only on the AR filters because they only have poles and it is simpler to focus only on the pole movement. These are shown in Fig. 3.25 and 3.26, for Type I and Type II AR filters with 5 rings respectively, together with the pole-zero plots for various transmission bandwidths. Note that the blue curve in Fig. 3.24 corresponds to the synthesized design reported in [14]. We can see that there is a consistent trend in terms of the *r* distribution between the synthesized and the pole-zero approach. The curves joining the *r* values may be fitted by some apodization functions, but they do not obey any universal analytical form. Two general trends are evident from the curves: (i) The larger the *r* values, the narrower is the transmission band for Type I, and the broader it is for Type II. (ii) The wider the bandwidth, the slower is the bandedge roll-off, hence the larger will be the crosstalk. The roll-off is related to the phase response and the group delay (the slope of the phase response), which are also shown in the figures. In general, the group delay is higher at the passband edges, and is larger for the narrower filters which have higher stop-band rejection. In terms of the pole-zero diagrams, the group delay is inversely related to the distance of the poles from the unit circle. The smaller the bandwidth, the closer the poles approach the unit circle, hence the larger is the group delay. We remark that both Type I and Type II filters belong to a class of filters called *minimum phase* filter (MPF) [27]. MP filters are those in which the amplitude response and the phase response are uniquely related by the Hilbert transform. Some consequences of the Hilbert transform are: (i) a constant amplitude response implies linear phase; (ii) the phase is directly related to the change in the amplitude response, hence the higher order terms it has near the passband edges, the faster the amplitude response changes.

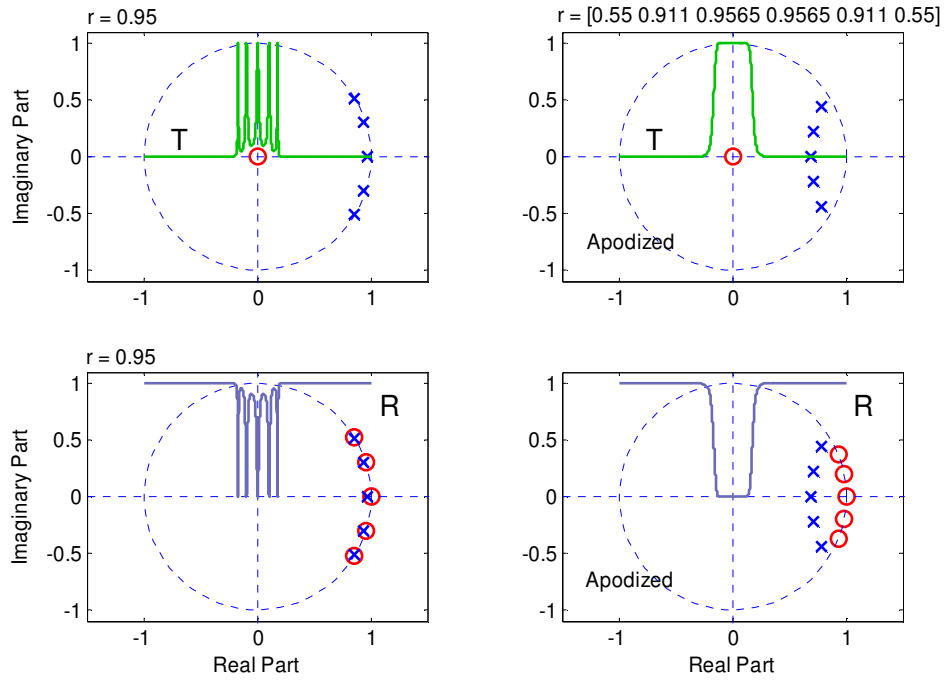

Fig. 3.24. The pole-zero diagram showing the comparison between the non-apodized case and the apodized case for a 5-ring double-bus Type I filter (a = 1).

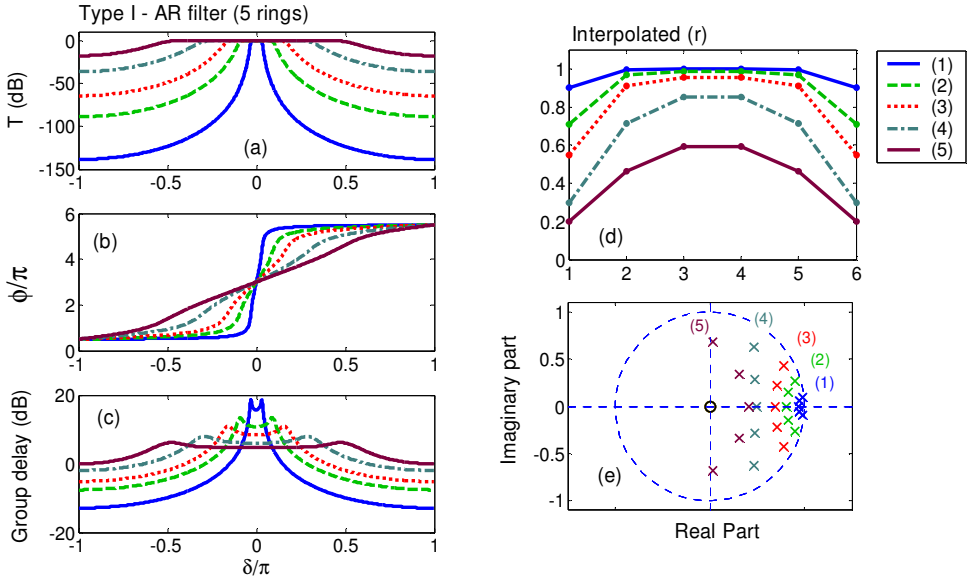

Fig. 3.25. The design of apodized 5-ring double-bus Type I AR filters for various bandwidths, showing the transmission spectra (a) and the corresponding phase response (b) and group delay (c). The associated combinations of r (interpolated) and the pole-zero diagrams are shown in (d) and (e) respectively. The r distribution (1) in solid blue line is adopted from [14].

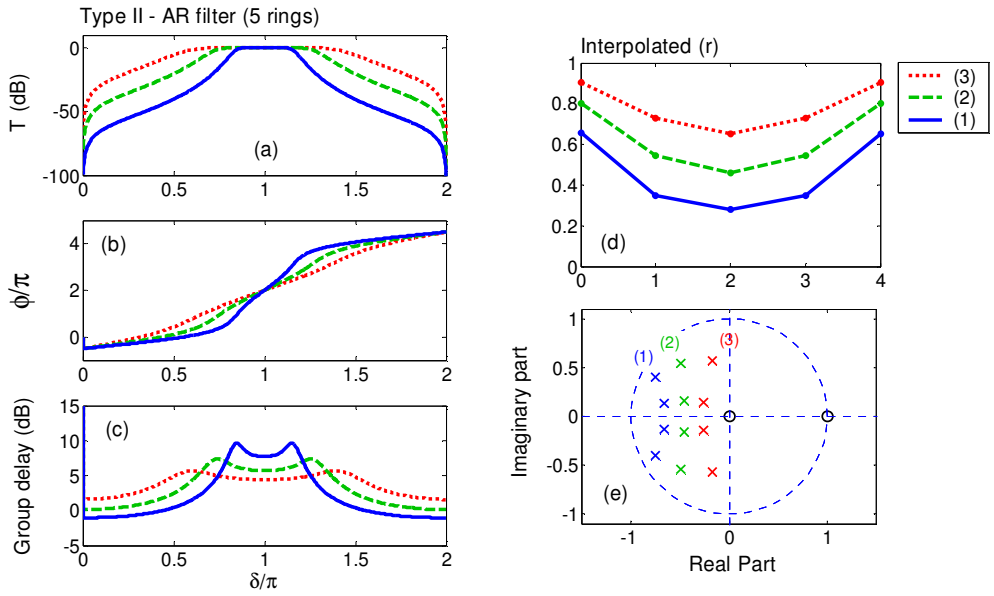

Fig. 3.26. The design of apodized 5-ring double-bus Type II AR filters for various bandwidths, showing the transmission spectra (a) and the corresponding phase response (b), group delay (c), distributions of *r* (d), and pole-zero diagrams (e).

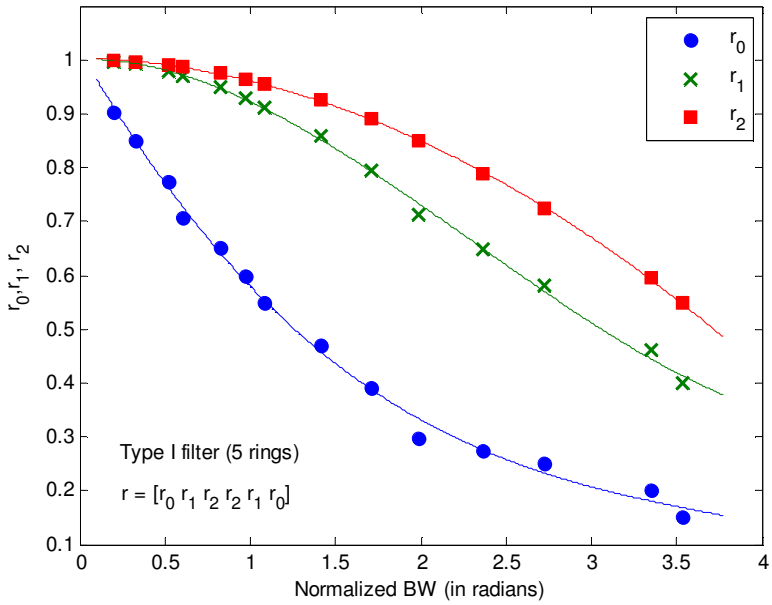

Fig. 3.27. Polynomial fit for graphical interpolation of *r* distribution as a function of normalized bandwidth (in radians) for the case of 5 rings double-bus Type I filter. Similar approach can be applied to double-bus Type II filter.

Based on Fig. 3.25(d) and 3.26(d), the relationships between each of the *r* values and the bandwidth can be translated into certain curve-fit polynomial equations, as shown in Fig. 3.27. These relationships can then be used to interpolate the optimum *r* combinations for any other required

bandwidth. Thus, the pole-zero approach can be a quick, intuitive and approximate method to arrive at first-order designs for apodized filters using double-bus Type I or Type II arrays with a given number of rings, once the pole-zero dynamics for the filters is understood. The optimized designs can then be found by fine-tuning around the initial set of *r* values. This design approach is different from, and may supplement, the traditional recursive synthesis method of apodized filters, which is widely established but relatively more tedious in implementation [3, 27, 37, 49-51, 56, 57].

3.6.4. Pole-zero analysis in 2D-RR array

We note that for the case of 2D-RR array filter [167], which can be seen as the extension of either Type I or Type II filter in either the row or column directions, the poles are distributed further away from the unit circle compared with those in the 1D case, and hence the 2D array has similar apodization effect. The output spectra of these arrays can easily be calculated using the transfer matrix method. The focus of this section is to present the design and analysis of these array filters in the context of pole-zero diagrams, relating the performance of the filter with the locations of the poles and zeros of the transfer function.

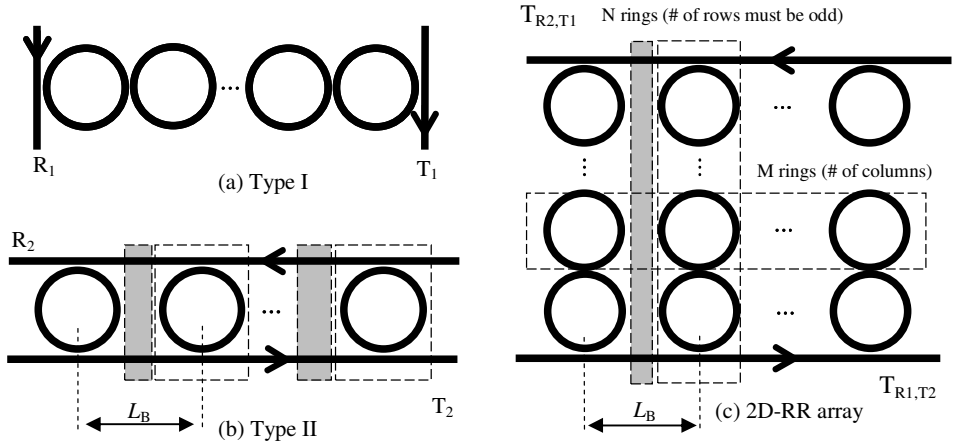

Fig. 3.28. Type I, Type II, and 2D-RR array configurations. Note that the port notations are relabeled, especially the 2D-RR array configuration. The new notation $T_{R2,T1}$ refers to the output port which is a hybrid of R_2 and T_1. Similarly the notation $T_{R1,T2}$ refers to the output port which is a hybrid of R_1 and T_2.

The transfer functions for reflection $R_{1,2} = |\rho_{1,2}|^2$ and transmission $T_{1,2} = |t_{1,2}|^2$, in general, have poles and zeros and hence can be expressed in terms of a polynomial form. By applying z-transform substitution $z^{-1} = \exp(i\delta)$ [27] into Eq. (3.2), (3.3), (3.11) and (3.12) for Type I, and into Eq. (3.21) and (3.22) for Type II, it is possible to factorize the output transfer function of Type I and Type II and express them in the form of Eq. (3.30). The formula for the 2D-RR array is not shown here due to overwhelming mathematics.

$$\rho_1(z)=\frac{r_0\prod_{n=1}^{N}(z-z_n)}{\prod_{n=1}^{N}(z-p_n)}\quad t_1(z)=\frac{(i)^{N+1}(az)^{\frac{N}{2}}\prod_{n=0}^{N}\kappa_n}{\prod_{n=1}^{N}(z-p_n)}$$
$$\rho_2(z)=\frac{-\kappa_{M-1}^2\sqrt{a}\prod_{m=0}^{M-1}(z-z_m)}{\sqrt{z}\prod_{m=0}^{M-1}(z-p_m)}\quad t_2(z)=\frac{a^{\frac{M-1}{2}}z^{\frac{M-3}{2}}(z-a)\prod_{m=0}^{M-1}r_m}{\prod_{m=0}^{M-1}(z-p_m)} \tag{3.30}$$

The zeros and poles are calculated by numerically solving the polynomial root of $B(z)$ and $A(z)$ in the transfer function $H(z)=B(z)/A(z)$, respectively. Here, we show the pole-zero dynamics of Type I, Type II, and the 2D-RR array simultaneously, as r is varied from zero to unity (for a lossless limit). Based on Fig 3.29(a), we deduce that Type I (Type II) filter is a reflection (coupling) based filter since when r is higher (lower); the light interaction within the ring (inter-ring) is stronger. The complementary feature between Type I and Type II is indicated by the pole-zero locations which are located in the right-hand side (RHS) and the left-hand side (LHS) respectively. Furthermore, the pole-zero separation is closer when r is higher (lower) for Type I (Type II), which physically implies stronger light interaction within the ring (inter-ring) cavity. Based on Eq. (3.30), the order of Type I is the number of rings (N), whereas the order of Type II is the number of inter-ring cavities (i.e., M-1). Fig. 3.29(b) shows similar dynamics for the case of 2D-RR array which has hybrid features of both Type I and Type II. Thus, the 2D-ring array can be both a 'reflection' and 'coupling' based filter, depending on the r value. This explains the reason why when r is varied from zero to unity, the pole-zero pairs move from extreme LHS to extreme RHS of the z-plane.

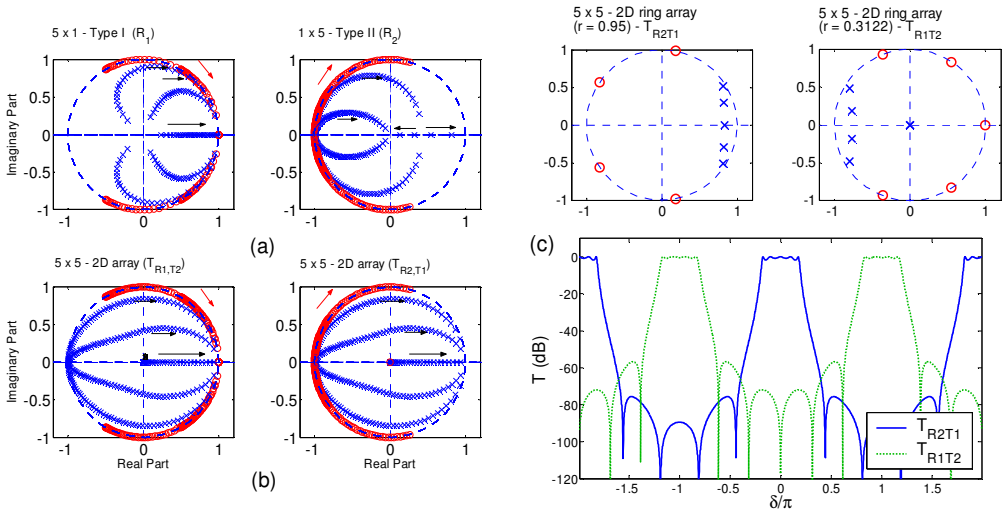

Fig. 3.29. The pole-zero dynamics for: (a) The reflection port of Type I and Type II filter as r is varied from zero to unity (indicated by the arrow), (b) 2D ring array filter as r is varied from zero to unity, (c) Apodization using 5×5 - 2D ring array filter when r = 0.95 for T_{R2T1} and $r=\sqrt{1-0.95^2}$ for T_{R1T2}, illustrating how Type I (Type II) dominates the overall performance (lossless limit).

A new method of apodizing can be achieved using a 2D-RR array configuration. Such structure combines both features of Type I and Type II configurations [167, 171]. The array can be realized by simply adding more columns (M rings) in Type I or by adding more rows (N rings) in Type II. Note that N must be an odd number to ensure proper feedback mechanism of the filter. In general, when r is higher (lower), the light interaction within the row (column) is stronger. As one increases the number of columns (rows), the poles location is re-distributed further away from the unit circle and suppresses each localized resonances (i.e., the poles move slightly away from the unit circle). The transmission spectrum in Fig. 3.29(c) corresponds to two different ports, which effectively are the transmission of Type I and Type II ports (AR filter). The difference here is that there are additional zeros contributed by the reflection counterpart. The zeros in the unit circle are caused by the same reflection of Type I and Type II configuration (refer to Eq. 3.30).

Lastly, we shall observe the effect of adding more rows or columns in the 2D-RR arrays, in the context of pole-zero analysis. Fig. 3.30 illustrates how the poles are apodized (moving away from the unity circle) and suppressing the ripples (sidelobes) in the passband (stopband) of T_{R2T1} (T_{R1T2}), as the number of columns (M) are increased.

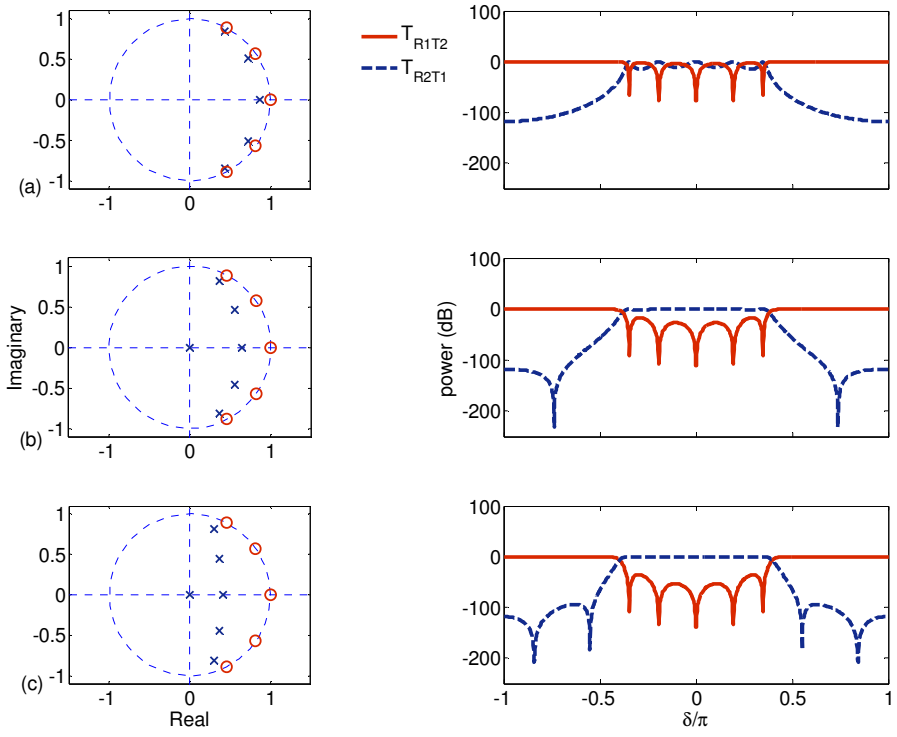

Fig. 3.30. Varying the number of columns (M) of the lossless (N×M) 2D-RR array: (a) 5×1, (b) 5×3, (c) 5×5 (r = 0.8). Left: Pole-zero diagrams for the T_{R1T2}, right: Transmission spectra for both output ports.

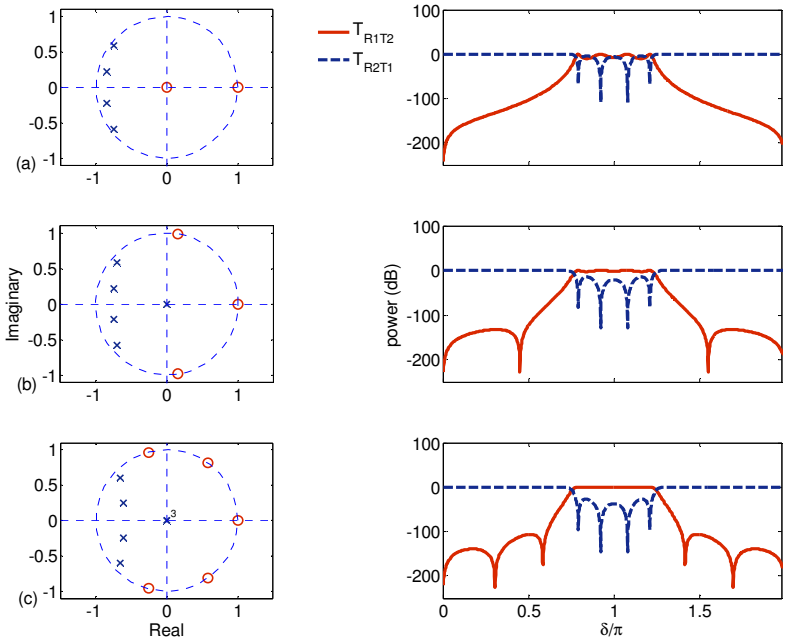

Fig. 3.31. Varying the number of rows (N) of the lossless (N×M) 2D-RR array: (a) 1×5, (b) 3×5, (c) 5×5 (r = 0.8). Left: Pole-zero diagrams for the T_{R1T2}, right: Transmission spectra for both output ports.

Similarly, Fig. 3.31 illustrates how the poles are apodized (moving away from the unity circle) and suppressing the ripples (sidelobes) in the passband (stopband) of T_{R1T2} (T_{R2T1}), as the number of rows (N) are increased.

3.7. Fabrication sensitivity, optical bandwidth and delays

So far, we have assumed an ideal condition where all resonators possessed exactly the same resonance wavelengths and with uniform inter-coupling coefficients. However, in real practice, it is common for ring resonator arrays to have slight variations in cavity length and in inter-coupling coefficients. The combined effects would normally degrade the overall device performance. In this section, we study such effect in order to understand the collective behavior of the ring array response. Normally, ring resonator arrays are sensitive to fabrication variations. For instance, fabrication deviations in the inter-coupling coefficients and cavity length could easily alter the resonance wavelength and degrade the device performance.

To understand the consequences in more details, we simulate 5% randomly distributed variations in inter-coupling coefficients (r), Bragg length (L_B), cavity length (L_C) for Type I, Type II and 2D-RR array. In Type II, we observe a narrow dip around $\delta = 2\pi m$, which is caused by Bragg resonance mismatch between the bus waveguides (L_B) and the ring cavity (L_C). This Bragg resonance would normally arise when the Bragg condition, $\lambda_j = 2n_{eff}L_b / j$ (j = 1, 2, 3…), is satisfied. However, these

resonances would no longer precisely overlap with the ring resonances when L_B does not match $L_C/2$. This results in unwanted narrow resonance dip around the center of the passband, for Type II configuration [Fig. 3.32(b)]. In the 2D-RR system, this effect is amplified by the mutual coupling interactions among the rings and translates into N narrow dips in the passband [Fig. 3.32(c)]. Higher finesse rings will have higher sensitivity to such variations. We estimate that the fabrication deviation in $\Delta L_{B,C}$ and Δr should be kept within 5% or even less. Normally, 3 rings in the row direction are sufficient to suppress the sidelobe in the stopband, whereas 10 rings in the column direction are sufficient to remove ripples in the passband (ripples < 0.1dB). Depending on the fabrication capability, the filter maybe limited to applications which uses lower (r) value (i.e., r~0.7). Another options, is to apply thin film heater to tune each ring resonances into the same resonance wavelength, especially if more rings are required.

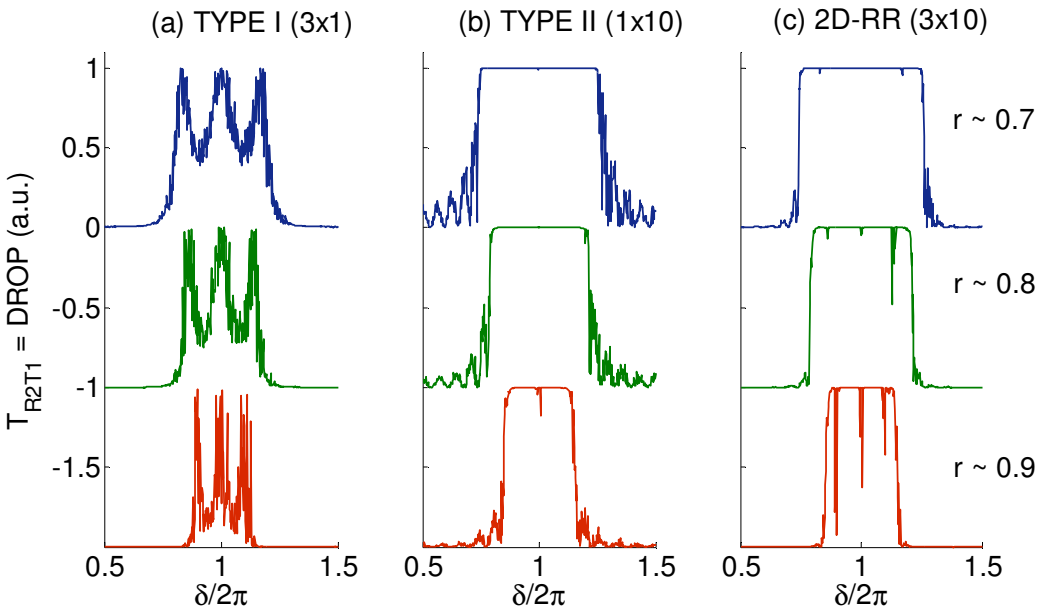

Fig. 3.32. The drop output (T_{R2T1}): Sensitivity study of (N×M) lossless ring-resonator array, given 5% randomly distributed variations in inter-coupling coefficient (r), Bragg length (L_B) and normalized cavity length (L_C).

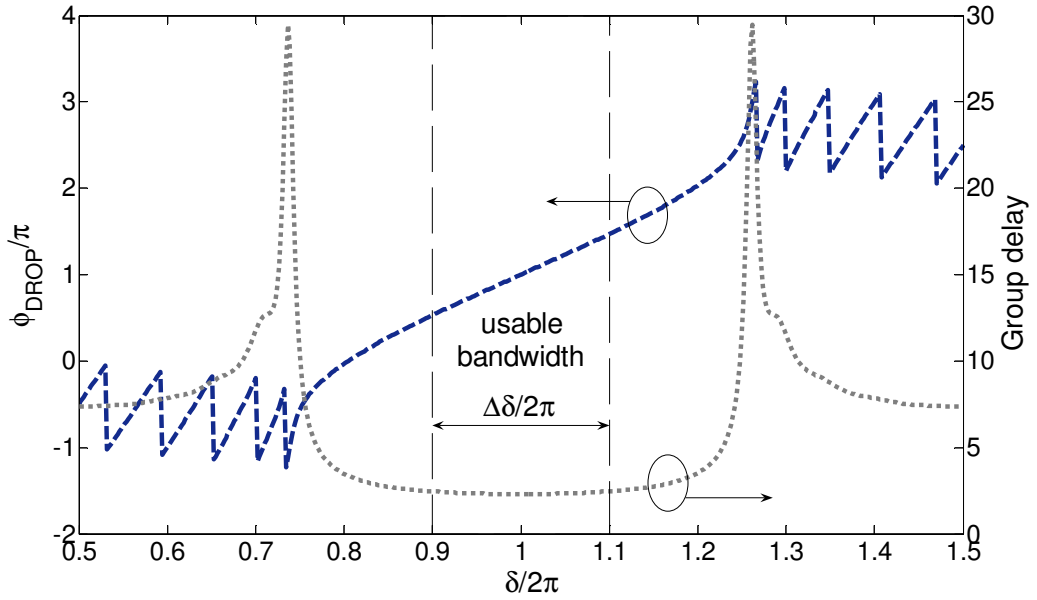

Fig. 3.33. The Drop port: The phase response (left) and the group delay (right) of 3×10 lossless 2D-RR array with *r*~0.7.

r	Usable Δδ/2π	Optical delay Δτ (ps)	Repetition rate T = 1/Δ*f* (ps)	Bandwidth (GHz)
0.70	0.20	1.00	5.00	200.00
0.80	0.15	1.30	8.67	115.38
0.90	0.04	1.85	46.25	21.62

Table. 3.1. The relationship between coupling coefficient (*r*), optical delay (Δτ), pulse repetition rate (T) and bandwidth associated with lossless 3×10 2D-RR array.

Of equal importance to the filter performance is its phase response which determines the group velocity and the dispersion of a pulse passing through it. As shown in Fig. 3.33, the phase responses for the 3×10 array are approximately linear over 80% of the band. The larger the arrays (larger M), the narrower is the flat, linear phase region. There is thus some trade-off, as we increase the array size, between more square and ripple-free amplitude response on the one hand, and more dispersion and group delay at the bandedge on the other. However, as long as the signal frequency bandwidth is within 80% of the passband where the phase is linear, the dispersion will be minimal [167].

Consider a 3×10 2D-RR array with 5μm radius, group index of ~4.3, and *r*~0.7. To be stricter, we only take half of the usable bandwidth (Δδ/2π ~ 0.2) considering the group delay is the lowest and more or less constant throughout the normalized frequency. Based on this requirement, we estimate an optical delay (Δτ) of ~1ps and a maximum operating bandwidth of 200GHz (δ/2π = Δ*f*Δτ), which corresponds to a minimum 5ps pulse repetition rate. In general, the usable bandwidth decreases as (*r*)

increases due higher latency (higher group delay). For instance, when r~0.9, the maximum bandwidth decreases by almost 10 times to ~20GHz, however, the optical delay (1.85ps) becomes insignificant as compared to the minimum repetition rate (~46ps), which relaxes the effect of the delay with respect to the pulse-train associated with it. This is a design trade-off between the optical delay and the bandwidth, which is summarized in Table 3.1.

3.8. Conclusion

In summary, we have shown that by combining the Type I and Type II filter, it is possible to design a hybrid 2D-RR array which can approximate an ideal bandpasss filter with a square "flat-top" amplitude response, sharp rolloff and sidelobe-free stopbands. The mechanism relies on the 2D periodic structure which exhibits complementary non-overlapping (2D) photonic bandgaps. We have also rigorously study the critical coupling and oscillation conditions for Type I and Type II filters, which is extended from the previous 1R1B case [1]. The study is verified with the pole-zero diagram, which is a convenient tool to observe the dynamics of critical coupling and oscillation in high-order ring-resonator system. Moreover, we show a pole-zero analysis for the apodization of these filters based on an actively tunable Mach-Zehnder (or MMI) type coupler, where it is shown that apodization corresponds to designing pole-zero pairs with wide separations, while the specific values of the coupling coefficient are determined by the required bandwidth. Thus, the pole-zero approach can be a quick and approximate method to arrive at first-order designs for apodized filters.

Lastly, we note that the 2D-RR arrays are sensitive to slight fabrication imperfections. We estimate that the error $\Delta L_{B,C}$ and Δr should be controlled within 5% deviation or less. Normally, a 3×10 configuration is sufficient to suppress sidelobes in the stopband, and to remove ripples in the passband (ripples < 0.1dB). Depending on the fabrication capability, the filter maybe limited to applications which uses lower (r) value (i.e., r~0.7), which is associated to optical delay of ~1ps and a maximum operating bandwidth of 200GHz.

Chapter 4

Phase engineering for ring enhanced Mach-Zehnder interferometers

4.1. Introduction

Mach-Zehnder interferometer (MZI) provides an efficient means for converting phase modulation to intensity modulation. In this device, a single input wave is split between two arms, and a phase shift is induced either in a single arm or in both arms in a push-pull manner. There could be a single output or two complementary outputs depending on whether the two arms are combined via a Y branch or a 2×2 3dB coupler. The phase difference could be induced by an electro-optic or all-optical effect, a change in temperature or one of many other possible control parameters. As such, the MZI is a versatile device with many applications, for examples, as a space switch [33, 169], intensity modulator [147], optical filter or sensor [153, 154].

To engineer the performance of MZI, one could tailor the phase shift by introducing different passive or active building blocks into the MZI. One effective way is by coupling a ring resonator (RR) to one of the MZI arms. Since the ring resonator is a resonant structure, the phase accumulated inside the ring will enhance the phase difference between the MZI arms. We shall generally call this MZI a ring-enhanced MZI (REMZI). In this chapter, we shall study the effect of introducing more complicated ring resonator configurations, in order to understand how far we can tailor the phase shift and the resulting MZI transfer function. The higher-order ring resonator structures are also filters [40] and have unique transmission and phase responses depending on the configurations. When coupled to MZI they greatly enhance the sensitivity of the MZI to frequency and effective index changes. In the most general case, we will consider 2D-RR arrays, coupled to the MZI in two possible configurations to be discussed below. The resonators will at first be assumed lossless so as to focus our study solely on the phase shift introduced by the ring structures. We will then discuss the effect of loss in the last section of this chapter.

4.2. Basic theory

In a REMZI, the ring resonator structure is coupled to one arm of an MZI. The outputs of the MZI can be expressed in general by the following matrix relation:

$$\begin{bmatrix} E_{BAR} \\ E_{CROSS} \end{bmatrix} = \begin{bmatrix} r & i\kappa \\ i\kappa & r \end{bmatrix} \begin{bmatrix} T\exp(i\Delta\varphi) & 0 \\ 0 & \exp(i\Delta\varphi_B) \end{bmatrix} \begin{bmatrix} r & i\kappa \\ i\kappa & r \end{bmatrix} \begin{bmatrix} E_{IN} \\ 0 \end{bmatrix} \tag{4.1}$$

where the first and the third matrices on the right-hand side represent the output and input couplers of the MZI [42, 87] respectively, and $t_{\text{eff}} \equiv T\angle\Delta\varphi$ in the second matrix summarizes the complex transfer function (amplitude and phase) of the ring structure which is coupled to the upper arm of the MZI. For generality we have included an additional static phase bias $\Delta\varphi_B$ (active or passive) at the lower MZI arm. However, for simplicity, we will assume that $\Delta\varphi_B = 0$ (balanced MZI) so as to focus on the phase shift introduced by the ring structures. To simplify the analysis, all rings and ring couplers are assumed to be identical, and for the input and output couplers 3-dB coupling ratios are assumed (i.e., $r = \kappa = 1/\sqrt{2}$). From (4.1), the bar and cross output powers are given by

$$\begin{aligned} T_{BAR} &= \left|E_{BAR}/E_{IN}\right|^2 = (1+T^2-2T\cos\Delta\varphi)/4 \\ T_{CROSS} &= \left|E_{CROSS}/E_{IN}\right|^2 = (1+T^2+2T\cos\Delta\varphi)/4 \end{aligned} \tag{4.2}$$

When $T = 1$, (4.2) reduces to the usual equation $T_{BAR} = \sin^2(\Delta\varphi/2)$ and $T_{CROSS} = \cos^2(\Delta\varphi/2)$ for a symmetric MZI. The two outputs are complementary.

We first consider the simplest case of a one-ring-one-bus (1R1B), which forms the basic building block for all higher-order structures. The coupler acts as a partly transmitting mirror with a reflectivity (r), which is related to the coupling coefficient by $\kappa = \sqrt{1-r^2}$. It can be shown that the transfer

function t_{eff} is given by the expression $t_{\text{eff}} = \dfrac{r - a\exp(i\delta)}{1 - ra\exp(i\delta)}$. If the ring is lossless $(a = 1)$, this configuration is an all-pass filter (i.e., $T = 1$ for all frequencies) with a pure resonant phase response. Resonance occurs when $\delta = 2m\pi$, where m is an integer. As shown in Fig. 4.1, we find that the *effective* phase shift is 2π across a resonance; varying the reflectivity r only changes the slope of the phase. In contrast, for the Fabry-Perot filter configuration shown by the 1R2B (one-ring-two-bus), the effective transmission phase shift across a resonance is π. In this case there are two outputs as the ring is coupled to two bus waveguides; the Drop (Through) output is denoted as T (R).

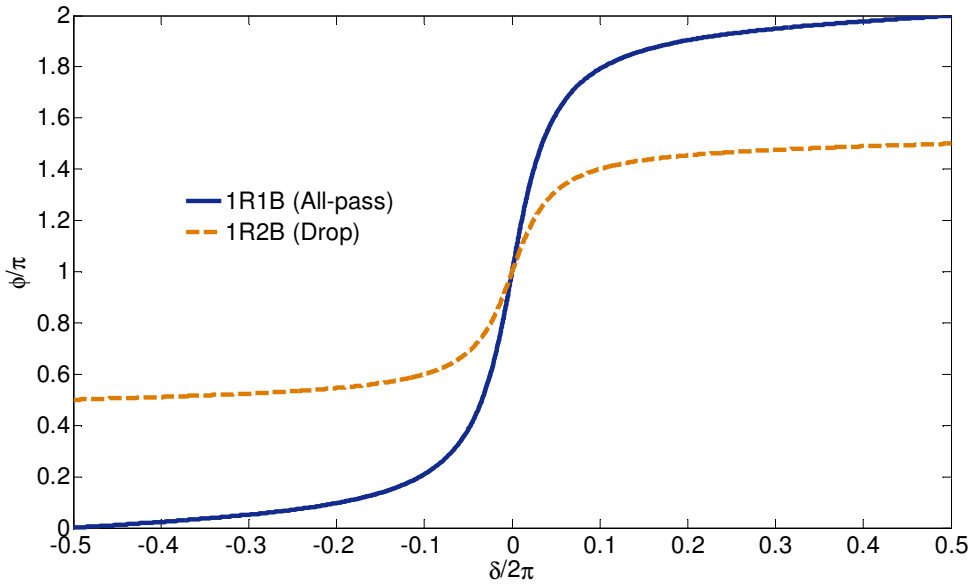

Fig. 4.1. The effective transmission phase shift versus the ring single-pass phase shift for a one-ring-one-bus (1R1B) and a one-ring-two-bus (1R2B), assuming lossless case ($r = 0.8$).

Using the single rings as building blocks, we next consider two general forms of higher-order 2D periodic ring structures that may be coupled with the MZI. In each form we will discuss first the special 1D geometry and then the more general 2D configuration. For simplicity we assume all the rings and the couplers to be identical and lossless. Because the structure is periodic, the transfer matrix method can be used to evaluate t_{eff}. This method has been applied to 1D structure [40, 42, 57] but, so far, not to a 2D structure. The details of the 2D-RR array transfer matrix formalism are presented in the previous Chapter 3.

4.3. Side-Coupled ring enhanced Mach-Zehnder interferometer (SC-REMZI)

Fig. 4.2 shows the generalized 2D array SC-REMZI configuration, which consists of columns of rings side-coupled to the upper MZI arm. The rings are mutually coupled in the same column, but not between columns.

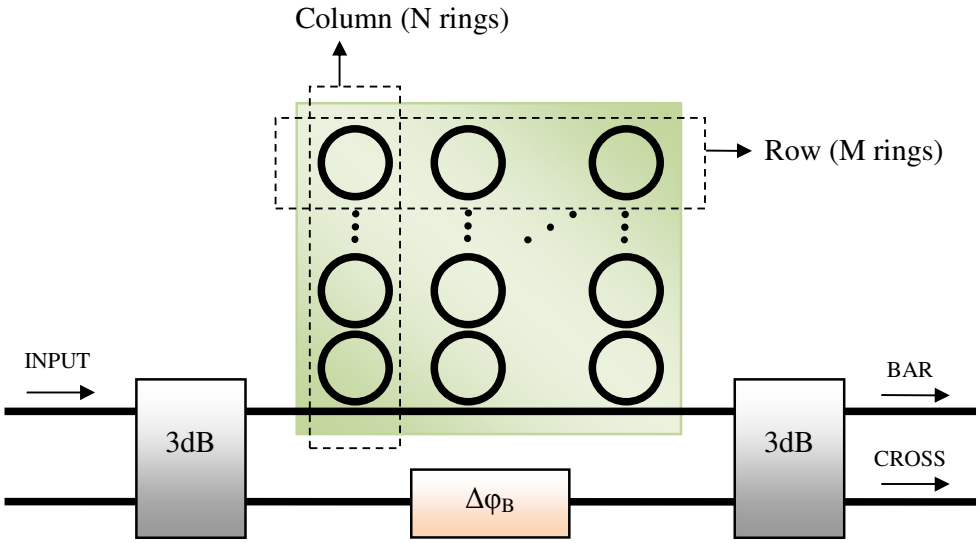

Fig. 4.2. SC-REMZI (inter-resonator coupling occurs within the columns, but not between the columns).

The mutually coupled ring structure is known as a coupled-resonator optical waveguide (CROW) [54], through which light can propagate when the rings are on resonance. Being an extension of the single-ring all-pass filter, the effective phase shift in each ring is 2π, and the total phase shift for N rings is $N \times 2\pi$. However, because of mutual coupling, the resonance frequency shows N-fold splitting, and the accumulated phase shift increases with N in a staircase manner. When coupled to the MZI, this ripple-like phase shift is converted into an intensity pattern with N sharp oscillations in the transfer function, as shown in Fig. 4.3(a). Note that the split peaks (in dotted red) are sharper relative to the original peak of the one-ring case (solid dark blue), and the spacing between them is determined only by the coupling coefficient between the resonators.

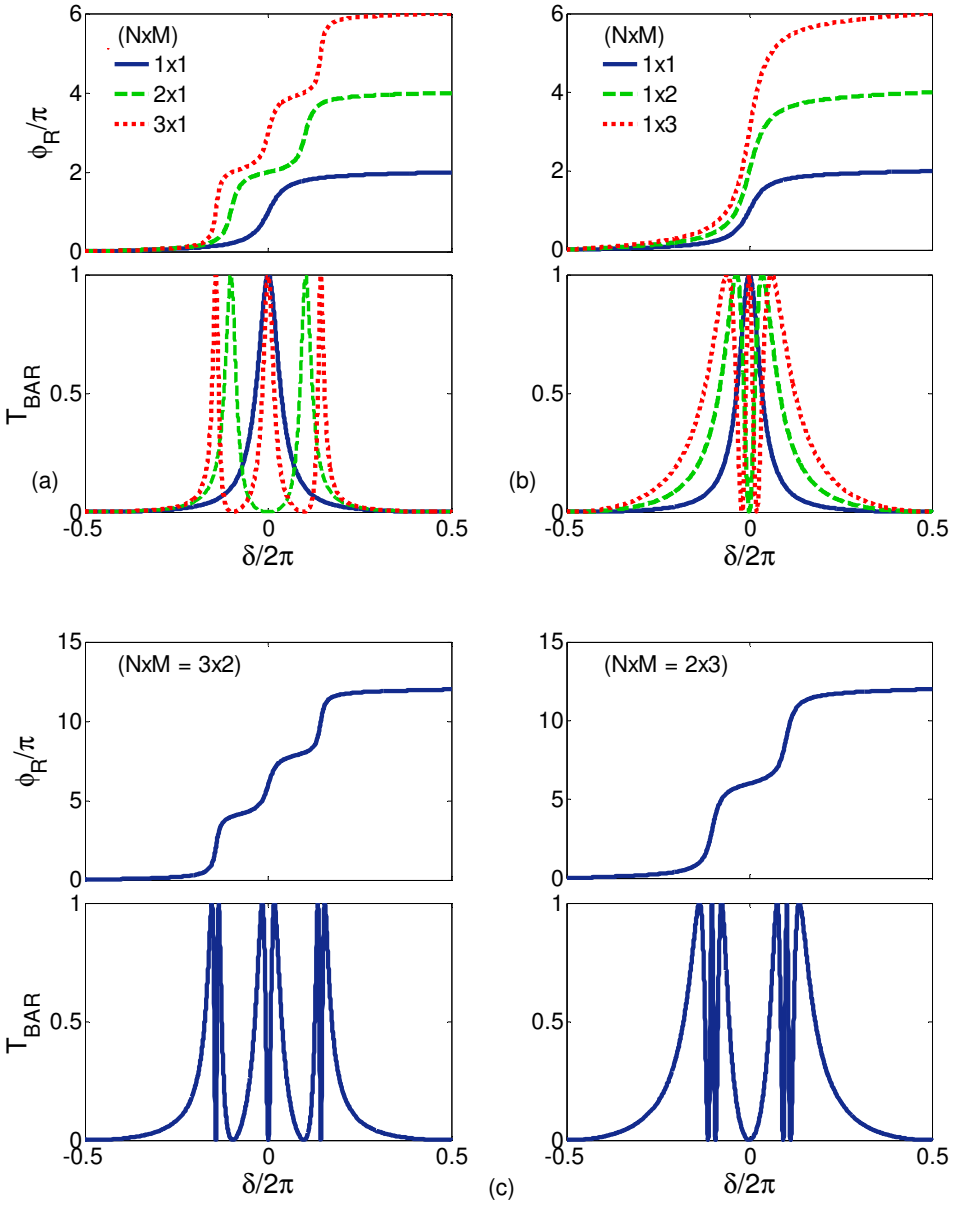

Fig. 4.3. SC-REMZI: Ring effective phase (upper curve) and the bar output transmission (lower curve) as a function of the ring round trip phase δ for (a) a single column of N (=1,2,3) resonators; (b) a single row of M (=1,2,3) resonators, and (c) N×M 2D arrays (lossless case $a = 1$; $r = 0.8$). The insets show the ring and REMZI configurations. Since $T = 1$ throughout, the amplitude responses are not shown.

In the case of a single row of M identical rings which are coupled to one arm of the MZI, but not mutually coupled to each other, we merely have a series of all-pass filters each accumulating a phase shift of 2π across a resonance, giving a total phase shift of M×2π. Hence, the MZI transfer function shows M oscillations, with the most rapid change occurring at the resonance, as shown in Fig. 4.3(b).

In the 2D case, each column can be reduced to an equivalent resonator with an effective transfer matrix. The 2D array is then reduced to a 1D cascade of these equivalent resonators. Therefore, the 2D array will contain the combined features of the row and column resonators, as clearly illustrated in Fig. 4.3(c). The general trends with the number of ring resonators in the row and column directions can be summarized as follows: The total accumulated phase shift is $\Delta\varphi = 2\pi(\mathrm{N}\times\mathrm{M})$, where N×M is the total number of ring resonators. Part of this total phase is from the N column resonators and contributes to the N resonances in the MZI transfer function. The other part is from the M row resonators and causes the (M-1) dips within each resonance. In total, there are N×M peaks spread over a bandwidth determined by *r*, where regions of rapid oscillation are interspersed with regions of more gradual change.

4.4. Mutually Coupled ring enhanced Mach-Zehnder interferometer (MC-REMZI)

In this configuration, the 2D ring array is inserted into one arm of the MZI, sandwiched between two parallel bus waveguides. Along the arm propagation direction the rings are mutually coupled, similar to the CROW in the previous case except that the CROW is now coupled to a waveguide on each end.

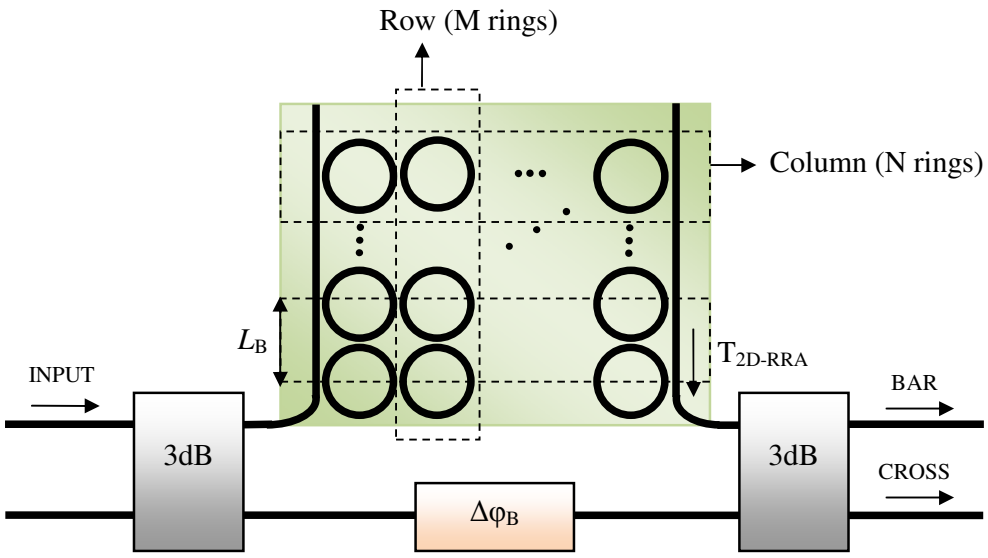

Fig. 4.4. MC-REMZI (inter-resonator coupling occurs within the columns, but not between the columns). The phase offset between the bare-MZI arms are neglected for simplicity. Note that $T_{2D\text{-}RRA}$ corresponds to the drop port of the 2D-RR array section.

Let us first consider the case of a single column of N resonators, where N is an odd integer. When the resonators are on resonance, input light will propagate through the array and be directed back into the MZI. Otherwise, the incident light will be reflected by the array and is assumed lost at the end of the input bus waveguide. This case has been demonstrated in [177]. Fig. 4.5(a) shows the sharp transmission bands when the resonators are on resonance. The N ripples in the passband are due to the mutual coupling between the N resonators. Similarly, the phase response shows a ripple pattern and

the total phase shift is Nπ, since the effective phase shift is π per ring in this case. The MZI output shows corresponding oscillatory behavior within the resonance bands. Outside the resonance band, the phase shift is zero since $T = 0$. Here the output at the bar port is a constant 0.25 which is the fraction of light that has passed through the two 3-dB couplers. The total power is conserved when both the bar and cross output powers and the reflected power are accounted for.

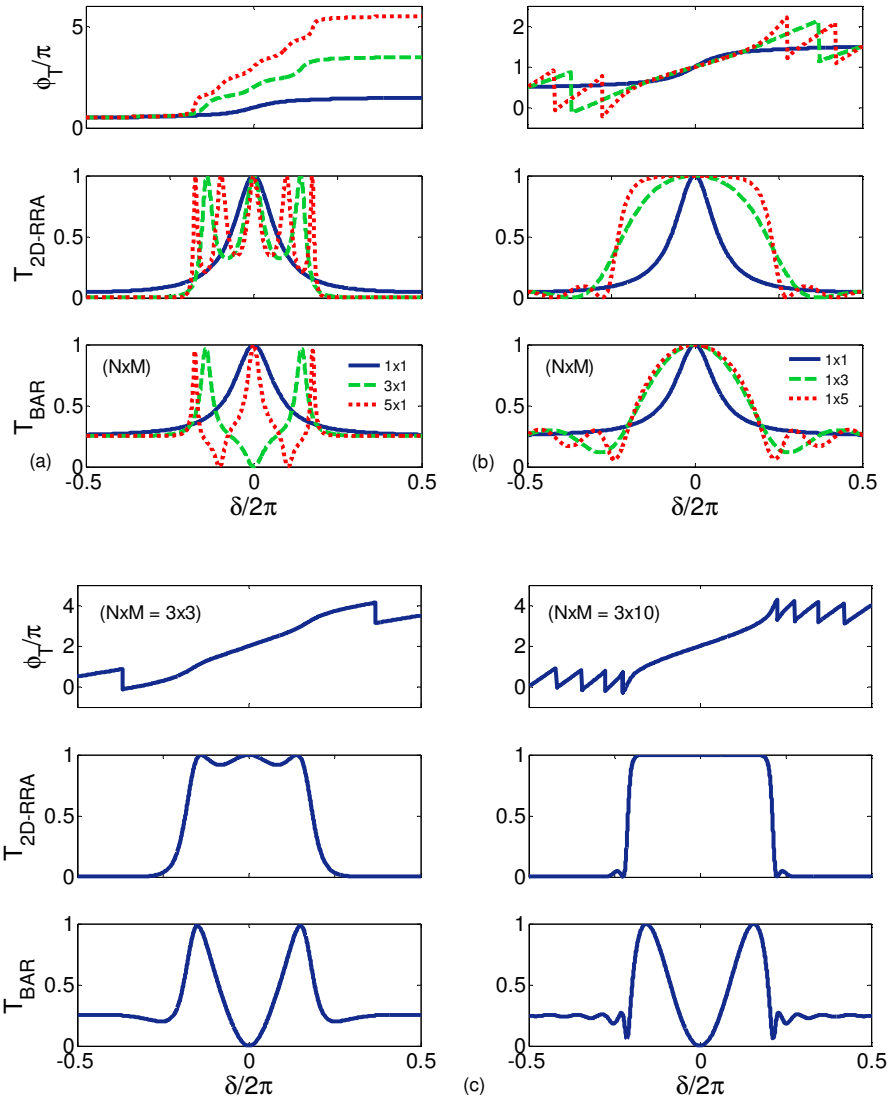

Fig. 4.5. MC-REMZI: Effective phase Δφ (top), transmission (drop port) of the 2D-RR array (middle), and the bar output transmission (bottom), in the absence of loss ($a = 1$), as a function of the ring round trip phase δ, for (a) a single column of N (=1,3,5) resonators; (b) a single row of M (=1,3,5) resonators; (c) N×M 2D-RR arrays ($r = 0.8$). The phase offset between the bare-MZI arms are neglected for simplicity.

In the case of the 1D side-coupled array with M resonators [refer to Fig. 4.5(b)], light cannot propagate through the array when the resonators are on resonance, but is instead reflected in the opposite direction and re-directed into the MZI via the other bus waveguide. Furthermore, because the double channels provide many paths for the waves to feedback to earlier resonators, the array is similar to a distributed feedback grating, giving rise to Bragg resonances when the Bragg condition, $\lambda_j = 2n_{eff}L_b / j$ (j = 1,2,3…), is satisfied [40]. The transfer function, therefore, shows two types of resonances in general, one that depends on the resonator cavity length (L_c) and another that depends on the resonator spacing (L_b). These two resonances, however, overlap if we set $2L_b = L_c$. This is the case shown in Fig. 4.5(b) and (c). In this case, the reflection bands may be considered as the photonic bandgaps (PBG) of the periodic structure. For an array of M rings, there are M zero crossings (or N-2 sidelobes) between two adjacent bands. These sidelobes are due to interference between the reflected waves from the resonators.

As shown in Fig. 4.5(b), the shape of the transmission band rapidly changes from Lorentzian to more box-like as M increases up to a point, after which the shape changes only slowly, because the first few rings are more effective than the subsequent ones. Correspondingly, the phase shift within the band becomes more *linear* compared to the single-ring case, but the magnitude does not scale up linearly with M. On the other hand, near the band edges the phase becomes more nonlinear with increasing M, giving rise to more group delay ("slow wave") at the band edges [40, 54]. This behavior is similar to the FBG filter operating in reflection mode, and is related to the nature of a type of filter called *minimum phase* filter [178]. At points outside the band where T = 0 there is a π-phase discontinuity which has no physical relevance. The resulting MZI output is sinusoidal near resonance where the phase is linear and more oscillatory near the band edges where the phase is nonlinear.

The 2D array can be analyzed column-wise first, then row-wise. Column-wise, each column can be reduced to an equivalent resonator represented by an effective transfer matrix. The 2D array is then reduced to a 1D row array of equivalent resonators, hence the phase response is similar to that discussed above. However, because embedded in each equivalent resonator is a CROW with its PBG structure, the sidelobes in the array transmission spectrum is significantly suppressed compared to the 1×M case [167]. In response, the ripples outside the resonance band in the MZI output are much more subdued.

In a nutshell, the general trends with the number of resonators in the MC-REMZI configuration can be summarized as follows: Increasing the number of resonators in a column has the effect of increasing the number of resonances (oscillations), whereas increasing the number of columns has the effect of smoothening the resonance curve to become more sinusoidal due to the higher phase linearity near the resonance band.

4.5. The effects of coupling and loss

It is convenient to study the impact of the ring resonator on the MZI by varying the coupling coefficient $\kappa = \sqrt{1-r^2}$, where r is the reflectivity coefficient at the ring coupling region. For example, when $r = 1$, the ring resonator structure is completely decoupled from the MZI. On the other hand, if $r = 0$, then the rings become a physical extension of the MZI arm, and the phase shift generated in the rings is proportional to the path length. Consider for example a 3×3 array: the light will propagate through all 9 rings sequentially in the SC-REMZI case, but will propagate only through 3 rings in the MC-REMZI case, hence the effective phase shifts are linear and total 18π and 3π, respectively, across a resonance as shown in Fig. 4.6(a).

The corresponding situation when $r = 0.7$ is shown in Fig. 4.6(b). It is clear that increasing the reflectivity r has a band-limiting effect in that the MZI response is compressed to a band with a bandwidth determined by r. The higher the reflectivity (the lower the coupling), the narrower will be the transmission band and the more nonlinear the phase shift, and hence the more resonant will be the device output. The number of resonances in the output depends on how many rings are effectively coupled to the MZI arm. In this regard the side-coupled configuration is more effective, whereas in the MC-REMZI case some of the rings in the array are quite redundant.

However, one must also consider another important effect that increases with the number of effectively coupled rings, that is, the response time of the device, which is the time it takes for an optical pulse to propagate through the large number of rings. The latency in a ring is proportional to the resonator's finesse which increases with increasing r. Hence, the more resonant the device output, the higher will be the latency through all the rings. Clearly if the latency exceeds the optical pulse width then there will be no interference effect at the MZI output. Hence, the long response time of a large array of micro-rings will limit the device bandwidth and the signal bit rate that can be passed through it.

The array size is not only limited by the response time consideration but also by the propagation loss in the micro-rings. The ring loss is defined using the round-trip attenuation factor a (for a lossless ring, $a = 1$). The effects of loss on the two REMZI configurations are shown in Fig. 4.7. It can be seen that even a 5% round trip loss has a detrimental effect on device performance, especially in the SC-REMZI configuration where the light propagates through all the rings. Since the signal must pass through all the rings, all the rings must have precisely overlapping resonant frequencies, identical coupling coefficients, and very low loss. Therefore, fabrication requirement is stringent, and these REMZI designs are practical only if very low loss and uniform rings can be realized. Recently, very high order multi-ring filters with very high Q resonators have been realized using low-loss Hydex material [3], showing the technological possibility of realizing large and uniform resonator arrays.

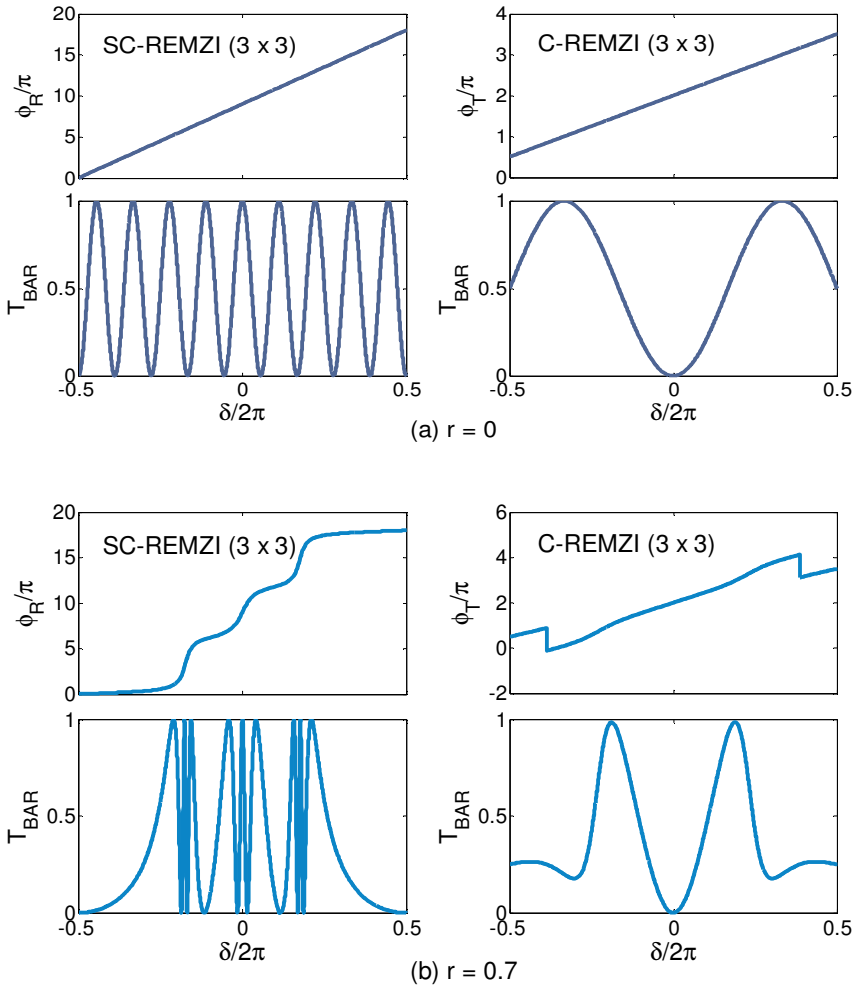

Fig. 4.6. The effect of coupling coefficient, or reflectivity (r), on the ring phase and the MZI bar output for the two ring array configurations. (a) $r = 0$, (b) $r = 0.7$.

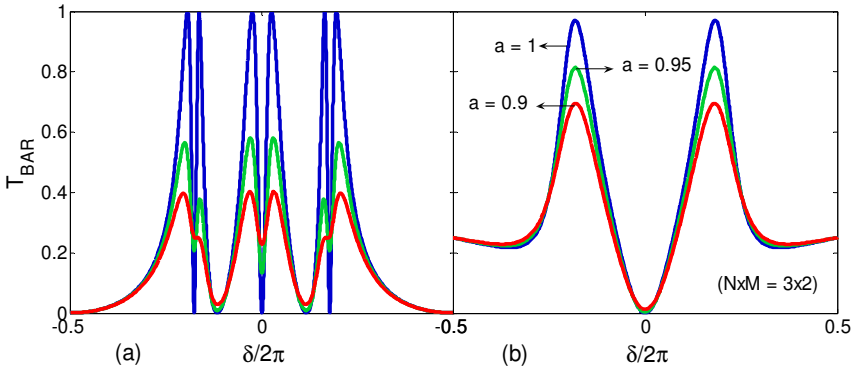

Fig. 4.7. The effect of ring loss on the 3×2 Array for: (a) SC-REMZI and (b) MC-REMZI configurations on the bar output ($r = 0.7$).

4.6. The effect of MZI imbalance

So far, we have assumed a balanced MZI, in order to focus on the study of the effective phase shift introduced by the ring structures alone. In practice, it is not easy to fabricate even an unloaded MZI with high-contrast waveguides whose arms are balanced. Therefore, it is necessary to study the effect of MZI imbalance in REMZI and its consequences. By taking account of MZI arm imbalance, we re-express the bar output as $T_{\mathrm{BAR}} = \sin^2\left\{[(\varphi-(v\delta+\Delta\varphi_B)]/2\right\}$, where φ is the phase shift introduced by the ring structures, $v = L_\Delta / L_C$ is the length ratio between the imbalanced section (L_Δ) and the ring circumference (L_C), and $\Delta\varphi_B$ is the static phase bias in the lower MZI arm.

Since now we have too many device parameters to play around with (i.e., N×M, v, $\Delta\varphi_B$), and due to the fact that we have different SC- or MC-REMZI configurations. It is not possible to show all of the cases here. Considering that the effect of the imbalance is localized only on the MZI arms, and has nothing to do with the rings, then it is more meaningful to study the MZI imbalance using simpler REMZI configuration. This way, we can focus our attention on the effect of the MZI imbalance, without being distracted with other ring parameters.

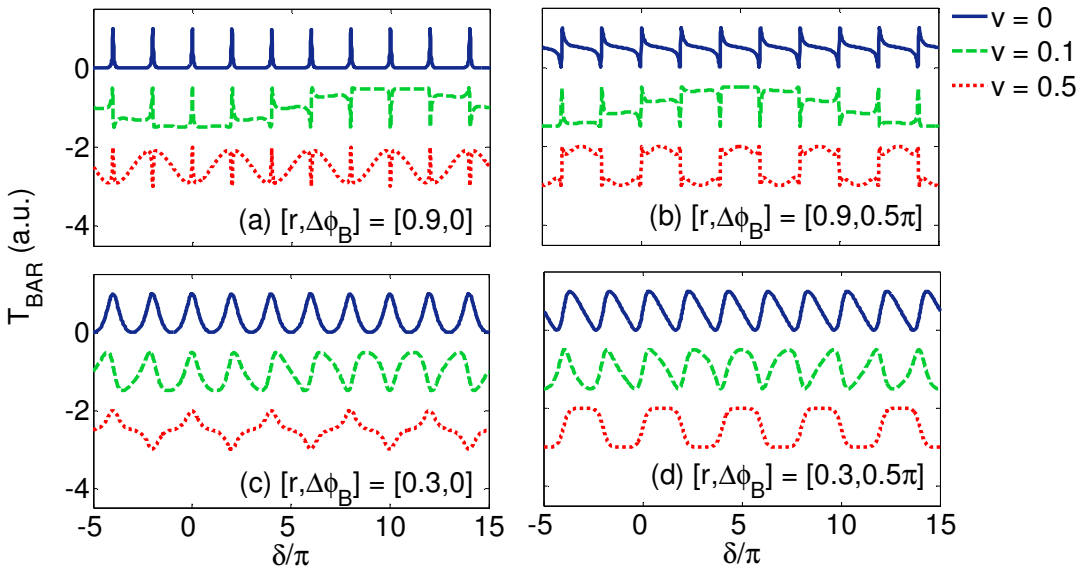

Fig. 4.8. The effect of MZI arm imbalance in one-ring side-coupled to MZI (SC-REMZI) using different combinations of r, v and $\Delta\varphi_B$.

Fig. 4.8 shows the bar transmission of a conventional one-ring side-coupled into MZI [also refer to Fig. 4.3(a)] having different combinations of r, v and $\Delta\varphi_B$ values. In a nutshell, when v and $\Delta\varphi_B$ is both zero, the MZI is "balanced" and its transmission is characterized by the interference pattern induced by the ring resonator only (Fig. 4.8(a) and (c), v = 0). When v or $\Delta\varphi_B$ is nonzero, the interference pattern is modified due to mixed interference contributed by the rings (φ) and the MZI imbalance ($v\delta+\Delta\varphi_B$). The term ($v\delta$) is frequency dependent, and when v is non integer or non half-integers, the spectra will be chirped by additional envelope-like function. However, when the

parameter v is a multiple of integer or half-integers, the spectra is not chirped and has periodicity of 2π or 4π, respectively (no additional envelope function). Note that the MZI arm imbalance never alters the resonance location, which is purely dependent on the rings. The static term $\Delta\varphi_B$ is a phase offset which is non-frequency dependent. Its effect is uniform throughout the normalized frequency. Such case is illustrated by the uniform Fano-resonances in Fig. 4.8(b), when $v = 0$.

To obtain independent verification, we compare our results with the literature. For instance, the simulated spectra with $v = 0.1$, is similar to the one Heebner implemented using a fiber loop configuration [179]. Based on Fig. 4.8(d), it can be seen that by taking $\Delta\varphi_B = 0.5\pi$ and $r \sim 0.3$ ($v = 0$), we can effectively remove the 3rd order harmonics and obtain a linearized transmission, which is a desirable feature for modulators [180, 181]. The readers may refer to Appendix A for more details on the linearization procedure. Lastly, using the same linearization parameters, but modifying the v parameter from 0 to 0.5, it is possible to engineer the imbalance in obtaining "box-like" spectra [65, 66]. These are some examples on how MZI imbalance can be engineered for some useful purposes.

4.7. Conclusion

We have presented in this chapter two generalized array configurations of ring-coupled MZI, namely SC-REMZI and MC-REMZI, and discussed their characteristics in terms of the amplitude and phase response of the ring arrays as well as the transmission output of the MZIs. Because the rings are resonant devices, they greatly enhance the sensitivity of the MZI to frequency and effective index changes. In the side-coupled (SC) structure, the array is coupled to waveguide only on one side and hence the wave can only propagate in the forward direction. In the mutually coupled (MC) structure, the array is coupled on both sides to waveguides so there is optical feedback between the resonators. Because of this fundamental difference the two types of array have distinct transfer functions and effective phase shifts, which can be tailored to phase-engineer a wide-range of MZI transmission functions.

From the application point of view, the side-coupling configuration is probably better as it can be designed to give any number of sharp resonances within a small band in the MZI output, which may be a desirable feature for some nonlinear switching and sensing applications [153, 154]. The 2D RR-array coupled between two waveguides, on the other hand, has been shown to form a near-ideal bandpass filter characterized by a flat-top, square and ripple-free amplitude response and a largely linear phase response, if the array is sufficiently large (e.g., M = 3 and N = 10). This characteristic is attributed to the 2D nature of the photonic bandgap exhibited by the 2D periodic structure [167]. Despite the large number of rings, the phase response is not greatly enhanced and is approximately linear except near the bandedges. For this reason this 2D-RR structure does not significantly modify the MZI output. Of course, MZI is not the only way to utilize the phase response of these ring resonator structures, but it is probably the simplest and the most effective device. In this study, we

have shown the amplitude and phase characteristics of various ring configurations and how they can be used to physically engineer the MZI transmission behavior. We have also discussed some of the practical issues involved, including the effects of loss, delay time, and the effect of MZI arm imbalance.

To sum up, we have presented two generalized array configurations of ring-coupled MZI and discuss their characteristics in terms of the amplitude and phase response of the ring arrays as well as the transmission output of the MZIs. The two types of array have distinct transfer functions and effective phase shifts, and can be tailored to phase-engineer a wide-range of MZI transmission functions. In the next two chapters (Chapter 5 and 6), we extend the study into novel types of ring-coupled MZIs. The devices combine the novel phase response of the coupled resonators with the simplicity and flexibility of MZI to give unique transmission properties not achievable by the individual components.

Chapter 5

Nested-ring Mach-Zehnder interferometer

5.1. Introduction

Ring resonator (RR) is a versatile photonic building block with applications for filtering [27, 48, 50, 56, 57], sensing [123, 140, 153, 154] and switching [9, 62, 99, 103, 144, 182]. Two basic configurations of ring resonator are shown in Fig. 5.1(a), showing a single ring coupled to one and two bus waveguides respectively. The fundamental design parameters are the ring cavity length (L_C) and the coupling coefficient (κ) between the ring and the bus. In this chapter, we introduce a modified single-ring building block that has interesting phase and transmission properties and applications. We shall call it the nested ring resonator (NRR) as it looks like a ring nested by a U-shaped waveguide. It is equivalent to the double-bus ring with the two buses connected by a loop with an arbitrary length L_v, which is expressed as a multiple of the inner-ring circumference $L_v = vL_C$. A key result of this chapter is that the NRMZI can give a box-like transmission when v is an integer or half-integer. The loop feedback path provides an alternative route for the propagation of light to that

through the ring. The interference between two pathways is required to generate Fano resonances [34, 144, 183, 184] as have been demonstrated in other ring-based structures. Thus, the nested ring is expected to exhibit a periodic phase response with sharp nonlinear phase changes. This phase response can be translated to a power spectrum with sharp filter-like response when the nested ring is coupled to one arm of a Mach-Zehnder interferometer. We study the dependence of the power spectrum on the length of the feedback loop and the coupling coefficient between the ring and the bus waveguide, and show that the nested ring MZI (NRMZI) can exhibit a box-like transmission spectrum with sharp transition edges, and thus is highly desirable as a "digital" sensor or switch as well as a filter.

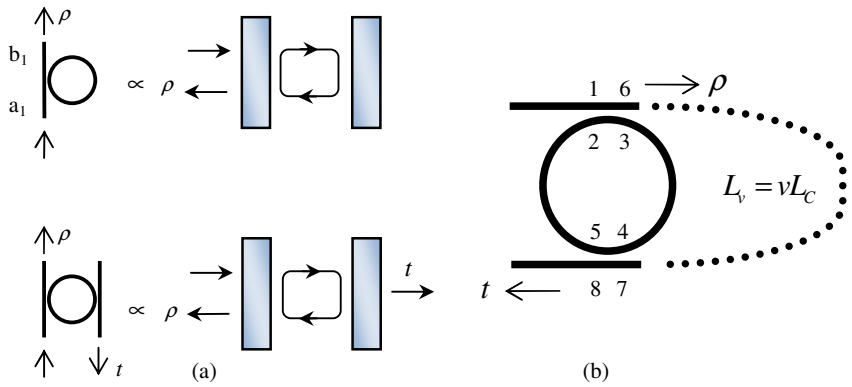

Fig. 5.1(a) Single-bus and double-bus coupled ring resonator; (b) The NRR. The dotted line refers to the outer feedback arm with a length of $L_v = vL_C$ where L_C is the cavity length.

In section 5.2 we present a theoretical formulation of NRR based on the transfer matrix formalism. In section 5.3 we discuss the unique properties of NRMZI and some potential limitations. In section 5.4, we compare the transfer matrix formalism with the finite-difference time-domain (FDTD) simulation. Lastly, we consider the effects of loss and sensitivity to fabrication variations in Section 5.5.

5.2. Theory of the nested ring resonator (NRR)

For a ring resonator coupled to one bus waveguide, the transfer function is given by the reflectivity $\rho = |\rho| \exp(i\varphi)$, which is defined as $\rho = b_1/a_1$, where b_1 (a_1) is the output (input) field [167, 172]:

$$\rho = \frac{r - a\exp(i\delta)}{1 - ra\exp(i\delta)}, \quad R = |\rho|^2 = \frac{r^2 - 2ar\cos\delta + a^2}{1 - 2ar\cos\delta + a^2 r^2} \tag{5.1a}$$

$$\varphi = -\tan^{-1}\left(\frac{a\sin\delta}{r - a\cos\delta}\right) + \tan^{-1}\left(\frac{ra\sin\delta}{1 - ra\cos\delta}\right) \tag{5.1b}$$

For switching and sensing applications δ shifts in response to a change in n_{eff}, hence a transmission function exhibiting a sharp response with δ is desirable. For a RR coupled to two bus waveguides, the two outputs are defined as the reflection *R* and the transmission *T*, which are given by

$$\rho = \frac{r(1-a\exp(i\delta))}{1-r^2 a\exp(i\delta)}, \quad R = |\rho|^2 = \frac{r^2 - 2ar^2\cos\delta + r^2a^2}{1-2ar^2\cos\delta + a^2r^4} \tag{5.2}$$

$$t = \frac{-\kappa^2\sqrt{a}\exp(i\delta/2)}{1-r^2 a\exp(i\delta)}, \; T = |t|^2 = \frac{\kappa^4 a}{1-2ar^2\cos\delta + a^2r^4} \tag{5.3}$$

where $t = |t|\exp(i\varphi_t)$, $\rho = |\rho|\exp(i\varphi_\rho)$. The corresponding phase terms are given by

$$\begin{aligned} \varphi_\rho &= \pi - \tan^{-1}\left(\frac{a\sin\delta}{1-a\cos\delta}\right) + \tan^{-1}\left(\frac{r^2 a\sin\delta}{1-r^2 a\cos\delta}\right) \\ \varphi_t &= \pi + \frac{\delta}{2} + \tan^{-1}\left(\frac{r^2 a\sin\delta}{1-r^2 a\cos\delta}\right) \end{aligned} \tag{5.4}$$

One effective approach to analyze the NRR is to consider the double-bus coupled ring as a "black box" with reflection and transmission coefficients, ρ and *t* given by Eqs. 5.2 and 5.3 respectively. The U-loop connecting the two buses has a length of vL_c. Hence, by summation, the total transmission is given by,

$$\begin{aligned} t_{NRR} &= t + \rho^2 a^v e^{iv\delta}(1 + ta^v e^{iv\delta} + ...) = (t + (\rho^2 - t^2)a^v e^{iv\delta})/(1 - ta^v e^{iv\delta}) \\ &= \frac{-\kappa^2\sqrt{a}e^{i\delta/2} + r^2 a^v e^{iv\delta} - a^{v+1}e^{i(v+1)\delta}}{1 - r^2 a e^{i\delta} + \kappa^2 a^{v+1/2} e^{i(v+1/2)\delta}} \end{aligned} \tag{5.5}$$

For a more detailed mathematical derivation of Eq. (5.5), one may refer to Appendix C. Next, to focus on the phase behavior, we first consider the lossless case where $a = 1$ and the nested ring behaves as an all-pass filter with phase-only response. In this case it can be shown in [167] that $|\rho|^2 + |t|^2 = 1$ and $(\rho^2 - t^2)/\rho = 1/\rho^*$, and with $\varphi_\rho - \varphi_t = \pi/2$ from Eq. (5.4), the transmission of the NRR can be simplified to,

$$t_{NRR} = \frac{t\{1 - |t|^{-1}\exp(i[v\delta + \varphi_t])\}}{1 - |t|\exp(i[v\delta + \varphi_t])} = \exp(i\phi_{NRR}) \tag{5.6}$$

Hence the phase response of the NRR may be written as $\varphi_{NRR} = \varphi_t + \varphi_{load}$, where

$$\varphi_{load} = -\tan^{-1}\left(\frac{\sin(v\delta + \varphi_t)}{|t| - \cos(v\delta + \varphi_t)}\right) + \tan^{-1}\left(\frac{|t|\sin(v\delta + \varphi_t)}{1 - |t|\cos(v\delta + \varphi_t)}\right) \tag{5.7}$$

The effect of feedback is embodied in φ_{load} (denoted as the loading term), which is similar to the phase response of a single-bus RR, Eq. (5.1b), with the modifications $\delta \to v\delta + \varphi_t$ and $r \to |t|$. This implies that the outer feedback loop behaves like a single-bus RR with respect to the inner one-ring-two-bus

(1R2B). The resonance in the outer loop depends on the transmission $|t|$ of the 1R2B, and increases with the coupling factor κ^2. The inner ring resonance, on the other hand, increases with the reflectivity (r). Since r and κ are complementary, it is impossible to have strong resonance in both loops simultaneously. As shown in Fig. 5.1, when r is low, the phase response is dominated by the loading phase, which is highly nonlinear with a step-like feature, where each step represents a 2π phase shift caused by resonance in the outer loop. On the other hand, when r is large, the phase response is dominated by the resonance in the inner ring.

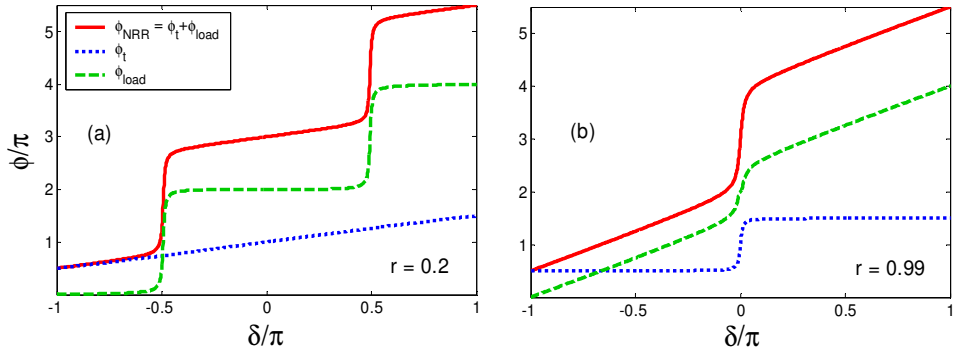

Fig. 5.2. The effect of r on the phase response of NRR (a = 1; v = 1.5).

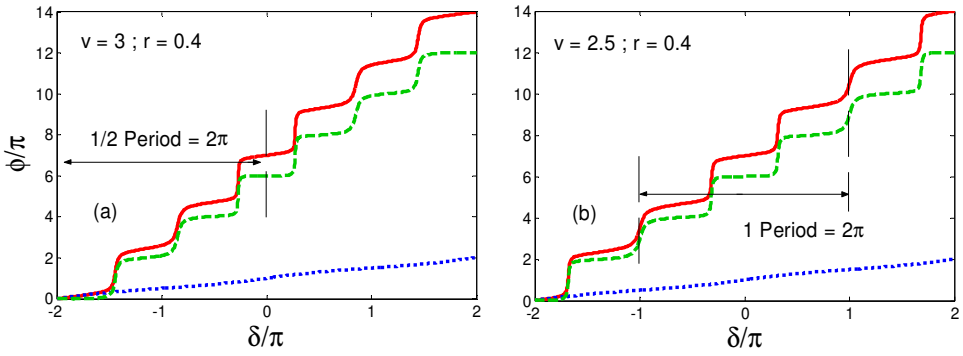

Fig. 5.3. Two different periodicities for the case of (a) $v = m$ and (b) $v = m$-1/2 (a = 1).

The phase term $(v\delta + \varphi_t)$ in φ_{load} contains primarily the factor (v+1/2)δ, which implies: (a) if v is an integer ($v = m$), then the period of φ_{load} is 4π and the number of possible resonances in the outer loop (corresponding to the number of steps in the phase response) is $2m$ in each period; (b) if v is a half-integer ($v = m$-1/2) then the period of φ_{load} is 2π and the number of resonances *per* period is m. Only these two cases are of interest, and two examples are shown in Fig. 5.3. For other values of v, the power spectrum would be irregular with relatively large periodicities.

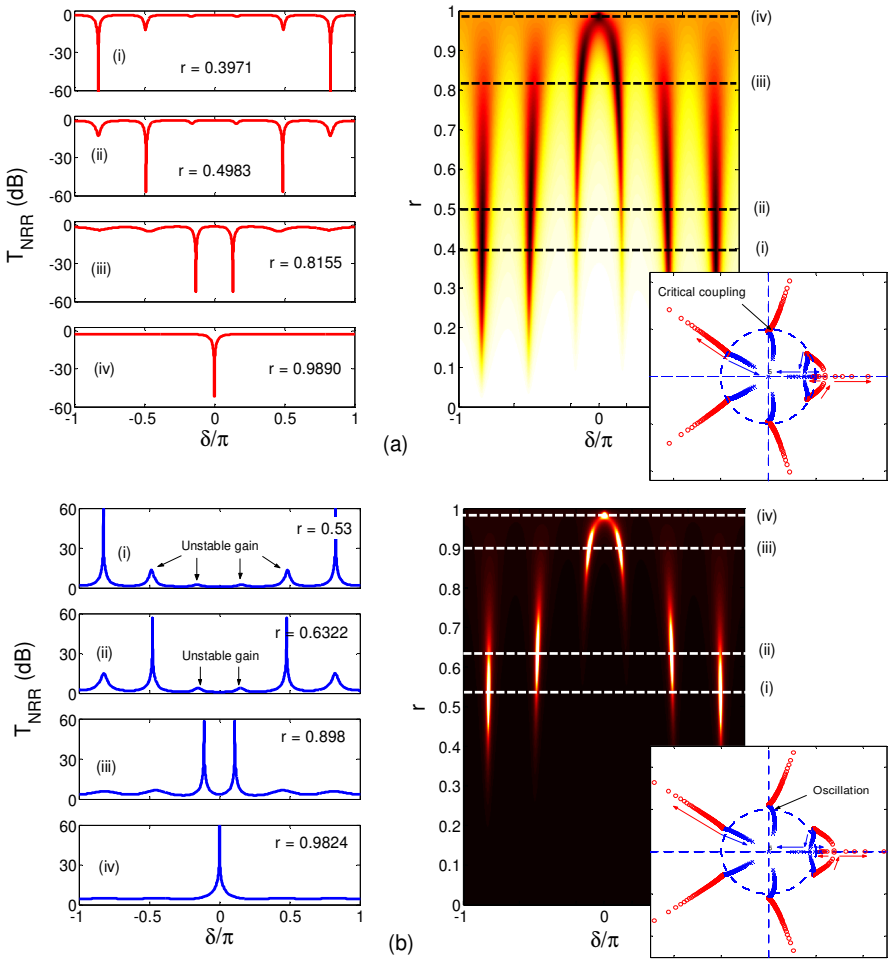

Fig. 5.4. The NRR transmission showing the critical coupling (a = 0.95) and (b) the oscillation (a = 1.1) conditions for the case v = 5.5, and for various values of r. The corresponding pole-zero diagrams and the contour plots of T_{NRR} on the r-δ plane are shown on the right. The zeros are red, the poles are blue, and the arrows indicate the direction of movement as r is increased from 0 to 1. The dashed lines in the contour plots correspond to the transmission curves.

In the more general case where $a \neq 1$, the transmission is no longer all-pass and depends critically on the value of a. In particular, for $a < 1$, specific combinations of r and a can result in the numerator of Eq. (5.5) becoming zero at specific values of δ_1 leading to the *critical coupling* condition similar to that in a single-bus ring [1, 62]. Likewise, for $a > 1$ (which is possible if an optical amplifier is incorporated in the ring cavity [106]), specific combinations of r and a can result in the denominator of Eq. (5.5) becoming zero at specific values of δ_1 leading to the *oscillation* condition [172]. As an illustration, Fig. 5.4 shows the transmission for an NRR with v = 5.5 for (a) $a < 1$ and (b) $a > 1$. The zeros and poles corresponding to critical coupling and oscillation respectively, occur in pairs and move closer to δ = 0 as r increases. The resonances at $\delta = 2\pi m$ correspond to the inner-loop, whereas other resonances correspond to the outer-loop. The inner-loop resonance requires a very high r value

as compared to the outer-loop resonances, which is consistent with the phase response shown in Fig. 5.2. The zeros and poles can be displayed on a pole-zero plot as a function of *r*, as discussed in detail elsewhere [8] and shown on the right of Fig. 5.4. There are 6 pole-zero pairs for v = 5.5. As *r* increases the zeros (poles) move outward (inward) from the unit circle, except for the pair nearest to the zero angle which give rise to the inner-ring resonance at $\delta = 0$ when *r* is sufficiently large. Critical coupling (oscillation) occurs when the zeros (poles) cross the unit circle. For stability, all poles must lie within the unit circle [27]. The resonances indicated as "unstable" correspond to poles which fall outside the unit circle.

5.3. Introducing NRMZI

To convert the phase response of the nested ring to a power spectrum the nested ring may be incorporated into a balanced Mach-Zehnder interferometer, as shown in Fig. 5.5. The bar and cross outputs of a *lossless* NRMZI are given by,

$$T_{\mathrm{BAR}} = \sin^2\{(\varphi_{NRR} - v\delta)/2\} \qquad T_{\mathrm{CROSS}} = \cos^2\{(\varphi_{NRR} - v\delta)/2\} \tag{5.8}$$

When $r = 1$, $\varphi_{NRR} = v\delta$ since no light is coupled into the ring as if the ring is equivalently not present, so both arms of the MZI are identical.

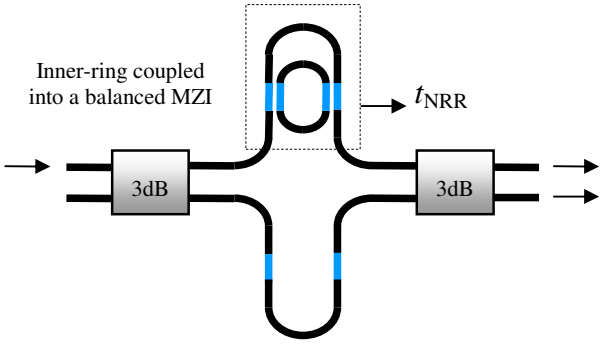

Fig. 5.5. The schematic of NRMZI.

The bar transmission is shown in Fig. 5.6 for various values of *r*. A smaller *r* results in steeper phase nonlinearity, which gives rise to the sharp asymmetric Fano resonances that define the sharp edges of the passband. However, the sharp Fano resonances are inevitably accompanied by ripples in and outside the passband which are undesirable for a bandpass filter. Increasing the value of *r* can flatten the ripples but at the expense of the band edge roll-off. This trade-off is an inherent limitation of this device, which fundamentally relies on the double Fano resonances to generate the box-like output. To investigate the origin of the Fano resonances, we analyze the behavior of the device in terms of the field build-up in each resonant loop. Referring to the labeling notations of Fig. 5.1, the inner-loop and outer-loop build-up factors are defined and given respectively, by

$$B_{31} = \left|\frac{E_3}{E_1}\right|^2 = \left|\frac{i\kappa(1 + a^{v+1/2}e^{i(v+1/2)\delta})}{1 - r^2 a e^{i\delta} + \kappa^2 a^{v+1/2} e^{i(v+1/2)\delta}}\right|^2 \tag{5.9}$$

$$B_{61} = \left|\frac{E_6}{E_1}\right|^2 = \left|\frac{r(1 - a e^{i\delta})}{1 - r^2 a e^{i\delta} + \kappa^2 a^{v+1/2} e^{i(v+1/2)\delta}}\right|^2 \tag{5.10}$$

Again, the extra term $+\kappa^2 a^{v+1/2} e^{i(v+1/2)\delta}$ in the denominator indicates the effect of the outer-loop 'coupling' based resonance. For the inner-loop we have defined the build-up factor as B_{31} instead of the conventional circular intensity B_{21} since the latter is still a part of the outer-loop branch.

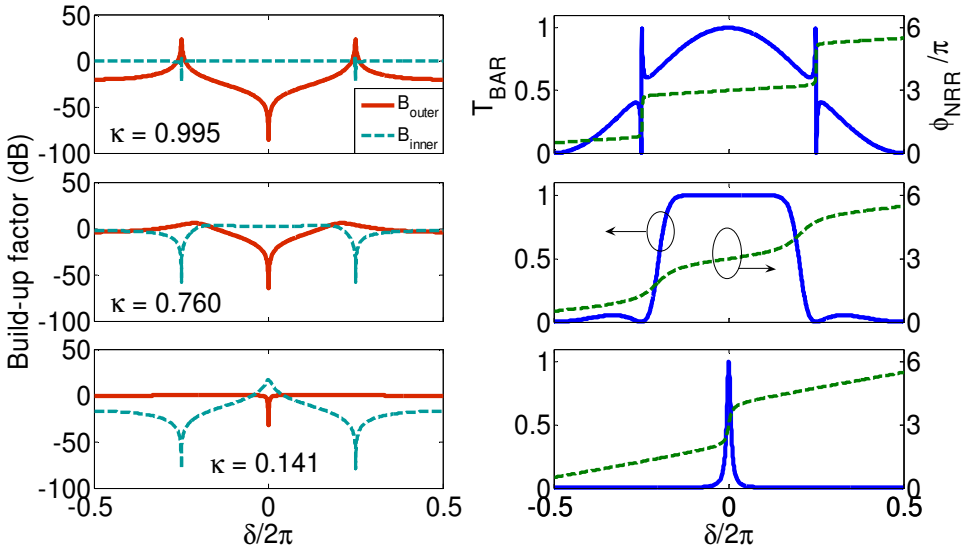

Fig. 5.6. Left: The build-up factor for the outer-loop (B_{61} = B_{outer}) and the inner-loop (B_{31} = B_{inner}) of NRR. Right: The corresponding T_{BAR} and φ_{NRR} as a function of normalized frequency, $\delta = 2\pi n_g L_c/\lambda$ assuming lossless case.

Fig. 5.6 shows the build-up spectra and the corresponding MZI output spectra for different values of *r*. In general, when κ is small, B_{outer} is flat and greater than B_{inner} everywhere except at the 1R2B resonance, where B_{inner} dominates and the NRR behaves like the Drop output of a double-bus RR which has a Lorentzian profile. On the other hand, when κ is high, B_{inner} is flat and greater than B_{outer} everywhere except at the Fano resonances where B_{outer} rises sharply, giving rise to the sharp asymmetric spikes in the MZI output. This shows that the double-Fano resonances in the MZI output are related to the resonant build-up in the outer-loop. For an intermediate value of κ (e.g., 0.76), the peaks in B_{outer} are broadened and hence the sharpness of the Fano resonances is reduced, while B_{inner} remains quite flat in between, thereby resulting in a flatter and rounder MZI output profile which is considered as a better approximation to a "box-like" filter. A more optimized κ value corresponds to the situation where the power is more evenly distributed between the outer and the inner rings.

5.4. FDTD simulation

To verify the accuracy of the transfer matrix formalism we compare the results with the one obtained using the finite-difference time-domain method (FDTD), a method which is able to calculate the fields everywhere in a device. For the FDTD simulations, the radius of the microring-resonator is taken to be 1.7 μm, the waveguide width is assumed to be 0.4 μm, the core-cladding index contrast is 3:1, and the gap between the ring and the bus is designed to give a nominal coupling of $r = 0.6$. The fields in the inner and outer rings are 'measured' at each wavelength and normalized by the input spectrum to give B_{31} and B_{61} respectively. A Gaussian light pulse of 15fs pulse width with near-resonant input wavelength is launched from one of the waveguides. In our simulation, we chose a grid size less than $\lambda/20n$ and set $v = 1$ to save computation time. As shown in Fig. 5.7, the build-up spectra are similar to those shown in Fig. 5.6 obtained by the transfer matrix formalism. The insets show the FDTD field distributions at the wavelengths corresponding to the two peaks and the one dip in B_{61}. The dashed curves show the results of the transfer matrix formalism, which are in good agreement with FDTD. To obtain these results, we have taken into account the wavelength dispersion using the expression $n_{\text{eff}}(\lambda) = 3.1334 - 0.2874\lambda$ for $1.7\mu\text{m} < \lambda < 1.8\mu\text{m}$, which is obtained by numerically solving the n_{eff} for various λ. Furthermore, to achieve good agreement the ring radius is increased to 1.717μm, consistent with the fact that the mode in the ring is slightly skewed outward from the waveguide axis. The excellent agreement with FDTD gives us confidence that the transfer matrix formalism provides a reliable analytical approach to this device. Note that the same transfer matrix method used to match the FDTD simulation, is also used to fit the experimental results (Section 5.5). This implies that the FDTD result, although only simulated in 2D, is reasonably accurate in describing the actual physical operation of the device.

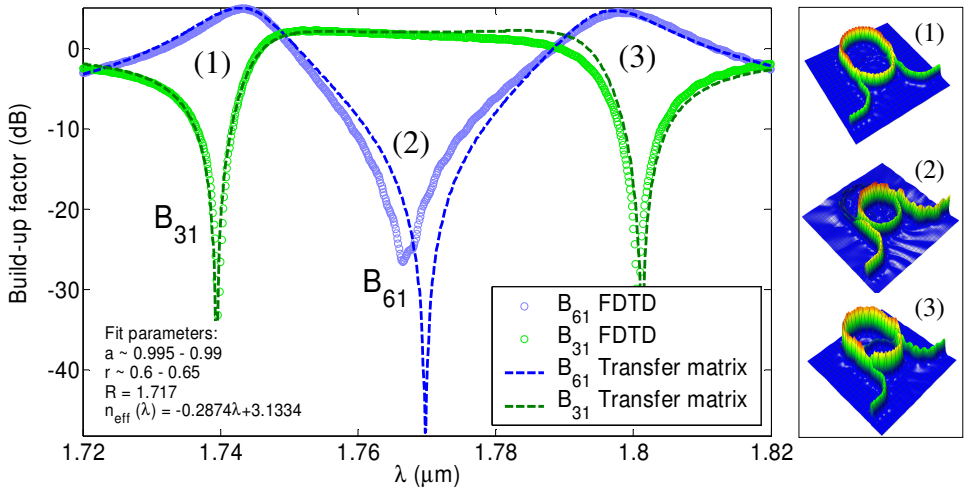

Fig. 5.7. The comparison between the 2D FDTD simulation and the analytic transfer matrix formalism (for the case $v = 1$) in terms of the outer-loop build-up factor B_{61} and the inner-loop build-up factor B_{31}. The insets show the field distributions at three different points of the spectrum as indicated.

Note that, in this section, we intentionally choose a slightly longer operating wavelength (around 1.7 to 1.8μm) to speed up the convergence time and avoid unwanted spurious effect due to discretization errors, in the FDTD computation. This way, we can have faster convergence time and better accuracy. The build-up signature remains the same if simulated around 1.55μm wavelength. This is because the spectra are periodic everywhere through out normalized frequency (refer to Fig. 5.6). The focus of the FDTD simulation is just to show how the light is physically distributed with respect to its inner- and outer-loop resonances in general (regardless of the ring dimensions or a specific operating wavelength).

5.5. Experimental results

The NRMZI are fabricated in IMEC under the ePIXnet Silicon photonics platform using a CMOS based deep-UV process [16]. The SOI consists of 220nm Silicon on a 2μm oxide buffer layer. In the DUV lithography process, the exposure dose is incrementally stepped up from the left to the right of the 8" wafer such that the gap width (waveguide width) increases (decreases) from left to right of the wafer. These variations imply that different devices on the wafer will have different coupling coefficients, and hence one can study the behavior of the NRMZI with various κ values of interest. The UV resist is then used as the etch mask for an ICP etch through the Si layer to form the photonic wire waveguides.

The propagation loss in single-mode photonic wires in SOI is caused by substrate leakage and scattering at sidewall roughness. In an SOI wire, only leaky modes exist. Although the confinement of the mode in the core is very good, the exponential tail of the mode still extends into the substrate, causing substrate leakage. This loss decreases exponentially with increasing oxide thickness. The typical loss of a 500nm width waveguide is ~3dB/cm, where almost half of it is contributed by substrate leakage, whereas the rest is contributed by the scattering loss, due to extreme light confinement in the strip waveguide and enhanced interaction of the waveguiding mode with the sidewall surface roughness [16].

To facilitate fiber input and output coupling each device is fabricated with vertical grating couplers [12] on a 10μm wide waveguide with an etch depth of 70nm giving a second-order peak efficiency of about 20% at 1550nm. In practice, the fiber to grating insertion loss ranges around ~7 to ~10dB for each fiber-to-grating interface. Since there are two I/O ports, the insertion loss may double up to ~15 to ~20dB. Such high insertion loss is also partly contributed by design errors and fabrication variations of the gratings. For devices incorporating MZI structures, the total insertion loss may reach up to ~25dB, due to the additional ~2.5dB insertion loss for each of the 3dB multi-mode interferometer (MMI) coupler. The 10μm width waveguides are tapered down to the single-mode waveguides with nominal width of 475nm. The 3dB couplers in the MZI are based on MMI with a width of 3.5μm and a length of 43.5μm, with 5μm taper length at the MMI I/O ports to minimize

insertion loss. For the NRR, both point-coupled and race-track resonators are used. The fabricated microring radius is 15µm.

The device transmission is measured with a broadband ASE light source (1.41µm to 1.62µm) and an optical spectrum analyzer (OSA). The input and output fibers are butt-coupled to the grating couplers at 10° from vertical. Since the gratings are not optimized and couple only the TE polarization, while the light source is unpolarized, the total fiber-to-fiber insertion loss is found to be about ~30dB. Fig. 5.8 shows the Drop output of a conventional 1R2B with 2-µm long race-track and a radius of 15µm also fabricated on the same wafer. The Drop spectra for the 1R2B can be curve-fitted with the analytical formula $D = a\kappa^4/(1-2ar^2\cos\delta + a^2r^4)$, to give an independent derivation of a, where a is the round-trip amplitude factor $a = \exp(-\alpha L_c/2)$, α is the loss coefficient, δ is the round-trip phase (or normalized frequency) and $r^2 = 1-\kappa^2$ is the self-coupling factor. So far, the best fit value for a thus obtained is ~ 0.96.

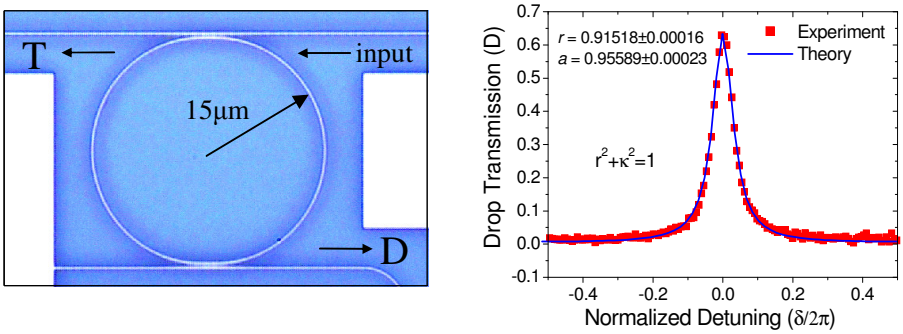

Fig. 5.8. Left: The fabricated 1R2B with racetrack DC of 2 µm and radius of 15µm. Right: The experimental (with marker) and the theoretical fit (in solid line) of the 1R2B Drop (D) transmission.

Based on pure scattering loss of ~3dB/cm, we estimate a roundtrip transmission factor a ~ 0.9966, which implies that ~3.7% (for a ~ 0.96) of the internal field is lost by other mechanisms such as substrate leakage and coupling loss due to mode mismatch between straight and bent sections in a racetrack resonator, assuming negligible intrinsic bending loss for 15µm ring radius using high-contrast waveguides [16]. Nevertheless, the performance of the resonator is still good enough for most practical applications. For the NRMZI, four devices were investigated: The first device (DUT 01) has a measured DC length of 17.58µm giving a relatively large calculated κ value of 0.89. The other three devices (DUT 02 to 04) consist of a point-coupled NRR with very small κ, with varying length of the outer loop corresponding to the nominal values of v = 1, 1.5 and 2.5 respectively. Fig. 5.9 gives the measured bar transmission spectra for these 4 devices, along with the theoretical fits that show good agreement with the data. The fit parameters are summarized in Table 5.1.

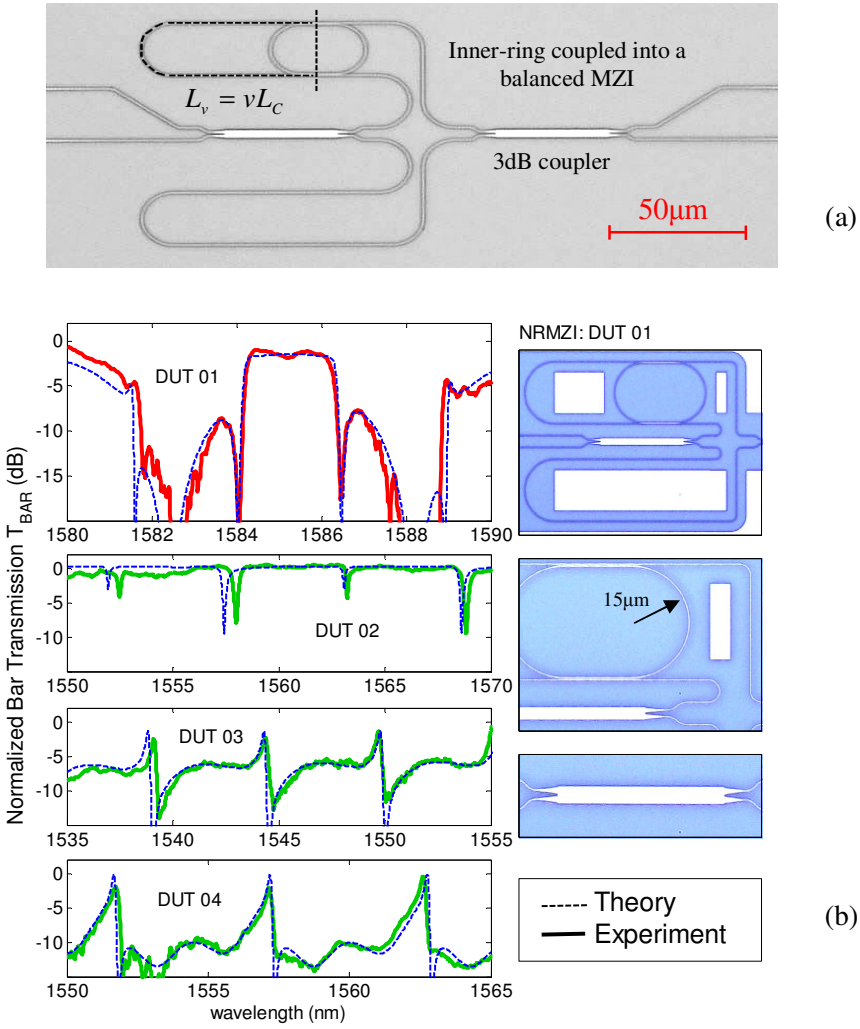

Fig. 5.9. The experimental results (solid lines) and theoretical fit (dashed lines) for the fabricated DUT 01 to 04. The right schematics show various parts of the fabricated DUT 01. The fitting parameters are shown in Table. 5.1.

Theoretical expressions for the spectra depend primarily on the parameters a, κ and γ, where γ is the ratio between the lengths of the lower and the upper bare-MZI arms, i.e., $\gamma = 1$ for balanced MZI arms. Therefore, $\Delta\gamma = \gamma - 1$ represents an imbalance between the two MZI arms and is equivalent to a phase offset in the lower arm $\Delta\varphi_{offset}$. As expected from theory, DUT 01 which has a relatively large κ exhibits the double Fano resonance feature, giving a fairly flat-top response (~2nm bandwidth) and a sharp band roll-off (~7.5dB extinction ratio between the flat-top and the sidelobes). The best fit with theory is given by $a = 0.97$ which is close to that given independently by Fig. 5.8, and by $\Delta\gamma \sim 3\times10^{-5}$ which is equivalent to a phase offset of $\Delta\varphi_{offset} \sim 0.0284\pi$. A combination of design and fabrication errors resulted in the value $v = 1.2287$, a significant deviation from the nominal integer or half-integer value, which partly accounts for the non-periodicity and asymmetry in the transmission spectrum.

DUT	Radius	DC length	κ	a	v	L_C	L_v	$\Delta\gamma = \gamma - 1$	$\Delta\varphi_{offset} \approx v\Delta\gamma\delta_0$	n_g
01	15	17.58	0.89	0.97	1.2287	129.44	159	$+3\times10^{-5}$	$+0.0284\pi$	4.6062
02	15	0	0.24	0.95	1.0006	94.3	94.3	-2×10^{-3}	-1.1260π	4.6275
03	15	0	0.24	0.98	1.5006	94.3	141.5	-2×10^{-3}	-1.6866π	4.621
04	15	0	0.15	0.95	2.4991	94.3	235.6	$+4\times10^{-5}$	$+0.00564\pi$	4.6428

Table. 5.1. The fit parameters for DUT 01 to 04: The isolated waveguide widths, DC widths, DC gaps are 490, 475, 130nm (01); 498, 484, 119nm (02, 03); 483, 468, 140nm (04) respectively. The values of v are measured. The $\Delta\varphi_{offset}$ is calculated around $\lambda_0 \approx 1.55\mu m$ with group index of $n_g \sim 4.6$ [16]. All length units are in μm.

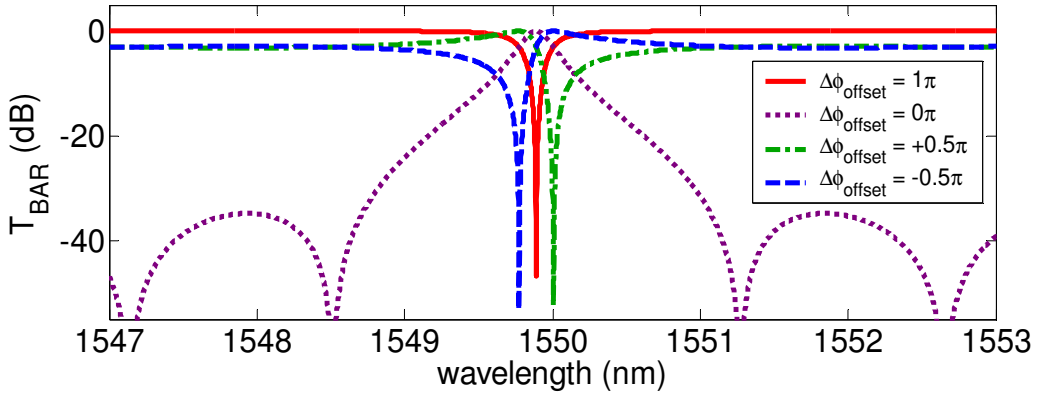

Fig. 5.10. The ideal theoretical plot of the bar transmission of the NRMZI $T_{BAR} = \sin^2([\varphi_{NRR}-(v\delta+\Delta\varphi_{offset})]/2)$ for the case of $v = 1.5$ (DUT 03) with various effective phase biases at the lower MZI arm, assuming lossless case.

For the other three cases using point couplers where κ is very small, the inner-loop of the NRR dominates, yet the output spectra can vary widely due to the random MZI arm imbalance. Similar to the case of microring-enhanced MZI (REMZI), and as illustrated in Fig. 5.10, the bar transmission of the NRMZI can manifest 3 different signatures depending on the phase offset in the lower arm ($\Delta\varphi_{offset}$). The output is: (1) similar to the Drop output of the 1R2B (in the linear scale) when $\Delta\varphi_{offset} \sim 0$, as in DUT 04, (2) similar to the Through output of the 1R2B when $\Delta\varphi_{offset} \sim \pm\pi$ as in DUT 02, and (3) exhibits asymmetric Fano-resonance when $\Delta\varphi_{offset} \sim \pm0.5\pi$, as in DUT 03. Similar spectral features have also been reported experimentally in [6, 7, 185]. The source of $\Delta\varphi_{offset}$ is due to fabrication variance and intrinsic phase imbalance. Even in perfectly fabricated MZI, the optical path in the upper MZI arm is bound to deviate slightly from that in the lower arm due to the perturbation of the microring in the upper arm, inducing a slight phase offset between the two MZI arms.

5.6. Conclusion

For the first time, we have demonstrated NRMZI based on the SOI platform using CMOS based process, and obtained good agreement between theory and experiment. The devices have two possible modes of operations depending on the ring-bus coupling coefficient κ: (1) When κ is small, the inner-loop resonance dominates leading to Drop-like, Through-like, or asymmetric Fano- resonance output, depending on the offset phase arising from the MZI arm imbalance; (2) when κ is relatively large, the outer loop resonance dominates giving rise to double Fano resonances and a box-like transmission profile with sharp roll-off. For the small-κ case, the microring has a higher Q, hence the device tends to be more sensitive to slight MZI arm imbalance as compared to the device with larger κ (lower Q). This sensitivity to offset phase implies that it may be desirable to have active bias control at the lower MZI arm (or in the NRR) in order to balance the MZI for better performance, or to tune the imbalance to achieve a variable output profile.

Chapter 6

Two-ring Mach-Zehnder interferometer

6.1. Introduction

Micro-ring resonators (RR) are flexible building blocks in photonic integrated circuits for realizing various optical functionalities such as filters, sensors, modulators, and switches. Of particular interest for sensing and switching applications is the microring-based Mach-Zehnder interferometer (MZI) structure where a single-ring is coupled to one arm of the MZI (1RMZI) to give a resonant enhancement of the phase shift in that arm [6]. Recently, the two-ring configuration was proposed by Landobasa in single-bus (2R1B) [15] and double-bus (2R2B) [76] excitation. These structures consist of two mutually coupled rings of possibly different sizes, where only one ring, referred to as the inner-ring, is coupled to the bus(es), as shown in the inset of Fig. 6.1(b) A significant resonance narrowing is predicted and observed when the size of the outer ring is twice that of the inner ring (i.e., $\gamma = 2$), which implies that the outer-ring resonance coincides with the inner-ring anti-resonance (refer to the narrow resonance in Fig. 6.1(c) at $\delta_1 = \pi$). In such case, the two-ring system can effectively localize the light strongly inside the outer-ring, giving rise to a sharp resonance with finesse limited only by the intrinsic and coupling losses.

In the two-bus case the finesse is lower compared to the one-bus because the coupling loss is twice as large, but it has the advantage of having two complementary outputs - Through (T) and Drop (D), and hence is useful as an add-drop filter. The Drop spectrum of the 2R2B structure over one full spectral range is shown in Fig. 6.1(c), where δ_1 is the inner-ring round-trip phase. Note that the sharp narrow resonance at $\delta_1 = \pi$ (anti-resonance in inner-ring) corresponds to the strong resonance in the outer-ring, while the broad split resonance at $\delta_1 = 2\pi$ occurs when both rings are resonant. The narrow resonance arises because of the 2π resonant phase response from the outer-ring which leads to rapid successive destructive and constructive interference.

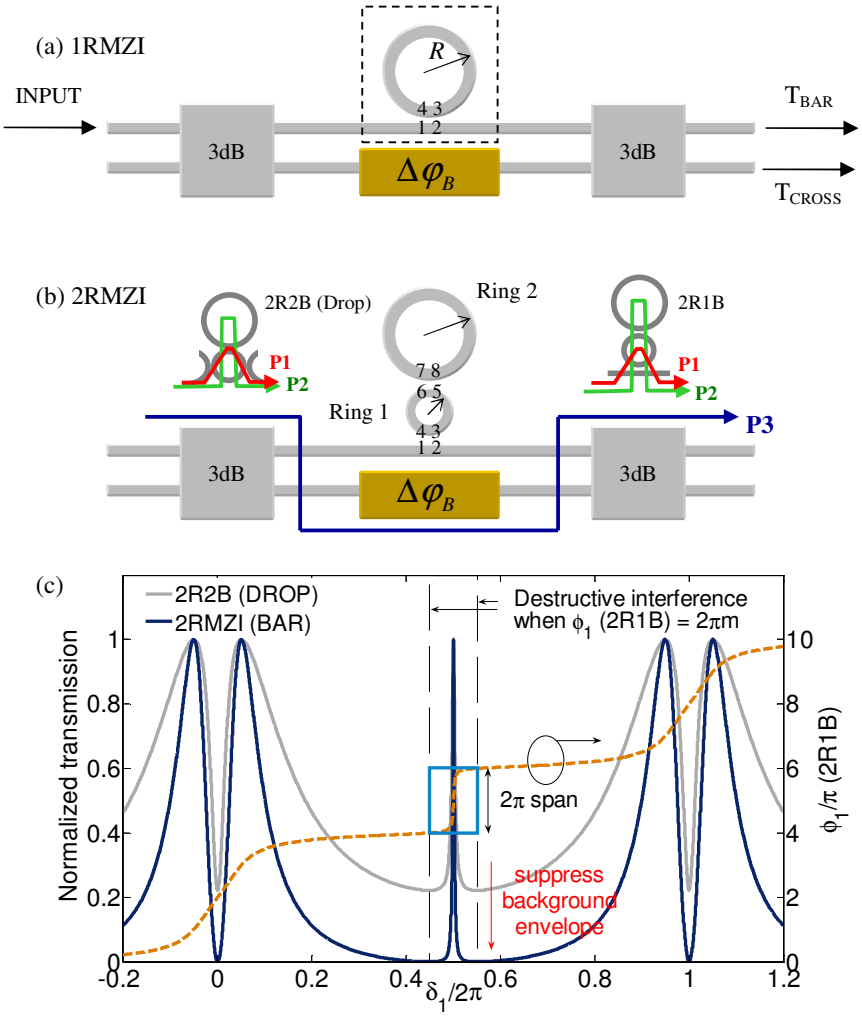

Fig. 6.1(a) The conventional 1RMZI configuration. (b) The 2RMZI configuration. The inset shows the 2R1B structure and the two possible optical pathways P1 and P2. The MZI provides additional optical pathway P3 for destructive interference with P1 and P2 at $\varphi_1=2\pi m$. (c) The transmission of 2R2B (Drop) (faded line) showing poor logic "0", the 2RMZI (bar) (solid line), and the phase response φ_1 of 2R1B (dashed line–right axis). Simulated parameters: r_1~0.6, r_2~0.9, assuming lossless case and balanced MZI for the 2RMZI.

However, the destructive interference is not complete, resulting in an off-resonant dip that does not go to zero. This background envelope limits the application of such narrow resonances, e.g., for switching, modulation, or sensing. For such applications, the important figures of merit are the finesse and the modulation depth (MD) or the contrast ratio (CR). The latter, MD (CR) is given by the difference (ratio) between the on-resonance and off-resonance transmission values, and is reduced by the background envelope.

To alleviate this problem, we propose to excite the 2R1B with a Mach-Zehnder interferometer (MZI), as shown in Fig. 6.1(b). This will have three advantages: (1) The double-bus excitation is converted into single-bus excitation, giving improved light localization inside the two-ring system. (2) The output is similar to 2R2B as the MZI has both complementary cross and bar outputs. In a balanced MZI, the bar (cross) port is similar to the Drop (add) port of the 2R2B. (3) The additional pathway through the MZI, shown as P3 in Fig. 6.1(b), together with the two possible pathways P1 and P2 through the 2R1B structure, allows a more complete destructive interference off the anti-resonance of ring 1 thereby giving improved contrast ratio, MD and finesse for the narrow resonance. This is borne out by the simulated spectrum for a balanced, lossless 2RMZI as shown in Fig. 6.1(c), where the backgrounds envelope has been significantly suppressed. It is interesting to note that the narrow resonance here resembles to the one reported in the literature [70-74]. Similar background envelope can also be found in other ring-based MZI [11], which consequently highlight the superiority of our proposed 2RMZI over the other ring-based MZI devices reported in the literature.

More generally, however, the MZI itself may not be balanced due to fabrication variations and the presence of rings near one arm [186]. This intrinsic asymmetry may be represented by a phase bias ($\Delta\varphi_B$) in the other arm. The 2RMZI outputs are then given by,

$$T_{BAR} = \left|[t_1 - \exp(i\Delta\varphi_B)]/2\right|^2, \qquad T_{CROSS} = \left|i[t_1 + \exp(i\Delta\varphi_B)]/2\right|^2 \tag{6.1}$$

where t_1 is the complex transmission amplitude of the two-ring structure given in [the phase of t_1 is shown in Fig 6.1(b)], which depend primarily on the round-trip loss in the rings, the reflectivity between the bus and ring 1 (r_1) and that between ring 1 and ring 2 (r_2). In the presence of $\Delta\varphi_B$ the output spectra are asymmetric and the narrow resonances look like Fano resonances [34].

In section 6.2, we first discuss the theory of 2R1B. In section 6.3 we present the experimental results of the 2R1B and 2RMZI devices. The conclusion is presented in section 6.3. Still very closely related with this chapter, we present in Chapter 7, the idea of bistability engineering for ring-coupled MZI devices, highlighting the flexibility of MZI in tuning symmetricity of the Fano resonance of the ring-coupled MZI devices. A rigorous performance comparison is presented between the 1R- and 2RMZI devices.

6.2. The basic theory of 2R1B

Fig. 6.1(a) and (b) show the schematics of 1RMZI and 2RMZI respectively. The 2RMZI makes use of the 2R1B structure consisting of two mutually coupled rings labeled 1 and 2. The 2RMZI has previously been proposed by V. Van in the context of linearized transmission [68], in which the two rings are identical. In our case, the design is different as the two rings need not be identical and, indeed, the ratio of their round-trip lengths is an important performance parameter and is denoted by $\gamma = \delta_2/\delta_1$, where δ_j is the round-trip phase of ring *j*. The 2R1B is essentially a 1R1B "loaded" with a second ring, hence the transmittance is expected to be similar to that of 1R1B and is expressed as,

$$t_1 = |t_1| \angle \varphi_1 = \frac{r_1 - a_1 t_{21} \exp(i\delta_1)}{1 - r_1 a_1 t_{21} \exp(i\delta_1)},\ t_{21} = \frac{r_2 - a_2 \exp(i\delta_2)}{1 - r_2 a_2 \exp(i\delta_2)} \tag{6.2}$$

where r_1 is the reflectivity between the bus and ring 1 and r_2 is that between ring 1 and ring 2; $a_j = \exp(-\alpha L_{cj}/2)$ is the round-trip amplitude transmission factor which represents the loss (where α is the power loss coefficient), $\delta_j = \omega n_{eff} L_{cj}/c$ is the round-trip phase, L_{cj} is the round-trip length in ring *j* and n_{eff} is the waveguide effective index. It can be seen from Eq. (6.2) that the resonance of ring 2 (as incorporated in the loading factor t_{21}) is embedded in the resonance of ring 1. This resonance-within-resonance is what gives rise to the resonance narrowing. The transmission may be reduced to that of an effective 1R1B:

$$T = |t_1|^2 = \left| [r_1 - \tilde{a}_1 \exp(i\tilde{\delta}_1)] / [1 - r_1 \tilde{a}_1 \exp(i\tilde{\delta}_1)] \right|^2 \tag{6.3}$$

where $\tilde{a}_1 = a_1 |t_{21}|$ is the effective loss experienced in ring 1 and $\tilde{\delta}_1$ is the modified *linear* round trip phase,

$$\tilde{\delta}_1 = \delta_1 - \left[\tan^{-1}\left(\frac{a_2 \sin\delta_2}{r_2 - a_2 \cos\delta_2} \right) - \tan^{-1}\left(\frac{r_2 a_2 \sin\delta_2}{1 - r_2 a_2 \cos\delta_2} \right) \right] \tag{6.4}$$

which is the phase difference between the two pathways depicted in the inset of Fig. 6.1(b). The first term (δ_1) corresponds to the pathway P1 whereas the bracketed term is the phase response from ring 2 corresponding to the pathway P2. The interference of the two pathways determines the features of the transmission spectra of the 2R1B. The transmission is minimum when $\tilde{\delta}_1 = 0$ or even multiples of π. Some examples are shown in Fig. 6.2 for γ values between 1 and 2, assuming $a_1 = 0.96$, $r_1 = 0.8$, and $r = 0.92$. These are typical values for easily realizable ring resonators. When the rings are identical, the resonance splitting is symmetrical. As γ deviates from 1 the resonance is split asymmetrically into a broad and a narrow resonance. The broad resonance is associated with ring 1 and the narrow resonance with ring 2. This is because ring 2 is isolated from the waveguide bus, hence the light needs to resonate in ring 1 before exiting the structure, and so the overall cavity lifetime is longer

corresponding to a narrower linewidth. For the same reason, the transmission at the narrow resonance is inevitably lower.

In general, as γ increases the separation between the split resonances increases, and the linewidth of the narrow resonance decreases and become more symmetrical. When $\gamma = 2$, there are three resonances. The broad resonance associated with ring 1 is symmetrically split around $\delta_1 = 2m\pi$ in a way similar to the case $\gamma = 1$. The third, narrow resonance is located at an odd value of δ_1/π (and even value of δ_2/π) and thus is centered exactly between two adjacent broad resonances and the lineshape is symmetrical. In this case, ring 1 is said to be "anti-resonant" while ring 2 is resonant, hence light is trapped more strongly in ring 2, giving rise to the narrowest linewidth.

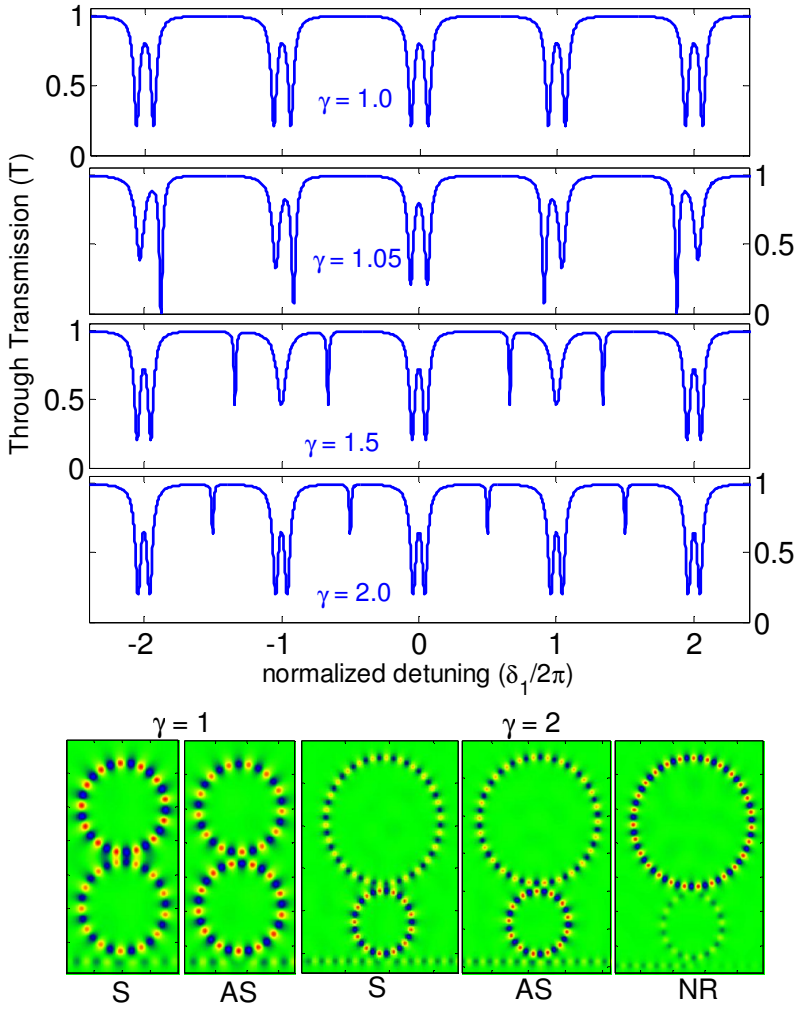

Fig. 6.2. Top: The Through transmission T for different values of γ. The loss is set to 0.96, the coupling coefficients are $r = 0.92$ and $r_1 = 0.8$. Bottom: The field distribution for $\gamma = 1$ and $\gamma = 2$ as calculated using FDTD. Note that the two symmetric resonances have a symmetric (S) and an anti-symmetric (AS) transverse field profile at the coupling point. The NR stands for near critical coupling corresponding to the narrow resonance for $\gamma = 2$ [15].

The factor by which the linewidth is reduced compared to that of the single-ring configuration is proportional to the intensity buildup factor in ring 2 relative to the intensity in ring 1, which is given by $B_{21} = (1-r_2^2)/(1-a_2 r_2)^2$. It can be shown that $\bar{B}_{21}$ is the maximum slope of the phase perturbation $\delta_{load} = \arg(t_{21})$ which is given in Eq. (6.2). This finesse enhancement factor can be quite large if the rings have very low loss and low coupling coefficient (high r). At such narrow resonance (dip) there is a very abrupt 2π phase jump which, in a MZI, gives rise to a very sharp peak in the bar transmission as shown in Fig. 6.3. The peak transmission and the finesse, however, are both very sensitive to and are quickly degraded by loss. Fortunately, even lower loss corresponding to a = 0.999 (α = 1.4 dB/cm) is quite feasible as has been demonstrated recently for a number of material systems [3, 58]. As long as the loss is small, the two-ring structure can achieve a given finesse with much smaller r_1 and r_2 values while a one-ring structure will require a much higher r to achieve the same finesse. In the following simulations we have assumed $a \sim 0.999$.

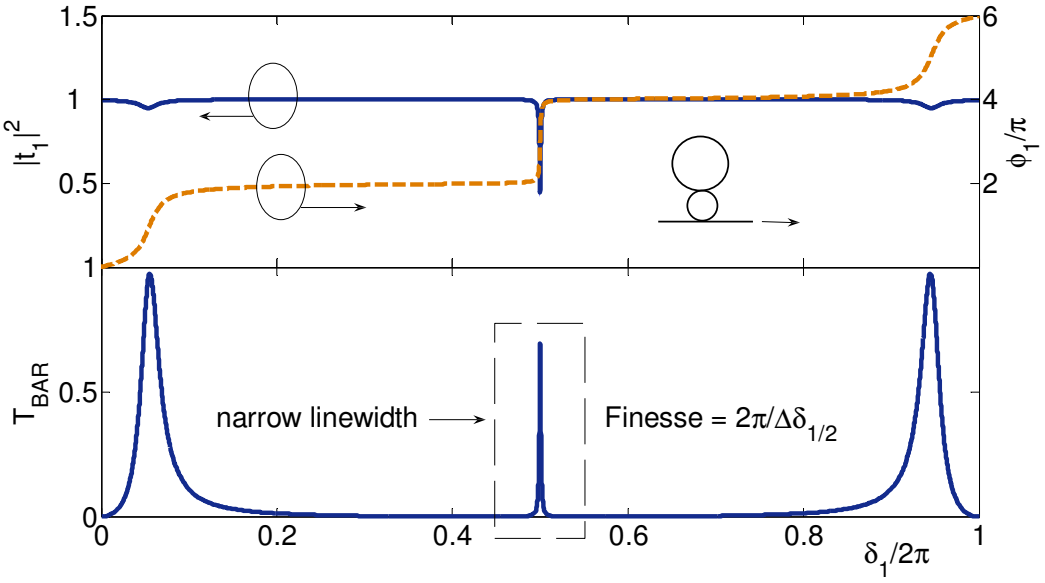

Fig. 6.3. Upper: The ring transmission $T = |t_1|^2$ (left axis) and the phase response (right axis). Lower: The bar transmission of 2RMZI (r_1 = 0.85, r_2 = 0.88 and a = 0.999).

Similar to the one-ring case, the critical coupling condition of 2R1B occurs when the transmittance (Eq. 6.2) is zero, i.e., $r_1 = a_1 t_{21} \exp(i\delta_1)$. In the case of $\gamma = 2$, where the resonance occurs when δ_1/π is an odd integer and δ_2/π even, the critical coupling condition is given by $r_1 = a_1 t_{21}(0) = 0$, which, for a given round-trip loss (a_1), corresponds to the set of (r_1,r_2) given by $r_1 = a_1(a_2 - r_2)/(1-a_2 r_2)$. These sets of ($r_1$, r_2) should be avoided for proper operation of the 2RMZI switch. With this proviso, the two-ring configuration with $\gamma \sim 2$ will have the sharpest resonance and hence will be used to engineer the lowest switching threshold as a switch.

6.3. Device measurement and characterization

In this section, we shall present the characterization of the fabricated 2R1B and 2RMZI based on the SOI platform. The devices are presented in this section was fabricated in CEA LETI, France. The fabrication and the measurement procedures are performed the same way as the previous 1R2B case in Chapter 2. Below is the list of the variation parameters associated with the 2R1B device under tests (DUTs).

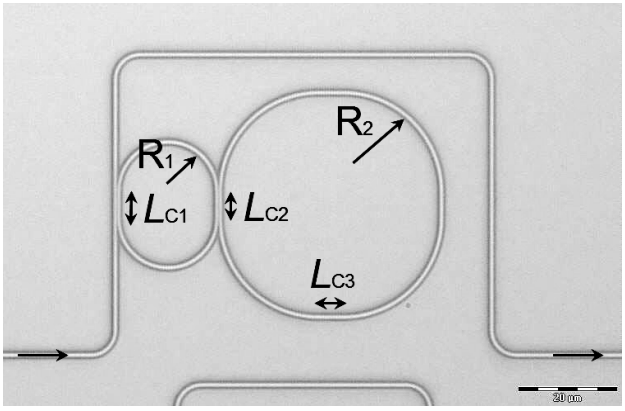

Fig. 6.4. The fabricated 2R1B based on SOI platform. The waveguide width is ~450nm and the gap separation is ~200nm. The silicon thickness is ~196nm and the oxide thickness is 2µm.

DUT #	γ (fit)	R_1	R_2	L_{C1}	r_1 (fit)	L_{C2}	r_2 (fit)	L_{C3}	n_g (fit)	a (fit)
1	0.9997	5	5	0	0.97	0	0.97	0	4.318	0.9965
2	0.9999	10	10	0	0.95	0	0.95	0	4.2887	0.995
3	0.9999	15	15	0	0.9	0	0.9	0	4.2812	0.994
4	0.9998	20	20	0	0.88	0	0.88	0	4.2788	0.993
5	1.0006	10	10	8.5	0.62	3	0.90	5.5	4.286	0.992
6	1.0007	10	10	8.5	0.62	5.5	0.79	3	4.285	0.992
7	1.0008	10	10	8.5	0.62	8.5	0.62	0	4.2833	0.993
8	2.0000	10	20	5.5	0.79	5.5	0.79	5.5	4.274	0.994
9	2.0020	10	20	5.5	0.79	4	0.86	7	4.2742	0.992
10	2.0020	10	20	5.5	0.79	3	0.90	8	4.2746	0.993
11	1.0012	5	5	8.5	0.62	3	0.90	5.5	4.2685	0.989
12	1.0012	5	5	8.5	0.62	5.5	0.79	3	4.2675	0.988
13	1.0016	5	5	8.5	0.62	8.5	0.62	0	4.267	0.99
14	2.0004	5	10	5.5	0.79	3	0.90	8	4.286	0.99
15	2.0008	5	10	5.5	0.79	2	0.93	9	4.2847	0.991
16	2.0008	5	10	5.5	0.79	1	0.96	10	4.2848	0.992
							Average:		**4.279**	**0.992**

Table. 6.1. The 2R1B-DUTs. The DUT 01 to 04 is based on the point coupler whereas DUT 05 to 16 is based on racetrack coupler. The estimated fit parameter (r) is based on the 1R2B structures around ~1520nm.

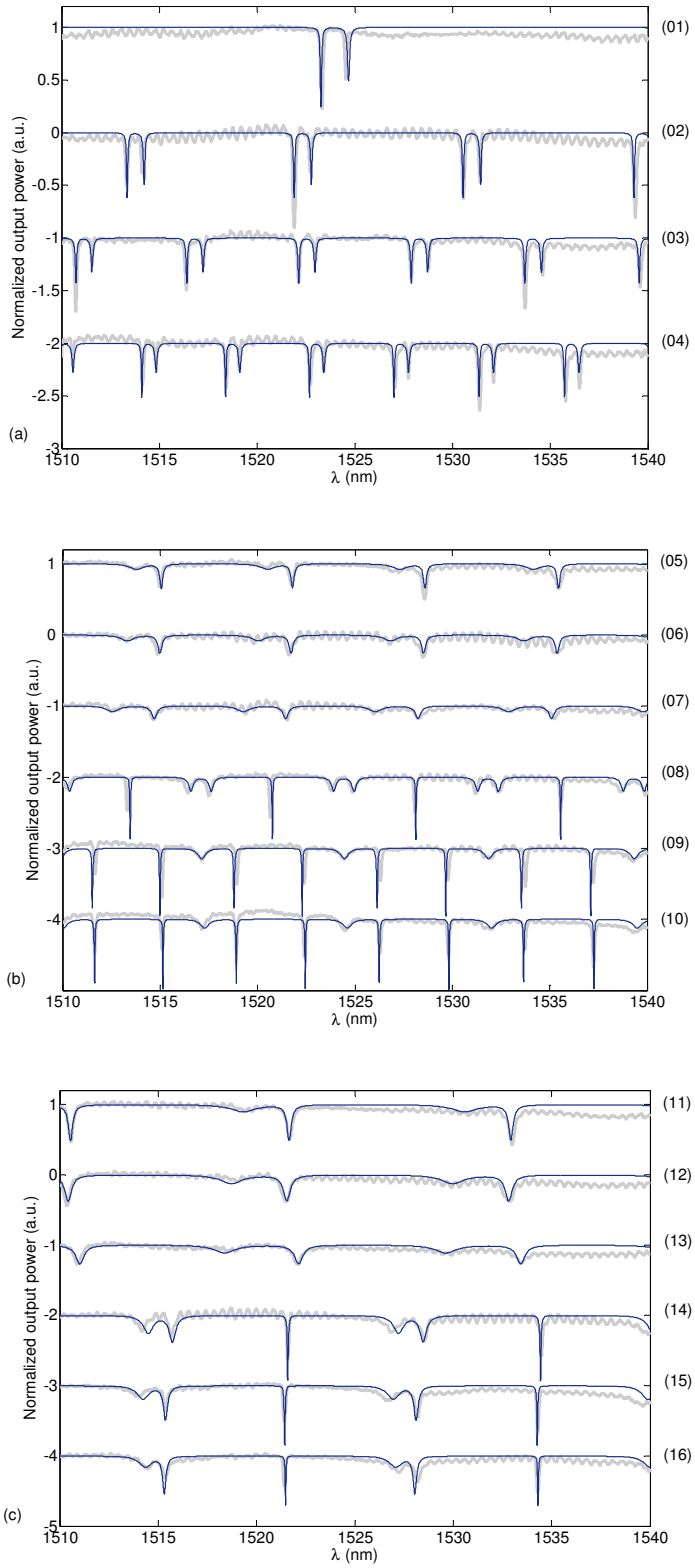

Fig. 6.5. The measured output spectra of 2R1B: (a) DUT 01 to 04, (b) DUT 05 to 10, (c) DUT 11 to 16. The dark line represents the theoretical fit, the fade-bold lines represents the experimental results.

The (r) values are estimated using the previous linear regression applied (around ~1520nm) for the 1R2B in Chapter 2 [i.e., $r \sim \cos(\pi(L_C + L_0)/(2L_\pi))$] where L_π and L_0 of 19.17 µm and 2.4767µm has been used respectively. The a value is deduced by matching the maximum Drop output (D_{MAX}) of the 1R2B [186]. By taking account of: (1) The wavelength dependence of (r), (2) slight fabrication variation in the (γ) values and (3) using a group index around ~ 4.28 based on the free spectral range (FSR) of the periodic spectra, we can always obtain a reasonable fit between the theory and the experiment, consistently. Fig. 6.5 shows the measured transmission and the theoretical fit applied in various wavelength spectra, for the 2R1B listed in Table 6.1. The overall trend is also consistent with the simulated results highlighted in Fig. 6.2. The uneven (slightly skewed) splitting in all of the broad resonances is caused by the slight deviation in the fabricated γ values (refer to Table. 6.1).

Next, we present the experimental results for the case of the 2RMZI device. Here, we are interested with 2RMZI with $\gamma = 2$, since this corresponds to the case where the overall finesse is maximized for a given (r) and (a) values. The fitting parameters are summarized in Table. 6.2.

DUT #	γ (fit)	R_1	R_2	L_{C1}	r_1 (fit)	L_{C2}	r_2 (fit)	L_{C3}	n_g (fit)	a (fit)	$\Delta\varphi_B$ (fit)
1	2.000	5	10.00	4	0.86	3	0.90	5	4.2984	0.995	0.58π
2	2.001	5	10.01	6	0.77	3	0.90	9	4.272	0.995	0.65π
3	2.000	5	10.00	8	0.65	3	0.90	13	4.253	0.995	0.61π

Table. 6.2. The 2RMZI-DUTs. The fit parameters are obtained based on the 1R2B structures, approximated around ~1520nm. Note that γ is the ratio between the circumference of the outer-ring (ring 2) and that of the inner-ring (ring 1).

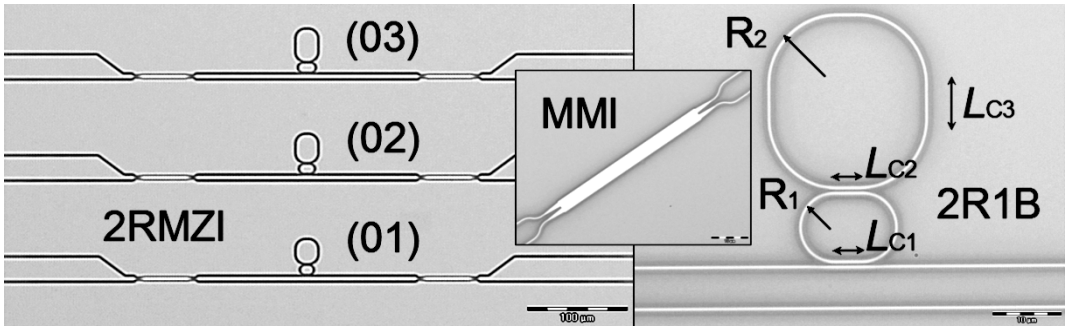

(a)

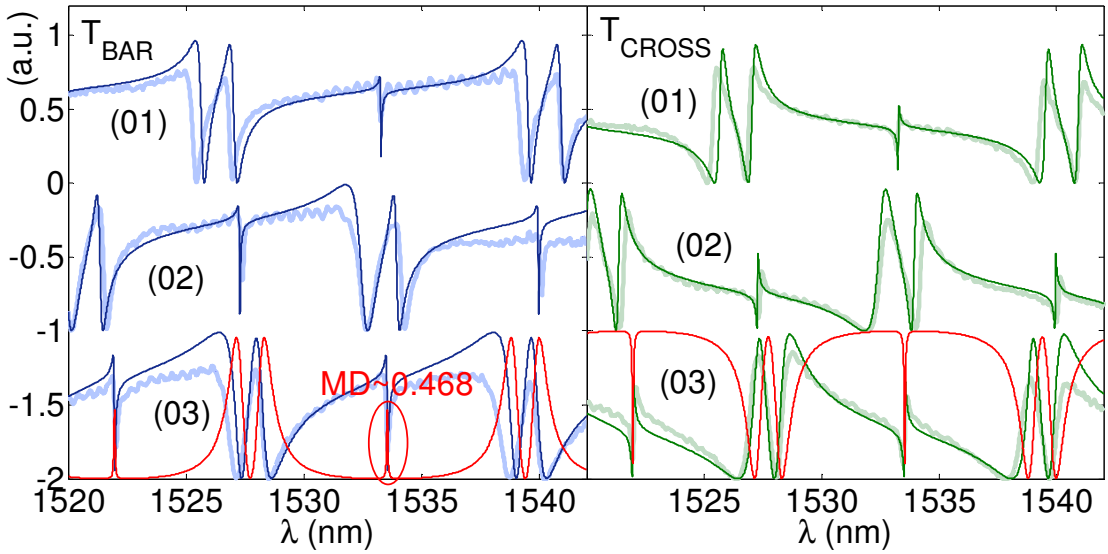

(b)

Fig. 6.6(a) The fabricated 2RMZI based on SOI. (b) The measured spectra of 2RMZI bar (in blue) and cross output (in green) for DUT 01 to 03. The faint bold curves are the experimental results, and the solid curves are the theoretical fit. The red curves represent the theoretical case if the bare-MZI is balanced ($\Delta\varphi_B = 0$). The loss factor is measured as $a_1 \sim 0.995$.

Fig. 6.6(a) shows the fabricated 2RMZI and (b) shows the measured bar and cross transmission spectra of the 2RMZI devices. The fabricated value of γ for all the devices is close to 2, the condition that gives the maximum finesse for the narrow resonance, which lies in the middle between the two broad resonances. Unfortunately, all the devices exhibit a substantial phase imbalance $\Delta\varphi_B$ between the two MZI arms, thus the narrow resonances resemble the asymmetric Fano resonances rather than the symmetric Lorentzian resonances. Such imbalances are to be expected and difficult to control by fabrication [186]. Good theoretical fits is obtained, as shown by the solid curves, can be obtained using the parameter values summarized in Table 1.

Based on the good theoretical fit, we can use the best-fit parameter values to project with some confidence the spectra of the ideal case when the MZI is balanced ($\Delta\varphi_B = 0$), and then compare its performance relative to the 2R2B and 1RMZI structures. Theoretical predictions of the bar output of a balanced MZI ($\Delta\varphi_B = 0$), for the three cases of r_1, while keeping $r_2 \sim 0.9$ and $a_1 \sim 0.995$, are shown in Fig. 6.7. The three curves show the dependence of the narrow resonance on r_1. The finesse and MD values for the three cases are summarized in the contour plot of Fig. 6.8(a), which gives the loci of finesse and MD as a function of r_1 and a_1. Similar projections are carried out for 2R2B and 1RMZI, and the finesse of their narrow resonances compared with the 2RMZI device. The relative finesse enhancements of 2RMZI over 2R2B and 1RMZI are shown in Fig. 6.8(b) as a function of r_1.

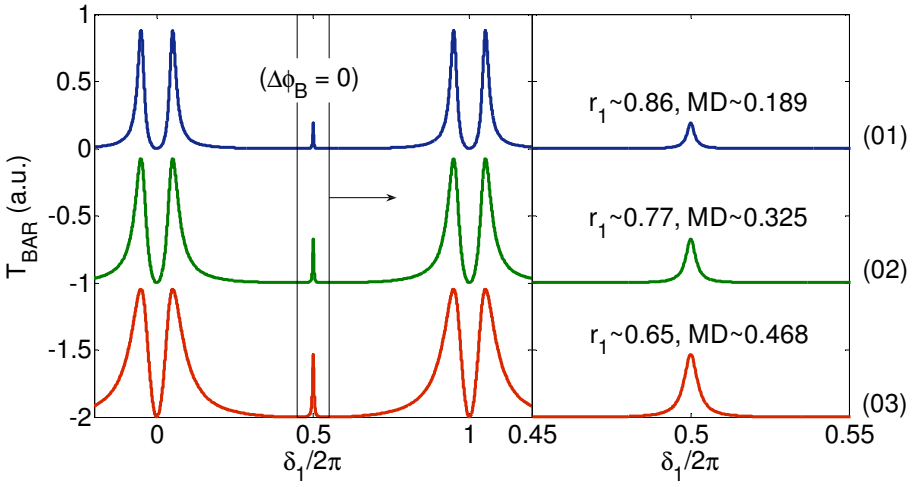

Fig. 6.7. The bar transmission of 2RMZI using the same parameters as the fabricated DUT 01, 02, and 03 (Table 1), assuming balanced MZI ($\Delta\varphi_B = 0$).

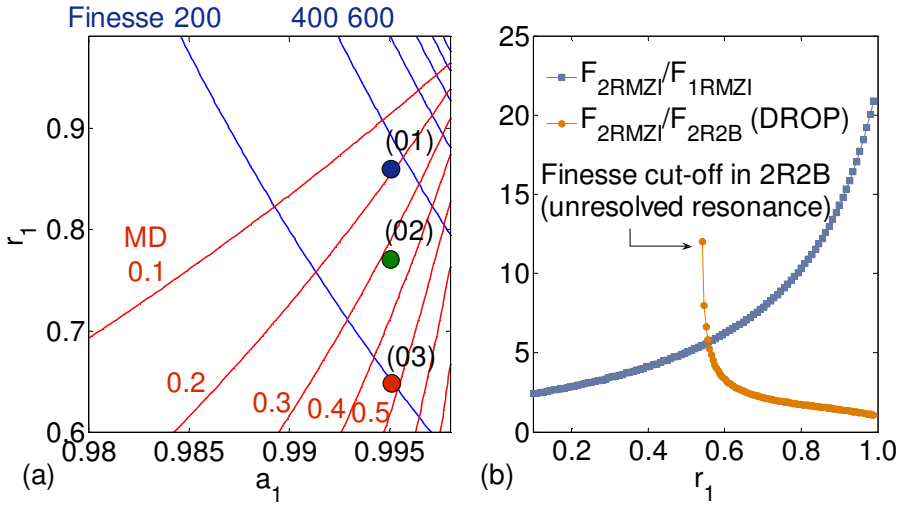

Fig.6.8(a) The Finesse (blue)-MD (red) contour plot on which the projected values for the three balanced 2RMZI devices with different r_1 values (given in Table 1) are indicated by three circles labeled 1, 2, and 3. (b) The finesse enhancement of 2RMZI relative to the 2R2B and 1RMZI counterparts. In the case of 1RMZI, the r value is assumed to be 0.9. For the 2RMZI and 2R2B, r_2 ~ 0.9 and a_1 ~ 0.995 are assumed.

Based on these projections for the three values of r_1 that best fit the experiment data, the performance of the 3 ideal (balanced) 2RMZI devices relative to 2R2B and 1RMZI may be summarized as follows. First, with increasing r_1, the finesse increases while the MD decreases, showing the intrinsic tradeoff between them. For the three cases, r_1 ~ 0.86, 0.77 and 0.65, the corresponding finesse values are ~355, 270, and 199, which give the finesse enhancement factor of ~12.4, 9.5, 7 times relative to the 1RMZI, and of ~1.5, 1.9 and 2.6 times relative to the 2R2B. Note the opposite trends for 1RMZI and 2R2B in their dependence on r_1, as is evident in Fig. 6.8(b).

Compared with 1RMZI, 2RMZI always gives superior finesse. Relative to 2R2B, 2RMZI is superior when r_1 is relatively small. In the high-r_1 regime the finesse of 2R2B is as good as 2RMZI because the light is so well localized inside the two-ring system it becomes insensitive to whether the inner-ring is coupled to one or two buses. In terms of MD, 2RMZI give betters result than 2R2B for the lower r_1 values, where the envelope effect dominates and degrades the MD for 2R2B. In the extreme case the resonance becomes unresolved. On the other hand, for higher r_1 values, the 2RMZI is more sensitive to loss due to higher finesse and the MD can be slightly lower than the 2R2B case. This is a natural occurrence in any high-finesse system. As a guideline, r_1 should be less than ~0.73 for the 2RMZI to have higher MD than the 2R2B (MD ≥ 0.37), in the case where r_2 ~ 0.9 and a ~ 0.995. Based on pure scattering loss of ~2.2dB/cm, we estimate a roundtrip transmission factor a ~ 0.999, which implies that less than 1% (for a ~ 0.995) of the internal field is lost by other mechanism such as substrate leakage and coupling loss due to mode mismatch between straight and bent sections in a racetrack resonator, assuming negligible intrinsic bending loss for 5µm ring radius using high-contrast waveguides [16]. The overall loss performance is better than the one we previously fabricated in IMEC (Chapter 5), due to the fact that thermal oxidation, and thinner waveguide dimension (~196nm silicon core thick) was used in the current batch fabricated in CEA LETI. Lastly, we also characterize the 3dB MMI coupler which is used in the MZI structures. The MZI (without the rings) performs as a cross coupler since it comprises of two 3dB MMI coupler in cascade configuration. To minimize insertion loss, a 5µm length taper is provided at the input and output of the port waveguides. Fig. 6.9 shows the simulation result of a single 3dB MMI coupler. The 3dB length is found to be around ~45µm while other parameters are directly taken from Table. 6.3.

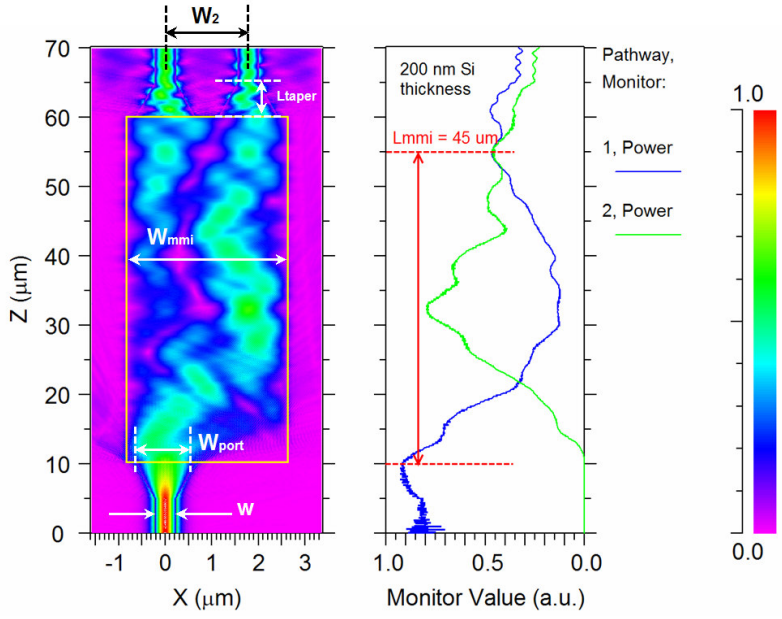

Fig. 6.9. The 3D-Beam Propagation Method (BPM) simulation of 3dB MMI coupler based on 200nm Si thickness with oxide cladding (operating λ = 1550nm).

DUT #	w	W_{port}	W_2	W_{mmi}	L_{mmi}	L_{taper}
01	0.45	1.3	1.78	3.5	43	5
02	0.45	1.3	1.78	3.5	44	5
03	0.45	1.3	1.78	3.5	45	5
04	0.45	1.3	1.78	3.5	46	5
05	0.45	1.3	1.78	3.5	47	5

Table. 6.3. The 3dB MMI coupler-DUTs (all unit lengths are in μm). The DUT 03 is used for all the fabricated 2RMZI structures in this chapter.

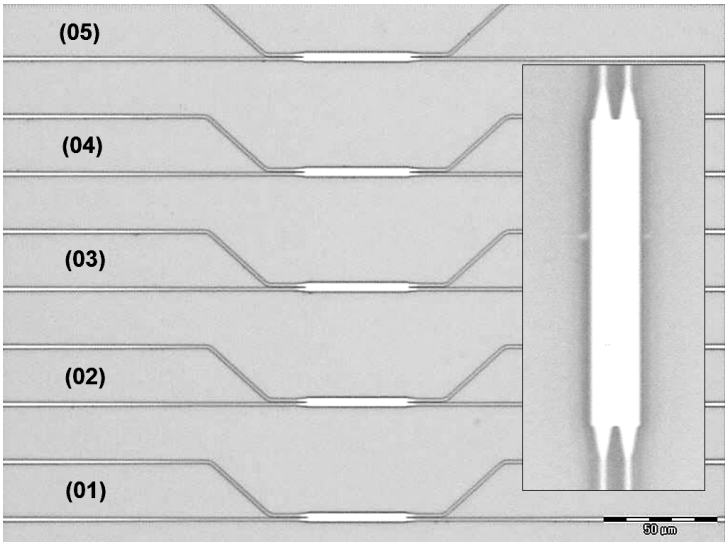

Fig. 6.10. The fabricated 3dB MMI coupler based on SOI.

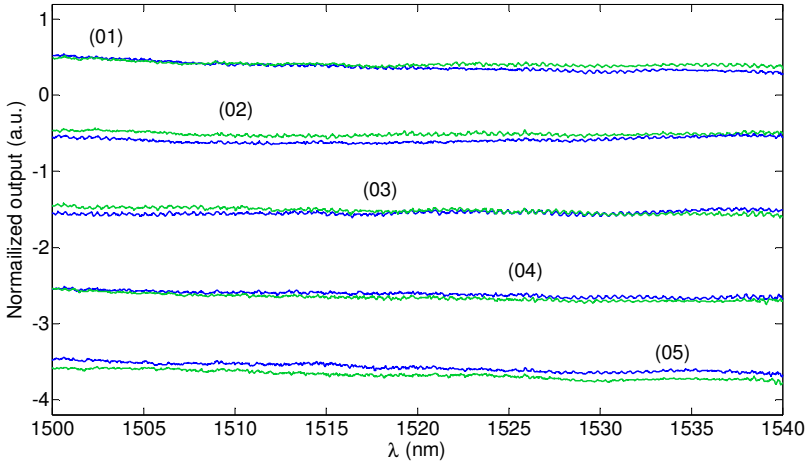

Fig. 6.11. The measured spectra for bar (solid blue) and cross (solid green) 3dB MMI output.

Based on the experimental results shown in Fig. 6.11, we verified that the 3dB MMI coupler works very nicely with the balanced output between the bar and the cross output. We note that among all the devices under tests, the DUT 03 considerably better since the spectra are the most flat throughout the

wavelength region and the bar/cross imbalance is minimized. This is as expected as DUT 03 corresponds to the simulated case in Fig. 6.9. With this in mind, all of the MZI is fabricated based on the DUT 03 parameters. In general, the MMI is wavelength independent within the range of ~40nm which is suitable for our application.

6.4. Conclusion

Firstly, we have proposed and demonstrated the 2RMZI device to remove the unwanted envelope effect in the transmission of 2R2B system [75]. The device is realized on SOI using 193nm CMOS-based deep UV lithography. By taking account of the MZI phase imbalance, good agreement is obtained between theory and experimental spectra. Overall, the 2RMZI offers higher finesse and MD compared with the 1RMZI and 2R2B counterparts. In this work, a projected finesse up to 355 with MD ~0.19 is realistically achievable by the fabricated 2RMZI devices but only if the fabrication-induced imbalance in the MZI is canceled out either by incorporating width variations in one of the MZI arms or by some sort of tuning mechanism (e.g., thermal tuning).

Chapter 7

Bistability engineering for ring-coupled Mach-Zehnder interferometer

7.1. Introduction

Ring resonator (RR) is a great candidate in realizing many useful devices such as modulators, switch, active/passive filter, sensors, and multiplexer, especially since recent fabricated RR have obtained reasonably high Q factor and low loss [3, 58, 187]. Such features are attractive, particularly in all-optical switching when combined with nonlinearity [188]. Bistability and multistability were previously demonstrated in various configurations, i.e. the ring resonator coupled to one or two bus waveguides [77, 189, 190], the ring resonator arrays [191], Bragg gratings [192] and photonic bandgap cavities [193]. A good optical switch is characterized by low input threshold power, high extinction ratio (ER) (i.e. >10 dB), high modulation depth (MD) and reasonable optical bandwidth. In general, the extinction ratio and modulation depth are determined by the shape of the resonance, while the switching power is largely dependent on its sharpness (finesse). Normally, it is difficult to achieve both high ER and large MD for a single-ring with a symmetric resonance. For example, for the first

silicon ring resonator switch using thermal nonlinearity [194], MD ~ 0.9 and ER ~ 10 dB, according to their definitions. Thus, there is a need to search for more optimal switch configurations with significantly better performance. It is important to note that the switching threshold is determined by the finesse of the resonance and not affected by the phase bias on the Mach-Zehnder interferometer (MZI). This delinking simplifies the concurrent optimization of switching threshold, ER and MD, and enables us to develop a complete optimization scheme for both one-ring MZI (1RMZI) and two-ring MZI (2RMZI). Comparing their performance shows that the 2RMZI can achieve switching threshold, orders of magnitude smaller, even with relatively low-finesse rings. However, the MD will be lower because the waveguide loss is amplified in a two-ring system. On the other hand, the 1RMZI is less sensitive to loss and is more suitable if the ring has very high finesse (both low loss and small coupling coefficient).

In section 7.2 we first discuss the bistability characteristic of a one-ring-one-bus (1R1B) configuration using a simple parametric approach [77]. In section 7.3 we introduce the idea of Fano resonance in ring-enhanced MZI which largely affects its switching performance. This work complements and improves on that reported in [34]. Finally, in section 7.4 we present a bistability engineering scheme for 1RMZI and 2RMZI devices and a performance comparison between the two devices in terms of their switching threshold power, ER, MD, and optical bandwidth.

7.2. Optical bistability in 1R1B

Optical bistability arises from a combination of the nonlinearity in light-matter interaction and a feedback mechanism, which can be induced absorptively or dispersively. Absorptive optical bistability normally occurs whenever the input wavelength is close to the atomic resonance of the material. An increase in the input power effectively produces an increase in absorption saturation (i.e., the degree of transparency of the medium). As a result, the cavity build-up increases which, in turn, increases the saturation even more. This is a positive feedback cycle which triggers the switch-up process. When the input power is decreased, the cavity build-up is intense enough to maintain the saturation level, thus, the transmitted power can be kept at the “ON” state. With this, one obtains a hysteresis curve. On the other hand, dispersive optical bistability occurs when the input wavelength is detuned far from the atomic resonance where the material is transparent. At the same time, the frequency of the incident field is tuned near the resonance frequency of the cavity, to give just sufficient offset for optical switching to take place. An increase in the input intensity increases the intensity of the cavity build-up field which changes the optical length of the medium in such a way that the cavity resonance is driven closer to the input frequency, which in turn, increases the internal field intensity even more. As a consequence, one will obtain a positive feedback loop which produces up-switching. When the incident field is decreased, the internal field is intense enough to maintain

resonance between the cavity and the input frequency. And again, another set of hysteresis curve is obtained.

For simplicity, the optical bistability presented in this chapter is based on Kerr effect (i.e., nonlinear refraction), which falls under the category of dispersive optical bistability. In this section, we discuss briefly the optical bistability property of a conventional 1R1B. Using the graphical method, the minimum switching threshold can be derived. We recall the graphical representation of the build up factor in the form of airy function and the linear line, as shown in Fig. 7.1.

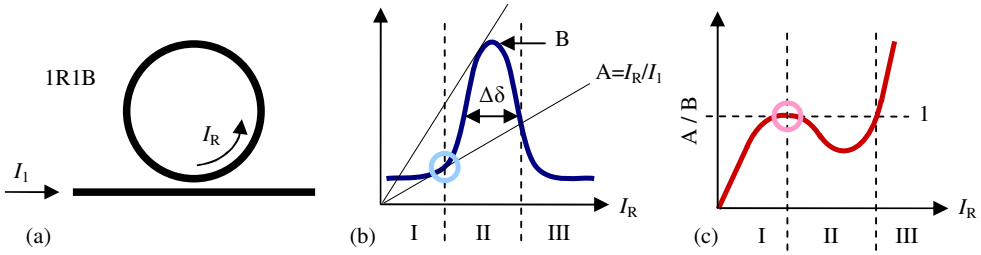

Fig 7.1. (a) The 1R1B configuration with build-up field I_R. (b) shows the graphical representation of the build-up factor B and I_R/I_1. The threshold is obtained by finding the gradient at the intersected tangential point. (c) shows relation of input intensity I_1 with I_R, here the I_1 is represented by A/B from (b).

Note that there are two linear lines tangentially intersect the airy function, these two tangential points signify the upward and downward transition. Since flatter line corresponds to higher input intensity, the tangential intersection associated with it should normally be the ON transition. The steeper line has lower input intensity. Thus that tangential intersection corresponds to the OFF transition. We can find these points by

$$\partial B/\partial I_R = 1/I_1, \qquad B(I_R) = I_R/I_1 \tag{7.1}$$

The condition mentioned in (7.1) is equivalent to finding $\partial I_1/\partial I_R = \partial(B^{-1}I_R)/\partial I_R = 0$ as can be verified from Fig. 7.1. The notion B^{-1} is the inverse build-up factor B where the 'root finding' takes place. Adopting the high finesse approximation (i.e., $\cos\delta \sim 1 - \delta^2$) we may write the B as,

$$B \equiv \frac{I_R}{I_1} = \frac{1-r^2}{1-2ra\cos\delta + r^2a^2} \simeq \frac{(1-r^2)/ar}{\delta^2 + (\Delta\delta^2/2)} \tag{7.2}$$

where $\Delta\delta = 2(1-ar)/\sqrt{ar}$ is the full width half maximum (FWHM). The total round trip phase is defined by $\delta = -\delta_0 + \bar{\gamma}_{NL} I_R$ where δ_0 is the initial detuning and $\bar{\gamma}_{NL} = k_0 n_2 \bar{L}$ is a nonlinear phase factor with characteristic length $\bar{L} = (1-\exp(-\alpha L_C))/\alpha$ with L_C as the cavity length. The extreme points of I_1 is obtained through $\partial(B^{-1}I_R)/\partial I_R = 0$, which yields a quadratic equation,

$$\{3\delta^2 + 2\delta_0\delta + (\Delta\delta^2/2)\} = 0 \tag{7.3}$$

By defining the minimum detuning for bistability as $\Delta\bar{\delta} = \Delta\delta\sqrt{3}/2$ [188], the possible roots of (7.3) are,

$$\delta^{(\uparrow\downarrow)} = -\frac{1}{3}\delta_0 \pm \frac{1}{3}\sqrt{\delta_0^2 - \Delta\bar{\delta}^2}\,; \qquad \bar{\gamma}_{NL} I_1^{(\uparrow\downarrow)} = \frac{2}{3}\delta_0 \pm \frac{1}{3}\sqrt{\delta_0^2 - \Delta\bar{\delta}^2} \tag{7.4}$$

The two possible roots show two possible transitions. They are the upward and the downward transitions as discussed earlier as noted by the $(\uparrow\downarrow)$ arrow in (7.4). Moreover, the existence of bistability is determined by the initial detuning δ. The bistability only occurs at $\delta_0 > \Delta\bar{\delta}$ so that the roots are real number, which verifies the critical detuning condition for bistability, that is $|\delta_0 - \delta_R| \geq \Delta\delta\sqrt{3}/2$. The threshold can be obtained by substituting (7.4) to (7.2). Note that, it is difficult to derive a simple analytical expression for the threshold at arbitrary detuning. However, since the switching threshold will be at its minimum at $\delta_0 \sim \Delta\bar{\delta}$ (where MD & ER is not yet well defined), it is more meaningful to formulate the minimum switching threshold rather than finding it at arbitrary detuning. Hence, the threshold can be further simplified as,

$$\bar{\gamma}_{NL} I_{TH} \sim \frac{8(\Delta\delta/2)^3}{3\sqrt{3}(1-r^2)/(ar)} \tag{7.5}$$

By simplifying (7.5) using (7.2) and (7.4), we can express the minimum switching threshold around the critical detuning as,

$$n_2 I_{TH} = \left(\frac{8}{3\sqrt{3}}\right)\left(\frac{(1-ar)^3}{(1-r^2)\sqrt{ar}}\right)\left(\frac{\ln(a)}{\pi(a^2-1)}\right)\left(\frac{\lambda}{L_C}\right) \tag{7.6}$$

Based on (7.6), we can see that the switching threshold is dependent on loss *a* and is inversely proportional with the normalized cavity length (L_C/λ). Implicitly, it is also inversely related with the cavity build up factor, we can re-express (7.6) according to its respective operating condition,

$$n_2 I_{TH}\big|_{r=a} \sim \left(\frac{8}{3\sqrt{3}}\right)\left(\frac{(1+r)^2 \ln(1/r)}{\pi r B_1}\right)\left(\frac{\lambda}{L_C}\right) \tag{7.7}$$

where $B_1 = (1+r)/(1-r)$ is the maximum build-up factor of 1R1B device [refer to Eq. (2.4)].

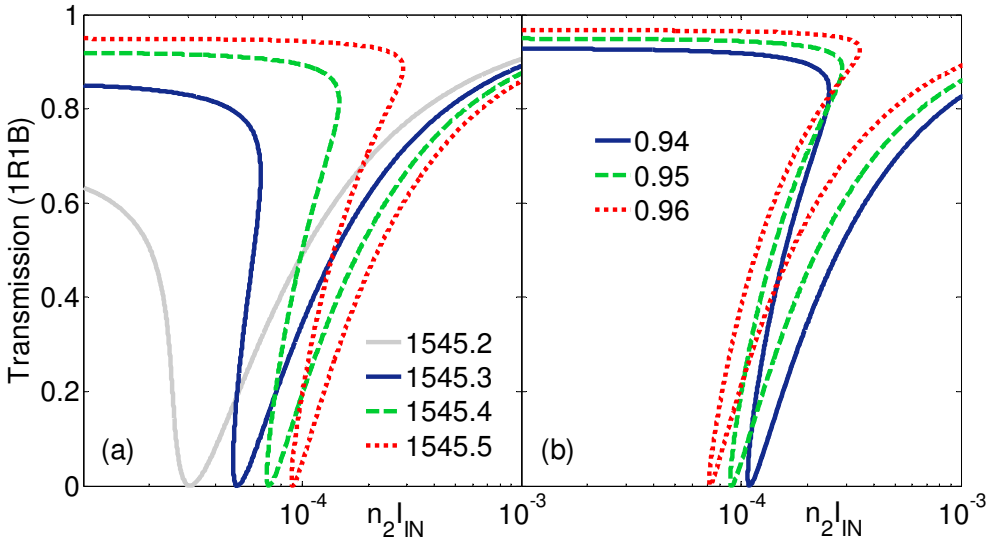

Fig. 7.2. The transmission of 1R1B as a function of incident power for a critically coupled ring for (a) $r = a = 0.95$ for various near-resonant wavelengths, and (b) at a fixed wavelength, $\lambda = 1545.5$ nm, for various losses under the critical coupling condition [144].

Some bistability switching examples are shown in Fig. 7.2(a) for several wavelengths below the resonance (the resonance is around $\lambda \sim 1545$ nm), all under the critical coupling condition ($r = a$). The operating wavelengths are all below the resonance wavelength. Note that the transmission shows bistability behavior only at certain wavelengths, but not all (e.g., no bistablity exists at 1545.2nm). This is consistent with what was pointed out by Miller [188], for bistability to occur there is a minimum critical detuning required, given by $\omega - \omega_o = \Delta\omega_{FWHM}\sqrt{3}/2$, where ω_0 is the resonance frequency and $\Delta\omega_{FWHM}$ is the FWHM linewidth of the resonator. The critical detuning is the point where the build-up resonant function [Eq. 7.2] reaches the inflection point where the condition $\partial I_1 / \partial I_R = \partial(B^{-1} I_R)/\partial I_R = 0$ is met. Then the bistability occurs as the incident power is increased because of the nonlinear shift of the resonance towards λ, causing the intra-cavity power to build up, which in turn hastens the shift, leading to an unstable situation. This positive feedback increases the slope of the leading edge of the transmission spectrum relative to the linear case [183]. At some critical power the slope can change sign, giving rise to two possible transmission values at the same wavelength. Hence, the transmission falls abruptly to the lower value on the other side of the resonance where the condition is stable (i.e., where further increase in I_{IN} reduces the build-up factor). This is the *turn-off* point indicated by the down arrow.

Similarly, a reduction in power from this point will lead to an upward transition at the *turn-on* point. Note that the minimum transmission is zero only under critical coupling. The ON/OFF ratio at the turn-off point is generally smaller than that at turn-on, and determines the extinction ratio (ER) of the switch if the power is held here in the OFF state. Hence, to maximize the ER and modulation

depth, it is important to minimize the off-state transmission around the turn-off point, while maximizing the on-state transmission at the initial detuning. To align the minimum transmission point closer to the turn-off point, one solution is to operate very close to the critical detuning, but the problem with this is that the ON transmission amplitude is also substantially reduced (hence the modulation depth is small), and the difference between the turn-on and turn-off powers becomes very small. Similar effect may be achieved by increasing the round-trip loss, as shown in Fig. 7.2(b). This is because increasing the loss broadens the resonance and increases the critical detuning, which has the same effect as having the operating wavelength closer to critical detuning. However, the broadened linewidth increases the switching threshold, as expected because of the smaller build-up factor. To maximize the build-up factor at the given loss, one must further satisfy the critical coupling condition $r = a$. Under this condition the achievable input threshold is in the order $n_2 I_{IN} \sim 10^{-4}$.

7.3. Fano-resonance in 1RMZI

Below is the analysis of certain aspects in 1RMZI based nonlinear switch. This includes the detuning where the destructive and constructive interference occur, in weak coupling regime. The expression for intensity transmission in both arms can be modeled as,

$$T_{BAR} = \sin^2(\varphi - \Delta\phi_B)/2 \qquad T_{CROSS} = \cos^2(\varphi - \Delta\phi_B)/2 \tag{7.8}$$

where for the lossless case, $a = 1$, we have the ring phase response φ as

$$\varphi = -\tan^{-1}\left\{\frac{\sin\delta}{r-\cos\delta}\right\} + \tan^{-1}\left\{\frac{r\sin\delta}{1-r\cos\delta}\right\} \tag{7.9}$$

The Fig. 7.3 shows the T_{BAR} for different phase shift, where different asymmetrical features can be imposed as a result of the interference between the upper and lower arm. The destructive interference can be seen from $T_{BAR} = 0$, which is at $\varphi(\delta) - \Delta\phi_B = 2\pi m$. Similarly, for the constructive interference, we have $\varphi(\delta) - \Delta\phi_B = (m + 1/2)2\pi$. The reverse is true for the cross output. For the case of no phase bias ($\Delta\phi_B = 0$), it is obvious to see that the bar destructive (constructive) interference happens at the OFF (ON) ring resonance, but for the case of non-zero phase bias such condition has to be solved, and most of the cases they are very close to each other. This close detuning where the transmission values are 0 and 1 result in a very sharp and almost linear line that connects the two.

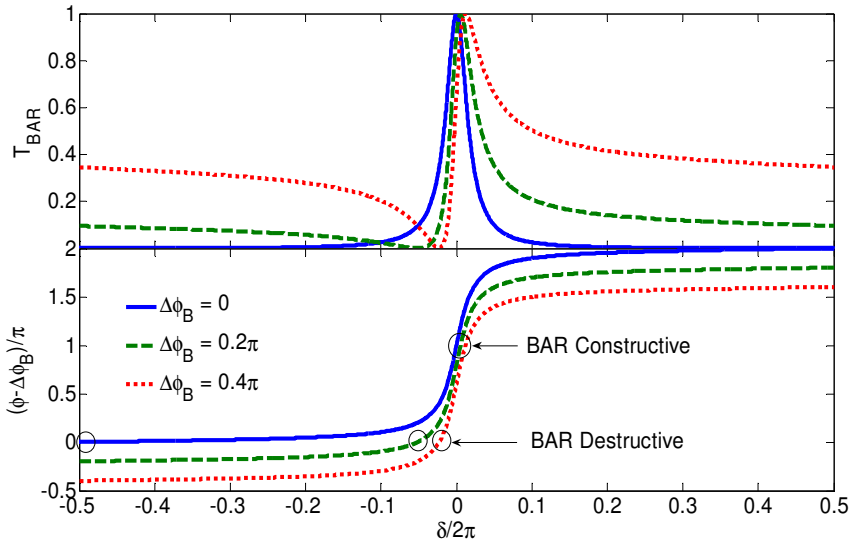

Fig. 7.3. The bar transmission for different values of $\Delta\phi_B$. The solid line represents the symmetric case. Simulated parameters: $r = 0.9$, $a = 1$.

Since the interferences occur around ring resonance, the Eq. (7.9) can be approximated as

$$\varphi \simeq \varphi(\delta = 2\pi m) + \frac{\partial \varphi}{\partial \delta}\delta = \pi - \left(\frac{1+r}{1-r}\right)\delta = \pi - B_1\delta \tag{7.10}$$

where the $\sin\delta \sim \delta$, $\cos\delta \sim 1$, and $\tan^{-1}\delta \sim \delta$ are used. The slope $\partial\varphi/\partial\delta = (1+r)/(1-r)$ which is actually the maximum build-up factor B_0, is very high when the r is close to 1 (weak coupling), this explains the very steep line around the resonance. The Eq. (7.10) also can be obtained from the more general definition of Taylor expansion $\varphi = \varphi(\delta = 2m\pi) + (\partial\varphi/\partial\delta)\delta$. The derivative of φ is $\partial\varphi/\partial\delta = (1-r^2)/(1+r^2-2r\cos\delta) = B$. The bar interference conditions are expressed as follow,

$$\begin{aligned} &\text{Constructive:} \quad \delta_{\text{MAX}} = \Delta\phi_{\text{B}}(1-r)/(1+r) \\ &\text{Destructive:} \quad \delta_{\text{MIN}} = (\Delta\phi_{\text{B}} - \pi)(1-r)/(1+r) \end{aligned} \tag{7.11}$$

The Fano peak shift to the right with the increasing phase shift, as in agreement with the $(\Delta\phi_{\text{B}})$ dependence from Eq. (7.11), similarly the dip also moves to the right, as noted from the $(\pi - \Delta\phi_{\text{B}})$ dependence. Although the T_{BAR} has become asymmetric with the presence of the MZI bias, the critical detuning will still correspond to that in the one ring one bus case, i.e., $\pm\Delta\phi/2\sqrt{3}$ from the resonance where the $\phi = \delta - \delta_{\text{NL}}$. This is affirmed by the root finding process, as explained in Miller's paper [188]. In the next section, we will show how the Fano lineshape generated in the ring-coupled MZI could be tailored to give improved bistability switching performance.

7.4. Bistability engineering for 1R- and 2R-MZI

In the ring-based MZI structure, the bistability occurs only in the ring configuration, and the phase bias at the lower MZI arm does not affect the bistability in itself [144]. This will be an advantage for optimization, since one can dedicate $\Delta\varphi_B$ as an independent control parameter to tailor the Fano-resonance (asymmetricity) without affecting the switching threshold. As highlighted earlier, bistability can be modeled using the parametric formulation [77, 144] whereby the fields at various points of the rings, as shown in Fig. 6.1 (Chapter 6), are all expressed in terms of a parametric field. For 1R1B the parametric field is E_3 while for 2R1B it is E_7. The intensity of the parametric field is then $I_R = I_{3,7} = \frac{1}{2}\varepsilon_0 c n_{\text{eff}} |E_{3,7}|^2$, where n_{eff} is the waveguide-mode effective index. In the case where the ring is a Kerr medium with nonlinear coefficient n_2, the δ_1 and δ_2 in Eq. (6.4) are modified by a nonlinear contribution which can be written as, $\delta_j \equiv \delta_j^{(L)} + \delta_j^{(NL)} = k_0 n_{\text{eff}} (1 + n_2 I_j \eta_j) L_{cj}$ where $k_0 = 2\pi/\lambda_0$ and the parameter η_j is defined as the length reduction factor $\eta_j = (1 - e^{-\alpha L_{cj}})/\alpha L_{cj}$ which accounts for the power loss segment in ring j, and I_j is the maximum intensity in ring j. In general, we can relate $n_2 I_{IN}$ with I_R as follow,

$$n_2 I_{IN} = 2 n_2 I_1 = 2 n_2 I_R B^{-1} \tag{7.12}$$

where I_{IN} is the input intensity to the MZI, and $I_{IN} = 2I_1$ (assuming 3-dB coupler) is the intensity in the bus waveguide, and B is the parametric build-up factor for the case of 1RMZI or 2RMZI, which are given below:

$$\begin{aligned} B^{(1R1B)} &= I_3 / I_1 = (1 - r^2) / |1 - ra \exp(i\delta)|^2 \\ B^{(2R1B)} &= I_7 / I_1 = a_1 B_{21} B_1 = a_1 (1 - r_2^2) / |1 - r_2 a_2 \exp(i\delta_2)|^2 \times (1 - r_1^2) / |1 - r_1 \tilde{a}_1 \exp(i\tilde{\delta}_1)|^2 \end{aligned} \tag{7.13}$$

With these relations one achieves a mapping between $n_2 I_{IN}$ and I_R, and consequently with Eq. (6.3), the bar transmission can be expressed as $T_{BAR} = \frac{1}{4}|t_1 - \exp(i\Delta\varphi_B)|^2$ [144]. For more mathematical details in the parametric formulation, please refer to Appendix D. Next, if n_2 is positive, bistability occurs if the operating wavelength (λ_0) is larger than the resonance wavelength (λ_R) and the initial detuning (λ_0-λ_R) is larger than certain critical value which is proportional to the linewidth (satisfying $|\delta_0 - \delta_R| \geq \Delta\delta\sqrt{3}/2$ [188], where δ_R corresponds to λ_R, and $\Delta\delta$ is the FWHM linewidth).

As illustrated in Fig. 7.4(a), the signature of bistability is found only in the region where T_{BAR} has three solutions for a given value of $n_2 I_{IN}$, of which one value is not stable (the green zone). The corresponding values of B and δ_1 for different zones are shown in Fig. 7.4(b). Note that δ_1 increases with increasing I_{IN}. Thus, in the red zone B increases with I_{IN} which further accelerates the nonlinear shift of λ_R toward λ_0, leading to an unstable situation. This positive feedback increases the slope of the leading edge of the T_{BAR} spectrum [188], until at some critical power the slope changes sign and the transmission switches abruptly to the ON state (the blue zone is stable since B decreases with

increasing I_{IN}). The input power is then held stable here in the ON state. Hence, to maximize the modulation depth (MD), it is desirable not only to maximize the ON transmission, but also to align the transmission peak over the ON transition point, as shown in Fig. 7.4(c). The same figure also shows that the transmission dip is quite sharp, and the extinction in the OFF state is very sensitive to the precise OFF state point. Hence, to maximize the extinction ratio (ER) it is desirable to align the OFF transition point roughly to the minimum transmission point, so as to achieve an ER greater than, say, 30dB. When so aligned, both the MD, given by $T(t_4)$-$T(t_1)$, and the ER, $T(t_4)/T(t_1)$, will be maximized at the same time.

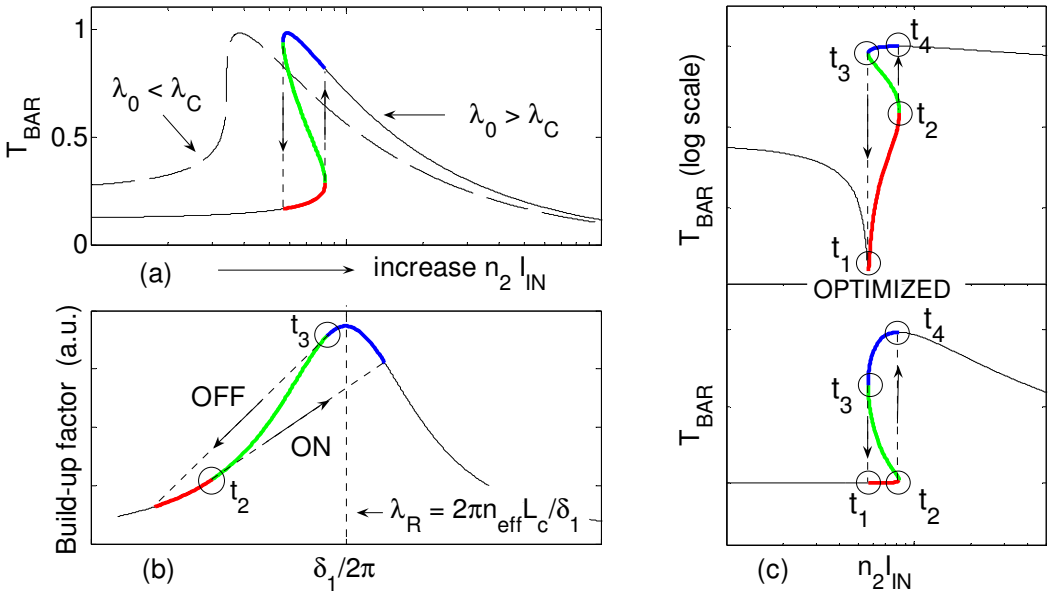

Fig. 7.4(a) The bistability characteristic without any applied bias ($\Delta\varphi_B = 0$). Bistability does not occur (dashed curve) if $\lambda_0<\lambda_C$, where λ_C is the critical detuning. (b) The build-up factor as a function of δ_1 which includes the nonlinear effect. (c) The optimized performance using the appropriate initial detuning λ_0 and bias $\Delta\varphi_B$. The same procedure can be applied to T_{CROSS}.

Both ER and MD can be maximized by using appropriate combination of phase bias $\Delta\varphi_B$ and initial detuning. This is shown in Fig. 7.5 for the case of a 1RMZI with $r = 0.9$ and $a = 0.999$. Because of the relatively high finesse, simultaneous maximization is achieved only for a very narrow range of wavelength, hence good control of the detuning is essential. The ER is also quite sensitive to $\Delta\varphi_B$, with an ER of say 30dB (above the dotted bar) possible only within a small range of $\Delta\varphi_B$.

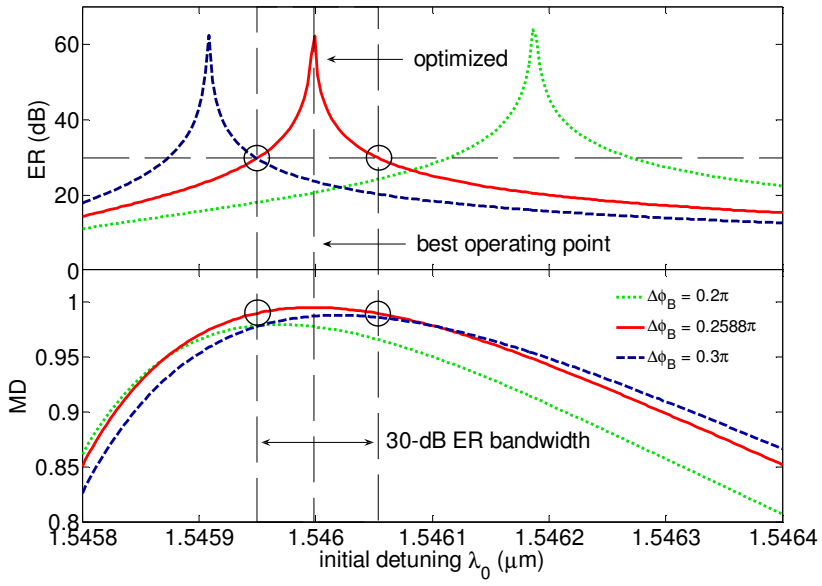

(a)

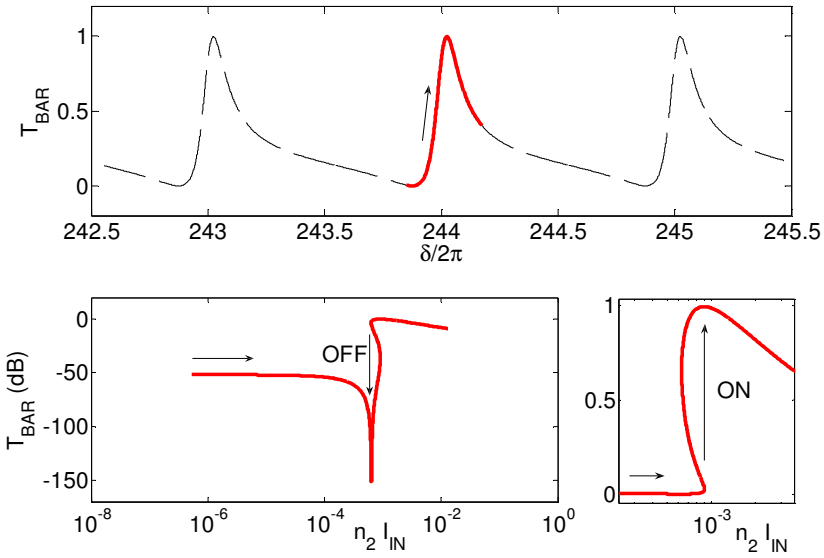

(b)

Fig. 7.5(a) The simulated 1RMZI: The optimization process in order to find proper operating point for (λ_0, $\Delta\varphi_B$). The solid line represents the best operating point for maximum ER & MD, (b) The bar transmission vs. normalized frequency δ_1 (upper) and $n_2 I_{IN}$ (lower) for 1RMZI. The simulation parameters are $r = 0.7$, $a = 0.999$, $n_{eff} = 3$, R = 20μm. Similar optimization scheme can also be applied to 2RMZI around the anti-resonance of ring 1 (i.e., the inner-ring).

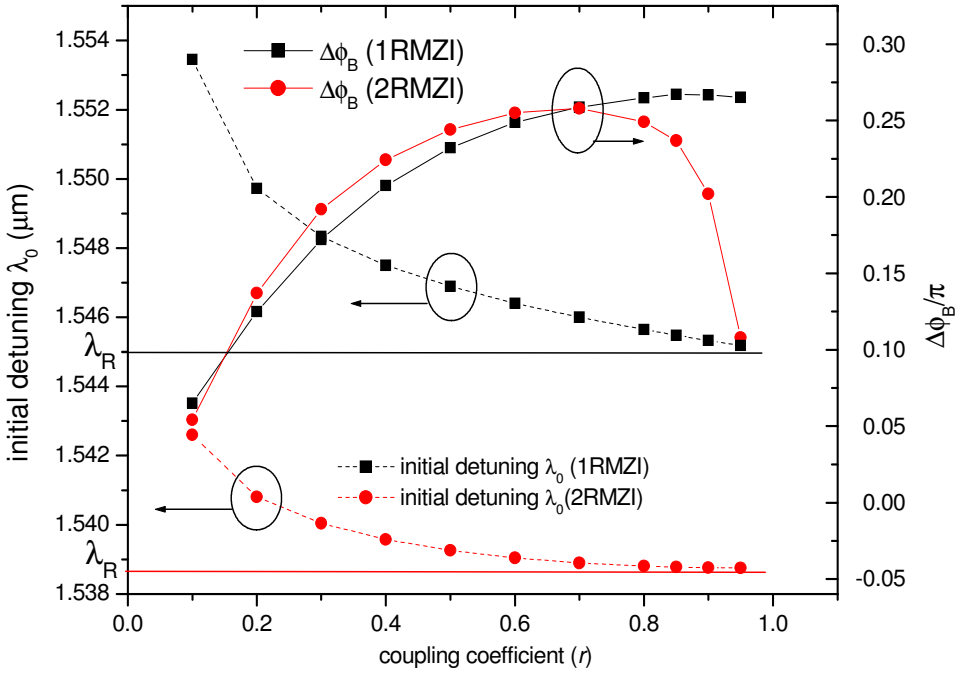

(a)

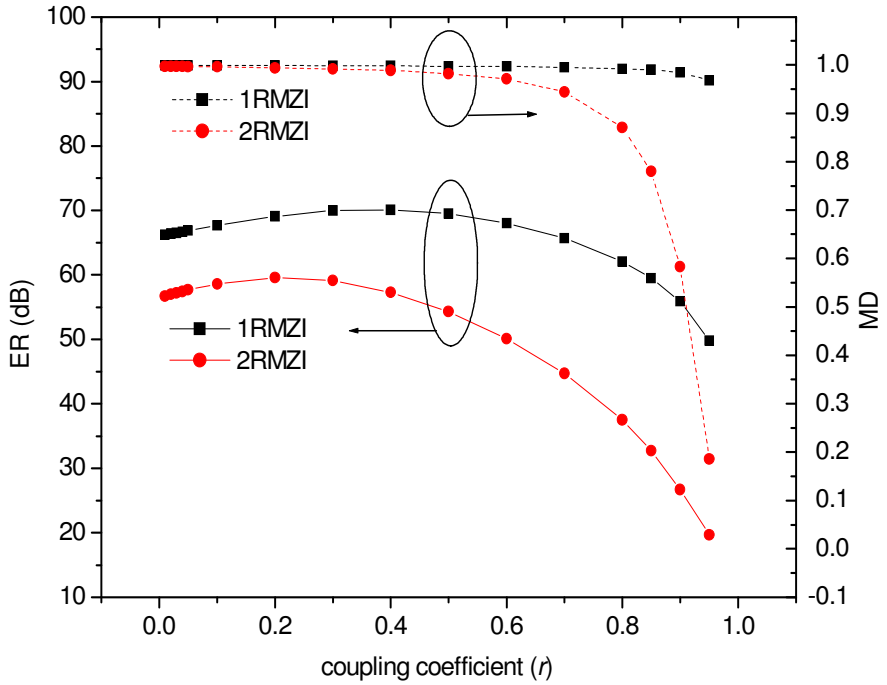

(b)

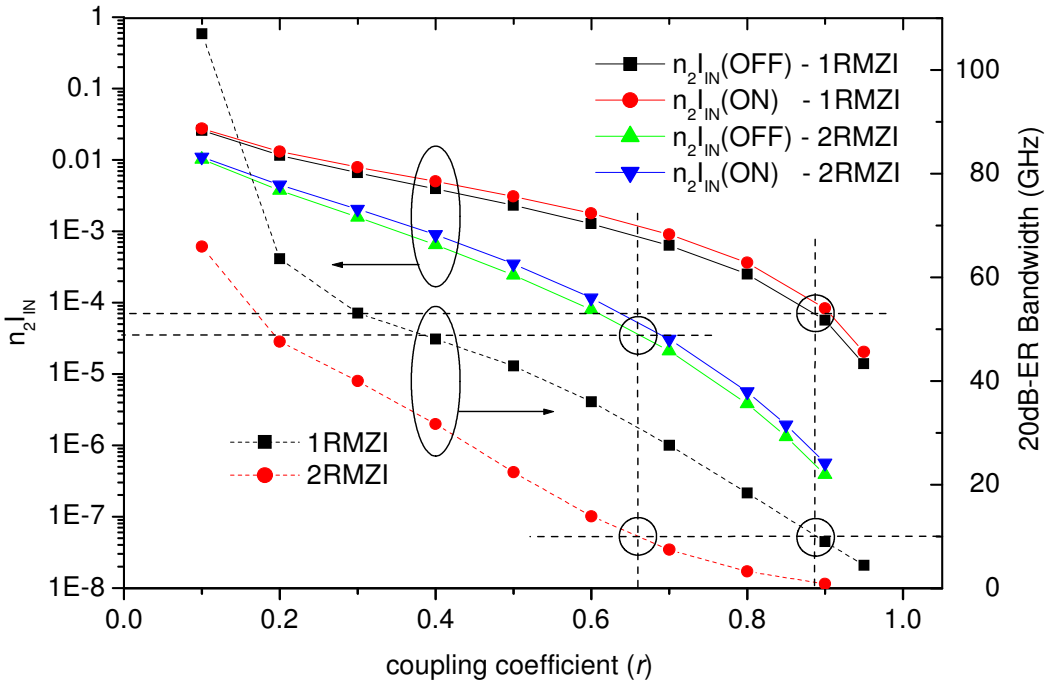

(c)

Fig. 7.6. Engineering bistability in ring-based MZI: (a) The optimized operating parameters (λ_0, $\Delta\varphi_B$) as a function of r. The resonant wavelengths λ_R are also shown. (b) The corresponding ER & MD, (c) The corresponding $n_2 I_{IN}$ (ON/OFF) and the 20dB-ER optical bandwidth (Fixed parameters are a = 0.999, R = R_2 = 20μm, R_1 = 10μm, n_{eff} = 3). Note that (b) and (c) are calculated based on the control parameters obtained in (a).

Fig. 7.6 summarizes and compares the optimization results for both 1RMZI and 2RMZI, where the ring radii are assumed to be R_1 = 10μm and R_2 = 20μm, and a = 0.999. Fig. 7.6(a) shows the combinations (λ_0, $\Delta\varphi_B$) required to maximize both ER and MD as a function of r. For simplicity and for fair comparison between the two devices, we assume all the r to be the same for both 2RMZI and 1RMZI (i.e., $r_1 = r_2 = r$). The resonance wavelengths λ_R are different because they are determined by δ_1 being an odd multiple of π for 2RMZI and even multiple of π for 1RMZI. The initial detuning (λ_0-λ_R) increases with decreasing r because it is proportional to the resonance linewidth and it is smaller for 2RMZI because its resonance linewidth is smaller. On the other hand, the trend for $\Delta\varphi_B$ is to increase with increasing r up to a point where r approaches a and the device becomes critically coupled. Under critical coupling, light is fully absorbed by the loss inside the cavity, and thus both MD and ER decrease rapidly as reflected in Fig. 7.6(b). As a result, this region of r is to be avoided. In terms of performance, it can be seen that the MD & ER of 2RMZI are smaller than 1RMZI. In particular, to achieve 30dB of ER, r has to be smaller than 0.85 for 2RMZI. This is because in the high-finesse region ($r > 0.85$) the loss, even though small, still has a significant effect in flattening the spectra 'dip' (OFF-state) of the bistability characteristics, thereby reducing the ER.

High finesse not only enhances sensitivity to loss, but also implies high sensitivity to operating wavelength and results in small optical bandwidth. The optical bandwidth is also related to ER and is the more constricted the higher the required ER. For 30dB ER the optical bandwidth for a 2RMZI with $r = 0.85$ is found to be less than 1 GHz which is an impractical value. Hence, either the value of r must be decreased to reduce the finesse, or the required ER must be lowered. On the other hand, high finesse is favorable for low switching threshold. Lower switching threshold is the only advantage for 2RMZI. At $r \sim 0.9$, it can be ~150 times lower compared with 1RMZI. Fig. 7.6(c) shows the tradeoff between the switching threshold and the optical bandwidth for both 1RMZI and 2RMZI. The optical bandwidth is that corresponding to ER ~ 20dB. For instance, we highlight that 10GHz operation can be realized using 2RMZI with r~0.66 or 1RMZI with r~0.88, giving $n_2 I_{IN}$ around 3.5×10^{-5} and 7×10^{-5} respectively. The threshold can be lowered if the required ER can be reduced. For example, if the required ER is set to ~10dB, then the achievable threshold becomes ~4×10^{-6} (2×10^{-6}) for the case of 1RMZI (2RMZI) with $r \sim 0.975$ ($r \sim 0.825$).

A typical value of n_2 for polymer, such as PTS (p-Toluene Sulfonate), is ~2.2×10^{-12} cm^2/W around 1600 nm [17]. For the 2RMZI with $n_2 I_{IN} \sim 2\times10^{-6}$ using such a purely refractive nonlinear material, the estimated threshold power is around ~10 mW if a waveguide with a cross section area of 1 μm^2 is used (based on 10GHz optical bandwidth). Such value is still within practical limit, knowing that only Kerr based nonlinearity is used in the modeling. In practice, the actual threshold can be lower in the presence free carrier refraction associated with two-photon absorption (TPA) or other nonlinear effects [180, 182, 194].

7.5. Conclusion

Indeed, that by operating in different r regions, both 1RMZI and 2RMZI can achieve almost the same performance in all respects. In other words, the 2RMZI does not enjoy any clear advantage over 1RMZI except that it is easier to realize a lower r value than a very high r value (i.e., very weak coupling). For example, a moderate coupling can be achieved with good control by using race-track directional coupler or even a multimode interferometer (MMI) while a very weak coupling requires a point coupler with relatively large separation (more stringent control in the fabrication is required). Only in the ideal lossless case (which may be achieved using an amplifier) does the 2RMZI pull away in performance largely because of the huge reduction in the switching intensity. However, as always this advantage will be compensated by extreme sensitivity to operating wavelength. Lastly, it should be noted that our optimization scheme can still be applied for other γ values. The $\gamma \sim 2$ is used for best-case scenario.

SUMMARY

The most important research contributions of the thesis could be summarized as follows:

(1) Theoretical study on the concept and conditions of critical coupling and oscillation for the Type I and Type II filters involving arrayed structures was conducted. Based on the pole-zero diagram technique, it can be shown that the pole-zero dynamics for Type I and Type II array filters are complementary to each other, confirming their non-overlapping and complementary photonic bandgaps.

(2) By combining the Type I and Type II filter, it is possible to design a hybrid 2D-RR array which can approximate an ideal bandpasss filter with a square "flat-top" amplitude response, sharp rolloff and sidelobe-free stopbands. The mechanism relies on the 2D periodic structure which exhibits complementary and non-overlapping (2D) photonic bandgaps. The effect of apodization is also shown by the pole-zero distribution of the 2R-RR array.

(3) Two novel types of MZIs, the nested MZI (NRMZI) and two-ring MZI (2RMZI) were proposed and demonstrated. For the NRMZI, it is possible to obtain flat-top response, shaped by the double-Fano resonances, due to interference among the different optical pathways available in the nested-ring and in the MZI. For the 2RMZI, it was shown that by using two-ring instead of one-ring, a more complete destructive interference could be achieved, which effectively suppresses the unwanted background envelope found in 2R2B system, resulting in improved contrast ratio, modulation depth and finesse associated to the narrow resonance.

(4) A scheme for bistability engineering through altering the Fano lineshape was theoretically discussed. It was shown that as a result of the resonance enhancement associated with the 2RMZI, the switching threshold can be reduced by two orders of magnitude as compared with that of the conventional 1RMZI.

For future works, we would like to further investigate the optical delays associated with microring arrays and two-ring devices. One main challenge lies in the fabrication of a perfectly balanced MZI devices (Chapter 5 and 6). In general, there are three main sources of imbalances: (1) The light in the upper MZI arm is perturbed by the neighboring ring structure, creating additional phase offset of $2\pi\Delta n L_{CAV}/\lambda$ where Δn can be considered as the effective index difference between the ring mode and the bus mode. (2) In optical lithography, the light gets diffracted from the structures in the mask and its optical pattern interferes constructively or destructively. This mechanism gets more complex in densely packed structures, which is generally known as the *optical proximity effect* (OPE). The OPE causes the photonic wires in close proximity [i.e., directional couplers (DC) with submicron gap separation] to have narrower waveguide width than the isolated wires. As a result, there is effectively a width difference between the upper MZI arm (the one with ring structures using DC) and the lower MZI arm (isolated lines). (3) The fabricated

photonic wires, in general, have certain *waviness* of the waveguide. These sidewall fluctuations are in the range of several nm, which slightly contribute to phase errors. The combined three effects will produce phase error between the MZI arms, which is difficult to control. Further optimization work can be done to offset the first two sources of imbalances, for instance, by varying the waveguide width of the lower MZI arm, or by applying an *optical proximity correction* (OPC) in the masks, etc. The third source of imbalance is more intrinsic in nature and is impossible to control based on the current CMOS based fabrication technology. The bistability model in Chapter 7 is only based on Kerr effect (i.e., nonlinear refraction). In future, we may want to include other effects such as the free carrier refraction associated with two-photon absorption (TPA), depending on the selection of the material used. Lastly, a robust active tuning mechanism of the ring-coupled MZI devices could be developed. For instance, by adding a thin film heater in one of the MZI arm, we could control the Fano-lineshape (i.e., symmetric or anti-symmetric) associated to the 1R- and 2RMZI devices, and demonstrate the bistability engineering scheme experimentally.

APPENDIX A

A.1. Linearity in REMZI

Linearity is one useful trait that is widely used in analog systems. MZI+X devices has been subject of research in the area of linearity in many works [67-69] . In this section, we would like to present a brief general overview of linearity using various ring-based MZI structures and compare their performances, in terms of linearity range and sensitivity to loss.

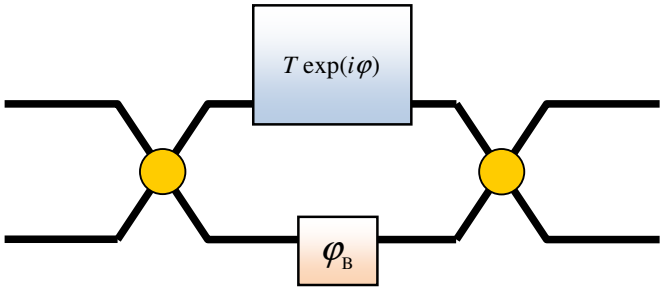

Fig. A1. Generalized ring-based MZI. The ring-inset can be of various configurations, i.e.: (i) a single-ring, (ii) a nested-ring, (iii) a two-ring configuration, etc.

In general, a continuous function can be expressed in terms of Taylor series:

$$f(\delta) = f(\delta_0) + f'(\delta_0)(\delta-\delta_0) + f''(\delta_0)(\delta-\delta_0)^2/2! + f'''(\delta_0)(\delta-\delta_0)^3/3! + \ldots \text{ etc} \quad \text{(A1)}$$

Identifying the higher-order terms in the bar transmission (similar analysis can be done with the cross output),

$$T_{BAR} = (T^2 + 1 - 2T\cos\theta)/4 \quad \text{(A2)}$$

$$T_{BAR}' = (TT' - T'\cos\theta + T\varphi'\sin\theta)/2 \quad \text{(A3)}$$

$$T_{BAR}'' = (T'^2 + TT'' - T''\cos\theta + 2T'\varphi'\sin\theta + T\varphi''\sin\theta + T\varphi'^2\cos\theta)/2 \quad \text{(A4)}$$

$$\begin{aligned} T_{BAR}''' = (&3T'T'' + TT''' - T'''\cos\theta + 3T''\varphi'\sin\theta + 3T'\varphi''\sin\theta \\ &+ 3T'\varphi'^2\cos\theta + T\varphi'''\sin\theta + 3T\varphi'\varphi''\cos\theta - T\varphi'^3\sin\theta)/2 \end{aligned} \quad \text{(A5)}$$

where $T = \sqrt{tt*}$ is the transmission and φ is the phase response of the ring structure. Note that $\theta = \varphi - \varphi_B$ is the phase difference between the upper MZI arm and the lower MZI arm.

A.2. RMZI: Setting T_{bar}'' and T_{bar}''' to zero

Linearity aspect of balanced 1RMZI has been previously studied in [67]. Mathematically, we can express T and φ as,

$$T = \left(\frac{r^2 + a^2 - 2ar\cos\delta}{1 + r^2a^2 - 2ar\cos\delta} \right)^{1/2} \qquad \varphi = \tan^{-1}\left(\frac{a(r^2-1)\sin\delta)}{r(1+a^2) - a(1+r^2)\cos\delta} \right) \tag{A6}$$

Since we are interested on the linearity when δ = π, it is important to deduce the linear slope (m). After some algebraic manipulation, one can express the linear slope (m) as,

$$m(a, r, \varphi_B) = T'_{BAR}(\pi) = \frac{a(r^2-1)\sin\varphi_B}{2(ar+1)^2} \tag{A7}$$

To remove the 2nd and 3rd order harmonics, one can simply set Eq. (A4) and (A5) to zero. Re-expressing the Taylor's expansion around $\delta_0 = \pi$, one can always deduce that $T' = T''' = 0$ and $\varphi = \varphi'' = 0$. This way, we can further simplify (A4) and (A5) into,

$$T'''_{BAR}(\pi) = \{3T''\varphi' + T\varphi''' - T\varphi'^3\}\sin\theta = 0 \tag{A8}$$

$$T''_{BAR}(\pi) = \frac{1}{2}(TT'' - T''\cos\theta + T\varphi'^2\cos\theta) = 0 \longrightarrow \cos\theta = \frac{TT''}{T'' - T\varphi'^2} \tag{A9}$$

This means that one can always find a combination of (a, r) values that makes (A5) to be zero and using that particular (a, r) combination, one can always use (A9) to find the necessary phase bias $\varphi_B = \varphi - \theta$ required to vanish the 2nd order harmonics [67]. Fig. A2 shows the conditions required that satisfy Eq. (A8) and (A9).

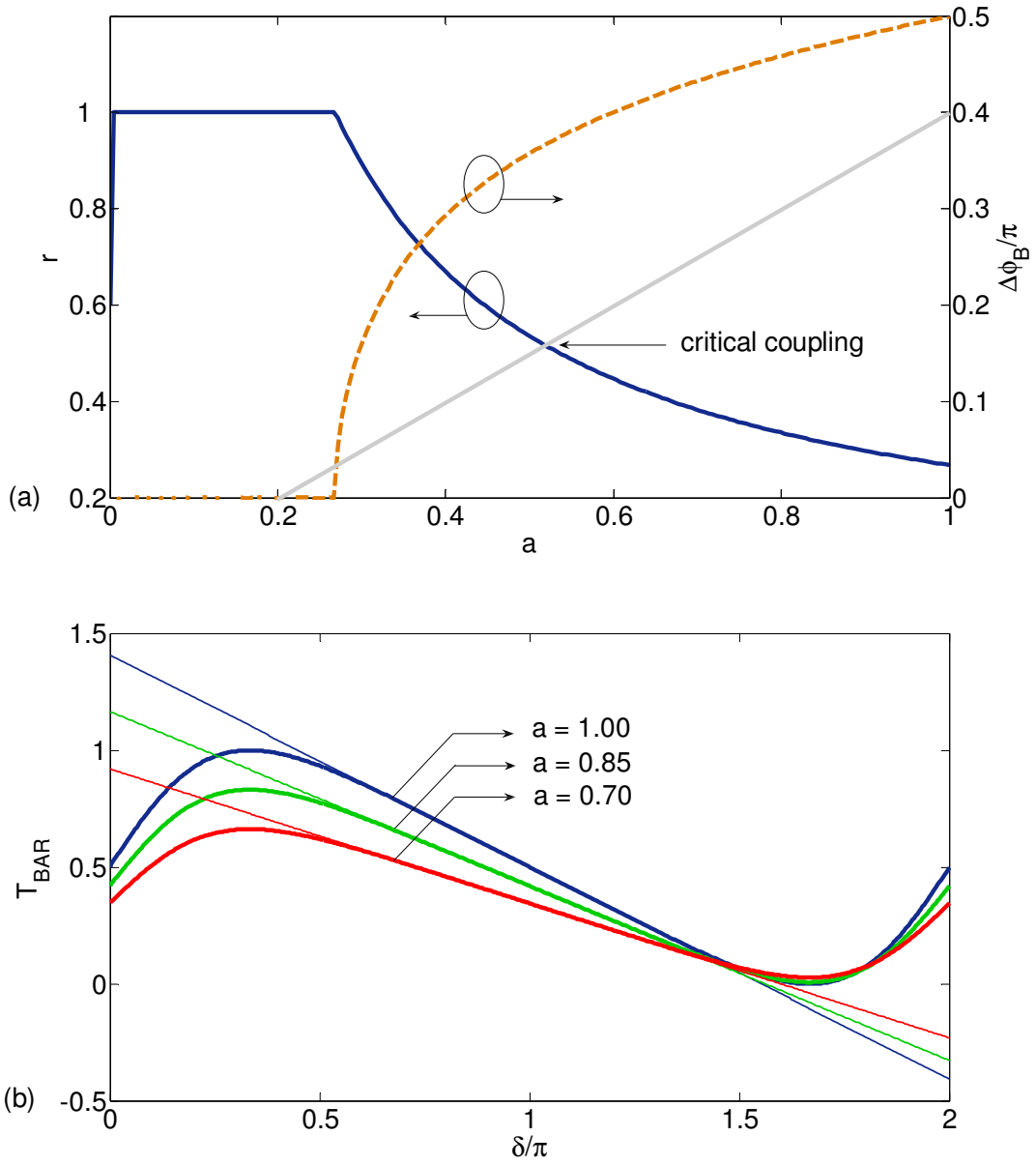

Fig. A2(a) The (a, r) combination removes the 3rd order harmonics and the corresponding phase bias removes the 2nd order harmonics. (b) The bar transmission of linearized 1RMZI for a = 0.7, 0.85, 1 respectively.

For a lossless case, it is easy to show that $T = 1 \text{and} T' = T'' = T''' = 0$. With this relation, we can further simplify (A5) to $T'''_{BAR} = (\varphi''' - \varphi'^3)\sin\theta = 0$, which leads to the condition of $\varphi''' = \varphi'^3$ and finally produces the simple quadratic equation $r^2 - 4r + 1 = 0$. This gives a valid solution exactly at $r = 2 - \sqrt{3} = 0.2689$ [67]. Similar technique can be applied to linearize many more MZI+X devices such as 2RMZI, NRMZI, etc.

APPENDIX B

B.1. Linear time response and cavity lifetime of 1R1B

It is also interesting to look at the under-, critical-, and over-coupling conditions in terms of the linear time response. To do this, we can apply the Inverse Fourier Transform (IFT) and Fourier Transform (FT) methods.

$$H(\delta)=\int_{-\infty}^{\infty} h(t_n)e^{-i\delta t_n}dt_n \;\; (FT); \qquad h(t_n) \;\; =\frac{1}{2\pi}\int_{-\infty}^{\infty} H(\delta)e^{i\delta t_n}d\delta \;\; (IFT) \tag{B1}$$

where t_n is the normalized roundtrip time $t_n \equiv t/T_R = t(c/nL)$ corresponding to a single roundtrip phase (δ). Fig. B1(a) shows the linear time response for a super-Gaussian input pulse. The output powers are normalized with respect to the input excitation whereas the circulating powers are normalized (scaled) to unity for better graph representation.

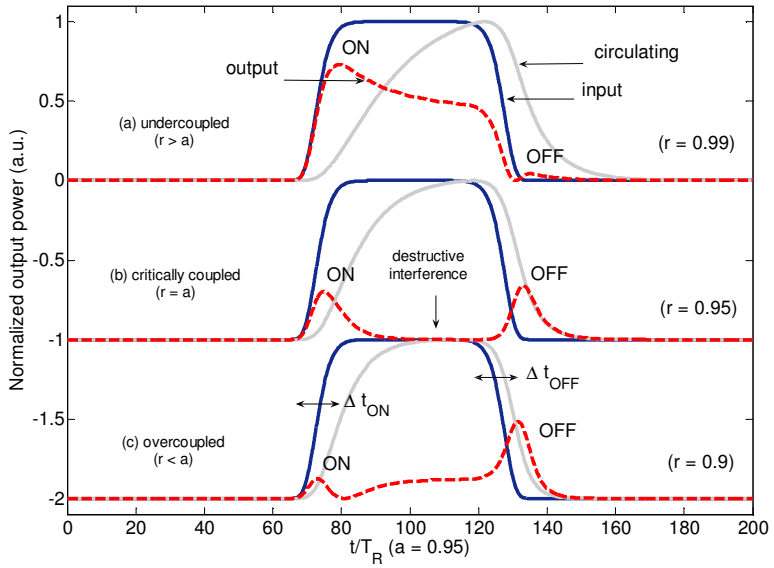

Fig. B1. The linear time response when 1R1B is excited by a super-Gaussian input pulse (Finesse ~30).

Based on the above figures, it can be seen how the three different coupling conditions may affect the linear time response. Based on the circulating power delay, it is clear that the higher the finesse, the longer the light circulates inside the ring and therefore the larger is the delay.

Under the critical coupling condition, there will be a perfect destructive interference between the circulating field κd_1 and the output field rb_1 [1]. The zero reflection is reached when the circulating field converges near the maximum value, a natural indication stating that the steady state condition is fulfilled. Fig. B1(a) and (c) shows the case when the 1R1B is undercoupled and overcoupled respectively. The main difference between the two can be seen during the ON/OFF switching

excitation from the input. For instance, when the ring is undercoupled [refer to Fig. B1(a)], the bus-to-cavity coupling rate is low (indicated by the slow build-up rate in the circulating field). So when the input is triggered ON (Δt_{ON}), the light coupled into the cavity at lower rate and as a result, most of the light is transferred into the output bus. Similarly, when the input is triggered OFF (Δt_{OFF}), the light from the cavity discharges at lower rate and thus, there is bound to have a sudden drop in the output since there is not enough light to sustain the output. Next when the ring is overcoupled [refer to Fig. B1(c)], the bus-to-cavity coupling rate is faster (indicated by the fast build-up rate in the circulating field). So when the input is triggered ON (Δt_{ON}), most of the light is transferred into the cavity and less goes into the output bus. Similarly, when the input is triggered OFF (Δt_{OFF}), the light from the cavity discharges at higher rate and produces a sharp transmission boost in the output bus and which later on decays to zero.

Fig. B2 shows how the pulse fidelity is distorted for input pulsewidth smaller than the cavity lifetime. The cavity lifetime can be defined as the average time that a photon coupled into the resonator will stay inside the cavity before it is absorbed or transmitted through. The cavity lifetime (or the effective delay) is thus given by,

$$\tau_{CAV} \equiv \frac{1}{\Delta f_{1/2}} = \frac{2\pi(nL/c)}{\Delta \delta_{1/2}} = F_1 T_R \tag{B2}$$

Eq. (B2) states that a photon circulates inside the cavity for a number of round trip times equal to the finesse, before it is transmitted to the output bus or absorbed (or scattered) inside the resonator. As a natural consequence, in order to sustain a pulse shape, the input pulsewidth must be at least equal to the cavity lifetime of the resonator. This will be an intrinsic limitation of optical signal processing for ultrafast process associated with the resonator.

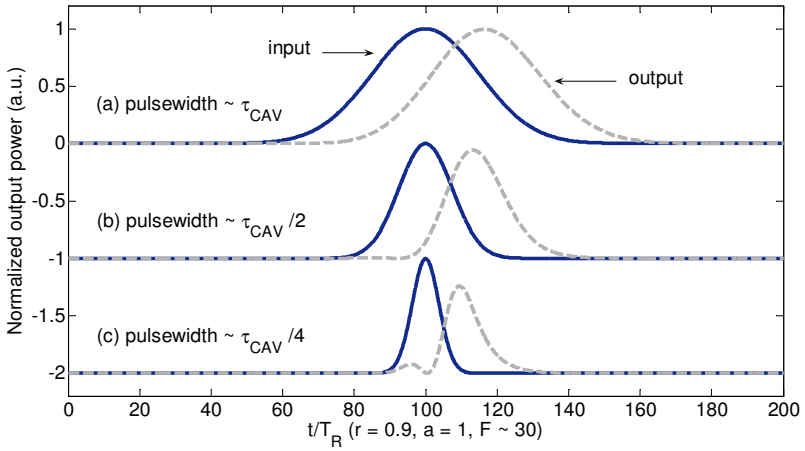

Fig. B2. The linear time response (overcoupling condition) excited by three different input pulsewidths. . The output pulse is preserved in the case of (a) as the input pulsewidth is $\geq \tau_{CAV}$. The output pulse is distorted in the case of (b) and (c) as the input pulsewidth is already $< \tau_{CAV}$.

APPENDIX C

C.1. Formulation of NRR

One effective approach to analyze the NRR is to consider the dual-bus coupled ring as a "black box" with reflection and transmission coefficients, ρ and *t* given by Eqs. 5.2 and 5.3 respectively (refer to Chapter 5). Hence, by summation, the total transmission is given by,

$$t_{NRR} = t + \rho^2 a^v e^{iv\delta}(1 + ta^v e^{iv\delta} + ...) = \frac{t + (\rho^2 - t^2)a^v e^{iv\delta}}{1 - ta^v e^{iv\delta}} \tag{C1}$$

Another alternative is to partition the NRR into 6 sections and applying the transfer matrix method [195]. The matrices M_2 and M_4 in Fig. C1 represent the couplers, which are assumed to have arbitrary split ratio. M_1 and M_5 refer to the transmission inside the quarter circle of the inner-ring and the input/output port, assuming zero length of port a_1 and b_1 without losing the qualitative outcome of the analysis. M_3 represents the transmission through the two arms of the unbalanced MZI, where *v* denotes the length of the outer loop as a multiple of the inner loop (ring). Note that *r* is the reflectivity of the coupler represented by M_2 and M_4,

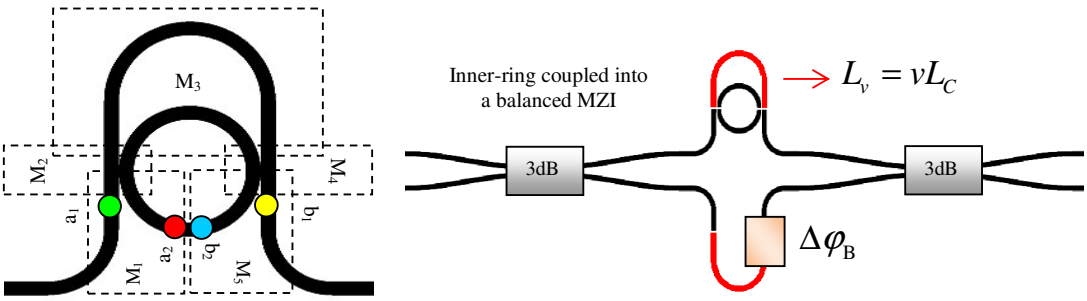

Fig. C1. Left: NRR comprising an outer 'MZI' arm and an inner RR which gives the optical feedback mechanism. The notation a_1, b_1 are the field inside the input and the output port of NRR respectively. Whereas a_2 and b_2 are the circulating field inside the lower-half of the inner-ring; Right: NRMZI comprising NRR coupled into the upper arm of MZI.

The transmission through the NRR section t_{NRR} can be derived as follows:

$$\begin{bmatrix} b_1 \\ b_2 \end{bmatrix} = M_5 M_4 M_3 M_2 M_1 \begin{bmatrix} a_1 \\ a_2 \end{bmatrix} = \begin{bmatrix} m_{11} & m_{12} \\ m_{21} & m_{22} \end{bmatrix} \begin{bmatrix} a_1 \\ a_2 \end{bmatrix}$$

$$M_1 = M_5 = \begin{bmatrix} 1 & 0 \\ 0 & a^{1/4} \mathrm{e}^{i\delta/4} \end{bmatrix}$$

$$M_2 = M_4 = \begin{bmatrix} r & i\kappa \\ i\kappa & r \end{bmatrix} \tag{C2}$$

$$M_3 = \begin{bmatrix} a^v e^{iv\delta} & 0 \\ 0 & a^{1/2} \mathrm{e}^{i\delta/2} \end{bmatrix}$$

By applying the continuity condition $a_2 = b_2$ we obtain $t_{NRR} = \mathrm{b}_1/\mathrm{a}_1 = m_{11}+m_{12}m_{21}/(1-m_{22})$, i.e.,

$$t_{NRR} = \frac{-\kappa^2 \sqrt{a} e^{i\delta/2} + r^2 a^v \mathrm{e}^{iv\delta} - a^{v+1} \mathrm{e}^{i(v+1)\delta}}{1 - r^2 a e^{i\delta} + \kappa^2 a^{v+1/2} \mathrm{e}^{i(v+1/2)\delta}} \tag{C3}$$

In this appendix, we will prove that (C1) is equivalent to (C3). To simplify, we employ the θ instead of $v\delta$. First, we work on the denominator of (C1)

$$1 - t a^v e^{i\theta} = 1 + \frac{\kappa^2 a^{(v+1/2)} e^{i(\theta+\delta/2)}}{1 - a r^2 e^{i\delta}} = \frac{1 - a r^2 e^{i\delta} + \kappa^2 a^{(v+1/2)} e^{i(\theta+\delta/2)}}{1 - a r^2 e^{i\delta}} \tag{C4}$$

Now, as we work on the numerator,

$$\begin{aligned}
& t + (\rho^2 - t^2) a^v e^{i\theta} \\
&= \frac{-\kappa^2 a^{1/2} e^{i\delta/2}}{(1 - a r^2 e^{i\delta})} + \frac{[r^2 (1 - a e^{i\delta})^2 - \kappa^4 a e^{i\delta}] a^v e^{i\theta}}{(1 - a r^2 e^{i\delta})^2} \\
&= \frac{1}{(1 - a r^2 e^{i\delta})} \{ -\kappa^2 a^{1/2} e^{i\delta/2} + \frac{[r^2 (1 - 2 a e^{i\delta} + a^2 e^{i2\delta}) - (1 - 2r^2 + r^4) a e^{i\delta}]}{(1 - a r^2 e^{i\delta})} \} a^v e^{i\theta} \\
&= \frac{1}{(1 - a r^2 e^{i\delta})} \{ -\kappa^2 a^{1/2} e^{i\delta/2} + \frac{[r^2 - 2 a r^2 e^{i\delta} + a^2 r^2 e^{i2\delta} - a e^{i\delta} + 2 r^2 a e^{i\delta} - r^4 a e^{i\delta}]}{(1 - a r^2 e^{i\delta})} a^v e^{i\theta} \\
&= \frac{1}{(1 - a r^2 e^{i\delta})} \{ -\kappa^2 a^{1/2} e^{i\delta/2} + \frac{r^2 (1 - a r^2 e^{i\delta}) - a e^{i\delta} (1 - a r^2 e^{i\delta})}{(1 - a r^2 e^{i\delta})} a^v e^{i\theta} \} \\
&= \frac{1}{(1 - a r^2 e^{i\delta})} \{ -\kappa^2 a^{1/2} e^{i\delta/2} + r^2 a^v e^{i\theta} - a^{(v+1)} e^{i(\theta+\delta)} \}
\end{aligned} \tag{C5}$$

By taking $C5/C4$ we obtain,

$$t_{\mathrm{NRR}} = \frac{-\kappa^2 a^{1/2} e^{i\delta/2} + r^2 a^v e^{i\theta} - a^{(v+1)} e^{i(\theta+\delta)}}{1 - a r^2 e^{i\delta} + \kappa^2 a^{(v+1/2)} e^{i(\theta+\delta/2)}} = (\mathrm{C3}) \tag{C6}$$

APPENDIX D

D.1. Parametric formulation of 1RMZI

In this section we formulate the parametric representation for 1RMZI device. Referring to the field notation in Fig. 6.1 (Chapter 6), we formulate the relation between the input of the 1R1B configuration (E_1) with the build-up field (E_3).

$$\frac{E_1}{E_3}=\frac{i\kappa}{1-rae^{i\delta}}\longrightarrow B_{13}=\frac{\kappa^2}{1-2ra\cos\delta+r^2a^2} \tag{D1}$$

Next, we shall take the variable $t\equiv n_2\,|E_3|^2$ as parametric field and slightly modifying Eq. (D1) and re-express them as,

$$n_2\left|\frac{E_{IN}}{E_3}\right|^2=2n_2B_{13}=2n_2\left|\frac{1-rae^{i\delta}}{i\kappa}\right|^2\longrightarrow n_2\left|E_{IN}\right|^2=2t(1-2ra\cos\delta+r^2a^2)/\kappa^2 \tag{D2}$$

This way we have established the relation between the MZI input $n_2\left|E_{IN}\right|^2$ with the parametric field $t\equiv n_2\,|E_3|^2$. The factor (2) in the formulation of the bar input is due to the existence of a 3dB coupler between the bar MZI input and the 1R1B configuration. The roundtrip phase can be divided into $\delta=\delta_L+\delta_{NL}$ where $\delta_L\equiv 2\pi n_{eff}L_c/\lambda_0$ is the linear roundtrip phase and $\delta_{NL}=\gamma_{NL}\bar{L}t$ is the nonlinear roundtrip phase which its nonlinear effective properties depends on the factor $\gamma_{NL}=\pi\varepsilon_0 cn_{eff}/\lambda$ [144, 191] and the effective nonlinear interaction length $\bar{L}=(1-e^{-\alpha L_c})/\alpha$. Based on eq. (D1), one can easily show that the onset of bistability occurs around the inflection point, which corresponds to the case where $\partial n_2 I_{IN}/\partial t\equiv\partial(B_{13}t)/\partial t=0$

$$\frac{\partial(B_{13}t)}{\partial t}=(2rat\gamma_{NL}\bar{L}\sin\delta+1-2ra\cos\delta+r^2a^2)/\kappa^2=0 \tag{D3}$$

The bistability characteristic can be shown by plotting the $n_2I_{IN}=2n_2I_1=\varepsilon_0 cn_{eff}B_{13}t$ in the x-axis and the $T_{BAR}=\left|(t_{RR}-\exp(i\Delta\varphi_B)/2\right|^2$ in the y-axis, using $t\equiv n_2\,|E_3|^2$ as the parametric field (i.e., the build-up field).

D.2. Parametric formulation of 2RMZI

In this section we shall briefly formulate the parametric representation for 2RMZI device. Referring to the field notation in Fig. 6.1 (Chapter 6), we formulate the relation between the input of the 2-ring configuration (E_1) with the build-up field in ring 2 (E_7),

$$\frac{E_1}{E_7}=\frac{E_1}{E_3}\frac{E_3}{E_5}\frac{E_5}{E_7}=\left(\frac{1-a_1r_1t_2e^{i\delta_1}}{i\kappa_1}\right)a_1^{-1/2}e^{-i(\frac{\delta_1}{2}+\gamma_{NL}\overline{L_1}|E_3|^2)}\left(\frac{1-a_2r_2e^{i\delta_2}}{i\kappa_2}\right) \tag{D4}$$

Next, we shall take variable $t\equiv n_2|E_7|^2$ as parametric field and slightly modifying Eq. (D4) and re-express them as,

$$n_2|E_1|^2=\frac{\left|(1-a_1r_1t_2e^{i\delta_1})(1-a_2r_2e^{i\delta_2})\right|^2 n_2|E_7|^2}{\kappa_1^{\,2}\kappa_2^{\,2}a_1} \tag{D5}$$

The round-trip phase $\delta_1=\delta_1^{(L)}+\delta_1^{(NL)}$ can be expressed in terms of parametric field $t\equiv n_2|E_7|^2$ as follow,

$$\begin{aligned}&\delta_1=\delta_1^{(L)}+\gamma_{NL}\overline{L_1}n_2(|E_3|^2+|E_6|^2)=\delta_1^{(L)}+\frac{\gamma_{NL}\overline{L_1}n_2|E_5|^2}{a_1}(1+a_1|t_{21}|^2)\\&\rightarrow n_2|E_5|^2=\left|\frac{1-a_2r_2e^{i\delta_2}}{i\kappa_2}\right|^2 n_2|E_7|^2=\left|\frac{1-a_2r_2e^{i\delta_2}}{i\kappa_2}\right|^2 t\end{aligned} \tag{D6}$$

where $\overline{L_1}=(1-e^{-i\alpha L_c/2})/\alpha$ refers to the interaction length in the inner-ring (half-ring). Similarly, the interaction in the outer-ring can be expressed as $\overline{L_2}=(1-e^{-i\alpha\gamma L_c})/\alpha$ and the round-trip phase δ_2 can be written as $\delta_2=\delta_2^{(L)}+\gamma_{NL}\overline{L_2}t$. Again, the factor (2) in the formulation of the bar input is due to the existence of a 3dB coupler between the bar MZI input and the 2-ring configuration. The bistability characteristic can be shown by plotting the $n_2I_{IN}=2n_2I_1=\varepsilon_0cn_{eff}B_{17}t$ in the x-axis and the $T_{BAR}=\left|(t_{RR}-\exp(i\Delta\varphi_B)/2\right|^2$ in the y-axis, using $t\equiv n_2|E_7|^2$ as the parametric field (i.e., the build-up field in the outer-ring).

AUTHOR'S PUBLICATIONS

Papers:

1. **S. Darmawan**, Y. M. Landobasa, P. Dumon, R. Baets, and M. K. Chin, "Resonance enhancement in silicon-on-insulator based two-ring Mach-Zehnder interferometer," *IEEE Photon. Technol. Lett.*, Vol 20, 1560 (2008).
2. **S. Darmawan**, Y. M. Landobasa, P. Dumon, R. Baets, and M. K. Chin, "Nested-Ring Mach-Zehnder Interferometer on Silicon-on-Insulator," *IEEE Photon. Technol. Lett.*, Vol. 20, 9-11 (2008).
3. **S. Darmawan** and M. K. Chin, "Nested-Ring Mach-Zehnder Interferometer," *Optical Quantum Electron.*, Vol. 38, 1151-1157 (2006).
4. **S. Darmawan**, Y. M. Landobasa, and M. K. Chin, "Nested Ring Mach-Zehnder Interferometer," *Optics Express*, Vol. 15, 437-448 (2007).
5. **S. Darmawan** and M. K. Chin, "Pole-zero Dynamics of High-Order Ring Resonator Filters," *J. Lightwave Technol.*, Vol. 25, 1568-1575 (2007).
6. **S. Darmawan** and M. K. Chin, "Critical Coupling, Oscillation, Reflection, and Transmission in Optical Waveguide-Ring Resonator Systems," *J. Opt. Soc. Am. B*, Vol. 23, 834-841 (2006).
7. **S. Darmawan**, Y. M. Landobasa, and M. K. Chin, "Phase Engineering for Ring Enhanced Mach-Zehnder Interferometers," *Optics Express*, Vol. 13, 4580-4588 (2005).
8. **S. Darmawan**, S. Y. Lee, C. W. Lee, and M. K. Chin, "A Rigorous Comparative Analysis of Directional Couplers and Multi-Mode Interferometers Based On Ridge Waveguides," *Journal of Selected Topics on Quantum Electronics*, Vol. 11, 466-475 (2005).
9. **S. Darmawan**, S. Y. Lee, C. W. Lee, and M. K. Chin, "Transformation of Directional Couplers to Multi-mode Interferometers based on Ridge Waveguides and Its Applications," *Journal of Nonlinear Optical Physics & Materials*, Vol. 14, 221-235 (2005).
10. Y. M. Landobasa, **S. Darmawan**, and M. K. Chin, "Matrix Analysis of 2-D Micro-resonator Lattice Optical Filters," *J. Quantum Electron.* Vol. 41, 1410-1418, (2005).
11. Y. M. Landobasa, **S. Darmawan**, and M. K. Chin, "Asymmetric Fano resonance and bistability for high extinction ratio, large modulation depth, and low power switching," *Optics Express*, Vol. 14, 12770-12781 (2006).
12. S. Y. Lee, **S. Darmawan**, C. W. Lee, and M. K. Chin, "Transformation between Directional Couplers and Multi-mode Interferometers based on Ridge Waveguides," *Optics Express*, Vol. 12, 3079-3085 (2004).
13. M. K. Chin, C. W. Lee, S. Y. Lee, and **S. Darmawan**, "High Index Contrast Waveguides and Devices," *Applied Optics*, Vol. 44, 3077-3086 (2005).

Conferences:

1. **S. Darmawan**, S. Y. Lee, C. W. Lee, and M. K. Chin, "Transformation Between Directional Couplers and Multi-mode Interferometers based on Ridge Waveguides," 4th International Symposium on Modern Optics and its Applications (ISMOA), Bandung, Indonesia, 2004.
2. **S. Darmawan**, S. Y. Lee, C. W. Lee, and M. K. Chin, "Transition and Comparison between Directional Couplers and Multimode Interference Couplers based on Ridge Waveguides," 4th Photonics Asia (SPIE) Conference, Beijing, China 2004.
3. **S. Darmawan**, Y. M. Landobasa, C. W. Lee, S. Y. Lee, and M. K. Chin**,** "Scattering Matrix Analysis for Cascaded Ring Enhanced Mach-Zehnder Interferometers," OSA Topical Meeting, San Diego, US, 2005.
4. Y. M. Landobasa, **S. Darmawan**, M. K. Chin, "Theoretical design of a 'perfect' filter based on coupled ring resonator arrays" Lasers and Electro-Optics, 2005. CLEO/Pacific Rim 2005, Tokyo, Japan.
5. **S. Darmawan** and M. K. Chin, "Box-like spectral output of nested ring feedback Mach-Zehnder interferometer" 6th International Conference on Numerical Simulation of Optoelectronic Devices - NUSOD 2006, Nanyang Technological University, Singapore.
6. **S. Darmawan**, Y. M. Landobasa, P. Dumon, R. Baets, and M. K. Chin,"Nested-ring Mach-Zehnder interferometer in silicon-on-insulator," SPIE Photonics Europe, Strasbourg, France, 2008.
7. **S. Darmawan**, Y. M. Landobasa, and M. K. Chin, "Bistability engineering in ring-coupled Mach-Zehnder interferometers for efficient all-optical switching," IEEE Photonics Global Singapore (2008).

REFERENCES

[1] A. Yariv, "Universal relations for coupling of optical power between microresonators and dielectric waveguides," *Electron. Lett.,* vol. 36, pp. 321-322, 2000.

[2] A. Yariv, "Critical coupling and its control in optical waveguide-ring resonator systems," *IEEE Photon. Technol. Lett.,* vol. 14, p. 483, 2002.

[3] B. E. Little, S. T. Chu, P. P. Absil, J. V. Hryniewicz, F. G. Johnson, F. Seiferth, D. Gill, V.Van, O.King, and M. Trakalo, "Very high-order microring resonator filters for WDM applications," *IEEE Photon. Technol. Lett.,* vol. 16, pp. 2263-2265, 2004.

[4] F. Xia, L. Sekaric, and Y. Vlasov, "Ultracompact optical buffers on a silicon chip," *Nat Photon,* vol. 1, pp. 65-71, 2007.

[5] M. Lipson, "Guiding, modulating, and emitting light on silicon - Challenges and Opportunities," *J. Lightwave Technol.,* vol. 23, pp. 4222-4238, 2005.

[6] J. E. Heebner, N. N. Lepeshkin, A. Schweinsberg, G. W. Wicks, R. W. Boyd, R. Grover, and P.-T. Ho, "Enhanced linear and nonlinear optical phase response of AlGaAs microring resonators," *Opt Lett.,* vol. 29, p. 769, 2004.

[7] P. P. Absil, J. V. Hryniewicz, B. E. Little, R. A. A. W. R. A. Wilson, L. G. A. J. L. G. Joneckis, and P. T. A. H. P. T. Ho, "Compact microring notch filters," *Photonics Technology Letters, IEEE,* vol. 12, pp. 398-400, 2000.

[8] C. Chung-Yen and L. Jay Guo, "A new interferometric sensor with ring-feedback MZI," in *Sensors, 2003. Proceedings of IEEE*, 2003, pp. 569-572 Vol.1.

[9] W. Green, R. Lee, G. DeRose, A. Scherer, and A. Yariv, "Hybrid InGaAsP-InP Mach-Zehnder Racetrack Resonator for Thermooptic Switching and Coupling Control," *Opt. Express,* vol. 13, pp. 1651-1659, 2005.

[10] G. Paloczi, Y. Huang, A. Yariv, and S. Mookherjea, "Polymeric Mach-Zehnder interferometer using serially coupled microring resonators," *Opt. Express,* vol. 11, pp. 2666-2671, 2003.

[11] Y. Lu, L. Xu, M. Shu, P. Wang, and J. Yao, "Proposal to produce coupled resonator-induced transparency and bistability using microresonator enhanced Mach-Zehnder interferometer," *IEEE Photon. Technol. Lett.,* vol. 20, p. 529, 2008.

[12] D. Taillaert, P. Bienstman, and R. Baets, "Compact efficient broadband grating coupler for silicon-on-insulator waveguides," *Opt. Lett.,* vol. 29, pp. 2749-2751, 2004.

[13] D. A. May-Arrioja, N. Bickel, and P. Likamwa, "Robust 2x2 multimode interference optical switch," *Opt. and Quantum Electron. Lett.,* vol. 38, pp. 557-566, 2006.

[14] Y. Chen and S. Blair, "Nonlinearity enhancement in finite coupled-resonator slow-light waveguides," *Opt. Express,* vol. 12, pp. 3353-3366, 2004.

[15] Y. M. Landobasa, P. Dumon, R. Baets, D. C. S. Lim, and M. K. Chin, "The transmission properties of one-bus two-ring devices," *IEICE Transactions on Electronics,* vol. E91-C(2), pp. 167-172, 2008.

[16] P. Dumon, W. Bogaerts, V. Wiaux, J. W. A.-J. Wouters, S. B. A.-S. Beckx, J. V. C. A.-J. V. Campenhout, D. T. A.-D. Taillaert, B. L. A.-B. Luyssaert, P. B. A.-P. Bienstman, D. V. T. A.-D. V. Thourhout, and R. B. A.-R. Baets, "Low-loss SOI photonic wires and ring resonators fabricated with deep UV lithography," *Photonics Technology Letters, IEEE,* vol. 16, pp. 1328-1330, 2004.

[17] B. L. Lawrence, M. Cha, J. U. Kang, W. Torruellas, G. Stegeman, G. Baker, J. Meth, and S. Etemad, "Large purely refractive nonlinear index of single crystal P-toluene sulphotane (PTS) at 1600 nm," *Electron. Lett.,* vol. 30, p. 447, 1994.

[18] K. K. Lee, D. R. Lim, L. C. Kimerling, J. Shin, and F. Cerrina, "Fabrication of ultralow-loss Si/SiO2 waveguides by roughness reduction," *Opt. Lett.,* vol. 26, pp. 1888-1890, 2001.

[19] F. R. Laughton, J. H. Marsh, and J. S. Roberts, "Intuitive model to include the effect of free-carrier absorption in calculating the two-photon absorption coefficient," *Appl. Phys. Lett.,* vol. 60, p. 166, 1992.

[20] T. K. Liang, L. R. Nunes, M. Tsuchiya, K. S. Abedin, T. Miyazaki, D. V. Thourhout, W. Bogaerts, P. Dumon, R. Baets, and H. K. Tsang, "High speed logic gate using two-photon absorption in silicon waveguides," *Opt. Commun.,* vol. 265, pp. 171-174, 2006.

[21] R. A. Soref and B. R. Bennett, "Kramers-Kronig analysis of E-O switching in silicon," *SPIE Integr. Opt. Circuit Eng. ,* vol. 704, pp. 32-37, 1987.

[22] R. A. Forber and E. Marom, "Symmetric directional coupler switches," *IEEE J. Quantum Electron.,* vol. QE-22, p. 911, 1986.

[23] L. B. Soldano and E. C. M. Pennings, "Optical Multi-mode Interference Devices based on Self-Imaging: Principles and Applications," *J. Lightwave Technology,* vol. 13, pp. 615-627, 199.

[24] Y. Ma, S. Park, L. Wang, and S. T. Ho, "Ultracompact Multimode Interference 3-dB Coupler with Strong Lateral Confinement by Deep Dry Etching," *IEEE Photon. Technol. Lett.,* vol. 12, pp. 492-494, 2000.

[25] M. K. Chin, "Polarization dependence in waveguide-coupled micro-resonators," *Opt. Express,* vol. 11, pp. 1724-1730, 2003.

[26] Y. Vlasov and S. McNab, "Losses in single-mode silicon-on-insulator strip waveguides and bends," *Opt. Express,* vol. 12, pp. 1622-1631, 2004.

[27] C. K. Madsen and J. H. Zhao, *Optical Filter Design and Analysis: A Signal Processing Approach*. New York: Wiley, 1999.

[28] P. Dumon, W. Bogaerts, D. V. Thourhout, D. Taillaert, V. Wiaux, S. Beckx, J. Wouters, and R. Baets, "Cascaded Mach-Zehnder Filters in Silicon-on-Insulator Photonic Wires fabricated with deep UV lithography," *European Conference on Optical Communication (ECOC), Th.(Post-deadline),* pp. 24-25, 2004.

[29] L. Caruso and I. Montrosset, "Analysis of a Racetrack MicroringResonator With MMI Coupler," *J. Lightwave Technol.,* vol. 21, p. 206, 2003.

[30] M.-k. Chin, C. Xu, and W. Huang, "Theoretical approach to a polarization-insensitive single-mode microring resonator," *Opt. Express,* vol. 12, pp. 3245-3250, 2004.

[31] D.-X. Xu, A. Densmore, P. Waldron, J. Lapointe, E. Post, A. Delâge, S. Janz, P. Cheben, J. H. Schmid, and B. Lamontagne, "High bandwidth SOI photonic wire ring resonators using MMI couplers," *Opt. Express,* vol. 15, pp. 3149-3155, 2007.

[32] Q. Xu, D. Fattal, and R. G. Beausoleil, "Silicon microring resonators with 1.5-?m radius," *Opt. Express,* vol. 16, pp. 4309-4315, 2008.

[33] J. E. Heebner and R. W. Boyd, "Enhanced all-optical switching by use of a nonlinear fiber ring resonator," *Opt Lett. ,* vol. 24, pp. 847-849, 1999.

[34] Y. Lu, J. Yao, X. Li, and P. Wang, "Tunable asymmetrical Fano resonance and bistability in a microcavity-resonator-coupled Mach Zehnder Interferometer," *Opt. Lett.,* vol. 30, p. 3069, 2005.

[35] S. Fan, "Sharp asymmetric line shapes in side-coupled waveguide-cavity systems," *Applied. Phys. Lett.,* vol. 80, p. 908, 2002.

[36] C. Chung-Yen and L. J. Guo, "Biochemical sensors based on polymer microrings with sharp asymmetrical resonance," *Appl. Phys. Lett.,* vol. 83, p. 1527, 2003.

[37] B. E. Little, S. T. Chu, H. A. Haus, J. A. F. J. Foresi, and J. P. A. L. J. P. Laine, "Microring resonator channel dropping filters," *Lightwave Technology, Journal of,* vol. 15, pp. 998-1005, 1997.

[38] B. E. Little, S. T. Chu, W. Pan, and Y. A. K. Y. Kokubun, "Microring resonator arrays for VLSI photonics," *Photonics Technology Letters, IEEE,* vol. 12, pp. 323-325, 2000.

[39] B. E. Little, S. T. Chu, W. Pan, D. A. R. D. Ripin, T. A. K. T. Kaneko, Y. A. K. Y. Kokubun, and E. A. I. E. Ippen, "Vertically coupled glass microring resonator channel dropping filters," *Photonics Technology Letters, IEEE,* vol. 11, pp. 215-217, 1999.

[40] J. E. Heebner, P. Chak, S. Pereira, J. E. Sipe, and R. W. Boyd, "Distributed and localized feedback in microresonator sequences for linear and nonlinear optics," *J. Opt. Soc. Am. B* vol. 21, pp. 1818-1832, 2004.

[41] J. E. Heebner and R. W. Boyd, "`Slow' and `fast' light in resonator-coupled waveguides," *J. Modern Optics,* vol. 49, pp. 2629-2636, 2002.

[42] J. K. S. Poon, J. Scheuer, S. Mookherjea, G. T. Paloczi, Y. Huang, and A. Yariv, "Matrix analysis of microring coupled-resonator optical waveguides," *Opt. Express,* vol. 12, pp. 90-103, 2004.

[43] J. K. S. Poon, H. Yanyi, G. T. Paloczi, and A. Y. A.-A. Yariv, "Soft lithography replica molding of critically coupled polymer microring resonators," *Photonics Technology Letters, IEEE,* vol. 16, pp. 2496-2498, 2004.

[44] J. K. S. Poon, L. Zhu, G. A. DeRose, and A. Yariv, "Polymer Microring Coupled-Resonator Optical Waveguides," *J. Lightwave Technol.,* vol. 24, p. 1843, 2006.

[45] J. K. Poon, L. Zhu, G. A. DeRose, and A. Yariv, "Transmission and group delay of microring coupled-resonator optical waveguides," *Opt. Lett.,* vol. 31, pp. 456-458, 2006.

[46] Y. Chen and S. Blair, "Nonlinear phase shift of cascaded microring resonators," *J. Opt. Soc. Am. B,* vol. 20, pp. 2125-2132, 2003.

[47] F. Xia, M. Rooks, L. Sekaric, and Y. Vlasov, "Ultra-compact high order ring resonator filters using submicron silicon photonic wires for on-chip optical interconnects," *Opt. Express,* vol. 15, pp. 11934-11941, 2007.

[48] R. Grover, V. Van, T. A. Ibrahim, P. P. Absil, L. C. Calhoun, F. G. Johnson, J. V. Hryniewicz, and P.-T. Ho, "Parallel-cascaded semiconductor microring resonators for high-order and wide-FSR filters," *J. Lightwave Technol.,* vol. 20, pp. 900-905, 2002.

[49] R. Orta, P. Savi, R. Tascone, and D. T. A.-D. Trinchero, "Synthesis of multiple-ring-resonator filters for optical systems," *Photonics Technology Letters, IEEE,* vol. 7, pp. 1447-1449, 1995.

[50] A. Melloni, "Synthesis of a parallel-coupled ring-resonator filter," *Opt. Lett.,* vol. 26, pp. 917-919, 2001.

[51] A. Melloni and M. Martinelli, "Synthesis of direct-coupled-resonators bandpass filters for WDM systems," *Lightwave Technology, Journal of,* vol. 20, pp. 296-303, 2002.

[52] Q. Xu, B. Schmidt, J. Shakya, and M. Lipson, "Cascaded silicon micro-ring modulators for WDM optical interconnection," *Opt. Express,* vol. 14, pp. 9431-9435, 2006.

[53] J. Scheuer, G. T. Paloczi, J. K. S. Poon, and A. Yariv, "Coupled Resonator Optical Waveguides: Toward the Slowing and Storage of Light," *Opt. Photon. News,* vol. 16, pp. 36-40, 2005.

[54] A. Yariv, Y. Xu, R. K. Lee, and A. Scherer, "Coupled-resonator optical waveguide: a proposal and analysis," *Opt. Lett. ,* vol. 24, pp. 711-713 1999.

[55] J. V. Hryniewicz, P. P. Absil, B. E. Little, R. A. Wilson, and P.-T. Ho, "Higher order filter response in coupled microring resonators," *Higher order filter response in coupled microring resonators,* vol. 12, pp. 320-322, 2000.

[56] B. E. Little, S. T. Chu, J. V. Hryniewicz, and P. P. Absil, "Filter synthesis for periodically coupled microring resonators," *Opt. Lett.,* vol. 25, pp. 344-346, 2000.

[57] G. Griffel, "Synthesis of optical filters using ring resonator arrays," *IEEE Photon. Technol. Lett. ,* vol. 12, pp. 810-812, 2000.

[58] J. Niehusmann, A. Vörckel, P. H. Bolivar, T. Wahlbrink, W. Henschel, and H. Kurz, "Ultrahigh-quality-factor silicon-on-insulator microring resonator," *Opt. Lett. 29,* vol. 29, pp. 2861-2863, 2004.

[59] W. Bogaerts, R. Baets, P. Dumon, V. A. W. V. Wiaux, S. A. B. S. Beckx, D. A. T. D. Taillaert, B. A. L. B. Luyssaert, J. A. V. C. J. Van Campenhout, P. A. B. P. Bienstman, and D. A. V. T. D. Van Thourhout, "Nanophotonic waveguides in silicon-on-insulator fabricated with CMOS technology," *J. Lightwave Technol.,* vol. 23, pp. 401-412, 2005.

[60] E. Dulkeith, F. Xia, L. Schares, W. M. J. Green, and Y. A. Vlasov, "Group index and group velocity dispersion in silicon-on-insulator photonic wires," *Opt. Express,* vol. 14, pp. 3853-3863, 2006.

[61] T. Tsuchizawa, K. Yamada, H. Fukuda, T. A. W. T. Watanabe, A. J.-i. T. Jun-ichi Takahashi, M. A. T. M. Takahashi, T. A. S. T. Shoji, E. A. T. E. Tamechika, S. A. I. S. Itabashi, and H. A. M. H. Morita, "Microphotonics devices based on silicon microfabrication technology," *Selected Topics in Quantum Electronics, IEEE Journal of,* vol. 11, pp. 232-240, 2005.

[62] J. M. Choi, R. K. Lee, and A. Yariv, "Control of critical coupling in a ring resonator-fiber configuration: application to wavelength-selective switching, modulation, amplification, and oscillation," *Opt Lett.,* vol. 26, p. 1236, 2001.

[63] V. Menon, W. Tong, and S. R. Forrest, "Control of quality factor and critical coupling in microring resonators through integration of a semiconductor optical amplifier," *IEEE Photon. Technol. Lett.,* vol. 16, p. 1343, 2004.

[64] D. G. Rabus, Z. Bian, and A. Shakouri, "A GaInAsP-InP double-ring resonator coupled laser," *IEEE Photon. Technol. Lett.,* vol. 17, p. 1770, 2005.

[65] K. Oda, N. Takato, H. Toba, and K. A. N. K. Nosu, "A wide-band guided-wave periodic multi/demultiplexer with a ring resonator for optical FDM transmission systems," *Lightwave Technology, Journal of,* vol. 6, pp. 1016-1023, 1988.

[66] M. Kohtoku, S. Oku, Y. Kadota, Y. A. S. Y. Shibata, and Y. A. Y. Y. Yoshikuni, "200-GHz FSR periodic multi/demultiplexer with flattened transmission and rejection band by using a Mach-Zehnder interferometer with a ring resonator," *Photonics Technology Letters, IEEE,* vol. 12, pp. 1174-1176, 2000.

[67] J. Yang, F. Wang, X. Jiang, H. Qu, M. Wang, and Y. Wang, "Influence of loss on linearity of microring-assisted Mach-Zehnder modulator," *Opt. Express,* vol. 12, pp. 4178-4188, 2004.

[68] V. Van, W. H. Hermann, and P. T. Ho, "Linearized microring-loaded Mach-Zehnder modulator with RF gain," *J. Lightwave. Technol.,* vol. 24, pp. 1850-1854, 2006.

[69] X. Xiaobo, J. Khurgin, K. Jin, and F. S. C. A.-F.-S. Chow, "Linearized Mach-Zehnder intensity modulator," *Photonics Technology Letters, IEEE,* vol. 15, pp. 531-533, 2003.

[70] D. D. Smith, H. Chang, K. A. Fuller, A. T. Rosenberger, and R. W. Boyd, "Coupled-resonator-induced transparency," *Phys. Rev. A,* vol. 69, p. 063804, 2004.

[71] A. Naweed, G. Farca, S. I. Shopova, and A. T. Rosenberger, "Induced transparency and absorption in coupled whispering-gallery microresonators," *Phys. Rev. A,* vol. 71, 2005.

[72] L. Maleki, A. B. Matsko, A. A. Savchenkov, and V. S. Ilchenko, "Tunable delay line with interacting whispering-gallery-mode resonators," *Opt Lett.,* vol. 29, 2004.

[73] Q. Xu, S. Sandhu, M. L. Povinelli, J. Shakya, S. Fan, and M. Lipson, "Experimental realization of an on-chip all-optical analogue to electromagnetically induced transparency," *Phys. Rev. Lett.,* vol. 96, p. 123901, 2006.

[74] K. Totsuka, N. Kobayashi, and M. Tomita, "Slow light in coupled-resonator-induced transparency," *Phys. Rev. Lett.,* vol. 98, p. 213904, 2007.

[75] Y. M. Landobasa, Desmond C. S. Lim, P. Dumon, R. Baets, and M. K. Chin, "Finesse enhancement in silicon-on-insulator two-ring resonator system," *Appl. Phys. Lett.,* vol. 92, p. 101122, 2008.

[76] L. Y. Mario, D. C. S. Lim, and M. K. Chin, "Proposal of ultranarrow passband using two coupled rings," *IEEE. Phot. Technol. Lett.,* vol. 19, p. 1688, 2007.

[77] F. Sanchez, "Optical bistability in a 2x2 coupler fiber ring resonator: parametric formulation," *Opt. Commun.,* vol. 142, p. 211, 1997.

[78] S. Darmawan, S. Y. Lee, C. W. Lee, and M. K. Chin, "Transformation of Directional Couplers to Multi-mode Interferometers based on Ridge Waveguides and Its Applications," *Journal of Nonlinear Optical Physics & Materials,* vol. 14, pp. 221-235, 2005.

[79] S. Darmawan, S. Y. Lee, C. W. Lee, and M. K. Chin, "A Rigorous Comparative Analysis of Directional Couplers and Multi-Mode Interferometers Based On Ridge Waveguides," *Journal of Selected Topics on Quantum Electronics,* vol. 11, pp. 466-475, 2005.

[80] A. A. Tovar and L. W. Casperson, "Generalized Sylvester theorems for periodic applications in matrix optics," *J. Opt. Soc. Am. A,* vol. 12, p. 578, 1995.

[81] C. J. Kaalund and P. Gang-Ding, "Pole-zero diagram approach to the design of ring resonator-based filters for photonic applications," *Lightwave Technology, Journal of,* vol. 22, pp. 1548-1559, 2004.

[82] E. A. J. Marcatili, "Bends in optical dielectric guides," *Bell Syst. Techn. J.,* vol. 48, pp. 2071-2101, 1969.

[83] L. Fabry and A. Perot, "A multipass interferometer," *Ann. Chim. Phys.,* vol. 16, p. 115, 1899.

[84] F. Gires and P. Tournois, "Interfromtre utilisable pour la compression dimpulsions lumineuses modules en frquence," *C. R. Acad. Sci.,* vol. 258, p. 6112, 1964.

[85] H. Li and K. Oguzu, "Analysis of optical instability in a double-coupler nonlinear fiber ring resonator," *Opt. Commun.,* vol. 157, pp. 27-32, 1998.

[86] H.-A. Bachor, M. D. Levenson, D. F. Walls, S. H. Perlmutter, and R. M. Shelby, "Quantum nondemolition measurements in an optical-fiber ring resonator," *Phys. Rev. A,* vol. 38, pp. 180-190, 1988.

[87] J. E. Heebner, V. Wong, S. Schweinsberg, R. W. Boyd, and D. J. Jackson, "Optical transmission characteristics of fiber ring resonators," *IEEE J. Quantum Electron.,* vol. 40, pp. 726-730, 2004.

[88] L. F. Stokes and M. Chodorow, "All-single-mode fiber resonator," *Opt. Lett.,* vol. 7, p. 288, 1982.

[89] R. M. Shelby, M. D. Levenson, and S. H. Perlmutter, "Bistability and other effects in nonlinear fiber-optic ring resonator," *J. Opt. Soc. Am. B,* vol. 5, pp. 347-357, 1988.

[90] J. Capmany, F. J. Fraile-Peláez, and M. A. Muriel, "Optical bistability and differential amplification in nonlinear fiber resonators," *IEEE J. Quantum Electron.,* vol. 30, pp. 2578-2588, 1994.

[91] Y. Ohtsuka, "Optical coherence effects on a fiber-sensing Fabry Pérot interferometer," *Appl. Opt.,* vol. 21, pp. 4316-4320, 1982.

[92] L. J. Cimini, L. J. Greenstein, and A. A. M. Saleh, "Optical equalization for high-bit-rate fiber-optic communications," *IEEE Photon. Technol. Lett.,* vol. 2, p. 200, 1990.

[93] B. Crosignani, B. Daino, P. Diporto, and S. Wabnitz, "Optical multistability in a fiber-optic passive-loop resonator," *Opt. Commun.,* vol. 59, pp. 309-312, 1986.

[94] S. Dilwali and G. S. Pandian, "Pulse response of a fiber dispersion equalizing scheme based on an optical resonator," *IEEE Photon. Technol. Lett.,* vol. 4, p. 942, 1992.

[95] B. Crosignani and A. Yariv, "Time-dependent analysis of a fiber-optic passive-loop resonator," *Opt. Lett.,* vol. 11, p. 251, 1986.

[96] P. Urquhart, "Compound optical-fiber-based resonators," *J. Opt. Soc. Am. A,* vol. 5, pp. 803-812, 1988.

[97] F. Sanchez, "Matrix algebra for all-fiber optical resonators," *J. Lightwave Technol.,* vol. 9, pp. 838-844, 1991.

[98] Y. H. Ja, "Optical bistability in a two-coupler fiber ring resonator by using degenerate two-wave mixing," *Opt Lett.,* vol. 17, p. 1337, 1992.

[99] V. Van, T. A. Ibrahim, K. Ritter, P. P. Absil, F. G. Johnson, R. Grover, J. Goldhar, and P.-T. Ho, "All-optical nonlinear switching in GaAs-AlGaAs microring resonators," *IEEE Photon. Technol. Lett.,* vol. 14, p. 74, 2002.

[100] M. K. Chin, C. Youtsey, W. Zhao, T. Pierson, Z. Ren, S. L. Wu, L. Wang, Y. G. Zhao, and S. T. Ho, "GaAs microcavity channel-dropping filter based on a race-track resonator," *IEEE Photon. Technol. Lett.,* vol. 11, p. 1620, 1999.

[101] V. Van, P. P. Absil, J. V. Hryniewicz, and P.-T. Ho, "Propagation loss in single-mode GaAs-AlGaAs microring resonators: Measurement and model," *J. Lightwave Technol.,* vol. 19, pp. 1734-1739, 2001.

[102] P. P. Absil, J. V. Hryniewicz, B. E. Little, P. S. Cho, R. A. Wilson, L. G. Joneckis, and P.-T. Ho, "Wavelength conversion in GaAs micro-ring resonators," *Opt Lett.,* vol. 25, p. 554, 2000.

[103] T. A. Ibrahim, W. Cao, Y. Kim, J. Li, J. Goldhar, P.-T. Ho, and C. H. Lee, "Lightwave switching in semiconductor microring devices by free carrier injection," *J. Lightwave Technol.,* vol. 21, pp. 2997-3003, 2003.

[104] D. G. Rabus and M. Hamacher, "MMI-coupled ring resonators in GaInAsP-InP," *IEEE Photon. Technol. Lett.,* vol. 13, pp. 812-814, 2001.

[105] S. Mikroulis, H. Simos, E. Roditi, A. Chipouras, and D. Syvridis, "40-Gb/s NRZ and RZ operation of an all-optical and logic gate based on a passive InGaAsP/InP microring resonator," *J. Lightwave Technol.,* vol. 24, pp. 1159-1164, 2006.

[106] D. G. Rabus, M. Hamacher, U. Troppenz, and H. Heidrich, "Optical filters based on ring resonators with integrated semiconductor optical amplifiers in GaInAsP-InP," *IEEE J. Selected Topics in Quant. Electron. ,* vol. 8, pp. 1405-1411, 2002.

[107] G. Griffel, J. H. Abeles, R. J. Menna, A. M. A. B. A. M. Braun, J. C. A. C. J. C. Connolly, and M. A. K. M. King, "Low-threshold InGaAsP ring lasers fabricated using bi-level dry etching," *Photonics Technology Letters, IEEE,* vol. 12, pp. 146-148, 2000.

[108] U. Troppenz, M. Hamacher, D. G. Rabus, and H. A. H. H. Heidrich, "All-active InGaAsP/InP ring cavities for widespread functionalities in the wavelength domain," in *Indium Phosphide and Related Materials Conference, 2002. IPRM. 14th*, 2002, pp. 475-478.

[109] W.-S. Choi, W. Zhao, J.-W. Bae, I. Adesida, B.-A. Yu, Y. L. Lee, and J.-H. Jang, "Micro-Racetrack Notch Filters Based on InGaAsP/InP High Mesa Optical Waveguides," *Jpn. J. Appl. Phys.,* vol. 46, pp. 2434-2439, 2006.

[110] Z. Bian, B. Liu, and A. Shakouri, "InP-based passive ring-resonator-coupled lasers," *IEEE J. Quantum Electron.,* vol. 39, pp. 859-865, 2003.

[111] F. Xia, L. Sekaric, and Y. A. Vlasov, "Mode conversion losses in silicon-on-insulator photonic wire based racetrack resonators," *Opt. Express,* vol. 14, pp. 3872-3886, 2006.

[112] H. Rong, Y.-H. Kuo, S. Xu, A. Liu, R. Jones, M. Paniccia, O. Cohen, and O. Raday, "Monolithic integrated Raman silicon laser," *Opt. Express,* vol. 14, pp. 6705-6712, 2006.

[113] X. Fengnian, S. Lidija, O. B. Martin, and V. Yurii, "Coupled resonator optical waveguides based on silicon-on-insulator photonic wires," *Applied Physics Letters,* vol. 89, p. 041122, 2006.

[114] A. Morand, Y. Zhang, B. Martin, K. Phan Huy, D. Amans, P. Benech, J. Verbert, E. Hadji, and J.-M. Fédéli, "Ultra-compact microdisk resonator filters on SOI substrate," *Opt. Express,* vol. 14, pp. 12814-12821, 2006.

[115] Q. Xu and M. Lipson, "All-optical logic based on silicon micro-ring resonators," *Opt. Express,* vol. 15, pp. 924-929, 2007.

[116] L. Martinez and M. Lipson, "High confinement suspended micro-ring resonators in silicon-on-insulator," *Opt. Express,* vol. 14, pp. 6259-6263, 2006.

[117] Q. Xu, J. Shakya, and M. Lipson, "Direct measurement of tunable optical delays on chip analogue to electromagnetically induced transparency," *Opt. Express,* vol. 14, pp. 6463-6468, 2006.

[118] S. Manipatruni, Q. Xu, and M. Lipson, "PINIP based high-speed high-extinction ratio micron-size silicon electrooptic modulator," *Opt. Express,* vol. 15, pp. 13035-13042, 2007.

[119] C. A. Barrios, V. R. Almeida, R. Panepucci, and M. A. L. M. Lipson, "Electrooptic modulation of silicon-on-insulator submicrometer-size waveguide devices," *Lightwave Technology, Journal of,* vol. 21, pp. 2332-2339, 2003.

[120] L. Chen, N. Sherwood-Droz, and M. Lipson, "Compact bandwidth-tunable microring resonators," *Opt. Lett.,* vol. 32, pp. 3361-3363, 2007.

[121] P. Dong, S. F. Preble, and M. Lipson, "All-optical compact silicon comb switch," *Opt. Express,* vol. 15, pp. 9600-9605, 2007.

[122] Y. Okawachi, M. Foster, J. Sharping, A. Gaeta, Q. Xu, and M. Lipson, "All-optical slow-light on a photonic chip," *Opt. Express,* vol. 14, pp. 2317-2322, 2006.

[123] K. De Vos, I. Bartolozzi, E. Schacht, P. Bienstman, and R. Baets, "Silicon-on-Insulator microring resonator for sensitive and label-free biosensing," *Opt. Express,* vol. 15, pp. 7610-7615, 2007.

[124] S. Ju-Han, K. Do-Hwan, and L. Sang-Shin, "Polymeric Ring Resonator Enabling Electrically Variable Extinction Ratio," in *Lasers and Electro-Optics Society, 2006. LEOS 2006. 19th Annual Meeting of the IEEE*, 2006, pp. 530-531.

[125] G.-D. Kim and S.-S. Lee, "Integrated Photonic Microwave Channel Selective Filter Using a Switch Based on Tunable Ring Resonators," in *Lasers and Electro-Optics Society, 2007. LEOS 2007. The 20th Annual Meeting of the IEEE*, 2007, pp. 397-398.

[126] K. Do-Hwan, I. Jung-Gyu, L. Sang-Shin, S. W. A. A. S. W. Ahn, and A. K.-D. L. Ki-Dong Lee, "Polymeric microring resonator using nanoimprint technique based on a stamp incorporating a smoothing buffer Layer," *Photonics Technology Letters, IEEE,* vol. 17, pp. 2352-2354, 2005.

[127] J. Scheuer, G. T. Paloczi, A. Yariv, A. C. Z. Cheng Zhang, and L. R. A. D. L. R. Dalton, "Reconfigurable wavelength-selective reflector consisting of coupled polymeric microring resonators," in *Lasers and Electro-Optics, 2005. (CLEO). Conference on*, 2005, pp. 437-439 Vol. 1.

[128] S. Mookherjea, "Principles and applications of coupled microring optical resonators," in *Fibres and Optical Passive Components, 2005. Proceedings of 2005 IEEE/LEOS Workshop on*, 2005, pp. 51-57.

[129] S. Mookherjea, "Mode cycling in microring optical resonators," *Opt. Lett.,* vol. 30, pp. 2751-2753, 2005.

[130] D. Rezzonico, M. Jazbinsek, A. Guarino, O. P. Kwon, and P. Günter, "Electro-optic Charon polymeric microring modulators," *Opt. Express,* vol. 16, pp. 613-627, 2008.

[131] Y. Huang, G. Paloczi, J. Scheuer, and A. Yariv, "Soft lithography replication of polymeric microring optical resonators," *Opt. Express,* vol. 11, pp. 2452-2458, 2003.

[132] L. J. Guo, "Recent progress in nanoimprint technology and its applications," *J. Phys. D: Appl. Phys. ,* vol. 37, pp. 123-141, 2004.

[133] C.-y. Chao and L. J. Guo, "Polymer microring resonators fabricated by nanoimprint technique," *J. Vac. Sci. Technol. B,* vol. 20, pp. 2862-2866, 2002.

[134] D. J. W. Klunder, F. S. Tan, T. v. d. Veen, H. F. Bulthuis, G. Sengo, B. Docter, H. J. W. M. Hoekstra, and A. Driessen, "Experimental and Numerical Study of SiON Microresonators With Air and Polymer Cladding," *J. Lightwave Technol.,* vol. 21, p. 1099, 2003.

[135] C. A. Barrios, B. Sánchez, K. B. Gylfason, A. Griol, H. Sohlström, M. Holgado, and R. Casquel, "Demonstration of slot-waveguide structures on silicon nitride / silicon oxide platform," *Opt. Express,* vol. 15, pp. 6846-6856, 2007.

[136] T. Barwicz, M. A. Popovic, M. R. Watts, P. T. A. R. P. T. Rakich, E. P. A. I. E. P. Ippen, and H. I. A. S. H. I. Smith, "Fabrication of add-drop filters based on frequency-matched microring resonators," *Lightwave Technology, Journal of,* vol. 24, pp. 2207-2218, 2006.

[137] D. J. W. Klunder, E. Krioukov, F. S. Tan, T. van der Veen, H. F. Bulthuis, G. Sengo, C. Otto, H. J. W. M. Hoekstra, and A. Driessen, "Vertically and laterally waveguide-coupled cylindrical microresonators in Si3N4 on SiO2 technology," *Applied Physics B: Lasers and Optics,* vol. 73, pp. 603-608, 2001.

[138] D. K. Sparacin, J. P. Lock, H. Ching-yin, K. K. A. G. K. K. Gleason, L. C. A. K. L. C. Kimerling, and J. A. M. J. Michel, "Trimming of silicon nitride microring resonators with a polysilane top cladding," in *Group IV Photonics, 2005. 2nd IEEE International Conference on*, 2005, pp. 117-119.

[139] R. Amatya, C. W. Holzwarth, H. I. Smith, and R. J. A. R. R. J. Ram, "Efficient Thermal Tuning for Second-order Silicon Nitride Microring Resonators," in *Photonics in Switching, 2007*, 2007, pp. 149-150.

[140] A. Yalcin, K. C. Popat, J. C. Aldridge, T. A. A. D. T. A. Desai, J. A. H. J. Hryniewicz, N. A. C. N. Chbouki, B. E. A. L. B. E. Little, A. O. K. Oliver King, V. A. V. V. Van, A. S. C. Sai Chu, D. A. G. D. Gill, M. A. A.-W. M. Anthes-Washburn, M. S. A. U. M. S. Unlu, and B. B. A. G. B. B. Goldberg, "Optical sensing of biomolecules using microring resonators," *Selected Topics in Quantum Electronics, IEEE Journal of,* vol. 12, pp. 148-155, 2006.

[141] S. T. Chu, W. Pan, T. Kaneko, Y. A. K. Y. Kokubun, B. E. A. L. B. E. Little, D. A. R. D. Ripin, and E. A. I. E. Ippen, "Fabrication of vertically coupled glass microring resonator channel dropping filters," in *Optical Fiber Communication Conference, 1999, and the International Conference on Integrated Optics and Optical Fiber Communication. OFC/IOOC '99. Technical Digest*, 1999, pp. 107-108 vol.3.

[142] C. Sai Tak, B. E. Little, P. Wugen, T. A. K. T. Kaneko, and Y. A. K. Y. Kokubun, "Second-order filter response from parallel coupled glass microring resonators," *Photonics Technology Letters, IEEE,* vol. 11, pp. 1426-1428, 1999.

[143] C. Sai Tak, B. E. Little, P. Wugen, T. A. K. T. Kaneko, and Y. A. K. Y. Kokubun, "Cascaded microring resonators for crosstalk reduction and spectrum cleanup in add-drop filters," *Photonics Technology Letters, IEEE,* vol. 11, pp. 1423-1425, 1999.

[144] L. Y. Mario, S. Darmawan, and M. K. Chin, "Asymmetric Fano resonance and bistability for high extinction ratio, large modulation depth, and low power switching," *Opt. Express,* vol. 14, pp. 12770-12781, 2006.

[145] K. L. Lee and C. Shu, "Switching-wavelength pulse source constructed from a dispersion-managed SOA fiber ring laser," *Photonics Technology Letters, IEEE,* vol. 15, pp. 513-515, 2003.

[146] S. Mikroulis, E. Roditi, and D. Syvridis, "Direct Modulation Properties of 1.55um InGaAsP/InP Microring Lasers," *Lightwave Technology, Journal of,* vol. 26, pp. 251-256, 2008.

[147] L. Liao, D. Samara-Rubio, M. Morse, A. Liu, D. Hodge, D. Rubin, U. D. Keil, and T. Franck, "High speed silicon Mach-Zehnder modulator," *Opt. Express. ,* vol. 13, pp. 3130-3135, 2005.

[148] M. K. Chin, C. Youtsey, W. Zhao, T. Pierson, Z. Ren, S. L. Wu, L. Wang, Y. G. Zhou, and S. T. Ho, "GaAs microcavity channel-dropping filter based on a race-track resonator," *IEEE Photon. Technol. Lett.,* vol. 11, p. 1620, 1999.

[149] H. Takahashi, R. Inohara, T. Hisamitsu, M. A. H. M. Hattori, K. A. N. K. Nishimura, and M. A. U. M. Usami, "Expansion of passband of tunable chromatic dispersion compensator based on ring resonators using negative group delay peak," in *Optical Fiber Communication Conference, 2004. OFC 2004*, 2004.

[150] K. Suzuki, I. Nakamatsu, T. Shimoda, S. A. T. S. Takaesu, J. A. U. J. Uhioda, E. A. M. E. Mizuki, M. A. H. M. Horie, Y. A. U. Y. Urino, and H. A. Y. H. Yamazaki, "WDM tuneable dispersion compensator with PLC ring resonators," in *Optical Fiber Communication Conference, 2004. OFC 2004*, 2004.

[151] C. K. Madsen, E. J. Laskowski, J. Bailey, M. A. A. C. M. A. Cappuzzo, S. A. C. S. Chandrasekhar, L. T. A. G. L. T. Gomez, A. A. G. A. Griffin, P. A. O. P. Oswald, and L. W. A. S. L. W. Stulz, "Compact integrated tunable dispersion compensators," in *Lasers and Electro-Optics Society, 2002. LEOS 2002. The 15th Annual Meeting of the IEEE*, 2002, pp. 570-571 vol.2.

[152] S. Sandhu, M. L. Povinelli, M. F. Yanik, and S. Fan, "Dynamically tuned coupled-resonator delay lines can be nearly dispersion free," *Opt. Lett.,* vol. 31, pp. 1985-1987, 2006.

[153] C.-Y. Chao and L. J. Guo, "A new interferometric sensor with ring-feedback MZI," *in Proceedings of IEEE on Sensors,* vol. 1, pp. 569-572, 2003.

[154] R. W. Boyd and J. E. Heebner, "Sensitive disk resonator photonic biosensor," *Appl. Opt.,* vol. 40, pp. 5742–5747, 2001.

[155] W. W. Tang and C. Shu, "All-optical regenerative mode-locking at adjustable repetition rates from a SOA fiber ring laser," in *Lasers and Electro-Optics, 2003. CLEO/Pacific Rim 2003. The 5th Pacific Rim Conference on*, 2003, p. 442 vol.2.

[156] K. Amarnath, R. Grover, S. Kanakaraju, and A. P.-T. H. Ping-Tong Ho, "Electrically pumped InGaAsP/InP microring optical amplifiers and lasers with surface passivation," in *Lasers and Electro-Optics, 2005. (CLEO). Conference on*, 2005, pp. 1846-1848 Vol. 3.

[157] K. Amarnath, R. Grover, S. Kanakaraju, and A. P.-T. H. Ping-Tong Ho, "Electrically pumped InGaAsP-InP microring optical amplifiers and lasers with surface passivation," *Photonics Technology Letters, IEEE,* vol. 17, pp. 2280-2282, 2005.

[158] L. R. Chen and J. Azana, "Electrically tunable, dual-wavelength actively mode-locked SOA-based fiber ring laser with superimposed fiber Bragg gratings," in *Lasers and Electro-Optics Society, 2003. LEOS 2003. The 16th Annual Meeting of the IEEE*, 2003, pp. 1056-1057 vol.2.

[159] I. Stamataki, S. Mikroulis, A. Kapsalis, and D. A. S. D. Syvridis, "Investigation on the Multimode Dynamics of InGaAsP-InP Microring Lasers," *Quantum Electronics, IEEE Journal of,* vol. 42, pp. 1266-1273, 2006.

[160] B. A. Yu, W. Shin, Y. L. Lee, T. J. A. E. T. J. Eom, Y. C. A. N. Y. C. Noh, J. A. L. J. Lee, and D. K. A. K. D. K. Ko, "Multiwavelength switchable SOA-fibre ring laser using digital micromirrors," *Electronics Letters,* vol. 42, pp. 742-743, 2006.

[161] Y. Bong-Ahn, K. Jaejoong, C. Seunghwan, A. S.-W. S. Seung-Woo Seo, and A. B. L. Byoungho Lee, "Multiwavelength-switchable SOA-fibre ring laser using sampled Hi-Bi fibre grating," *Electronics Letters,* vol. 39, pp. 649-650, 2003.

[162] B. Corbett, "Spectral characteristics of single-In0.7Ga0.3As quantum-well microring lasers," *Photonics Technology Letters, IEEE,* vol. 10, pp. 3-5, 1998.

[163] C. W. Tee, K. A. Williams, R. V. Penty, I. H. A. W. I. H. White, M. A. H. M. Hamacher, U. A. T. U. Troppenz, and H. A. H. H. Heidrich, "Vertically-coupled Microring Laser Array for Dual-Wavelength Generation," in *Optical Society of America - CLEO/QELS Conference*, 2007, pp. 1-2.

[164] L. Bin, A. Shakouri, and J. E. Bowers, "Wide tunable double ring resonator coupled lasers," *Photonics Technology Letters, IEEE,* vol. 14, pp. 600-602, 2002.

[165] A. Kapsalis, I. Stamataki, S. Mikroulis, D. A. S. D. Syvridis, and M. A. H. M. Hamacher, "Widely Tunable All-Active Microring Lasers," *Photonics Technology Letters, IEEE,* vol. 18, pp. 2641-2643, 2006.

[166] E. H. Miller, "A note on reflector arrays (Periodical style—Accepted for publication)," *IEEE Trans. Antennas Propagat., to be published.*

[167] Y. M. Landobasa, S. Darmawan, and M. K. Chin, "Matrix analysis of 2-D micro-resonator lattice optical filters," *J. Quantum Electron,* vol. 41, pp. 1410-1418, 2005.

[168] N. Yoshimoto, Y. Shibata, S. Oku, S. Kondo, and Y. Noguchi, "Design and demonstration of polarization-insensitive Mach-Zehnder switch using a lattice-matched InGaAlAs/InAlAs MQW and deep-etched high-mesa waveguide structure," *J. Lightwave Technol.,* vol. 17, pp. 1662 - 1669, 1999.

[169] L. Chun-Fei and B. Alireza, "Finesse-enhanced ring resonator coupled Mach-Zehnder Interferometer all-optical switches," *Chin. Phys. Lett. ,* vol. 21, pp. 90-93, 2004.

[170] N. V. Pedersen, K. B. Jakobsen, and M. Vaa, "Mode-locked 1.5um semiconductor optical amplifier fiber ring," *Lightwave Technology, Journal of,* vol. 14, pp. 833-838, 1996.

[171] S. Darmawan, Y. Landobasa, and M. Chin, "Phase engineering for ring enhanced Mach-Zehnder interferometers," *Opt. Express,* vol. 13, pp. 4580-4588, 2005.

[172] S. Darmawan and M. K. Chin, "Critical coupling, oscillation, reflection, and transmission in optical waveguide-ring resonator systems," *J. Opt. Soc. Am. B,* vol. 23, pp. 834-841, 2006.

[173] M. Hamacher, U. Troppenz, and H. Heidrich, "Optically amplifying microring resonator components based on GaInaAsP/InP: challenges and perspectives," in *IEEE Semiconductor Conference - CAS Proceedings (2004).* 2004.

[174] H. Ma, X. J. Yi, and S. H. Chen, "1.55 μm AlGaInAs/InP polarization insensitive optical amplifier with tensile strained wells grown by MOCVD," *Optical and Quantum Electron.,* vol. 35, pp. 1107-1112, 2003.

[175] M. A. Dupertuis, J. L. Pleumeekers, T. P. Hessler, P. E. A. S. P. E. Selbmann, B. A. D. B. Deveaud, B. A. D. B. Dagens, and J. Y. A. E. J. Y. Emery, "Extremely fast high-gain and low-current SOA by optical speed-up at transparency," *Photonics Technology Letters, IEEE,* vol. 12, pp. 1453-1455, 2000.

[176] M. A. Dupertuis, J. L. Pleumeekers, T. P. Hessler, P. E. A. S. P. E. Selbmann, B. A. D. B. Deveaud, B. A. D. B. Dagens, and J. Y. A. E. J. Y. Emery, "Extremely fast, high-gain and low-current semiconductor optical amplifier by optical speed-up at transparency," in *Lasers and Electro-Optics, 2000. (CLEO 2000). Conference on*, 2000, p. 470.

[177] G. T. Paloczi, Y. Huang, and A. Yariv, "Polymeric Mach-Zehnder interferometer using serially coupled microring resonators," *Opt. Express,* vol. 11, pp. 2666-2671, 2003.

[178] G. Lenz, B. J. Eggleton, C. R. Giles, C. K. Madsen, and R. E. Slusher, "Dispersive properties of optical filters for WDM systems," *IEEE J. Quantum Electron,* vol. 34, pp. 1390-1402, 1998.

[179] J. E. Heebner, "Nonlinear Optical Whispering Gallery Microresonators for Photonics," in *PhD thesis*, 2003, p. 199.

[180] L. Wei, S. Song, and Y. N. Wang, "Influence of nonlinear absorption effects on optical bistability semiconductor ring resonators," *Opt. & Laser Technol.,* vol. 37, pp. 432-437, 2004.

[181] H. Tazawa and W. H. Steier, "Bandwidth of Linearized Ring Resonator Assisted Mach–Zehnder Modulator," *IEEE Photon. Technol. Lett.,* vol. 17, p. 1851, 2005.

[182] M. Notomi, A. Shinya, S. Mitsugi, G. Kira, E. Kuramochi, and T. Tanabe, "Optical bistable switching action of Si high-Q photonic-crystal nanocavities," *Opt. Express,* vol. 13, pp. 2678-2687, 2005.

[183] A. R. Cowan and J. F. Young, "Optical bistability involving photonic crystal microcavities and Fano line shapes," *Phys. Rev. E,* vol. 68, p. 46606, 2003.

[184] S. Fan, W. Suh, and J. D. Joannopoulos, "Temporal coupled-mode theory for the Fano resonance in optical resonators," *J. Opt. Soc. Am. A,* vol. 20, pp. 569-572, 2003.

[185] L. Zhou and A. W. Poon, "Fano resonance-based electrically reconfigurable add-drop filters in silicon microring resonator-coupled Mach-Zehnder interferometers," *Opt. Lett.,* vol. 32, pp. 781-783, 2007.

[186] S. Darmawan, Y. M. Landobasa, P. Dumon, R. Baets, and M. K. Chin, "Nested-Ring Mach-Zehnder Interferometer on Silicon-on-Insulator," *IEEE Photon. Technol. Lett.,* vol. 20, pp. 9-11, 2008.

[187] T. A. Ibrahim, R. Grover, L.-C. Kuo, S. Kanakaraju, L. C. Calhoun, and P.-T. Ho, "All-optical AND/NAND logic gates using semiconductor microresonators," *IEEE Photon. Technol. Lett.,* vol. 15, pp. 1422-1424, 2003.

[188] D. A. B. Miller, "Refractive Fabry-Perot Bistability with Linear Absorption: Theory of Operation and Cavity optimization," *IEEE J. Quantum Electron.,* vol. 17, pp. 306-311, 1981.

[189] Y. Dumeige, D. Arnaud, and P. Feron, "Combining FDTD with coupled mode theories for bistability in micro-ring resonators," *Opt. Commun.,* vol. 250, pp. 376-383, 2005.

[190] V. Van, T. A. Ibrahim, P. P. Absil, F. G. Johnson, R. Grover, and P.-T. Ho, "Optical signal processing using nonlinear semiconductor microring resonators," *IEEE J. Quantum Electron.,* vol. 8, pp. 705-713, 2002.

[191] Y. Dumeige and P. Feron, "Dispersive tristability in microring resonator," *Phys. Rev. E,* vol. 72, p. 66609, 2005.

[192] J. Danckaert, K. Fobelets, and I. Veretennicoff, "Dispersive optical bistability in stratified structures," *Phys. Rev. B,* vol. 44, p. 8214, 1991.

[193] B. Maes, P. Bienstman, and R. Baets, "Switching in coupled nonlinear photonic crystal resonators," *J. Opt. Soc. Am. B,* vol. 22, pp. 1778-1784, 2005.

[194] V. R. Almeida and M. Lipson, "Optical bistability on a silicon chip," *Opt. Lett.,* vol. 29, pp. 2387-2389, 2004.

[195] G. Barbarossa, A. M. Matteo, and M. N. Armenise, "Theoretical analysis of triple-coupler ring-based optical guided-wave resonator," *Lightwave Technology, Journal of,* vol. 13, pp. 148-157, 1995.